Collective oscillations
of an ultracold quantum gas
in the BEC-BCS crossover regime

Dissertation

zur Erlangung des akademischen Grades
Doktor der Naturwissenschaften

eingereicht an der
Fakultät für Mathematik, Informatik und Physik
der Universität Innsbruck

von

Alexander Altmeyer

durchgeführt am Institut für Experimentalphysik
unter der Leitung von
Univ.-Prof. Dr. Rudolf Grimm

Innsbruck, Mai 2007

Abstract

This thesis reports on detailed studies of collective oscillations of an ultracold gas of fermionic ^{6}Li atoms. A key feature for our experiments is the tunability of particle-particle interactions. This is realized in the vicinity of a broad magnetic Feshbach resonance. The Feshbach resonance also has the effect that there exists a stable bosonic molecular ^{6}Li$_2$ state on the repulsive interaction side of the resonance. These molecules can form a Bose-Einstein condensate (BEC). On the other side of the resonance fermionic atoms form Cooper pairs and the system can enter a superfluid Bardeen-Cooper-Schrieffer (BCS) state. There is a smooth crossover between the limits of a molecular BEC and a superfluid fermionic quantum gas in the BCS state. This BEC-BCS crossover is an interesting model system for other fields of physics, e.g. neutron stars or high-temperature superfluidity. Our experiments allow for measurements in this crossover regime.

Collective oscillations are a useful tool to study the properties of many-body systems. In this thesis, we present different low-energy collective oscillation modes. We focus on radial modes of a cigar-shaped gas cloud, as these are suited best for measurements in our experimental setup. In particular, we give a theoretical description of the radial compression mode, the radial quadrupole surface mode and the radial scissors mode.

We conduct precision measurements of the frequency of the radial compression mode. This probes the equation of state of the system and allows for a detection of beyond mean-field effects. The experimental results fully agree with theoretical predictions in the unitarity and in the BEC limit. High precision results in the strongly interacting BEC regime allow for a detailed quantitative analysis of theoretical models and favor quantum Monte Carlo theory over mean-field BCS theory.

The radial quadrupole surface mode is not affected by the equation of state of the system. Therefore we use this mode to determine if the gas is in the hydrodynamic or in the collisionless regime. We examine frequency and damping of this mode, along with its expansion dynamics. Our results show the transition between the collisional regimes in the BEC-BCS crossover.

We present first results on the radial scissors mode that show the way to future experiments. A detailed characterization of the temperature dependence of this mode together with studies of rotating systems open up possibilities to test superfluidity. This enables us to study superfluidity at temperatures of a few ten percent of the Fermi temperature. In this way our experiments with ultracold gases in the BEC-BCS crossover regime are connected to theories of high-temperature superconductivity.

Zusammenfassung

In dieser Arbeit präsentieren wir detaillierte Untersuchungen der kollektiven Oszillationen eines ultrakalten Gases von fermionischen ^{6}Li Atomen. Für unsere Experimente ist die Abstimmbarkeit der Teilchen-Teilchen Wechselwirkung fundamental, was wir mittels einer breiten magnetischen Feshbach Resonanz realisieren. Diese Feshbach Resonanz ermöglicht auf der Seite mit abstoßender Wechselwirkung die Bildung stabiler, bosonischer ^{6}Li$_2$ Moleküle, die ein Bose-Einstein Kondensat (BEC) bilden können. Auf der anderen Seite der Resonanz bilden sich Cooper-Paare aus fermionischen Atomen, was zur Bildung des suprafluiden Bardeen-Cooper-Schrieffer (BCS)-Zustands führen kann. Zwischen den beiden Grenzfällen eines BECs und eines BCS-Zustandes findet ein kontinuierlicher Übergang statt. Dieser BEC-BCS Crossover ist ein interessantes Modellsystem für andere Teilgebiete der Physik wie beispielsweise Neutronensterne oder Hochtemperatursupraleitung. Unsere Experimente ermöglichen konkrete Messungen in diesem Crossover-Regime.

Kollektive Oszillationen sind eine Methode zur Untersuchung der Eigenschaften von Vielteilchensystemen. Wir stellen niederenergetische kollektive Oszillationsmoden vor, wobei wir uns auf die für unseren experimentellen Aufbau geeigneten radialen Moden einer zigarrenförmigen Wolke beschränken. Wir beschreiben insbesondere die radiale Kompressionsmode, die radiale Quadrupolmode und die radiale Schermode.

Wir messen die Frequenz der radialen Kompressionsmode, was eine Untersuchung der Zustandsgleichung des Systems, insbesondere auf über die mean-field Beschreibung hinausgehende Effekte, ermöglicht. Unsere Ergebnisse stimmen mit theoretischen Berechnungen im Limes unitärer Wechselwirkung und im BEC-Limes überein. Hochpräzisionsmessungen im stark wechselwirkenden BEC Regime erlauben außerdem eine detaillierte quantitative Überprüfung theoretischer Modelle und bestätigen die Quanten-Monte-Carlo Theorie gegenüber der mean-field BCS Theorie.

Die radiale Quadrupolmode wird nicht von der Zustandsgleichung des Systems beeinflußt. Deshalb nutzen wir diese Mode um festzustellen, ob sich das Gas im hydrodynamischen oder im kollisionsfreien Regime befindet. Wir messen neben Frequenz und Dämpfung dieser Mode auch ihre Expansionsdynamik. Unsere Ergebnisse zeigen den Übergang zwischen diesen beiden Regimen im BEC-BCS Crossoverbereich.

Wir zeigen abschließend erste Ergebnisse zur radialen Schermode. Eine genaue Charakterisierung der Temperaturabhängigkeit dieser Mode zusammen mit einer Untersuchung rotierender Systeme eröffnet neue Untersuchungsmöglichkeiten von Suprafluidität. Auf diese Weise können wir Suprafluidität bei Temperaturen von mehreren zehn Prozent der Fermitemperatur erforschen. Unsere Experimente mit ultrakalten Gasen im BEC-BCS Crossover ermöglichen somit den Brückenschlag zur Theorie der Hochtemperatursupraleitung.

Contents

Contents

x

Chapter 1

Introduction

Progress in physics is connected with both qualitative and quantitative understanding of new phenomena. In recent years, the study of ultracold quantum gases with new experimental techniques has greatly advanced our understanding in many-body quantum physics. New qualitative phenomena have been observed, most prominently the experimental realization of Bose-Einstein condensates (BEC) [And95, Bra95, Dav95]. After the initial qualitative experiments, there have been quantitative measurements. These measurements have been conducted with great precision, which improved the understanding of theoretical models.

Particles can be classified according to their total spin. Particles with integer spin are bosons, whereas particles with half-integer spin are fermions. After the first creation of a BEC in dilute atomic gases in 1995 [And95, Bra95, Dav95], a rapid progress in the field of bosonic gases occurred. In a similar way, the exploration of fermions has been increasingly successful in recent years. Spectacular achievements have been the creation of quantum degenerate Fermi gases [DeM99, Tru01, Sch01] and of BECs of molecules with fermionic constituents [Joc03a, Gre03, Zwi03, Bou04, Par05]. The two main species for the creation of ultracold Fermi gases are the alkali atoms ^{40}K [DeM99, Roa02, Köh05, Osp06, Aub06] and ^{6}Li [Tru01, Sch01, Gra02, Had02, Joc03a, Sil05]. In this thesis, we will focus on experiments with ^{6}Li.

A key feature in experiments with ultracold fermionic atoms is the control of the interactions between the particles. Feshbach resonances [Ino98], which are magnetically tunable scattering resonances, serve as powerful tools for the control of interactions. In the vicinity of a Feshbach resonance, one can change the interactions from attractive to repulsive behavior.

An additional aspect is the existence of a weakly bound, diatomic molecular state on the repulsive interaction side of a Feshbach resonance. These weakly bound molecules consist of two fermionic atoms, but they are bosons themselves. For temperatures below a critical temperature, the bosonic molecules form a superfluid BEC.

There is also a superfluid state on the other side of the Feshbach resonance, the Baarden-Cooper-Schrieffer (BCS) state [Bar57b]. The BCS state does not consist of localized molecules, but of pairs correlated in momentum space. These pairs are called

Cooper pairs [Coo56].

The region of strong interactions around the Feshbach resonance links the two superfluid limits of the BEC and the BCS states; it is called BEC-BCS crossover region. Here, the quantum gas is governed by many body physics. The gas can be in different collective interaction regimes, in particular the hydrodynamic and the collisionless regime. The BEC-BCS crossover has attracted large theoretical interest for more than 35 years [Eag69, Leg80, Noz85, Eng97]. Experimental exploration started only a couple of years ago in the field of ultracold gases [Bar04b, Reg04, Zwi04, Bou04, Kin04a], after it became possible to tune interactions around a Feshbach resonance. Since then, several experiments probed the crossover regime with different experimental techniques. In this thesis, we focus on measurements of collective oscillations.

Collective oscillations of a trapped gas are a powerful tool for investigations of the macroscopic properties of the system. In the field of atomic BEC research, there have been intense studies of collective modes both in theory [Edw96, Str96, Fet96, Sin96] and in experiments [Jin96, Mew96, Jin97, SK98b, Ono00, Mar00, Che02]. Based on the rich experience with bosonic atoms, the study of collective oscillations of strongly interacting Fermi gases was a logical next step. The first experiments investigated the compression mode of a gas in an elongated trap geometry [Kin04a, Bar04a]. These experiments yielded qualitative results for the behavior in the BEC-BCS crossover. Detailed studies with quantitative results were conducted only in the near-unitarity regime [Kin04a].

Quantitative studies of the whole BEC-BCS crossover are the main topic of this thesis. Detailed results of collective oscillations in a cylindrically symmetric trap geometry enable us to conduct such studies. We present precision measurements of the radial compression mode that allow to distinguish between different theoretical models. Furthermore, we use the radial quadrupole surface mode and the radial scissors mode as a sensitive probe to map out the hydrodynamic or collisionless behavior of the gas in the BEC-BCS crossover regime.

Our results help to better understand the physics in the BEC-BCS crossover. We can experimentally test theoretical models, which have their origin even in other fields of physics. In this way, our results for an ultracold gas could also improve the knowledge of more complex systems, in particular in the field of high temperature superconductivity.

At the beginning of this thesis in chapter 2, we shortly introduce the properties of degenerate quantum gases in the BEC-BCS crossover that are relevant for our measurement. Then, in chapter 3 we describe the physics of the collective oscillations that we examine in our experiments. A brief description of our experimental setup with the focus on recent changes and additions is given in chapter 4. Afterwards, we present basic experimental methods in chapter 5. Our experimental results of measurements of the radial compression mode are shown in chapter 6. Then, in chapter 7, the results for the radial quadrupole surface mode are presented. Finally, chapter 8 gives an outlook for future experiments based on our most recent results of measurements of the scissors mode.

Chapter 2

Degenerate quantum gases in the BEC-BCS crossover

Experimental studies of degenerate quantum gases have opened a new field of physics in the past decades. In such degenerate gases exciting quantum mechanical features can be studied. This chapter introduces some basic concepts and definitions, which will be used throughout this thesis. First the basic properties of degenerate Bose and Fermi gases are presented in section 2.1 and 2.2, respectively. Then we will concentrate on the BEC-BCS crossover in section 2.3; in this section the focus of interest shifts from a general view to a more specific description of a ^{6}Li experimental system. In particular, a Feshbach resonance is a crucial tool to tune the particle-particle interaction strength and in this way explore this crossover. A very broad Feshbach resonance in ^{6}Li [Bar05b] enables us to study the BEC-BCS crossover between the limits of two superfluid systems: The one superfluid system is a dilute Bose-Einstein condensate (BEC) consisting of weakly bound molecules. The other is a Bardeen-Cooper-Schrieffer (BCS) state of Cooper pairs, which are correlated in momentum space only. This crossover region has been a subject of great theoretical interest for almost forty years [Eag69, Leg80, Noz85, Ran95, Che04] and has recently become accessible for experimental studies [Bar04b, Reg04, Zwi04, Bou04, Kin04a, Bar04a, Chi04a, Gre05, Kin04b, Kin05b, Gri07]. In this chapter the BEC-BCS crossover is introduced. Later in this thesis the central question how superfluid and hydrodynamic behavior is present throughout the BEC-BCS crossover arises. Collective oscillations as a unique probing tool help to answer this question.

The behavior of a gas, especially its statistical properties, depends on the temperature T. Fig. 2.1 shows an overview how decreasing temperature changes the characteristics of a gas. At higher temperatures, a gas can be considered to consist of point-like particles, like billiard balls, and is governed by Maxwell-Boltzmann statistics. In the classical limit, there is no difference between a gas consisting of bosons or fermions.

For decreasing temperatures, the particles can no longer be treated as point-like. These gases now are better described as quantum mechanical wave packets with a non-negligible spatial extent. As a quantity to describe the spatial extent of these quantum

mechanical wave packets, we introduce the thermal de Broglie wavelength

$$\lambda_{dB} = \sqrt{\frac{2\pi\hbar^2}{mk_BT}}, \tag{2.1}$$

where m is the mass of the particle and k_B is Boltzmann's constant.
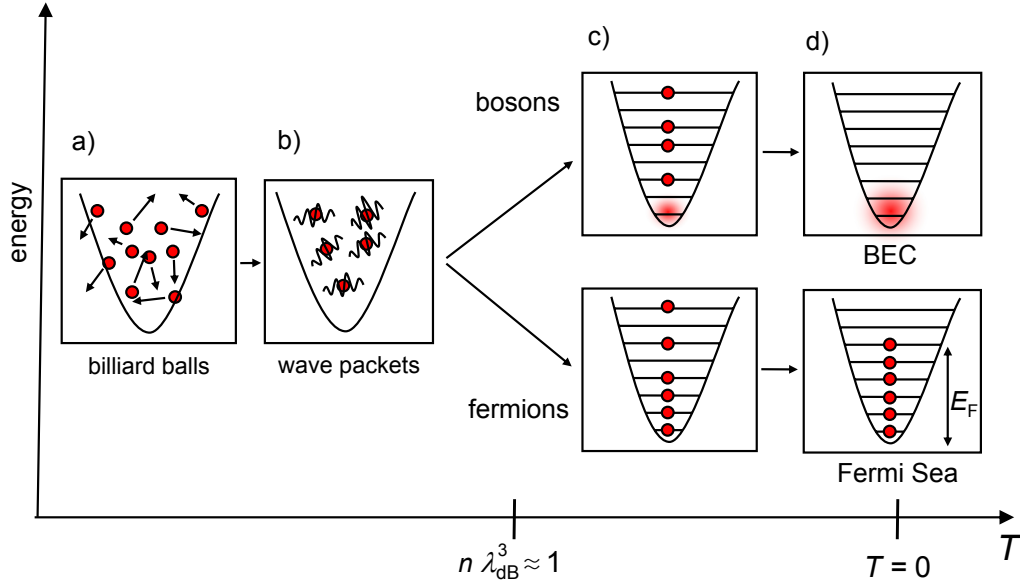
Figure 2.1: Transition from a classical gas of identical particles into a quantum mechanically governed degenerate gas. At high temperature the mean interparticle distance is much larger than the size of the particles and they can be considered as point-like (a). If the temperature is lowered, the wave-packet nature of the particles gives rise to quantum mechanical behavior (b). For temperatures where the de Broglie wavelength is on the order of the interparticle spacing ($n\lambda_{dB}^3 \approx 1$), bosons begin to form a BEC and occupy the ground state of the trap (c, upper row). fermions however fill up the lowest lying states, occupying each state by only one particle (c, lower row). In the limit of $T = 0$ a pure BEC and a completely filled Fermi sea are formed, respectively (d).

At even lower temperatures, the extent of the wave packets starts to get larger than the interparticle spacing, which is given by $n^{-1/3}$ in a gas of density n. Thus the individual wave-packets begin to overlap. The phase space density D of a gas is defined as

$$D = n\lambda_{dB}^3. \tag{2.2}$$

For $D \approx 1$ the gas becomes degenerate. Here the wave packets start to overlap. For a degenerate quantum gas, differences between bosons and fermions emerge. bosons would condense in the ground state, which marks the onset of Bose-Einstein condensation . For $T = 0$, bosons form a pure Bose-Einstein condensate (BEC), all particles populate the ground state.

Fermions, however, can occupy each state by only one particle. Therefore, there is no macroscopic occupation of the ground state for fermions, which fill up the lowest lying states instead. The Fermi energy E_F marks the energy, up to which all lower lying states are filled with exactly one particle. The corresponding temperature T_F is called Fermi temperature. A degenerate Fermi gas at $T < T_F$ consists only of a gapless series of filled energy states, which is also called a Fermi sea.

2.1 Degenerate Bose gases

This section describes some basic features of Bose gases and BECs. First, in 2.1.1, an ideal, noninteracting Bose gas and the degenerate case of a noninteracting BEC are described. This simplified system can already be used to describe some main features of a BEC. Later, in 2.1.2, the case of an interacting BEC is considered. Including interactions enables us to describe the whole system with a single wave-function in the Gross-Pitaevskii equation. Furthermore, a description in the Thomas-Fermi limit enables us to calculate the density and the chemical potential of the system in a simple way.

Both noninteracting and interacting BEC are superfluid, which is important in the context of collective oscillations (see 3.1). For a detailed overview of the phenomenon of Bose-Einstein condensation, the textbooks of Pethick and Smith [Pet02] as well as of Pitaevskii and Stringari [Pit03] are recommended.

2.1.1 Ideal, noninteracting Bose gas

The simplest approach to describe a Bose gas is to consider it as an ideal, noninteracting gas. This approach leads to the Bose-Einstein distribution function and includes the feature of Bose-Einstein condensation. We derive the critical temperature T_c for the onset of Bose-Einstein condensation and calculate the number of particles in a BEC for temperatures below T_c.

An ideal Bose gas consists of noninteracting particles. For an ideal Bose gas in thermodynamic equilibrium, the mean occupation number N_i of a single particle state i with energy ϵ_i is given by the Bose-Einstein distribution function

$$N_i = n(\epsilon_i) = \frac{1}{\exp\left[(\epsilon_i - \mu)/k_B T\right] - 1},$$
(2.3)

where μ is the chemical potential. μ is fixed by the normalization condition $N = \sum_i N_i$ and can be calculated as a function of T and total particle number N. For the limit of high temperatures, the Bose-Einstein distribution is well approximated by the classical Maxwell-Boltzmann distribution.

For low temperatures, the chemical potential μ approaches the energy ϵ_0 of the

ground state. The occupation number N_0 of the ground state is given by:

$$N_0 = n(\epsilon_0) = \frac{1}{\exp\left[(\epsilon_0 - \mu)/k_B T\right] - 1}.$$
(2.4)

For $\mu \to \epsilon_0$, N_0 becomes increasingly large. This macroscopic occupation of the ground state is the origin of Bose-Einstein condensation.

The total number of particles $N = N_0 + N_T$ consists of the particles in the ground state N_0 and the number of excited particles N_T given by

$$N_T(T, \mu) = \sum_{i \neq 0} N_i(T, \mu).$$
(2.5)

For fixed T and $\mu \to \epsilon_0$, there is a maximum of N_T given by

$$N_{T,max} = \sum_{i > 0} \frac{1}{\exp\left[(\epsilon_i - \epsilon_0)/k_B T\right] - 1}.$$
(2.6)

In a harmonic trap with trap frequency ω, Eq.(2.6) can be written as

$$N_{T,max} = \int_0^\infty d\epsilon \, \frac{\epsilon^2}{2\hbar^3 \omega^3 \left(\exp\left(\epsilon/k_B T\right) - 1\right)}.$$
(2.7)

If $N_{T,max} < 0$, there must be a macroscopic number of particles in the ground state. This is the onset of Bose-Einstein condensation. A critical temperature T_c can be connected with this onset and is given by [Pit03]

$$T_c = \frac{\hbar \omega}{k_B} \left(\frac{N}{\zeta(3)}\right)^{1/3},$$
(2.8)

where ζ is Riemann's zeta function.

For the number of particles in the condensate N_0, one finds for $T < T_c$ [Pit03]

$$N_0 = N\left(1 - \left(\frac{T}{T_c}\right)^{3/2}\right).$$
(2.9)

2.1.2 Interacting BEC

In contrast to the ideal noninteracting Bose gas, we now include particle-particle interactions in the theoretical concepts. For ultracold temperatures, the relevant parameter to describe these interactions is the s-wave scattering length a [Pit03]. As long as interactions are weak, they can be described by a meanfield interaction. Such a description is only valid as long as the following condition of diluteness is valid

$$n|a|^3 \ll 1.$$
(2.10)

With such a meanfield-approach, Gross [Gro61] and Pitaevskii [Pit61] showed independently that at $T = 0$ and in the limit of $N \gg 1$ the condensate wave function $\Phi(\mathbf{r}, t)$ (also referred to as the order parameter) obeys the Gross-Pitaevskii equation

$$i\hbar \frac{\partial}{\partial t} \Phi(\mathbf{r}, t) = \left(-\frac{\hbar^2 \nabla^2}{2m} + V_{\text{ext}}(\mathbf{r}) + g|\Phi(\mathbf{r}, t)|^2 \right) \Phi(\mathbf{r}, t), \tag{2.11}$$

where $g = 4\pi\hbar^2 a/m$ is the coupling constant. The Density and the wave function of the condensate are related by $n(\mathbf{r}, t) = |\Phi(\mathbf{r}, t)|^2$.

Stationary solutions of the Gross-Pitaevskii eqn.(2.11) take the form

$$\Phi(\mathbf{r}, t) = \Phi(\mathbf{r}) \exp\left(\frac{-i\mu t}{\hbar} \right), \tag{2.12}$$

where $\Phi(\mathbf{r})$ is normalized by $\int d\mathbf{r}\, |\Phi(\mathbf{r})|^2 = N$.

With Eq.(2.12), the Gross-Pitaevskii equation reduces to

$$\left(-\frac{\hbar^2 \nabla^2}{2m} + V_{\text{ext}}(\mathbf{r}) + g|\Phi(\mathbf{r})|^2 \right) \Phi(\mathbf{r}) = \mu \Phi(\mathbf{r}). \tag{2.13}$$

From Eq.(2.11) one also obtains the continuity equation

$$\frac{\partial n}{\partial t} + \nabla \mathbf{j} = 0, \tag{2.14}$$

where $\mathbf{j}$ is the current density of the gas [Pit03].

Thomas-Fermi limit

In the Thomas-Fermi limit, the kinetic energy term in the Gross-Pitaevskii equation ((2.11) and (2.13)) can be neglected. In this limit, the Gross-Pitaevskii equation simplifies to an equation which coincides to a classical Euler equation of a gas with pressure $P = gn^2/2$ and superfluid velocity $\mathbf{v_s}$ [Pit03]

$$m\frac{\partial}{\partial t} \mathbf{v_s} + \nabla \left(\frac{1}{2} m \mathbf{v_s}^2 + V_{\text{ext}} + gn \right) = 0. \tag{2.15}$$

Also the continuity equation (2.14) simplifies to

$$\frac{\partial n}{\partial t} + \nabla(\mathbf{v_s} n) = 0. \tag{2.16}$$

The density profile in the Thomas-Fermi regime is given by [Bay96]

$$n(\mathbf{r}) = \begin{cases} [\mu - V_{\text{ext}}(\mathbf{r})]/g & , \mu \geq V_{\text{ext}} \\ 0 & , \mu < V_{\text{ext}}. \end{cases} \tag{2.17}$$

With the normalization $N = \int d\mathbf{r}\, n(\mathbf{r})$, the chemical potential in a harmonic trapping potential is given by [Pit03]

$$\mu = \frac{\hbar\omega_i}{2}\left(\frac{15Na}{a_{\text{ho}}}\right)^{2/5},$$
(2.18)

where we introduced the harmonic oscillator length

$$a_{\text{ho}} = \left(\frac{\hbar}{m\omega_i}\right)^{1/2},$$
(2.19)

where ω_i is the trap frequency in the direction of interest.

The density profile of a BEC in the Thomas-Fermi limit takes the form of an inverted parabola and becomes zero at the Thomas-Fermi radius R_{TF}, which is described by

$$R_{TF} = \sqrt{\frac{2\mu}{m\omega_i^2}} = a_{\text{ho}}\left(\frac{15Na}{a_{\text{ho}}}\right)^{1/5}.$$
(2.20)

The peak density is determined by

$$n_{max} = \frac{\mu}{g} = \frac{1}{8\pi}\left(\frac{(15N)^2}{a^3 a_{ho}^{12}}\right)^{1/5}.$$
(2.21)

2.2 Degenerate Fermi gases

This section describes the properties of a degenerate Fermi gas. An ideal Fermi gas is described in 2.2.1. There, we focus on the case of an ideal Fermi gas at $T = 0$ in a harmonic trapping potential. In 2.2.2 the influence of interactions on a Fermi gas are described.

2.2.1 Ideal Fermi gas

For identical fermions, the distribution function $f(\epsilon)$ of a single particle state i with the energy ϵ_i is given by the Fermi-Dirac distribution function

$$f(\epsilon_i) = \frac{1}{\exp\left[(\epsilon_i - \mu)/k_B T\right] + 1},$$
(2.22)

where μ is the chemical potential.

In the presence of a harmonic trapping potential with trap frequency ω, the normalization condition

$$N = \int d\epsilon \frac{\epsilon^2}{2(\hbar\omega)^3} f(\epsilon)$$
(2.23)

for a number of N identical fermions determines the chemical potential μ in Eq.(2.22).

In the limit of $T = 0$, all states with energies smaller than the chemical potential $\mu(T = 0)$ are occupied, whereas all states with larger energies are unoccupied (see Fig. 2.1). This crucial energy $\mu(T = 0)$ is also called Fermi energy E_F, with

$$E_F = \mu(T = 0) = k_B T_F, \tag{2.24}$$

where T_F is the so-called Fermi temperature. For temperatures $T < T_F$ the gas is said to be quantum degenerate.

With the definition of the Fermi energy (2.24) one can also define the Fermi wavenumber k_F by

$$k_F = \frac{\sqrt{2mE_F}}{\hbar}. \tag{2.25}$$

From Eq.(2.23), the Fermi energy in a harmonic trap is found to be

$$E_F = \hbar\omega(6N)^{1/3}, \tag{2.26}$$

which results in a Fermi wave number

$$k_F = \sqrt{2m\frac{\omega(6N)^{1/3}}{\hbar}}. \tag{2.27}$$

Similar to the Thomas-Fermi radius of a degenerate Bose gas (see Eq.(2.20)), from (2.26) one finds a characteristic size R_F of a Fermi gas with

$$R_F = \sqrt{\frac{2E_F}{m\omega^2}} = a_{\text{ho}}(48N)^{1/6}. \tag{2.28}$$

For the experimentally relevant case of a cylindrically symmetric trap with axial trap frequency ω_z, axial width Z, radial trap frequency ω_r and radial width R, the spatial density distribution $n(\mathbf{r})$ is found to be [Pit03]

$$n(\mathbf{r}) = \frac{8}{\pi^2} \frac{N}{R^2 Z} \left(1 - \frac{r^2}{R^2} - \frac{z^2}{Z^2}\right)^{3/2}. \tag{2.29}$$

Using the Fermi wavenumber k_F, one can derive the corresponding momentum distribution [Pit03]

$$n(\mathbf{k}) = \frac{8}{\pi^2} \frac{N}{\hbar^3 k_F^3} \left(1 - \frac{k^2}{k_F^2}\right)^{3/2}. \tag{2.30}$$

2.2.2 Interacting Fermi gas and BCS theory

In 2.2.1 an ideal Fermi gas consisting of identical particles is described. Such a Fermi gas is noninteracting, as Pauli's exclusion principle prohibits collisions between cold particles. In a mixture of cold fermions with different spin states however, interactions via collisions are possible. This case becomes important in our experiment as we work with a mixture of two spin states of ^{6}Li (for details see 2.3.1.

For a spin mixture of fermions with attractive interactions, there exists a superfluid state at low temperatures ($T \lesssim 0.1 T_\mathrm{F}$). This phase transition is equivalent to the transition of electrons into the superconducting state. The theory describing this transition is called BCS theory after the work of Bardeen, Cooper and Schrieffer [Bar57b]. According to BCS theory, two fermions with opposite spin and momentum can be coupled by an effective attractive interaction to form a bound state of delocalized, composite particles. These pairs in momentum space are called Cooper pairs [Coo56] and are bosons, even though their constituents are fermions. Therefore, Cooper pairs can condensate in the ground state in a way quite similar to Bose-Einstein condensation.

A consequence of BCS theory is the existence of a pairing gap in the excitation spectrum of the superfluid gas. For a uniform Fermi gas at zero temperature, that interacts with attractive s-wave interactions, the pairing gap is found to be [Gor61]

$$\Delta = \left(\frac{2}{e} \right)^{7/3} E_\mathrm{F} \exp\left(-\frac{\pi}{2 k_\mathrm{F} |a|} \right) \approx 0.49 E_\mathrm{F} \exp\left(-\frac{\pi}{2 k_\mathrm{F} |a|} \right). \quad (2.31)$$

The transition from the normal to the superfluid phase takes place at a critical temperature T_c. This temperature is directly related to the value of the pairing gap at zero temperature (2.31) and is given by [Gor61]

$$T_\mathrm{c} = \frac{e^C}{\pi} \left(\frac{2}{e} \right)^{7/3} \frac{E_\mathrm{F}}{k_\mathrm{B}} \exp\left(-\frac{\pi}{2 k_\mathrm{F} |a|} \right) \approx 0.28 \frac{E_\mathrm{F}}{k_\mathrm{B}} \exp\left(-\frac{\pi}{2 k_\mathrm{F} |a|} \right), \quad (2.32)$$

with C being Euler' s constant ($C \approx 0.577$). Note that due to an exponential factor the critical temperature in a dilute gas, obeying the condition $k_\mathrm{F} |a| \ll 1$, is much smaller than the Fermi energy.

2.3 BEC-BCS crossover

In sections 2.1 and 2.2, we introduced the superfluid regimes of BEC and BCS, and described both in a general way. In this section, we want to leave the general description and focus on the specific case of a system consisting of ^{6}Li atoms. Both regimes can be realized with pairs consisting of two fermionic ^{6}Li atoms. In the case of localized molecules, a molecular BEC can be created. For dimers consisting of Cooper pairs, which are not localized and only correlated in momentum space, the BCS state can be reached. Repulsive interactions are necessary for a stable BEC state, whereas the BCS regime requires attractive interactions of the particles. By changing the interactions from repulsive to attractive ones, a transition from a BEC to a BCS state is possible.

In this section we describe the control of interactions in a gas of ^{6}Li atoms by a magnetically tunable Feshbach resonance. The Feshbach resonance provides the possibility to smoothly change the particle-particle interactions in the gas from repulsive to attractive ones by changing the scattering properties of the particles. The Feshbach resonance is also connected with the existence of a weakly bound molecular state. This

enables us to create extremely stable dimers of ^{6}Li atoms with lifetimes of > 30s at magnetic fields below the position of the Feshbach resonance at 834G [Bar05b]. These molecules can form a weakly interacting BEC of molecules, which is one of the two limits of the BEC-BCS crossover. Approaching the resonance from this "BEC-side" interactions get stronger and our system of a strongly interacting BEC is no longer described by mean-field interactions. The precise quantitative exploration of this strongly interacting BEC regime is the major goal of the collective compression mode experiments(see section 3.2 for a theoretical and chapter 6 for an experimental description). In the vicinity of the resonance position, interactions get so strong that they are only limited by unitarity. In this so called unitarity regime, our system can be considered as a strongly interacting Fermi gas. Unique features like resonance superfluidity and universal behavior of a Fermi gas are predicted in this regime. For magnetic fields above the resonance position, interactions are attractive and no molecular state exists like on the other side of the resonance. Here, on the so-called "BCS-side" of the resonance, Cooper pairs are formed, which can lead to the existence of a superfluid BCS state for low enough temperatures. Being strong near to the resonance, interactions get weaker for increasing magnetic fields so that finally the limit of a weakly interacting BCS state is reached.
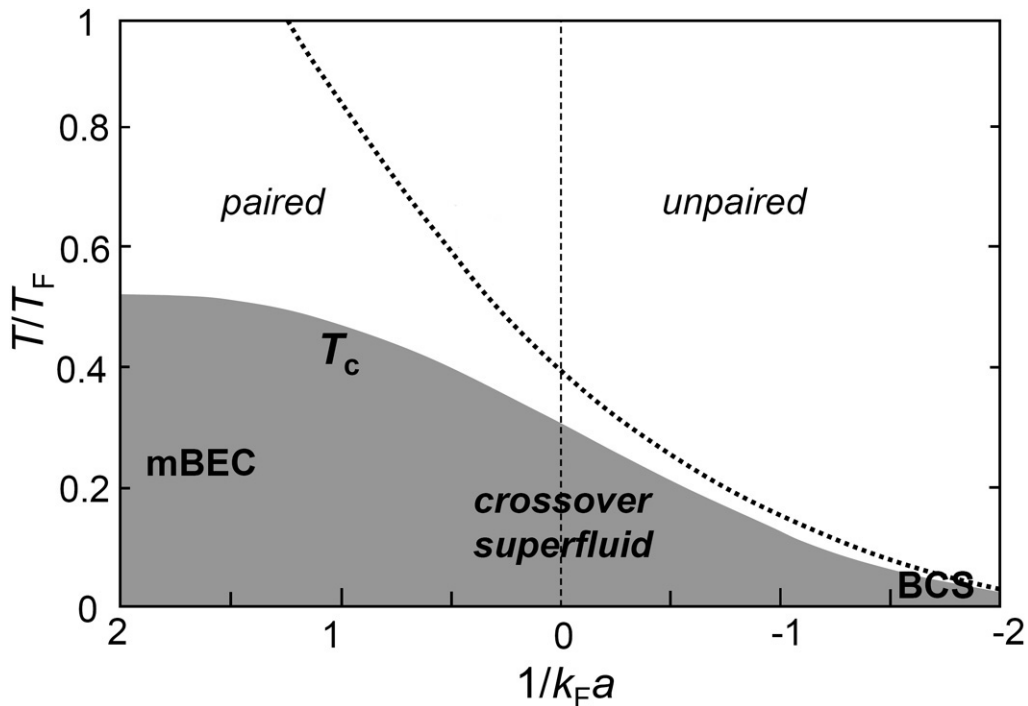
Figure 2.2: Schematic phase diagram of a gas in a harmonic trapping potential for the BEC-BCS crossover [Per04]. The range of $1/k_F a$ spans from the molecular BEC regime over the unitarity regime at resonance ($1/k_F a = 0$) until the BCS regime. The phase transition from the normal to the superfluid phase is marked by the critical temperature T_c.

In order to describe the BEC-BCS crossover, the interaction parameter $1/k_F a$ turned out to be useful. Here k_F is the Fermi wave number (see Eq.(2.25)) and a is the atomic s-wave scattering length (see the following subsection).

2.3.1   Interactions in ^{6}Li and Feshbach resonance

Interactions in a gas of ultracold ^{6}Li atoms are mainly determined by s-wave scattering. An important parameter to describe the interactions is the atomic s-wave scattering length a. For $a > 0$, interactions are repulsive, for $a < 0$ attractive. According to Pauli's exclusion principle a mixture of different spin states is necessary for interactions between fermionic ^{6}Li atoms. We therefore use an equal mixture of the two lowest lying spin states of the electronic $S_{1/2}$ ground state of ^{6}Li.
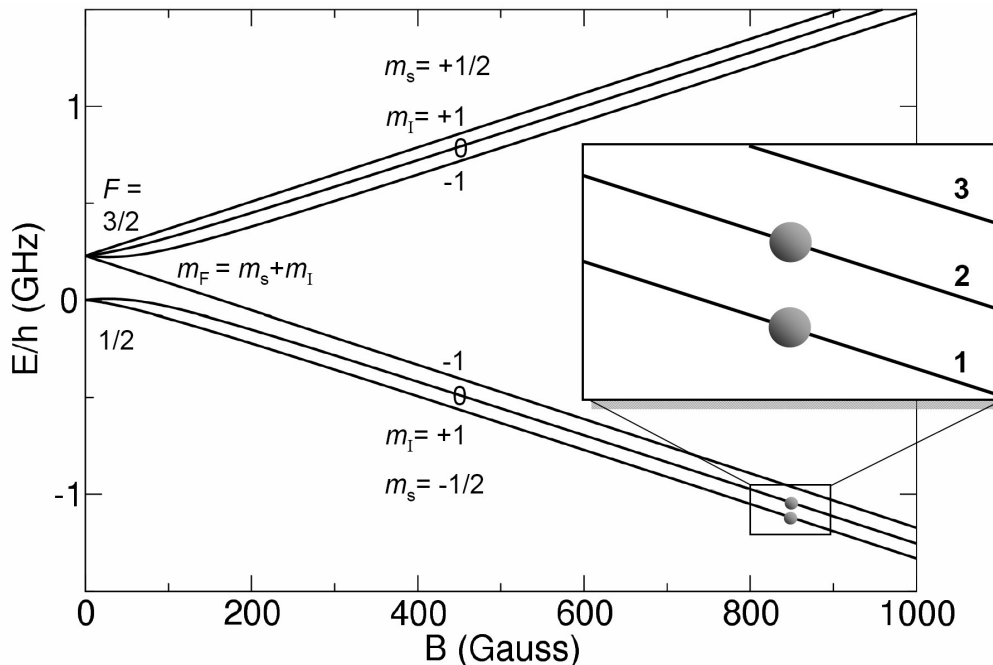
Figure 2.3: Energies of the different spin configurations for the electronic ground state of ^{6}Li atoms in a magnetic field. Important for our experiments is mainly the high magnetic field range, where the nuclear spin essentially decouples from the electron spin. We use a two component mixture of atoms in the lowest two states, labeled with 1 and 2 (inset), close to the broad Feshbach resonance centered at 834 G.

Fig. 2.3 shows the magnetic field dependence of the energy structure of ^{6}Li in the $S_{1/2}$ state. In general, ^{6}Li behaves similar to any alkali atom [Ari77] and is described by the Breit-Rabi formula. There is a coupling of the nuclear spin I to the angular momentum of the electron J at zero magnetic field. This leads to a hyperfine splitting of 228.2 MHz between the states with quantum number $F = I + J = 1 + 1/2 = 3/2$ and $F = I - J = 1/2$. For higher magnetic fields, when the Zeeman energy

becomes larger than the energy of the hyperfine splitting, the nuclear spin decouples from the electron spin. In this so-called Paschen-Back regime the quantum number F is no longer suited to distinguish between the different energy levels. Instead, the atom's energy structure is well described by the orientation of electron spin m_s and the orientation of the nuclear spin m_I. Two triplets of energy levels are formed, which show the same magnetic field dependence for the same orientation of m_s. Throughout this thesis, the energy levels are labeled with numbers according to increasing energy (see inset in Fig. 2.3). For our experiments we use mixtures of the two energetically lowest spin states $|1\rangle$ ($m_s = -1/2, m_I = +1$) and $|2\rangle$($m_s = -1/2, m_I = 0$). These states are adiabatically connected with the states $F = 1/2$, $m_F = 1/2$ and $F = 1/2$, $m_F = -1/2$ at low magnetic fields.
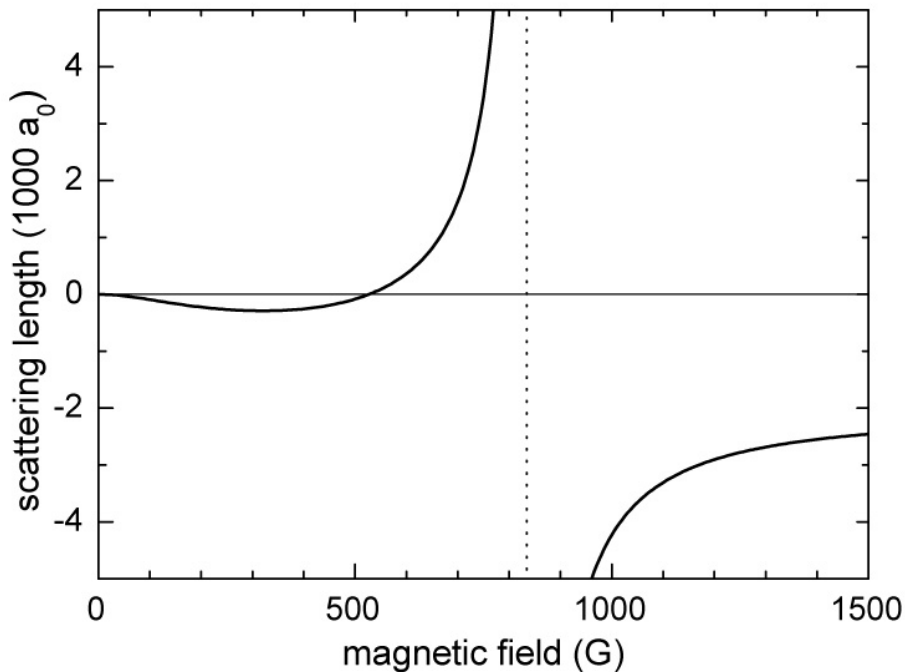
Figure 2.4: Magnetic tunability of the s-wave scattering length a around a broad Feshbach resonance [Hou98, Bar05a]. a is plotted versus magnetic field for a spin mixture of ^{6}Li atoms in the two lowest spin states. The vertical dotted line indicates the exact resonance field (834G), where a goes to infinity and the interaction is only limited through unitarity.

For a mixture of ^{6}Li atoms in the two lowest spin states $|1\rangle$ and $|2\rangle$, there exists a Feshbach resonance [Fes58, Tie93, Ino98] in the atomic s-wave scattering length a [Hou98]. The scattering length a as a function of the magnetic field B is displayed in

Fig. 2.4. There is a pronounced resonance feature around the central magnetic field of $B_0 = 834.15$ G. In the vicinity of the Feshbach resonance both large positive and negative scattering lengths can be achieved. At magnetic fields below B_0, particle-particle interactions are repulsive and the scattering length a is positive, until at a zero-crossing at about 530 G [O'H02b, Joc02] a starts becoming negative for decreasing magnetic field strength. For all experimental reachable magnetic fields above B_0, the scattering length is negative (i.e. interactions are attractive).

In order to describe of the s-wave scattering length from the magnetic field B, we introduce a fit formula [Bar05a]. For magnetic fields between 600 and 1200 G the scattering length a can be fitted to better than 99% by the formula

$$a(B) = a_{\text{bg}} \left(1 + \frac{\Delta B}{B - B_0} \right) (1 + \alpha(B - B_0)), \tag{2.33}$$

with the background scattering length $a_{\text{bg}} = -1405\ a_0$, the width of the resonance $\Delta B = 300$ G and $\alpha = 0.040\ \text{kG}^{-1}$. Here $a_0 = 0.0529177$ nm is Bohr's radius.

This Feshbach resonance enables us to change interactions and in this way access the BEC-BCS crossover regime by changing the magnetic field B. The ^{6}Li Feshbach resonance at 834 G is especially broad compared to other resonances. This broadness enables one to precisely tune $a(B)$ within the experimentally achievable precision of magnetic field control.

Besides the broad 834 G resonance for a spin mixture in the states $|1\rangle$ and $|2\rangle$, there exists a similar broad s-wave resonances for spin mixtures in the states $|1\rangle$ and $|3\rangle$ ($|2\rangle$ and $|3\rangle$), which is centered at 690 G (811 G). Furthermore, there is a significantly narrower resonance of the states $|1\rangle$ and $|2\rangle$ centered at 543 G [Die02, O'H02b, Str03]. There have also been p-wave scattering resonances of ^{6}Li observed [Zha04, Sch05].

For magnetic fields below the Feshbach resonance at 834 G, where the scattering length is positive, the atoms are weakly bound in a molecule. This molecular state is crucial for the creation of a molecular BEC like described in 5.1. A condition for the existence of this molecular state is a large enough scattering length with

$$a \gg R_{\text{vdW}}, \tag{2.34}$$

where

$$R_{\text{vdW}} = (mC_6/\hbar)^{1/4} /2 = 31.26 a_0 \tag{2.35}$$

is the characteristic length of the van der Waals interaction between two ^{6}Li atoms.

The binding energy of the weakly bound molecular state is given by [Gri93]

$$E_{\text{b}} = \frac{\hbar^2}{m(a - \bar{a})^2}, \tag{2.36}$$

where $\bar{a}$ is the mean scattering length given by $\bar{a} = 0.956 R_{\text{vdW}}$. Eq.(2.36) is based on the universal expression $E_{\text{b}} = \hbar^2/(ma^2)$ [Lan77] and includes a correction for the non-zero range of the van der Waals potential. Fig. 2.5 shows the binding energy E_{b}

calculated by Eq.(2.36) as a function of the magnetic field. For magnetic fields below approximately 600 G equation 2.36 starts to deviate because the scattering length is decreasing and becomes similar to R_{vdW}.
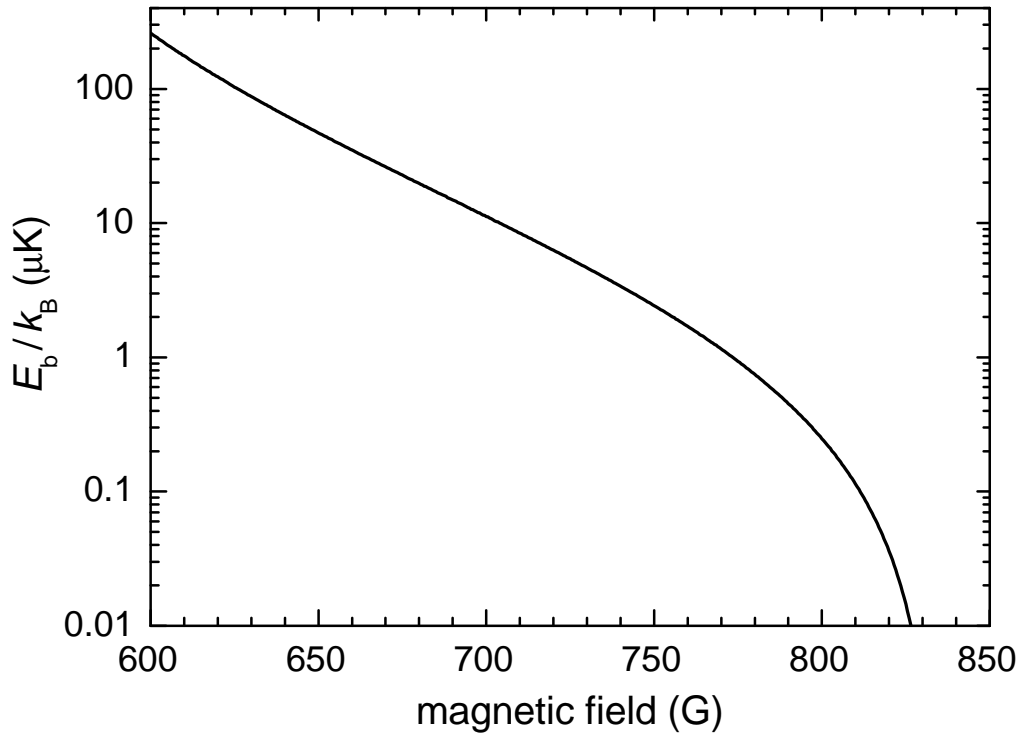
Figure 2.5: Calculated molecular binding energy for ^{6}Li molecules. The calculation is based on equation 2.36. The units are chosen for comparison with experimental temperatures ($k_B \times 1\mu K \approx h \times 20.8$kHz).

A characteristic feature of the weakly bound molecules is their large size. The molecular wave function extends over a much larger range than the interaction potential and falls off exponentially for large interatomic distances $r \gg R_{vdW}$. This regime, where the size of the bound quantum object exceeds the size of the classical system, is also called "quantum halo regime" [Jen04]. Details of the short-range interaction are no longer relevant for such quantum halo states and their physics acquires universal character [Bra06]. Therefore, the two-body interactions for these quantum halo molecules are completely characterized by a single parameter, the atomic s-wave scattering length a.

These molecules show a remarkable stability against inelastic decay in atom-dimer and dimer-dimer collisions, as they consist of two fermionic atoms [Pet04]. The suppression of these loss mechanisms is based on Pauli blocking. An inelastic collision requires three particles to be at the same time at very short distances towards each other. So necessarily two identical fermions are involved, which is blocked by Pauli's exclusion principle.

The loss-rate coefficients α_{ad} and α_{dd}, which describe inelastic atom-dimer and dimer-dimer collision, respectively, are found to be [Pet04]

$$\alpha_{\text{ad}} = c_{\text{ad}} \frac{\hbar R_{\text{vdW}}}{m} \left(\frac{R_{\text{vdW}}}{a} \right)^{3.33}, \tag{2.37}$$

$$\alpha_{\text{dd}} = c_{\text{dd}} \frac{\hbar R_{\text{vdW}}}{m} \left(\frac{R_{\text{vdW}}}{a} \right)^{2.55}, \tag{2.38}$$

where c_{ad} and c_{dd} are dimensionless coefficients depending on short-range physics. Note that in the vicinity of the Feshbach resonance, where $a \gg R_{\text{vdW}}$, α_{ad} and α_{dd} get extremely small.

Based on the atomic scattering length a, the elastic atom-dimer and dimer-dimer scattering lengths involving such molecules can be calculated [Pet04] to be

$$a_{\text{ad}} = 1.2 \, a, \tag{2.39}$$

$$a_{\text{dd}} = 0.6 \, a. \tag{2.40}$$

Note that the inelastic scattering rate is much smaller than the elastic one [Pet04, Pet05], which enables high thermalization rates in combination with low losses during the evaporation process (see also 5.1.2).

2.3.2 BEC regime

One limit of the BEC-BCS crossover is the BEC limit, which is achieved for $1/k_{\text{F}}a \gg 0$. In this limit, the gas is described by the Gross-Pitaevskii equation (2.11), where the weak particle-particle interactions are described by a mean-field term. The BEC can be considered as consisting of point-like bosons and is superfluid.

On the BEC side of the resonance, dimers of two fermionic ^{6}Li atoms form a weakly bound molecule. This means that the constituents of the molecule are correlated in local and in momentum space. Far from the resonance, where interactions are weak, the inner structure of these molecules as bosons composed of two fermions can be neglected. But the closer one gets to the resonance, the stronger the interactions get and the fermionic nature of the ^{6}Li atoms also starts effecting the bosonic molecules. Furthermore, the binding energy of the molecules gets weaker when approaching the Feshbach resonance and also the size of these quantum halo molecules gets larger.

Interactions become stronger when one is approaching the resonance. At $1/k_{\text{F}}a \approx 2$, the system starts behaving different than predicted by the mean-field description. Besides the strong interactions, also the increasingly large size of the molecules and the onset of fermionic behavior of the constituents of the molecules start to play a role. These beyond-mean-field effects are examined by precise studies of the radial compression mode. A theoretical description of this mode can be found in 3.2, the results of our measurements are presented in chapter 6.

2.3.3   Unitarity regime

The central position of the Feshbach resonance is reached for $1/k_F a = 0$. Here, the scattering length a diverges and the scattering cross section reaches the unitarity limit given by $4\pi/k^2$, where k is the relative wave number of the two scattering atoms (for details see [Bar05b]). In this unitarity regime in the vicinity of the Feshbach resonance $(-1 < 1/k_F < 1)$, the strong interactions are the dominant influence on the system.

The scattering length a is no longer a relevant length scale in this regime and the thermodynamic properties of the gas are expected to depend only on the temperature and the density [Hei01, Ho04b, Car03, Ho04a]. Because the properties of the gas become independent of the specific details of the interaction, the gas is said to be universal (see also [Die04] and references therein). In a universal quantum gas the only relevant length scale is the interparticle spacing given by $n^{-1/3}$ and the relevant energy scale is the Fermi energy E_F [Hei01, Ho04a].

A simple heuristic description of a universal gas is given in the following [O'H02a, Geh03]. Two-body interactions give rise to a mean field potential U_{MF} which in a two-component Fermi gas of equal density $n/2$ is given by

$$U_{\mathrm{MF}} = \frac{4\pi\hbar^2}{m} a_{eff} \frac{n}{2}, \tag{2.41}$$

where a_{eff} is the effective scattering length. In the vicinity of a Feshbach resonance, unitarity limits the effective scattering lengths to be $|a_{eff}| \approx 1/k$ [Lan77]. Here, the wave number k of a single atom can be replaced by the typical wave number k_F, so that we end up with $|a_{eff}| \approx 1/k_F$ [Geh03]. By employing the relation $n \propto k_F^3$, the mean field potential in Eq.(2.41) can then be written in terms of the Fermi energy E_F. We get

$$U_{\mathrm{MF}} = \beta E_F, \tag{2.42}$$

where β is a universal scaling parameter. The equation of state for a uniform interacting Fermi gas is then given by [Geh03, Men02]

$$\mu = E_F + U_{\mathrm{MF}} \tag{2.43}$$

This reveals that on resonance, where $U_{\mathrm{MF}} = \beta E_F$, the equation of state no longer depends on the value of the scattering length nor on its sign. Here, the equation of state becomes proportional to the one of an ideal Fermi gas

$$\mu = (1 + \beta) \frac{\hbar^2}{2m} (3\pi^2 n)^{2/3}, \tag{2.44}$$

with the characteristic density dependence of $n^{2/3}$.

There is also a close connection between an interacting and an ideal Fermi gas in a harmonic trapping potential with the trap frequencies ω_i. At unitarity, the spatial distribution of a zero temperature, interacting Fermi gas corresponds to the one in

the noninteracting case with scaled trap frequencies $\omega_i' = \omega_i/\sqrt{1+\beta}$ [Bar05a]. This finally leads to the chemical potential μ^* in a harmonic trapping potential of

$$\mu^* = \sqrt{1+\beta}E_\text{F}. \tag{2.45}$$

For magnetic fields slightly higher than the center position of the Feshbach resonance, the scattering length is large and negative. This is of great interest for the investigation of the phase transition into a superfluid Fermi gas, because the transition temperature depends exponentially on the scattering length (see equation 2.32). So an arbitrarily large a should in principle result in a critical temperature on the order of the Fermi temperature.

It is possible to derive an effective mean field theory even in the direct vicinity of a Feshbach resonance, where the resonance occurs due to the coupling to a molecular state [Tim01, Hol01]. These resonance superfluidity theories explicitly treat the coupling between the atomic and molecular gases. The theories again replace the diluteness criterion ($k_\text{F}a \ll 1$) by the weaker condition that the characteristic range of the interparticle van der Waals potential R_vdW is smaller than the interparticle spacing, i.e. $k_\text{F}R_\text{vdW} \ll 1$. A detailed description of the resonance superfluid theories is found in [Kok02]. The current estimates for the transition temperature into the superfluid state range from about 0.5 to $0.2\,T_\text{F}$ [Hol01, Mil02, Chi02, Oha02].

2.3.4   BCS regime

At magnetic fields higher than $834\,\text{G}$, one enters the so called BCS side of the resonance. The BCS limit is achieved for temperatures below the critical temperature T_c (see Eq.(2.32)) and for weak interactions, which means far from resonance ($1/k_\text{F}a \ll 0$). The pure BCS state in this limit is superfluid due to the existence of Cooper pairs, which is closely linked with superconductivity [Tin66]. Closer at resonance, interactions are stronger and for temperatures above T_c, there is a non-superfluid, strongly interacting Fermi gas. In this strongly interacting Fermi gas, "preformed pairs" exist. For an overview of the different phases see also Fig. 2.2. As the crossover between BEC- and BCS side of the resonance is smooth, the critical temperature for the superfluid regime T_c smoothly changes if crossing the resonance. Therefore, the onset of superfluidity is expected on the BCS side near resonance at much higher temperatures than in the BCS limit. As in this way a system of superfluid fermions is experimentally accessible, the BEC-BCS crossover region is very interesting from the point of view of superfluid theory. Also the region of non-superfluid fermions with pre-formed pairs is expected to provide further insights in the onset of superfluidity.

Chapter 3

Theory of collective oscillations

The observation of collective oscillations allows for detailed studies of the macroscopic properties of quantum gases. In this chapter the essential theoretical background of the measurements in this thesis is given. There are two main regimes for collective oscillations in the BEC-BCS crossover: the hydrodynamic and the collisionless regime. Starting with a general treatment of collective modes in the hydrodynamic and collisionless regime in 3.1, the different collective modes are described more detailed in 3.2, 3.3 and 3.4. In 3.5 corrections to fit the results under real experimental conditions to the idealized theoretical calculations are presented. We concentrate on the experimental important case of the radial modes of a cigar-shaped cloud.
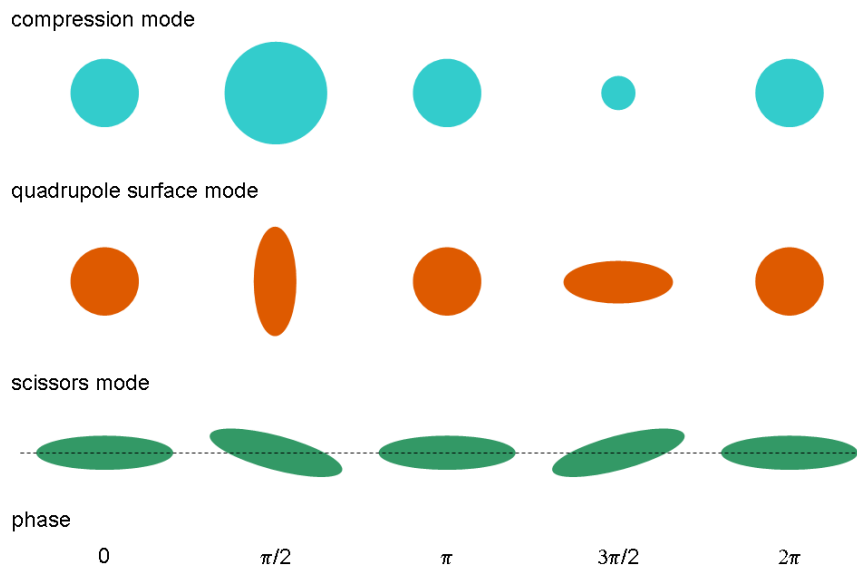
Figure 3.1: Scheme of the different radial collective oscillation modes described in this chapter: Compression mode(upper row), quadrupole surface mode (middle row) and scissors mode (lower row).

A schematic overview of the described collective oscillation modes is given in Fig. 3.1. The compression mode (upper row) shows a change in volume whereas the aspect ratio of horizontal and vertical width remains constant. In the quadrupole surface mode (middle row), the volume does not change but the aspect ratio is changing. The scissors mode (lower row) shows an oscillation of the tilting angle of an elliptic cloud.

3.1 Collective modes in the hydrodynamic and collisionless regimes

Collective oscillations are dynamic phenomena, which are described by a periodic motion of the system. One main criterion for the classification of collective modes in the BEC-BCS crossover are the interaction properties of the system. Depending on the presence of collective long-range interactions (that should not be mixed up with particle-particle interactions), one distinguishes between the hydrodynamic and the collisionless regime. Another property that influences collective oscillations is the confining potential for the gas cloud.

The following descriptions will deal with the hydrodynamic and the collisionless regime in a separate way, starting with an unspecified description of the confining potential. Later, especially the case of a harmonic trapping potential with cylindrical symmetry, which is most relevant for the experiments presented in this thesis, will be described.

In order to distinguish the different interaction regimes of collective oscillations in a gas, it is useful to summarize the main characteristics of the hydrodynamic and the collisionless regime. For the description of collisions we introduce ω as the frequency of the collective oscillation and τ_R as the relaxation time in the gas [Pit03]. In this way we can characterize the two regimes:

- in the hydrodynamic regime, long-range interactions between all particles of the system are present and mediated via many-particle effects. This can be the case for a superfluid system as well as for a normal one. In a non-superfluid hydrodynamic gas, the long-range interactions are mediated via collisions. So collisions have to be dominant, which is the case if the product of the relaxation time τ_R and the frequency of the collective oscillation is much larger than 1: $\omega\tau_R \ll 1$. This regime is realized in a superfluid BEC of molecules, a superfluid of generalized Cooper pairs as well as in a highly collisional system of bosonic molecules consisting of fermionic constituents and a strongly interacting Fermi gas (see chapter 2).

- in the collisionless regime, there are no long-range interactions between the particles. The system is non-superfluid and, as the name of this regime already

implies, collisions happen seldom. As a quantitative criterion, the frequency of the collective oscillation has to be much larger than the inverted relaxation time: $\omega \tau_R \gg 1$. A collisionless regime is realized in weakly interacting degenerate Fermi gases, where elastic collisions are blocked due to the Pauli exclusion principle [Fer99, DeM01, Gup04].

To describe the dynamics of a gas, we introduce a velocity field $\mathbf{v}$ and a density field n of the gas.

3.1.1 Hydrodynamic regime

A gas in the hydrodynamic regime is characterized by the dominant role of collective long-range interactions. In general, the dynamics of a hydrodynamic gas are described by the following two equations, called equation of continuity (3.1) and classical Euler equation (3.2) [Str96, Pit03]:

$$\frac{\partial n}{\partial t} + \nabla(\mathbf{v}n) = 0. \tag{3.1}$$

$$\frac{\partial \mathbf{v}}{\partial t} = -\nabla\left(\frac{\mathbf{v}^2}{2} + \frac{V_{\text{ext}}(\mathbf{r})}{m}\right) - \frac{\nabla P}{mn} + \mathbf{v} \times (\nabla \times \mathbf{v}). \tag{3.2}$$

Here m is the mass of one particle of the gas, n is the density, P is the pressure of the gas at the corresponding density and V_{ext} the confining potential of the gas. The last term on the right hand side of equation (3.2), $\mathbf{v} \times (\nabla \times \mathbf{v})$, describes a rotational flow and is absent in irrotational systems. We concentrate on a hydrodynamic gas with no rotational flow as is the case for any superfluid gas. Also for a non-superfluid hydrodynamic gas rotational motion can be neglected for the oscillation modes described in the following. So, for an irrotational hydrodynamic gas, the Euler equation simplifies to

$$\frac{\partial \mathbf{v}}{\partial t} = -\nabla\left(\frac{\mathbf{v}^2}{2} + \frac{V_{\text{ext}}(\mathbf{r})}{m}\right) - \frac{\nabla P}{mn}. \tag{3.3}$$

For $T = 0$ the thermodynamic relationship $\nabla P = n\nabla\mu$ is valid and equation (3.3) becomes to

$$\frac{\partial \mathbf{v}}{\partial t} = -\nabla\left(\frac{\mathbf{v}^2}{2} + \frac{V_{\text{ext}}(\mathbf{r})}{m} + \frac{\mu(n)}{m}\right). \tag{3.4}$$

Here $\mu(n)$ denotes the chemical potential of the gas.

Equation of state

In order to derive the motion of the gas from the coupled differential equations (3.1) and (3.3), it is necessary to have a closer look at the chemical potential $\mu(n)$. The dependence of the chemical potential μ on the density n is in general called equation of state. For a weakly interacting BEC, like in our case for a molecular BEC far

away from the Feshbach resonance ($1/k_F a \gg 1$), the equation of state is given by the Bogoliubov relation [Bog47, Pit03]:

$$\mu(n) = gn. \tag{3.5}$$

In the unitary limit, in our experiments the region around the Feshbach resonance ($|1/k_F a| \ll 1$) , the system is described by the equation of state of an ideal single-component Fermi gas [Pit03]:

$$\mu(n) = \frac{\hbar^2}{2m}(3\pi n)^{2/3}. \tag{3.6}$$

The description of interacting systems in the whole range of the BEC-BCS crossover needs a more sophisticated equation of state. A power law approach [Men02] has turned out to be useful:

$$\mu(n) \propto n^\gamma. \tag{3.7}$$

The polytropic index γ depends on the interactions in the system. In the weakly interacting BEC limit for instance, one gets $\gamma = 1$ and ends up with the linear relation (3.5). In the case of an ideal Fermi gas like in equation(3.6), one gets $\gamma = 2/3$. There are different approaches to derive the value of γ over the BEC-BCS crossover, which are especially interesting for the case of compression modes, see section 3.2 of this thesis and [Str04, Hei04, Ast04, Hu04, Bul05, Kim04b, Man05, Ast05].

Scaling approach

A scaling ansatz [Kag96, Cas96] is a well-suited approach to simplify dynamic equations like (3.1) and (3.4). The idea behind this ansatz is to transfer the time dependence of the dynamics of the gas into a scaling function. With a density dependence of the chemical potential like in equation(3.7) such a scaling ansatz turns out to be an effective method to describe the dynamics of the gas. We choose the following scaling functions:

$$\tilde{x}(t) = \frac{x}{b_x(t)},$$
$$\tilde{y}(t) = \frac{y}{b_y(t)}, \tag{3.8}$$
$$\tilde{z}(t) = \frac{z}{b_z(t)}.$$

The original spatial coordinates x, y and z are transferred into the time-dependent coordinates $\tilde{x}(t)$,$\tilde{y}(t)$ and $\tilde{z}(t)$ by the corresponding scaling functions $b_i(t)$, with $i = x, y, z$ respectively. These scaling functions $b_i(t)$ only depend on time. One chooses the following starting conditions:

$$b_i(0) = 1,$$
$$\dot{b}_i(0) = 0. \tag{3.9}$$

So the density n is transformed in the following way:

$$n(x, y, z, t) = \frac{1}{b_x b_y b_z} \tilde{n}_0(\tilde{x}, \tilde{y}, \tilde{z}), \tag{3.10}$$

where n_0 denotes the density at the time $t = 0$.

By inserting the equations (3.8),(3.9)and (3.10) into equation (3.1), one gets the following relation for the velocity field **v**:

$$v_x(t) = \frac{\dot{b}_x}{b_x} x,$$

$$v_y(t) = \frac{\dot{b}_y}{b_y} y, \tag{3.11}$$

$$v_z(t) = \frac{\dot{b}_z}{b_z} z.$$

The insertion of equation (3.11) into equation (3.4) yields:

$$\tilde{x} \ddot{b}_x(t) = -\frac{1}{m}\frac{dV_{ext}}{dx} - \frac{1}{mn}\frac{\partial P}{\partial x}, \tag{3.12}$$

and analog equations for y and z respectively.

The next step consists in integrating equation (3.12) over the density in order to get averaged quantities. Averaged quantities like $\langle \tilde{x} \rangle$ are defined as follows:

$$\langle \tilde{x} \rangle = \frac{1}{N} \int \tilde{x} n_0(\tilde{x}, \tilde{y}, \tilde{z}) d\tilde{x} d\tilde{y} d\tilde{z}, \tag{3.13}$$

with the normalization to particle number

$$N = \int n_0(\tilde{x}, \tilde{y}, \tilde{z}) d\tilde{x} d\tilde{y} d\tilde{z}. \tag{3.14}$$

Such an integration of equation (3.12) and a multiplication with $n/\tilde{x}$ finally results in the following equation:

$$\frac{\ddot{b}_x}{b_x b_y b_z} \langle \tilde{x} \rangle^2 + \frac{1}{m b_x^2 b_y b_z} \left\langle \tilde{x} \frac{dV_{ext}}{d\tilde{x}} \right\rangle + \frac{1}{m b_x} \left\langle \tilde{x} \frac{dP}{d\tilde{x}} \right\rangle = 0, \tag{3.15}$$

and analog results for y and z.

Now we use the polytropic equation of state (3.7) and insert it into equation (3.12). Starting at equilibrium, which means $\dot{\mathbf{v}} = 0$ at $t = 0$, this procedure gives

$$\frac{dP}{d\tilde{x}} = -\frac{n_0}{(b_x b_y b_z)^{\gamma+1}} \frac{\partial V_{ext}}{\partial \tilde{x}}. \tag{3.16}$$

Inserting equation (3.16) into equation (3.15) finally results in:

$$\ddot{b}_x(t) = \frac{1}{m b_x \langle \tilde{x}^2 \rangle} \left(\frac{1}{(b_x b_y b_z)^{\gamma}} \left\langle \tilde{x} \frac{dV_{ext}(\tilde{x}, \tilde{y}, \tilde{z})}{d\tilde{x}} \right\rangle - \left\langle \tilde{x} \frac{dV_{ext}(b_x \tilde{x}, b_y \tilde{y}, b_z \tilde{z})}{d\tilde{x}} \right\rangle \right), \tag{3.17}$$

and analog equations for y and z.

Equation (3.17) is valid for all confining potentials V_{ext}. In the following, we will leave this general point of view and take a look at more specific potentials.

Harmonic potentials

The following calculations will be based on a harmonic trapping potential of the form:

$$V_{\text{ext}} = \frac{m}{2}(\omega_x^2 x^2 + \omega_y^2 y^2 + \omega_z^2 z^2). \tag{3.18}$$

ω_x, ω_y and ω_z are the trap frequencies in the spatial directions x, y and z. Such a harmonic potential is a very good approximation for the potential used in the experiments described in this thesis. In 3.5.2 a non-harmonic potential which describes the real potential in the experiment with very high precision will be treated. But also there the potential is mainly described by harmonic terms with only small additional anharmonic terms.

Inserting the potential of equation (3.18) in equation (3.17) gives:

$$\begin{aligned}
\ddot{b}_x(t) &= \frac{\omega_{x0}^2}{b_x(b_x b_y b_z)^\gamma} - b_x \omega_x^2(t), \\
\ddot{b}_y(t) &= \frac{\omega_{y0}^2}{b_y(b_x b_y b_z)^\gamma} - b_y \omega_y^2(t), \\
\ddot{b}_z(t) &= \frac{\omega_{z0}^2}{b_z(b_x b_y b_z)^\gamma} - b_z \omega_z^2(t).
\end{aligned} \tag{3.19}$$

Here ω_{x0}, ω_{y0} and ω_{z0} are the trap frequencies for $t = 0$, when the particles are in a state of equilibrium with the trapping potential. The time dependent trap frequencies $\omega_i(t)$ include changes in the trapping potential or a release from the trap like is the case in expansion measurements. From (3.19), one is able to calculate the different solutions for the scaling function $b(t)$. By calculating $b(t)$ one easily can determine the time-dependent shape of the cloud and the velocity field $\mathbf{v}$ by using equation (3.11).

There are three solutions of equation (3.19) which result in collective oscillations of the compression and quadrupole surface modes [Coz03, Pit03]. These solutions lead to velocity fields of the form

$$\mathbf{v} \propto \nabla(ax^2 + by^2 + cz^2). \tag{3.20}$$

One finds the following equation for the frequencies ω corresponding to these solutions:

$$\omega^6 - (2 + \gamma)(\omega_x^2 + \omega_y^2 + \omega_z^2)\omega^4$$
$$+4(\gamma + 1)(\omega_x^2\omega_y^2 + \omega_x^2\omega_z^2 + \omega_y^2\omega_z^2)\omega^2 - 4(2 + 3\gamma)\omega_x^2\omega_y^2\omega_z^2 = 0. \tag{3.21}$$

Scissors mode

In a similar way, the case of a rotating collective oscillation can be described. In this so-called scissors mode, an elliptic cloud is oscillating around its equilibrium position.

One tries to find solutions of the irrotational hydrodynamic equations (3.1) and (3.3) with an ansatz including the coupling of the different axes due to the rotation. One chooses the ansatz [Pit03]

$$\delta n \propto xy,$$
$$\delta n \propto xz, \tag{3.22}$$
$$\delta n \propto yz,$$

for the density n and

$$\mathbf{v} \propto \nabla(xy),$$
$$\mathbf{v} \propto \nabla(xz), \tag{3.23}$$
$$\mathbf{v} \propto \nabla(yz),$$

for the velocity fields $\mathbf{v}$.

This ansatz leads to three solutions that are the scissors modes [GO99, Pit03] relative to the three pairs of axes, with the frequencies $\sqrt{\omega_x^2 + \omega_y^2}$, $\sqrt{\omega_x^2 + \omega_z^2}$ and $\sqrt{\omega_y^2 + \omega_z^2}$ respectively.

Elongated trap

For the experiments presented in this thesis the case of $\omega_x, \omega_y \gg \omega_z$ is relevant. This geometry of the trapping potential V_{ext} results in an elongated shape of the trapped gas cloud and is known as cigar-type geometry. In this case we concentrate on radial collective modes, i.e. modes along the x and y-axis, and neglect ω_z. For radial oscillations, equation (3.21) simplifies to:

$$\omega^4 - (2 + \gamma)(\omega_x^2 + \omega_y^2)\omega^2 + 4(\gamma + 1)(\omega_x^2 \omega_y^2) = 0. \tag{3.24}$$

In section 3.5 we will use equation (3.24) to calculate the frequency shifts of an elliptic trapping potential.

For many experimental situations it is legitimate to simplify the trapping potential V_{ext} even further to the case of an axially symmetric trapping potential with $\omega_x = \omega_y \equiv \omega_r$. This leads to a confining potential as follows:

$$V_{ext} = \frac{m}{2}\omega_r^2(x^2 + y^2), \tag{3.25}$$

where ω_r is the radial trapping frequency.

Equation (3.24)delivers several solutions for radial collective modes [Coz03, Pit03]. One solution is the radial breathing or compression mode (see also section 3.2), another solutions is the radial quadrupole surface modes (see section 3.3). The radial quadrupole mode is characterized by a velocity field of the form

$$\mathbf{v} \propto \nabla(x \pm iy)^2 \tag{3.26}$$

with i being the imaginary parameter. The frequency ω_q of the corresponding oscillation is given by

$$\omega_q = \sqrt{2}\omega_r. \tag{3.27}$$

Note that the frequency in equation(3.27) is independent of the equation of state.

The compression mode leads to a velocity field of the form

$$\mathbf{v} \propto \nabla(\alpha(x^2 + y^2)). \tag{3.28}$$

This velocity field corresponds to a compression oscillation perpendicular to the z-axis, whose frequency fulfills the following equation

$$\omega_c^2 = 2(\gamma + 1)\omega_r^2. \tag{3.29}$$

3.1.2   Collisionless regime

Collective modes in the collisionless regime are characterized by the minor or even absent influence of collisions. This is the case for $\omega\tau_R \gg 1$ with ω being a typical oscillation frequency and τ_R being the collisional relaxation time [Pit03]. In the experiments presented in this thesis we enter the collisionless regime on the BSC-side of the Feshbach resonance, i.e. for $1/(k_F a) < 0$. For $1/(k_F a) < -1$, which is far away from the unitarity region around the Feshbach resonance, we can realize the limit of a collisionless Fermi gas, where the elastic collision rate is strongly reduced by Pauli blocking (see section 2.2). Closer to the resonance, collisions in the "collisionless" regime become more important and play a crucial role for thermalization. We call this regime the near-collisionless regime.

Before describing the collisionless limit and the near-collisionless regime in detail, we start with some general considerations. We consider the classical Boltzmann-Vlasov kinetic equation which is described by [Hua87, Ped03]

$$\frac{\partial f}{\partial t} + \mathbf{v} \cdot \nabla f - \frac{1}{m}\nabla V_{\text{ext}} \cdot \frac{\partial}{\partial \mathbf{v}}f = I_c(f), \tag{3.30}$$

where $f = f(t, \mathbf{r}, \mathbf{v})$ is the phase space density, $\mathbf{v}$ is the single particle velocity, m the mass of an atom and V_{ext} is the external trapping potential. To simplify the model, we ignore mean-field effects.

The collisional information is bound into the term I_c. This term allows the gas to exchange energy among the different degrees of freedom. For $I_c = 0$, the system is in the collisionless limit. In the following, we use the relaxation-time approximation

$$I_c(f) = \frac{f - f_e}{\tau_R}. \tag{3.31}$$

The term f_e is the phase-space distribution after the gas has fully thermalized and τ_R is the relaxation time which describes the time scale of collisions. The limit of $\tau_R \to \infty$ is realized in the collisionless limit.

Non-interacting Fermi gas

In order to describe the dynamics of an collisionless, non-interacting Fermi gas, we can use a scaling ansatz like in the hydrodynamic case, see section 3.1.1. The same scaling functions as in equations (3.8), (3.9) and (3.10) are used. With this scaling ansatz and the condition $I_c = 0$ for the collisionless limit, we find solutions for the differential equation (3.30). This finally leads to

$$\ddot{b}_x(t) = \frac{1}{mb_x\langle\tilde{x}^2\rangle}\left(\frac{1}{b_x^2}\left\langle\tilde{x}\frac{dV_{ext}(\tilde{x},\tilde{y},\tilde{z})}{d\tilde{x}}\right\rangle - \left\langle\tilde{x}\frac{dV_{ext}(b_x\tilde{x},b_y\tilde{y},b_z\tilde{z})}{d\tilde{x}}\right\rangle\right), \qquad (3.32)$$

and analog equations for y and z.

By assuming a harmonic trapping potential V_{ext} like in equation (3.18) and using $\partial\mathbf{v}/\partial t = -\nabla(V_{ext}/m)$ one gets [Bru00]

$$\ddot{b}_x(t) = \frac{\omega_{x0}^2}{b_x^3} - b_x\omega_x^2(t),$$

$$\ddot{b}_y(t) = \frac{\omega_{y0}^2}{b_y^3} - b_y\omega_y^2(t), \qquad (3.33)$$

$$\ddot{b}_z(t) = \frac{\omega_{z0}^2}{b_z^3} - b_z\omega_z^2(t).$$

A linearization of equation (3.33) with the substitution $b(t) = 1 + \epsilon(t)$ for $\epsilon \ll 1$ yields

$$\ddot{\epsilon}_x(t) = -4\omega_x^2\epsilon_x, \qquad (3.34)$$

and analog equations for y and z.

From equation (3.34) the frequency of all oscillations along one direction are easily derived to be:

$$\omega = 2\omega_i, \qquad (3.35)$$

with i being x, y or z.

Near-collisionless Fermi gas

In the near-collisionless regime, which we realize in a strongly interacting Fermi gas close to the Feshbach resonance, collisions are strong enough to provide thermalization. During a collective oscillation in the trap as well as during expansion after release from the trapping potential thermalization effects can influence the gas. In order to model these effects, we follow a theory based on a classical gas in the crossover between the hydrodynamic and the collisionless regime described in [Ped03]. An application of this theory for the compression mode in the hydrodynamic regime has been done in [J.K05]. Here we will adapt the theory to handle thermalization effects in the collisionless regime.

In order to solve the differential equation (3.30) for a harmonic trapping potential V_{ext} like in equation (3.18), the following scaling ansatz is made,

$$f(t, \mathbf{r}, \mathbf{v}) = \frac{1}{\Pi_i b_i \sqrt{\vartheta_i}} f_0(\tilde{\mathbf{r}}, \tilde{\mathbf{v}}), \qquad (3.36)$$

where b_i is a scaling function like described in 3.1.1, ϑ_i is a scaling parameter directly related to the temperature, $\tilde{r}_i = r_i/b_i$, and $\tilde{v}_i = \frac{1}{\sqrt{\vartheta_i}}(v_i - \dot{b}_i R_i)$. f_0 is assumed to be the phase space distribution when $I_c = 0$.

The result of plugging equation (3.36) and (3.31) into (3.30) and then determining $\langle \tilde{r}_i \tilde{v}_i \rangle$ and $\langle \tilde{v}_i^2 \rangle$ is true for the following coupled differential equations

$$\ddot{b}_i(t) = \omega_{0i}^2 \frac{\vartheta_i}{b_i} - \omega_i^2 b_i(t) \qquad (3.37)$$

and

$$\dot{\vartheta}_i(t) = \frac{1}{\tau_R}(\vartheta_i - \bar{\vartheta}) - 2\frac{\dot{b}_i}{b_i}\vartheta_i(t), \qquad (3.38)$$

where $\bar{\vartheta} = \frac{1}{3}\Sigma_k \vartheta_k$.

The collisionless limit with no collisions happening at all is realized when $\tau_R \to \infty$. In this case, the differential equations of Eq.(3.37) simplify to the simple form presented in Eq.(3.33). For solving equations (3.37) and (3.38) we must also include the initial condition for ϑ_j. As long as the gas is in equilibrium at the moment of the excitation $t = 0$, we set $\vartheta_i(0) = 1$.

In a similar way, the equation of motion for a scissors mode can be described (for the hydrodynamic regime compare section 3.1.1). For small rotational angles θ one gets [GO99]

$$\left(\frac{d^4\theta}{dt^4} + 2(\omega_x^2 + \omega_y^2)\frac{d^2\theta}{dt^2} + (\omega_x^2 - \omega_y^2)^2\theta\right) + \frac{1}{\tau_R}\left(\frac{d^3\theta}{dt^3} + (\omega_x^2 + \omega_y^2)\frac{d\theta}{dt}\right) = 0, \qquad (3.39)$$

with the initial conditions $\theta(0) = \theta_0$, $\ddot{\theta} = -(\omega_x^2 + \omega_y^2)\theta_0$ and $\dot{\theta}(0) = \dddot{\theta}(0) = 0$.

3.2   Compression mode

Among the most important radial collective oscillation modes in the BEC-BCS crossover regime are the modes with compression character, also known as breathing modes. Compared to the quadrupole surface mode and the scissors mode, which are described later in section 3.3 and 3.4 respectively, such a compression mode is strongly influenced by the equation of state of the system. Therefore a detailed treatment of this mode together with precision measurements, as described later in chapter 6, provides new insights in the physics of an ultracold quantum gas in the BEC-BCS crossover. Especially in a strongly interacting molecular BEC, which is realized in the

regime where $1/(k_\mathrm{F}a) \lesssim 4$, effects which go beyond the usual mean-field description of a BEC are expected. This section will present the two different theoretical models describing this regime: a mean-field BCS model and a quantum Monte Carlo model.

In the following, we consider a cigar-shaped trap geometry with trapping frequencies ω_x, ω_y and ω_z, with $\omega_z \ll \omega_x, \omega_y$. For the axial symmetric case we call $\omega_\mathrm{r} = \omega_x = \omega_y$ the radial trap frequency, whereas ω_z is called axial trap frequency. The radial compression mode consists of coupled oscillations along the *x*- and *y*-axis respectively, which are in phase. So the gas cloud describes a periodic radial motion with shrinking and expanding radial width. Fig.3.2 gives a schematic impression of the radial compression mode.
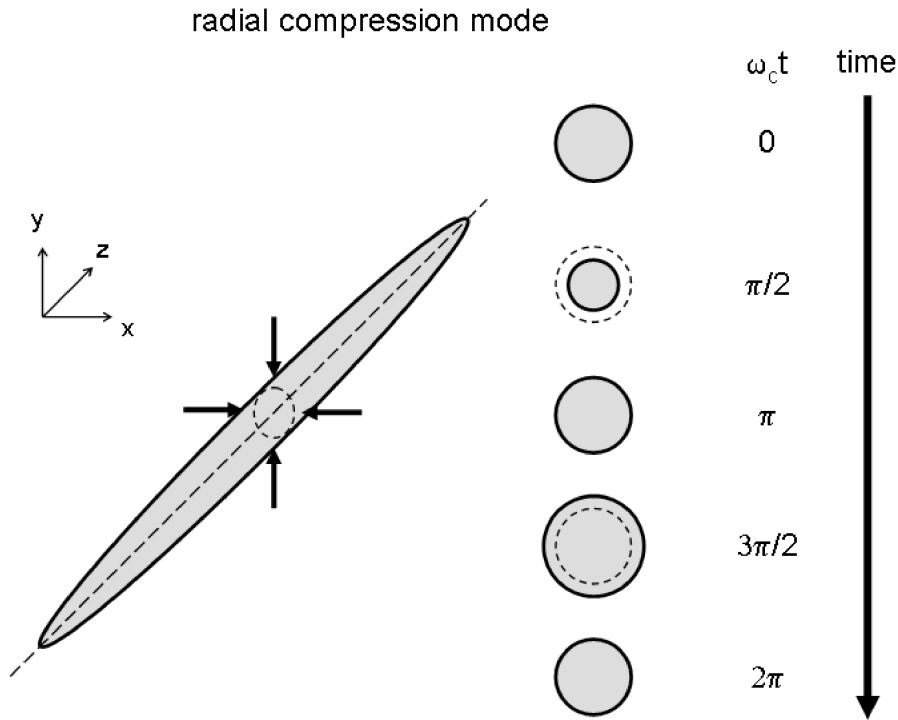
Figure 3.2: Radial compression mode of an elongated cloud. The cloud is tightly confined in the radial x- and y-directions and weakly confined in the axial z-direction. A periodic compression and decompression of the cloud along the radial directions takes place.

The frequency of this oscillation depends on the interaction regime of the gas and can be directly calculated for certain special cases. In the non-interacting limit of an collisionless gas, the frequency ω_c of the radial compression mode is described by (compare equation (3.35)):

$$\omega_\mathrm{c} = 2\omega_\mathrm{r}. \tag{3.40}$$

For a hydrodynamic gas, ω_c depends on the equation of state of the system and in this way on the polytropic index γ in the equation of state (3.7). From equation (3.29) one

gets

$$\omega_c = 2\omega_r \tag{3.41}$$

for a gas in the weakly interacting BEC limit with $\gamma = 1$. Similarly equation (3.29) yields for a quantum gas in the unitarity limit with $\gamma = \frac{2}{3}$:

$$\omega_c = \sqrt{\frac{10}{3}}\omega_r. \tag{3.42}$$

Between these fixed values, ω_c also can be described, but it is not always possible to directly give the value of ω_c.

In the regime of a collisionless Fermi gas with weak interactions, ω_c can be calculated numerically from equations (3.37) and (3.38), and lies between 2 and $\sqrt{\frac{10}{3}}$.

The regime of a strongly interacting BEC depends on the value of the polytropic index γ, which is difficult to calculate all over this regime. In the following, we will deal with this case in a more detailed way.

The strongly interacting BEC regime is located closer to the resonance than the weakly interacting BEC regime. There has already been some experimental [Jin96, Jin97, Mew96, SK98b, Che02] and theoretical exploration [Str96, Edw96, Dal97a, Dal97b, Dal99b] of the weakly interacting BEC regime. In order to include many body physics, interactions in such a weakly interacting BEC are described by a mean-field approach [Gro61, Pit61, Pet02, Pit03]. This mean-field approach is expected to be no longer valid in a strongly interacting BEC and the occurrence of beyond-mean-field effects is predicted [Pit98, Ast04]. Furthermore the fermionic nature of the constituents of the molecules in the BEC plays an increasing role when approaching the resonance. All these effects affect the equation of state, which is influencing the frequency of the compression mode. There is a competition between these two effects of strong interactions in a Bose gas and onset of fermionic behavior. In a strongly interacting Bose gas the average energy per particle is increased by quantum depletion. These beyond-mean-field effects lead in lowest order to a term which has been first predicted by Lee, Huang and Yang [Hua57, Lee57b]. So the equation of state is corrected in a way that reduces the compressibility of the gas. The emerging of fermionic behavior however leads to an increase in the compressibility of the gas.

The effects of the polytropic index γ from the equation of state (3.7) on the frequency of the compression mode can be directly seen in equation (3.29). In the case of an axially symmetric trapping potential where the axial confinement is neglected, one gets:

$$\omega_c = \sqrt{2(\gamma + 1)}\omega_r. \tag{3.43}$$

There are two theoretical models describing the index γ in the strongly interacting BEC regime:

- a mean-field BCS theory

- a quantum Monte Carlo theory.

The mean-field BCS theory is more simplified than the quantum Monte Carlo theory, so that one would expect the more sophisticated theory to deliver more precise results. But the frequency ω_c predicted by these two models for different interaction parameters $1/(k_F a)$ differ maximally by a few percent in the strongly interacting BEC regime, so that high precision measurements are necessary to compare experimental results with the theoretical predictions (see chapter 6). This includes small corrections to the predictions for idealized trap geometries which are necessary for the real experimental set-up. These corrections are presented in section 3.5 of this chapter.

Mean-field BCS theory

This theoretical model stems from standard BCS theory [Bar57a, Bar57b, Eag69, Leg80, Noz85, Eng97] which connects the two known limits of a strong-coupling BEC of molecules consisting of two fermionic atoms and a weak-coupling superfluid BCS-state consisting of Cooper-pairs of these fermionic atoms. Starting from the BCS-limit, the connection to the BEC-limit is done by introducing a mean-field term. This mean-field includes the interaction and in this way describes the chemical potential μ as a function of the density n of the ultracold gas [Str04, Hei04, Hu04, Com04b, Com04a, Kim04b, Kim04a, Pie04, Man05, Bul05, Pie05]. Note that this theoretical approach is based on a temperature $T = 0$. Mean-field BCS theory provides relatively simple models for the equation of state in the whole BEC-BCS crossover regime, which are analytically solvable.

Beyond-mean-field effects are not included in this model, so that in precision experiments slightly higher frequencies should be detected. Another disadvantage of this approach is connected with the value of the molecular scattering length a_M in terms of the atomic scattering length a_A. The mean-field BCS model leads to a value of $a_M = 2a_A$, whereas a value of $a_M = 0.6a_A$ is considered to be true by both theory [Pet04, Pet05] and experiment [Bar04b, Bou04].

Furthermore, the mean-field BCS model also leads to a wrong value for the universal parameter β in the unitarity regime (for further details on β see 2.3.3 and [Hei01, O'H02a, Geh03, Bar05a]). Mean-field BCS theory yields $\beta = -0.41$ [Ast05], whereas experiments support smaller values [Bou04, Kin05a], e.g. $\beta = -0.73^{+0.12}_{-0.09}$ [Bar05a].

Data calculated by using this model are shown in figure 3.3 as the dashed lines.

Quantum Monte Carlo theory

The quantum Monte Carlo approach uses numerical methods to calculate the equation of state in the BEC-BCS crossover [Car03, Ast04, Ast05]. Like the mean-field BCS theory also this model is based on a zero temperature assumption. A scaling ansatz is used to calculate the equation of state of the system in the crossover region. This ansatz is not limited to a polytropic model for the equation of state, like in 3.7, and so can take into account even corrections to the polytropic model.
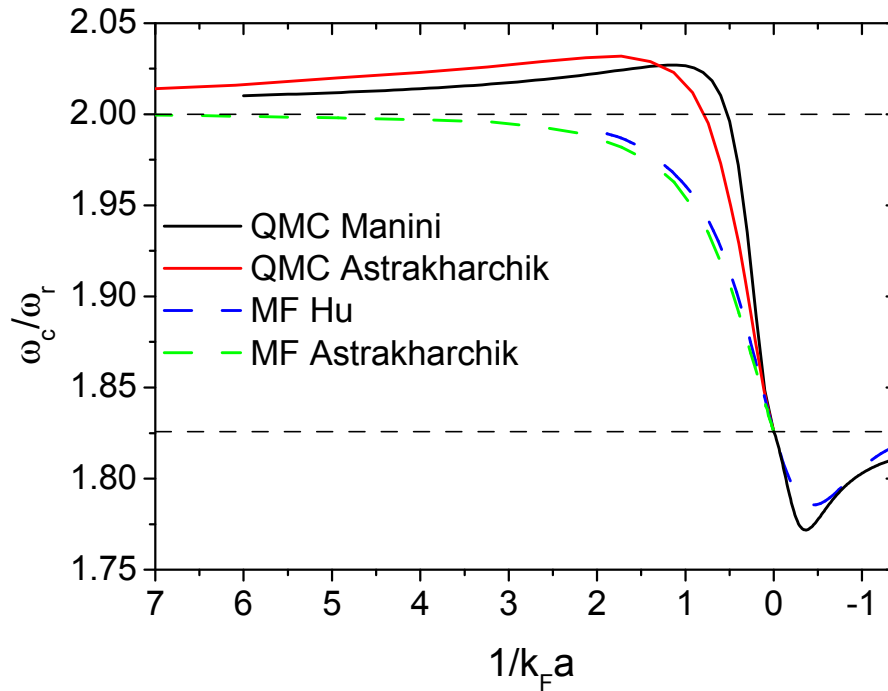
Figure 3.3: Normalized compression mode frequency ω_c/ω_r versus interaction parameter $1/k_F a$ in the strongly interacting BEC regime. The dashed curves are based on mean-field BCS models by Hu et al. [Hu04] and Astrakharchik et al. [Ast05], the solid curves on quantum Monte-Carlo models from Manini et al. [Man05] and Astrakharchik et al. [Ast05]. The horizontal dashed lines indicate the values for the BEC limit ($\omega_c/\omega_r = 2$) and the unitarity limit ($\omega_c/\omega_r = \sqrt{10/3} = 1.826$).

Furthermore the quantum Monte Carlo model results in a molecular scattering length $a_M = 0.6 a_A$, where a_A is the atomic scattering length. This value of the molecular scattering length is consistent with both theoretical [Pet04, Pet05] and experimental [Bar04b, Bou04] results.

Also the prediction of the universal parameter $\beta = -0.56$ of the quantum Monte Carlo model [Ast05] agrees much better with experimental results , e.g. $\beta = -0.73^{+0.12}_{-0.09}$ [Bar05a] (see also [Bou04, Kin05a]), than the predictions of mean-field BCS models.

Altogether the quantum Monte Carlo model is a more sophisticated approach than the mean-field BCS theory. The solid lines in figure 3.3 show data corresponding to quantum Monte-Carlo models.

3.3 Quadrupole surface mode

In order to study the BEC-BCS crossover the quadrupole surface mode is a suited tool. This collective oscillation mode is characterized by an non-compressing periodic motion of the gas, which makes the surface mode independent of the equation of state of the gas. This is a significant difference compared with the compression mode presented in section 3.2. The frequency of the surface mode strongly depends on the collisional regime of the gas. Therefore the frequency of the surface mode ω_q is different in the hydrodynamic and in the collisionless regime. As we will see in section 7.2, the phase of the oscillation after expansion provides also information of the collisional regime.

For comparison with experimental results, especially the case of an axially symmetric, cigar-shaped harmonic trapping potential is relevant. For trap frequencies ω_x, ω_y and ω_z along the x-,y- and z-axis this results in the conditions $\omega_x, \omega_y \gg \omega_z$ and $\omega_x = \omega_y \equiv \omega_r$ with ω_r being the radial trap frequency.

A schematic impression of the radial quadrupole mode is given in Fig. 3.4.
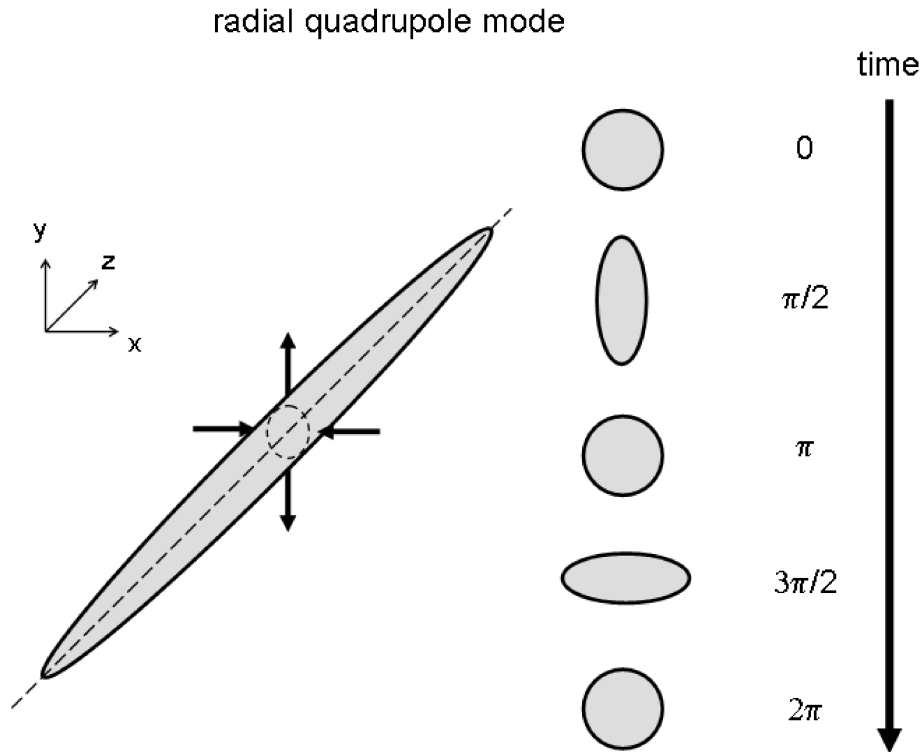
Figure 3.4: Radial quadrupole mode of an elongated cloud. The cloud is tightly confined in the radial x- and y-directions and weakly confined in the axial z-direction. The surface of this mode is oscillating and no compression takes place.

The radial quadrupole surface mode consists of oscillations of the width of the gas cloud along x- and y-direction, which are shifted by a phase of π compared to each

other. So maximal width in *x*-direction comes along with minimal width in *y*-direction and vice versa. For a harmonic trapping potential the frequency of the quadrupole surface mode in the hydrodynamic regime, according to equation (3.27), is

$$\omega_{\mathrm{q}} = \sqrt{2}\omega_{\mathrm{r}}. \tag{3.44}$$

In the collisionless regime, where collisions are strongly suppressed, the atoms freely oscillate in the trap. Unlike the hydrodynamic limit, the motions in the radial degrees of freedom are independent from each other. When a cloud in the collisionless regime is excited with a phase difference of π between the oscillations, the motion of the cloud also can be described by a quadrupole surface mode frequency and one gets from equation (3.35)

$$\omega_{\mathrm{q}} = 2\omega_{\mathrm{r}}. \tag{3.45}$$

Other properties of the quadrupole surface mode are connected with expansion dynamics of the cloud. A treatment of the expansion dynamics will be given in section 7.2. Especially phase and amplitude of the surface mode after expansion will be treated there.

3.4 Scissors mode

Similar to the quadrupole surface mode described in section 3.3, also the scissors mode is a collective surface mode. So also for the scissors mode the compressibility of the gas and in this way the equation of state of the gas has no effect on the properties of the oscillation[GO99]. For the excitation of the scissors mode an anisotropic trap geometry is necessary. In our experimental setup a cigar-shaped harmonic trap geometry with trap frequencies ω_x, ω_y and ω_z and the condition $\omega_z \ll \omega_x, \omega_y$ is used. In addition an ellipticity between the trapping potential in *x*- and *y*-direction is necessary. This is the main difference to the trap geometry for compression and surface modes, which is almost symmetric to the *z*-axis. In such an elliptic trap geometry the scissors mode is described by a periodic rotational movement with the *z*-axis being the rotational axis (see Fig. 3.1). This motion which reminds of the motion of scissors gave name to this collective mode and goes back to a similar mode in nuclear physics, where it corresponds to the out-of-phase rotation of the neutron and proton clouds [Iud78, Lip83].

As for the quadrupole surface mode, also the frequency of the scissors mode depends on the interactions of the gas. For small rotational angles θ, the following differential equation can be derived from the equations of motion [GO99] (see also 3.1.2)

$$\left(\frac{d^4\theta}{dt^4} + 2(\omega_x^2 + \omega_y^2)\frac{d^2\theta}{dt^2} + (\omega_x^2 - \omega_y^2)^2\theta\right) + \frac{1}{\tau_{\mathrm{R}}}\left(\frac{d^3\theta}{dt^3} + (\omega_x^2 + \omega_y^2)\frac{d\theta}{dt}\right) = 0, \tag{3.46}$$

where τ_{R} is the relaxation collision time given by $\tau_{\mathrm{R}} = 5/(4\Gamma_{coll})$ and Γ_{coll} is the collisional rate . In the hydrodynamic regime τ_{R} gets small and the second term of equation

(3.46) becomes dominant. Then the frequency of the scissors mode ω_{scis} is given by

$$\omega_{scis} = \sqrt{\omega_x^2 + \omega_y^2}. \tag{3.47}$$

Note that this is consistent with the general approach in section 3.1 and equation (3.23).

In the collisionless regime, τ gets large and the first term in equation (3.46) becomes important. In this case the scissors mode consists of a superposition of two frequencies ω_{scis+} and ω_{scis-}:

$$\omega_{scis+} = |\omega_x + \omega_y|,$$
$$\omega_{scis-} = |\omega_x - \omega_y|. \tag{3.48}$$

3.5   Corrections for real trap geometries

The theoretical calculations in sections 3.1, 3.2 and 3.3 are done for idealized conditions. In this section some corrections to these idealized collective frequencies are introduced to match real experimental conditions. These corrections are small, on the sub-percent-level for the experiments described in this thesis. But especially for the compression mode in the strongly interacting BEC regime they have to be taken into account, as the highest possible precision is needed to distinguish between the different theoretical predictions from 3.2 and 3.2, which differ only by a few percent themselves.

There are several parameters which are responsible for corrections:

- Ellipticity: For compression and surface modes we assume a axially symmetric trap geometry. In real experiments there is a remaining asymmetry which leads to an elliptic trap geometry.

- Anharmonicity: The trapping potential is not perfectly harmonic, because it is created by a Gaussian intensity profile of the confining light field. Furthermore, the trapped cloud is not point-like but has got a spatial extension.

3.5.1   Ellipticity corrections

In the theoretical approach in section 3.1 we concentrated on a axially symmetric trap geometry with $\omega_x = \omega_y$. In the experimental set-up however, there is a small ellipticity ϵ which leads to slightly different trap frequencies. ϵ is defined by

$$\epsilon = (\omega_y - \omega_x)/\omega_\perp, \tag{3.49}$$

where $\omega_\perp$ is the mean radial trap frequency given by

$$\omega_\perp = \sqrt{\omega_x \omega_y}. \tag{3.50}$$

So the trap frequencies ω_x and ω_y can be written as

$$\omega_x = \omega_y - \epsilon\omega_\perp,$$
$$\omega_y = \omega_x + \epsilon\omega_\perp. \tag{3.51}$$

This ellipticity of the trap frequencies causes small corrections of the compression mode frequency, which is especially important to know in the strongly interacting BEC regime.

Compression mode

For the compression mode in the hydrodynamic limit and a trap geometry with $\omega_z \ll \omega_\perp$, where ω_z can be neglected, one gets from equation (3.24)

$$\omega_c^2 = (1 + \frac{\gamma}{2})(\omega_x^2 + \omega_y^2) + \frac{1}{2}\sqrt{(2+\gamma)^2(\omega_x^2 + \omega_y^2)^2 - 16(1+\gamma)\omega_x^2\omega_y^2}. \tag{3.52}$$

Simple transformations of equation (3.52) and use of the definitions (3.49) and (3.50) yield

$$\omega_c^2 = \omega_\perp^2 \left((1 + \frac{\gamma}{2})(\epsilon^2 + 2) + \frac{1}{2}\sqrt{(2+\gamma)^2(\epsilon^2 + 2)^2 - 16(1+\gamma)} \right). \tag{3.53}$$

For small ϵ the term under the square-root in equation (3.53) can be simplified by using a Taylor expansion:

$$\sqrt{(2+\gamma)^2(\epsilon^2 + 2)^2 - 16(1+\gamma)} = 2\gamma + \epsilon^2\frac{(2+\gamma)^2}{\gamma} + O(\epsilon^4). \tag{3.54}$$

Inserting equation (3.54) into equation (3.53) and a Taylor expansion for the compression mode frequency finally yield

$$\omega_c = \omega_\perp \sqrt{2 + 2\gamma} \left(1 + \epsilon^2\frac{\gamma + 2}{4\gamma} \right). \tag{3.55}$$

Quadrupole surface mode

For the quadrupole surface mode, the corrections are calculated very similar to the above calculation for the compression mode. We start instead of (3.52) with

$$\omega_q^2 = (1 + \frac{\gamma}{2})(\omega_x^2 + \omega_y^2) - \frac{1}{2}\sqrt{(2+\gamma)^2(\omega_x^2 + \omega_y^2)^2 - 16(1+\gamma)\omega_x^2\omega_y^2}, \tag{3.56}$$

where the only difference lies in the different sign in front of the squareroot.

Analogous to the derivation of equation (3.55), after some simplifications one ends with

$$\omega_q^2 = \omega_\perp^2(2 - \epsilon^2\frac{(\gamma + 2)}{\gamma}). \tag{3.57}$$

A final Taylor expansion gives the result

$$\omega_q = \omega_\perp \sqrt{2}\left(1 - \epsilon^2 \frac{\gamma + 2}{4\gamma}\right). \tag{3.58}$$

Note that for the quadrupole surface mode, the relative correction due to ellipticity is exactly the same except the opposite sign as for the compression mode.

3.5.2 Anharmonicity corrections

In order to describe the confining potential V_{ext} for our gas cloud, a harmonic potential like in equation (3.18) serves as a god first approximation. For more detailed studies, we have to take into account a more precise description of the trapping potential. As later described in chapter 4, in the described experimental set-up a focused laser beam creates the trapping potential for the particles of the gas cloud. So the shape of the potential is linked directly with the intensity profile of the laser. For a Gaussian intensity profile of the laser one gets the following trapping potential:

$$V_{ext}(r) = -V_0 \exp\left(-\frac{m\omega_x^2 x^2}{2V_0} - \frac{m\omega_y^2 y^2}{2V_0}\right), \tag{3.59}$$

where a confinement along the z-axis is neglected. The maximal trapping potential V_0 is defined by:

$$V_0 = m\omega_r^2 \frac{w_0^2}{4}, \tag{3.60}$$

with w_0 being the waist of the laser beam (see also 4.2.3) and $\omega_r = \sqrt{\omega_x \omega_y}$ being the mean radial trap frequency.

Equation (3.59) can be expanded to orders of x^4:

$$V_{ext}(x, y) = -V_0 + \frac{m}{2}(\omega_x^2 x^2 + \omega_y^2 y^2) - \frac{1}{8}\frac{m^2}{V_0}(\omega_x^4 x^4 + 2\omega_x^2\omega_y^2 x^2 y^2 + \omega_y^4 y^4). \tag{3.61}$$

Note that equation (3.61) differs from a harmonic potential only by the last two terms proportional to y^2 and y^4 respectively. For an cylindrically symmetric potential, equation (3.61) simplifies to:

$$V_{ext}(r) = -V_0 + \frac{1}{2}m\omega_r^2 r^2 - \frac{1}{8V_0}m^2\omega_r^4 r^4. \tag{3.62}$$

In the following calculations the anharmonic parts of the trapping potential as well as the spatial expansion of the cloud are taken into account, which leads to corrections to the calculations for a point-like cloud in a harmonic potential.

Sloshing mode

The frequencies of collective oscillations in an axially symmetric trapping potential always depend on the mean radial trap frequency ω_r. In order to determine ω_r experimentally, it is very useful to measure the radial dipole mode frequency $\omega_\perp$ of the center-of-mass motion of the gas cloud in the trapping potential (see 5.2.1 in chapter 5). In a harmonic trapping potential, $\omega_r = \omega_\perp$. But for an anharmonic trapping potential, corrections have to be taken into account. Using the definition

$$\omega_\perp^2 = \frac{1}{m} \left\langle \frac{\partial^2}{\partial r^2}(V_{ext}) \right\rangle, \tag{3.63}$$

and inserting the potential from equation (3.62) yields:

$$\omega_\perp = \omega_r \left(1 - \frac{1}{2} \frac{m\omega_r^2 \langle r^2 \rangle}{V_0} \right). \tag{3.64}$$

Compression mode

As a precise knowledge of the frequency of the compression mode ω_c is needed to evaluate experimental results , especially in the strong interacting BEC regime, it is crucial to take anharmonicity corrections into account. We will first calculate these corrections in the hydrodynamic interaction regime and later get the corrections for the noninteracting Fermi gas in a similar way.

For the hydrodynamic interaction regime, the potential of equation (3.61) has to be inserted into the differential equation for the corresponding scaling function (3.17). As the potential (3.61) can be considered to be time-independent during the whole oscillation, one gets:

$$\ddot{b}_x = \omega_x^2 \left(\frac{1}{b_x^{\gamma+1} b_y^{\gamma}} \left(1 - \frac{m}{2V_0} \omega_x^2 \frac{\langle \tilde{x}^2 \tilde{y}^2 + \tilde{x}^4 \rangle}{\langle \tilde{x}^2 \rangle} \right) - b_x \left(1 - \frac{m}{2V_0} \omega_x^2 \frac{\langle \tilde{x}^2 \tilde{y}^2 + \tilde{x}^4 \rangle}{\langle \tilde{x}^2 \rangle} b_x^2 \right) \right), \tag{3.65}$$

and an analog result for *y*.

With the relations $\langle \tilde{x}^2 \tilde{y}^2 + \tilde{x}^4 \rangle = \frac{4}{3} \langle \tilde{x}^4 \rangle$ and $\langle \tilde{x}^4 \rangle = 3 \frac{(2+5\gamma)}{(2+7\gamma)} \langle \tilde{x}^2 \rangle^2$ for Thomas-Fermi-like density profiles $n = n_0 \left(1 - \frac{x^2}{R_x^2} \right)^{1/\gamma}$, equation (3.65) becomes to

$$\ddot{b}_x = \omega_x^2 \left(\frac{1}{b_x^{\gamma+1} b_y^{\gamma}} \left(1 - \frac{m}{V_0} \omega_x^2 \langle \tilde{x}^2 \rangle \frac{2(2 + 5\gamma)}{(2 + 7\gamma)} \right) - b_x \left(1 - \frac{m}{V_0} \omega_x^2 \langle \tilde{x}^2 \rangle \frac{2(2 + 5\gamma)}{(2 + 7\gamma)} b_x^2 \right) \right). \tag{3.66}$$

For the compression mode, we choose the approach

$$b_x = b_y = 1 + \delta, \tag{3.67}$$

and get from equation (3.66) after linearization:

$$\ddot{\delta} = -\delta \left(\omega_x^2 (2\gamma + 2) \left(1 - \frac{m}{V_0} \omega_x^2 \langle \tilde{x}^2 \rangle 2 \frac{(2 + 5\gamma)(2 + \gamma)}{(2 + 7\gamma)(1 + \gamma)} \right) \right). \tag{3.68}$$

For a cylindrically symmetric geometry, by using the relation $2\omega_x^2\langle\tilde{x}^2\rangle = \omega_r^2\langle r^2\rangle$ equation (3.68) can be simplified to

$$\ddot{\delta} = -\delta\left(\omega_r^2(2\gamma+2)\left(1 - \frac{m}{V_0}\omega_r^2\langle r^2\rangle\frac{(2+5\gamma)(2+\gamma)}{(2+7\gamma)(1+\gamma)}\right)\right). \tag{3.69}$$

From equation (3.68) and expansion to a Taylor series, the frequency ω_c of the compression mode can be determined to be:

$$\omega_c = \omega_r\sqrt{2\gamma+2}\left(1 - \frac{m}{V_0}\omega_r^2\langle r^2\rangle\frac{1}{2}\frac{(2+5\gamma)(2+\gamma)}{(2+7\gamma)(1+\gamma)}\right). \tag{3.70}$$

The general form of equation (3.70) includes the two limits of a weakly interacting BEC and of a universal quantum gas.

For the weakly interacting BEC limit($\gamma = 1$),one gets:

$$\omega_c = 2\omega_r\left(1 - \frac{7}{12}\frac{m}{V_0}\omega_r^2\langle r^2\rangle\right), \tag{3.71}$$

whereas the frequency in the universal limit ($\gamma = \frac{2}{3}$) is determined by:

$$\omega_c = \sqrt{\frac{10}{3}}\omega_r\left(1 - \frac{16}{25}\frac{m}{V_0}\omega_r^2\langle r^2\rangle\right). \tag{3.72}$$

In order to calculate the compression mode frequencies in the non-interacting Fermi gas regime quite a similar approach like the one above for the hydrodynamic regime is used. By inserting the anharmonic potential from equation (3.61) into equation (3.32), one gets similar to equation (3.65):

$$\ddot{b}_x = \omega_x^2\left(\frac{1}{b_x^3}\left(1 - \frac{m}{2V_0}\omega_x^2\frac{\langle\tilde{x}^2\tilde{y}^2 + \tilde{x}^4\rangle}{\langle\tilde{x}^2\rangle}\right) - b_x\left(1 - \frac{m}{2V_0}\omega_x^2\frac{\langle\tilde{x}^2\tilde{y}^2 + \tilde{x}^4\rangle}{\langle\tilde{x}^2\rangle}b_x^2\right)\right), \tag{3.73}$$

and an analog result for y.

As the non-interacting Fermi gas has got the density profile of an ideal gas (like a hydrodynamic gas in the unitarity limit), the relations $\langle\tilde{x}^2\tilde{y}^2 + \tilde{x}^4\rangle = \frac{4}{3}\langle\tilde{x}^4\rangle$ and $\langle\tilde{x}^4\rangle = \frac{12}{5}\langle\tilde{x}^2\rangle^2$ are valid. Using these results together with a scaling ansatz like above results in a frequency of the compression mode of:

$$\omega_c = 2\omega_r\left(1 - \frac{3}{5}\frac{m}{V_0}\omega_r^2\langle r^2\rangle\right). \tag{3.74}$$

Quadrupole surface mode

There are also corrections on the frequency of the quadrupole surface mode ω_q due to anharmonicity effects of the confining potential.

In the hydrodynamic interaction regime one gets equation (3.66) exactly as in the case of the compression mode described above. In contrast to the compression mode the following ansatz for the scaling function b is used for characterizing the quadrupole surface mode:

$$b_x = 1 + \delta,$$
$$b_y = 1 - \delta. \tag{3.75}$$

Using the ansatz in equation (3.75) in equation (3.66) results in

$$\ddot{\delta} = -\delta \, 2\omega_r^2 \left(1 - 2\frac{m}{V_0}\omega_r^2 \langle r^2 \rangle \frac{(2 + 5\gamma)}{(2 + 7\gamma)} \right) = 0, \tag{3.76}$$

which finally leads to the collective frequency:

$$\omega_q = \sqrt{2}\omega_r \left(1 - \frac{m}{V_0}\omega_r^2 \langle r^2 \rangle \frac{(2 + 5\gamma)}{(2 + 7\gamma)} \right). \tag{3.77}$$

For the two limits of a weakly interacting BEC ($\gamma = 1$) and a universal quantum gas ($\gamma = \frac{2}{3}$), equation (3.77) leads to

$$\omega_q = \sqrt{2}\omega_r \left(1 - \frac{7}{9}\frac{m}{V_0}\omega_r^2 \langle r^2 \rangle \right) \tag{3.78}$$

in the BEC limit and

$$\omega_q = \sqrt{2}\omega_r \left(1 - \frac{4}{5}\frac{m}{V_0}\omega_r^2 \langle r^2 \rangle \right) \tag{3.79}$$

in the universal regime.

In the non-interacting Fermi gas regime, for each axis exactly the same formalism as applied above for the compression mode can be used. So the frequencies of quadrupole and compression modes of a non-interacting Fermi gas are equal, the only difference lies in the phase difference of π occurring in the surface mode. Therefore the quadrupole surface mode frequency of a non-interacting Fermi gas in an anharmonic trapping potential is calculated to be

$$\omega_q = 2\omega_r \left(1 - \frac{3}{5}\frac{m}{V_0}\omega_r^2 \langle r^2 \rangle \right). \tag{3.80}$$

Chapter 4

Experimental setup

The first step in all our experiments is the cooling and trapping of ultracold fermionic atoms. Together with the tuning of the scattering properties of our atoms via a magnetic Feshbach resonance, these are the basic features of our experimental setup, which are described in this chapter. Main parts of the experiment have already been described in previous diploma [Joc00, Els00, Mor01, Hen03, Rie04, Koh07] and PhD theses [Joc04, Bar05a]. Thus this chapter will only give a short overview of the experimental setup and focus on recent changes and improvements of the apparatus.

The following section 4.1 gives a short overview of our vacuum system and our Zeeman slower for a beam of ^{6}Li atoms. Next, in section 4.2, the details of magneto-optical and optical traps used during experiments are uncovered. In particular our most recent improvement, the new scanning system for the dimple laser that enables us to write arbitrary potentials, is a central part of this section. Then, in section 4.3, the coils designed to create magnetic fields in order to make use of the magnetic Feshbach resonance are described. Finally we examine the detection of particles in section 4.4.

4.1   Vacuum system and atomic beam

Successful experiments with ultracold gases require lifetimes of the particles that are as long as possible. As collisions limit the lifetime of a gas in the apparatus, a vacuum system is a necessary device for conducting experiments with ultracold atoms.

The vacuum chamber we use in all our experiments is shown in figure 4.1. It consists of an oven chamber operating at a moderate pressure of about 10^{-8} mbar and an ultra-high vacuum chamber with a pressure of below 10^{-10} mbar. A 45 cm long slower tube, which works as a differential pumping tube, connects both chambers. The vacuum in the UHV cell and in the oven chamber is maintained by ion getter pumps. In addition, there is a titanium sublimation pump; however, we have not needed to use this within the last four years.

The oven consists of a small hollow copper cube ($32 \times 22 \times 22 \, \text{mm}^3$) that is filled with about 0.2 g of ^{6}Li enriched to 95%. A gas of ^{6}Li atoms escapes from a 1 mm hole
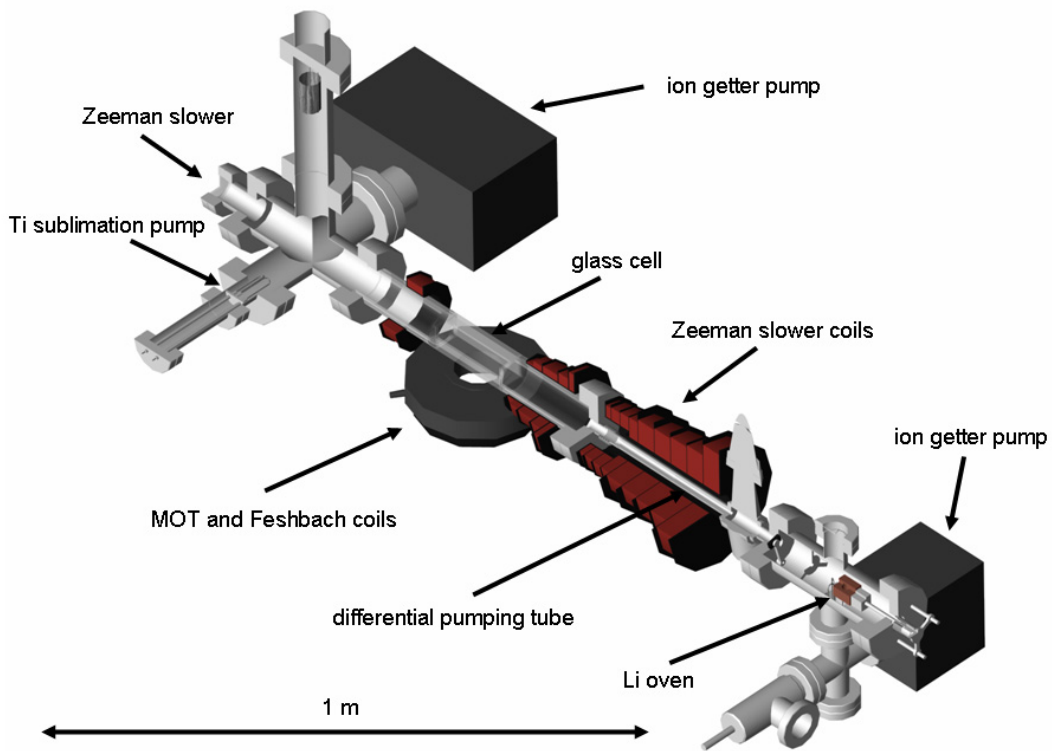
Figure 4.1: Overview of the vacuum chamber with pumps, ^{6}Li oven and Zeeman slower. All our experiments are performed inside the glass cell which is surrounded by the MOT and Feshbach coils.

on the front side of the copper cube. In all our experiments, we operate the oven at a temperature of 340° C.

The central part of our UHV chamber consists of a glass cell with the outer dimensions $4 \times 4 \times 12 \, \text{cm}^3$. It consists of 4 mm thick, high purity, uncoated fused silica.

In Figure 4.1 also the 45 cm long Zeeman slower tube is shown. It is used to decelerate the atomic beam and reduce the width of its velocity distribution. The Zeeman slower is set up as a decreasing field Zeeman slower with a designed maximum capture velocity of 600 m/s. The necessary magnetic field is produced by 14 individual magnetic field coils with a maximum field of 560 G. The design of the coils ensures that the corresponding magnetic field smoothly matches with the quadrupole field of the MOT [Joc00]. The laser light for the slowing beam enters the chamber through a viewport on the other side of the glass cell.

4.2 Trapping techniques

Trapping an ultracold gas is an essential precondition for many experiments. Only a trap enables us to manipulate and study the particles of the gas. Therefore it is not surprising that the ultracold atom physics community developed a variety of different traps for atoms [Ket99, Gri00]. During an experimental cycle, we use several different trapping techniques. First we describe a we use a Magneto-optical trap (MOT) in 4.2.1. We use the MOT for capturing and trapping atoms directly from the atomic beam. In the next experimental step, the atoms are transferred from the MOT into a purely optical resonator trap. This is done in order to cool and increase the density of the ensemble, as will be described in 4.2.2. The final experimental step is done in a single focused beam dimple trap. This purely optical trap configuration is described in further detail, including in particular the scanning system for the trapping laser, in 4.2.3.

4.2.1 Magneto-optical trap

The first step in all our experiments is to load atoms in the magneto-optical trap (MOT) [Raa87, Phi98]. We can trap a large number of still relatively hot atoms in the MOT. Our MOT is loaded from the Zeeman slowed atoms. The whole laser system for trapping and cooling the atoms in the MOT is based on diode lasers. The main features of the laser system are described in the following, whereas further details can be found in [Joc00, Rie04, Joc04].

For laser cooling of the ^{6}Li atoms, we use the $D2$ line at a transition wavelength of about 671 nm, that connects the $2S_{1/2}$ ground state and the $2P_{3/2}$ excited state. We operate the MOT with two different laser frequencies. The first drives the cooling transition from the $F = 3/2$ ground state. The second is used to repump from the $F = 1/2$ ground state. In addition, for the Zeeman slower another laser frequency, which is red detuned with respect to the cooling light, is used.

We use a system of master lasers and injection seeded slave lasers to create the frequencies needed for cooler, repumper and Zeeman slower. The frequency reference for the master laser is provided by saturation spectroscopy of ^{7}Li vapor produced in a heat pipe (see [Joc04] for details) that is operated at about 300° C. A grating stabilized diode laser is used as master laser and is locked by frequency modulation to the ^{7}Li D1 line [Joc00]. This line possesses a blue detuning of +698 MHz and +469 MHz with respect to the D2 lines that are used for the cooling and repumping transitions, respectively.

A frequency offset locking technique [Sch99] is used to lock another laser with an offset frequency of −870 MHz to the master laser. This locking technique enables us to shift the laser frequency over a wide range of about ±100 MHz. An individual adjustment of the frequency for the cooling and repumping transition is achieved by splitting the laser beam into two beams and individually shift the frequencies by an acousto-optic modulator (AOM). Finally, both cooling and repumping frequencies are

amplified by injection locked slave laser diodes that each provide an output power of about 20 mW.

The light for the Zeeman slower laser is obtained from the cooling transition light. Using an AOM we shift the frequency of this light by 65 MHz to the red and seed an injection locked slave laser. Experimentally it turned out that the loading rate of the MOT was optimized when the laser diode of this slave laser was modulated at about 40 MHz [Joc04]. The optimum value leads to loading rates of about 7×10^6 atoms/s when the trapping lasers are tuned about 4-5 natural linewidths (a natural linewidth is 5.9 MHz for ^{6}Li [Gri00]) to the red of the resonance.

4.2.2 Resonator trap

After loading atoms into the MOT, the next experimental step is to transfer them into a purely optical trap. We use a resonator trap, which provides much deeper trapping potentials than the MOT. Before describing details of the resonator trap, some general properties of optical dipole traps for neutral cold particles are presented.

Optical dipole traps offer great possibilities to trap atoms as well as molecules independent of their internal state [Gri00]. Based on the induced dipole moment of the atomic or molecular oscillator in the electro-magnetic light field of a far-detuned laser, particles are trapped in a potential which is dependent on the intensity of the light field. Depending on the phase between the oscillation of the induced dipole and the incident light beam, the atoms experience a force towards the intensity minimum (out-of-phase oscillation) or intensity maximum (in phase oscillation). The corresponding dipole potential V_{dip} is given by [Gri00]

$$V_{\mathrm{dip}}(\mathbf{r}) = -\frac{3\pi c^2}{2\omega_0^3} \left(\frac{\Gamma}{\omega_0 - \omega} + \frac{\Gamma}{\omega_0 + \omega} \right) I(\mathbf{r}), \qquad (4.1)$$

and is negative (positive), if the light frequency ω is red (blue) detuned with respect to the atomic resonance frequency ω_0. Here, Γ is the natural linewidth of the transition (with $\Gamma = 2\pi \times 5.9$MHz for ^{6}Li) and $I(\mathbf{r})$ describes the position-dependent light intensity. The condition of the laser being far-detuned keeps the induced photon-scattering rate of the trapped particles low and thus prevents heating.

In order to characterize such an optical trapping potential, one assumes that the potential is harmonic and defines the trap frequency ω_{trap} by

$$\omega_{trap}/2\pi = \frac{1}{w_0\pi} \sqrt{\frac{V_{dip}}{m}}, \qquad (4.2)$$

where m is the mass of the particle and w_0 is the minimal waist of the laser beam.

The resonator trap consists of a optical dipole trap created by a laser beam in an optical resonator. The resonator setup results in an optical standing wave, whose maxima possess an enhanced intensity compared to the one of the single laser alone. In this way, the transfer of atoms from the MOT into the resonator trap is highly efficient

due to two effects. First, the intensity in each potential well is high enough to make the trap depth larger than the kinetic energy of the atoms loaded from the MOT. Second, the existence of many intensity maxima leads to a reasonable spatial overlap between the positions of atoms in the MOT and atoms captured by the resonator trap.

The resonator setup enhances the intensity of the light from initially ~1 W at a wavelength of 1064 nm by a factor of ~ 150. This laser light is obtained from an ultra-stable diode pumped Nd:YAG laser that emits 2 W (Mephisto 2000 by Innolight). The resonator geometry is a near confocal geometry with a distance between the two mirrors of 15.3 cm and a mirror curvature of 15 cm. The resulting waist w_0 is about 160 μm and the Rayleigh range stretches out to about 75 mm from the center of the resonator. Both resonator mirrors are outside the vacuum chamber. To minimize the optical losses at the glass cell, the symmetry axis of the resonator is aligned in Brewster's angle. A Hänsch Couillaud lock is employed to stabilize the resonator [Hän80]. To control and stabilize the intensity of the light in the resonator we monitor the transmitted light with a photodiode. The measured signal is used in a closed loop feedback system to stabilize the intensity using an acousto-optic modulator [Joc04]. The standing wave creates potentials with a maximum potential depth of about 1 mK. The separation between the individual potential wells is fixed by the wavelength of the laser and amounts to 532 nm. From the MOT we load approximately 1500 individual wells with typically about 8×10^6 atoms.

4.2.3 Dimple trap

The final trap configuration, in which all measurements described later take place, consists of an optical dipole trap created by a single focused laser beam. This trap setup provides great flexibility in trap depth and trap geometry, which we use for evaporation and more advanced experimental schemes. As the potential of this trap is steep and possesses small spatial extension, it is also called a dimple trap [Pin97, SK98a, Web03, Ryc04]. The particles in the spatially extended and shallower resonator trap described in 4.2.2 serve as a reservoir, from which the dimple is loaded. So, the dimple is filled with rather cold particles with high phase space density. By lowering the intensity of the dimple laser, we can perform evaporative cooling and finally reach temperatures low enough to achieve quantum degeneracy and a BEC of molecules.

In the following, the properties of the focused beam trap needed for our standard experimental scheme to reach a molecular BEC, especially intensity profile and intensity control, are described. Then, the two-dimensional scanning system of the dimple beam as a tool for the creation of more complex optical potentials is presented. This scanning system enables us to perform more advanced experiments, e.g. the measurements described in chapters 6, 7 and 8.1.

A simplified schematic overview of the setup of the dimple trap including the scanning system is given in Fig. 4.2. There the effect of a modulation of the scanning system is shown. In addition, Fig. 4.2 also shows the setup of the imaging system along the *z*-axis, which is the symmetry axis of the cloud.
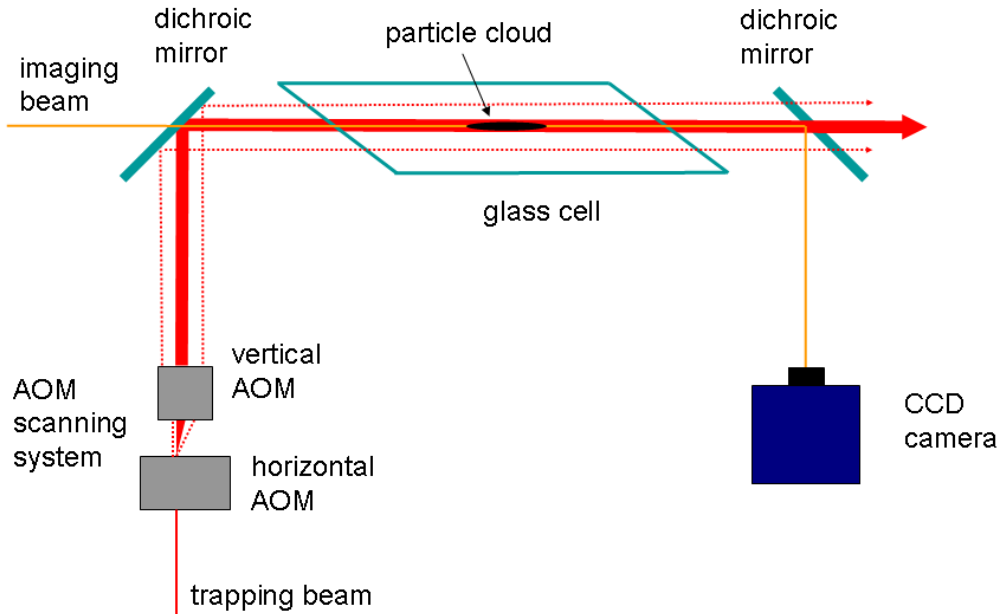
Figure 4.2: Schematic overview of the scanning system together with the imaging system along the symmetry axis of the cloud. Two crossed AOMs allow for horizontal and vertical displacement of the trapping beam. The thick solid line represents the unmodulated trapping beam. The dotted lines represent the trapping beam with maximal modulation in horizontal direction, so that the horizontal beam width is largely increased.

Focused beam trap

For the optical dimple trap we use a focused laser beam. The optical setup is described in Fig. 4.3. We use an Yb:YAG laser (ELS VersaDisc 1030-50-SF) with a power of 26 W at a wavelength of $\lambda = 1030$ nm, which is far red detuned from all relevant transitions. The laser runs at a stable TEM$_{00}$ mode and possesses an initial ellipticity of $\epsilon = 0.06$ (for the definition of ϵ see Eq.(3.49)). The initial beam waist of the laser is $w = 316\,\mu$m at a position of 0.7 mm after the window of the laser casing.

We stabilize the intensity of the laser using a feedback system [Joc04]. A first acousto-optic modulator (AOM) is used to control the power of the laser. Therefore the signal of a calibrated photo diode is used in a feedback-loop to control the driver power of the AOM and in this way the intensity of the light in the first scattered order. A logarithmic amplifier of the photo diode enables precise intensity control over several orders of magnitude.

A system of telescopes is used to focus the laser at the position of the cloud in the glass cell. The Gaussian intensity profile of the focused beam is

$$I(x, y, z) = P \frac{2}{\pi w_x(z) w_y(z)} \exp\left(-2\left(\frac{x^2}{w_x^2(z)} + \frac{y^2}{w_y^2(z)}\right)\right), \quad (4.3)$$

where P is the power of the laser and $w_x(z), w_y(z)$ are the beam waists in x- and y-direction at the position z from the focus given by

$$w_x(z) = w_{x,0} \sqrt{1 + \left(\frac{z}{z_0}\right)}, \quad (4.4)$$

and analog for $w_y(z)$. $w_{x,0}$ and $w_{y,0}$ are the minimal waists in the corresponding direction and z_0 is the Rayleigh length defined by

$$z_0 = \pi \frac{w_0^2}{\lambda}. \quad (4.5)$$

The intensity profile of Eq.(4.3) results, according to Eq.(4.1), in an optical trapping potential. The maximal potential depth can be calculated to be

$$V_{\text{dip;max}} = -\frac{3c^2}{\omega_0^3} \left(\frac{\Gamma}{\omega_0 - \omega} + \frac{\Gamma}{\omega_0 + \omega}\right) \frac{P}{w_0^2}, \quad (4.6)$$

with P being the power of the dimple laser. The corresponding temperature T_{trap}, up to which particles are trapped in this potential, is given by

$$T_{\text{trap}} = \frac{V_{\text{dip;max}}}{k_{\text{B}}}, \quad (4.7)$$

where k_{B} is Boltzmann's constant.

For given beam waist w_0 and dimple laser power P, the characteristics of the trap is calculated. The maximal trap depth $V_{\text{dip;max}}$ can be calculated to be

$$V_{\text{dip;max}} = 5.575 \times 10^{-37} (\text{m}^2\text{s}) \frac{P}{w_0^2}. \quad (4.8)$$

The corresponding trap frequency ω_{r} is determined by

$$\omega_{\text{r}} = 2\pi \times 2.38 \times 10^{-6} \left(\text{m} \sqrt{\frac{\text{s}}{\text{kg}}}\right) \frac{\sqrt{P}}{w_0^2}. \quad (4.9)$$

In addition, there is a magnetic confinement in the axial z-direction due to a residual magnetic field curvature (see section 4.3). For low optical trapping power, the magnetic confinement has to be taken into account. The axial optical trap frequency $\omega_{\text{z;opt}}$ is given by

$$\omega_{\text{z;opt}} = \frac{\lambda}{\pi w_0^2} \sqrt{\frac{2V_{\text{dip;max}}}{m}} = 2\pi \times 5.51 \times 10^{-13} \left(\text{m}^2 \sqrt{\frac{\text{s}}{\text{kg}}}\right) \frac{\sqrt{P}}{w_0^2}. \quad (4.10)$$

The axial magnetic trap frequency $\omega_{z;mag}$ is found to be

$$\omega_{z;mag} = 2\pi \times 0.775 \left(s^{-1}G^{-1/2}\right) \sqrt{B}. \tag{4.11}$$

Altogether, the total axial trap frequency ω_z is determined by

$$\omega_z = \sqrt{\omega_{z;opt}^2 + \omega_{z;mag}^2}. \tag{4.12}$$

The adjustment of the beam waists $w_{0,x}$ and $w_{0,y}$ in x- and y- direction, respectively, turns out to be crucial for evaporation process (see 5.1.2 for details of the evaporation process). Due to the initial ellipticity of the beam profile from the laser, the optical system has to be carefully aligned to minimize the ellipticity. In our latest setup, we achieve an ellipticity of $\epsilon = 0.06$. This makes the trapping potential almost cylindrically symmetric, with only small corrections due to ellipticity.

Besides differences between $w_{0,x}$ and $w_{0,y}$, also the absolute size of the mean radial beam waist w_0 has severe consequences for the experiment.

A larger w_0 results in a larger spatial extension of the dimple trap with lower trap depth for a given laser power. This improves the number of particles transferred from the resonator trap to the dimple trap, but also lowers the phase space density and collision rate of the particles in the dimple trap.

A smaller w_0 results in a higher phase space density and collision rate in the trap, which enables a more efficient evaporative cooling process by lowering the trap depth. But as less particles are transferred from the resonator trap into the spatially less extended dimple trap, the evaporation process starts with less particles.

The experimental challenge consists in finding a w_0 which is large enough to provide a sufficient particle number in the deepest trap depth at the beginning of evaporation, but which is also small enough to provide an efficient evaporation ramp to achieve a molecular BEC. We can change w_0 by changing the position of the last lens in front of the atoms (see Fig. 4.3). By changing w_0 between 35 μm and 80 μm, we experimentally found an optimum for $w_0 \approx 54\,\mu$m.

Scanning system

In the following, a short overview of the new scanning system shown in Fig. 4.3 is given. A more detailed description can be found in the diploma thesis of Christoph Kohstall [Koh07]. The scanning system enables us to manipulate the position and the shape of our trap in the x-y-plane. This system is a versatile tool that allows to manipulate our optical dipole trap. We can rapidly displace the trap laterally. Fast modulation of the beam position enables us to create time-averaged potentials for the trapped particles [Mil01, Fri01].

As shown in the rough scheme in Fig. 4.2 and the more detailed overview in fig. 4.3, the central part of the scanning system consists of two crossed AOMs (AOM 3110-197 from Crystal Technology). These deflect the trapping light beam in horizontal and
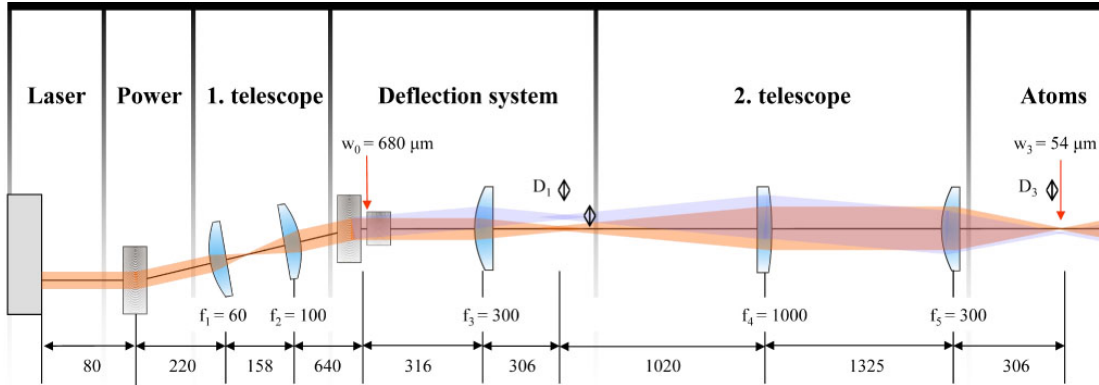
Figure 4.3: Optical setup for the focused beam trap including the scanning system

vertical direction. The deflection is based on Bragg scattering of the light at sound waves in the AOM crystal. The acoustic waves in the AOM crystal are excited by an external RF driving frequency, which determines the wavelength of the sound and in this way the deflection angle of the light. So, by changing the RF driving frequency, the deflection angle can be changed. We always use the first scattered order of each AOM.

Fig. 4.4 illustrates the principle of our scanning system for one dimension. A collimated beam passes through an AOM and is deflected depending on the driving frequency. The deflection results in a parallel displacement with a lens placed within the distance of one focal length behind the AOM. By changing the frequency with which the AOM is driven, the lateral position of the focus is shifted. This system enables us to displace the focus of the trapping beam in horizontal and vertical direction by up to four times the beam waist in all directions. Furthermore, the deflection can be modulated by frequencies of up to > 950kHz within 3dB bandwidth, which is much larger than the trap frequency. In our trap configuration, we typically use modulation frequencies of 100kHz. We can create an elliptic potential shape by modulating the trap potential along a specific direction. By choosing a suited modulation function, these elliptic potentials are nearly harmonic. We realized that a periodic modulation with an arc sine-like function results in much better harmonic potentials than a simple sawtooth modulation ramp (see also [Koh07]). The first telescope in front of the crossed AOMs is used to achieve a beam waist of 680μm, which makes the beam slightly smaller than the maximum diameter of 1400μm of the AOM. In this way, the scattering efficiency of the AOMs is optimized to be $> 90\%$. The laser beam is collimated when passing the AOMs. So, a change in deflection angle results in a parallel translation of the focussed beam after the second telescope and the last focussing lens. We measured the deviation from parallelism of the deflected beams to be $< 0.5\%$.
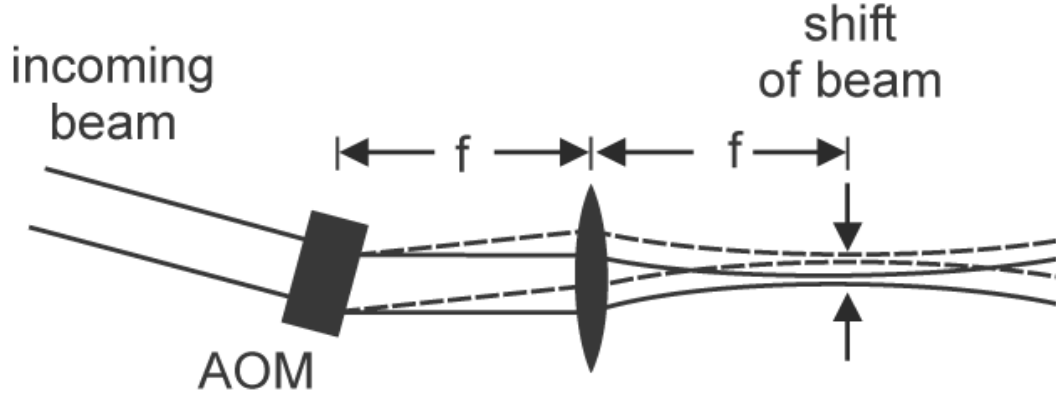
Figure 4.4: Schematic illustration of the scanning system. A wide collimated beam passes through an AOM. The resulting deflection angle depends on the driving frequency of the AOM. The beam passes through a lens in the distance of one focal length behind the AOM. The lens focuses the beam for atom trapping. Deflection results in a parallel shift of the beam position in the focal plane. The solid and dashed lines show the beam's path for different deflection angles. The zeroth order beams are not shown.

4.3 Magnetic field coils

In order to tune the scattering properties of our ^{6}Li gas over the full range of interest (see section 2.3) we use a pair of magnetic field coils that creates magnetic fields of up to 1470 G at a current of 200 A. The main features of our design are a small size, an efficient cooling and small Eddy currents. These requirements are met by using flat cooper wire from which two individual coils with a small gap between them are formed. There is a constant flow of cooling water in the gap. The water is in contact with every winding and thus leads to efficient cooling. Finally the water proof housing is made from PVC and avoids Eddy currents. In principle, it enables fast switching of the magnetic field. The technical details of the coils are found in [Joc04, Hen03]. Reference [Joc04] also provides the technical details of our current stabilization which results in a stability of 22 mG (± 3 mA). This enables us to tune the atomic s-wave scattering length a very precisely.

A special detail in the setup of these magnetic field coils is a small curvature in the created magnetic field. This curvature leads to a weak trapping potential for lithium atoms and molecules along the axial z-direction. The trapping potential is described by

$$V_{mag} = -\frac{1}{2}\mu\,B''z^2,\tag{4.13}$$

where μ is the magnetic moment of the particles and B'' is the curvature of the magnetic field. This results in magnetic trap frequencies of

$$\omega_{mag} = \sqrt{\frac{\mu\,B''}{m}}.\tag{4.14}$$

For our experimental parameters we find $B'' = -0.0255\,\text{cm}^{-2} \times B$ and $\mu = \mu_B$, as the magnetic moment of ^{6}Li atoms equals Bohr's magneton.

In addition to the large coils that create the magnetic bias field, a pair of small coils for fast changes in the magnetic field is also installed. The space between the mount for the optical resonator and the large magnetic field coils contains a second pair of small coils. In contrast to the big coils these coils are not water cooled and can be operated continuously up to 500 mA. This results in a homogenous field of about 25 G or, if alternatively operated in anti-Helmholtz configuration, in a field gradient of about 8.5 G/cm. Moreover these coils can for short times < 1 s produce homogenous fields exceeding 300 G (or alternatively gradients > 100 G/cm).

In our experiments, these coils are used in anti-Helmholtz configuration to compress the MOT during the transfer into the standing wave, to compensate for gravity and for residual magnetic field gradients in the vertical direction.

4.4 Detection system

We use two different techniques to detect cold atoms and molecules in our trap. Measuring the fluorescence light with a calibrated photo diode is a robust tool to gain information about the number of particles in our trap. The technique of fluorescence measurement is shortly described in 4.4.1. A more sophisticated technique uses absorption imaging of the cloud. From absorption images, we determine density profiles of the cloud. Absorption imaging enables us not only to measure the total number of particles, but also their density distribution in phase space. In our experimental setup, some imperfections have been taken into account. The absorption imaging system including some corrective optics is presented in 4.4.2.

A very important parameter of all our experiments is the total number of particles. Therefore, the determination of the number of particles with both methods is described more detailed in 4.4.3.

4.4.1 Fluorescence measurement

A simple and robust way to detect the cold particles in our trap is to recapture the particles into the MOT and to measure their fluorescence.

A calibrated photodiode is used to detect the light that is scattered into a solid angle Ω. We define the rate of photons hitting the photodiode as Γ_{PD}. Together with Γ,the photon scattering rate of the atoms in the MOT, the total number of atoms N is determined by

$$N = \frac{\Gamma_{PD}}{\Gamma\Omega}. \tag{4.15}$$

In our case the atom number calibration yields [Joc04]

$$N = 2.85 \times 10^6 \text{ atoms/V}, \tag{4.16}$$

with a relative uncertainty of about 25%.

To detect the number of molecules at a given magnetic field, we employ a technique that is based on the dissociation of the molecules by ramping the magnetic field across the Feshbach resonance [Reg03]. This ramp shifts the bound level above the continuum and the molecules quickly dissociate. After this dissociation process we quickly ramp the magnetic field down to zero. This fast ramp speed avoids the molecule formation when crossing the Feshbach resonance and the region where $a > 0$. In addition, we heat the sample by abruptly turning on the full trapping laser power to avoid molecule formation. This step turned out to be crucial as even while all molecules might be dissociated during the ramp across the resonance, molecules could be formed again from a cold sample during the ramp back to zero magnetic field before detection. Furthermore, we limit the heating of the sample in a way that no evaporative loss occurs. This is done by minimizing the time for the magnetic field ramps so that the atoms would spend only negligible time in regions with large scattering length. After reaching zero magnetic field, we recapture the atoms in the MOT and measure the atom number as described above.

This measurement yields the total number of atoms $N_{tot} = 2N_{mol} + N_{at}$, where N_{mol} and N_{at} denote the number of molecules and atoms, respectively. In order to obtain N_{at}, we repeat the same measurement without the Feshbach dissociation ramp by immediately ramping down to zero magnetic field from the initial magnetic field. This ramp down to zero magnetic field increases the molecular binding energy to a large value of about $k_B \times 80\,\text{mK}$ so that the molecules are lost without leading to any fluorescence light in the MOT. The number of molecules is determined by the difference in atom numbers measured in the two subsequent runs with and without the dissociating Feshbach ramp.
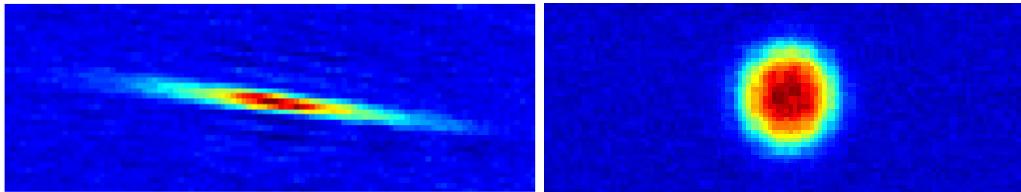
4.4.2 Absorption imaging

Our main detection technique is absorption imaging. The basic idea lies in the imaging of the intensity profile of a resonant laser beam, which has been partially absorbed by a particle cloud, on a CCD camera [Ket99].

We use absorption imaging along two imaging axes. An older optical setup, described in detail in [Joc04] and [Rie04], images the longer axis of the cigar-shaped cloud in the dipole trap under an angle of $46° \pm 1°$ to the horizontal plane. In this way, the axial profile of the cloud can be detected. Recently, an additional imaging system has been set up parallel to the trapping laser beam (see Fig. 4.2). This enables us to detect the full radial profile of the cloud. In contrast to the older imaging system, which included only information of the vertical radial direction y, the new system provides information of both vertical and horizontal radial directions x and y. Furthermore, we are able to take absorption images along both imaging axes at the same time, which provides both axial and radial profile of the cloud.

To image the particles at high magnetic field in the vicinity of the Feshbach resonance we use a grating stabilized diode laser at $\lambda = 671\,\text{nm}$, that is locked

by a frequency offset locking technique to our reference laser. This enables us to tune the frequency of the imaging laser over a wide range of $\pm 1.8\,$GHz. A detailed description of the setup is given in [Rie04]. The imaging of the atoms is based on a closed σ^--transition from the $2S_{1/2}$ ground state to the $2P_{3/2}$ excited state ($|2S_{1/2}, m_J = -1/2, m_I\rangle \rightarrow |2P_{3/2}, m_J = -3/2, m_I\rangle$). Because the transition frequency depends on the orientation of the nuclear spin ($m_I = -1, 0, 1$), the imaging at high magnetic field also offers a state selective detection. The magnetic moment of the excited and ground state amounts to $2\,\mu_B$ and μ_B, respectively and therefore the transition frequency tunes with $-\mu_B \approx -1.4\,$MHz/G. We are also able to image weakly bound molecules at high magnetic fields with the same light like atoms. This is possible as long as the shift of the transition frequency for molecule compared to atoms is smaller than the linewidth of the transition [Zwi03]. Estimations (see [Bar05a]) show that for magnetic fields > 720G, the shift is below 1MHz, whereas the natural linewidth of ^{6}Li is $\Gamma = 2\pi \times 5.9$MHz. So the weakly bound molecules at magnetic field above 720G can be imaged as if they were free atoms.

For radial imaging, the resonant light of the imaging laser possesses a typical power of $180\,\mu$W and is collimated to a waist of 1.48 mm, resulting in an intensity $I_{0;max} \approx 10\,$mW/cm^2. Typical durations of the imaging light pulse are $5\,\mu$s.

Figure 4.5: Typical absorption images of the ultracold gas cloud. On the left-handed side an in-situ image of the trapped cloud along the axial direction of the cigar-shaped geometry is shown. The right-handed image displays the expanded cloud after release from the trap in a time-of-flight picture along the radial direction.

In our experiments, there are two ways of gaining information from a trapped particle cloud by absorption imaging. By imaging the cloud in the trap, the in-situ imaging, the spatial density distribution of the cloud can be deducted [Ket99]. In our setup, in-situ imaging is only useful for axial images of the trapped cloud, as the radial size of the cloud is to small to be resolved by our imaging system. On the other hand, the time-of-flight imaging of an expanding cloud being released from the trap, is suitable for both imaging axes of our experimental setup. After expansion (in our case the expansion time t_{TOF} lasts typically a few ms), also the size of the cloud in radial direction is large enough to provide a satisfying resolution. From time-of-flight images, the density distribution of the cloud in phase space can be extracted [Ket99]. Typical absorption images are shown in Fig. 4.5. On the left-hand side, an in-situ-image of the longer axial side of the cigar-shaped cloud is shown. The right-hand side shows a time-of-flight image of the radial expansion of the cloud.
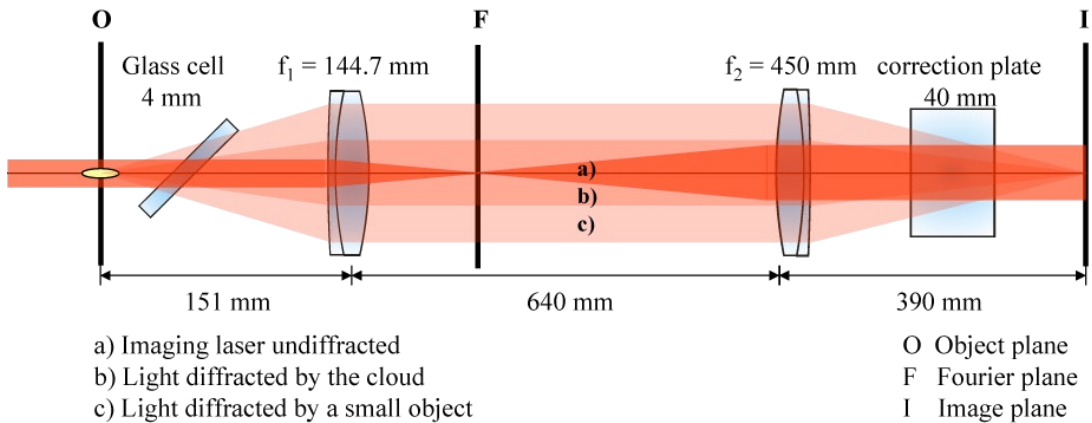
Figure 4.6: Optical setup for the absorption imaging system of the radial cloud profile. The cloud in the object plane is imaged on the CCD camera in the image plane. A telescope is magnifying the cloud, whereas imaging imperfections induced by the glass cell are corrected for by the correction plate. Note that the object distance is for experimental reasons not exactly the focal length of the first lens. The light distributions represent the undiffracted light of the laser and the diffracted light of two objects with different size.

Detailed information on the optical setup of the new radial imaging system is given in Fig. 4.6. We want to image the particle cloud in the object plane on the CCD chip of the camera in the image plane. In order to magnify the object, a telescope is integrated in the optical setup. Due to limitations of optical access, the object distance from the cloud to the first lens is not exactly the focal length of the first lens. Therefore, the magnification is not the ideal value of $450/145 \approx 3.103$ but the slightly higher value of ~ 3.2. Together with a pixel size of the CCD chip of $13\mu m$, this results in a resolution of the cloud of $\sim 8\mu m$.

Diffracted light from the cloud passes the 4mm thick glass cell under an angle of about 45°. So we find the situation of an uncollimated beam passing through a tilted glass plate [Wya92], which causes several aberration effects. A detailed study of these effects and how to compensate them is given in the diploma thesis of Christoph Kohstall [Koh07]. In summary, the aberration effects mainly result in imaging errors like astigmatism, coma error and spherical aberration. Suited correction schemes have to take into account the limited available space for corrective optics. A correction of coma is done by a decentering of the first lens. Astigmatism can be corrected for by introducing a 40 mm thick glass plate after the last lens. The effects of spherical aberration are negligible within experimental parameters.

4.4.3 Particle number determination

A crucial parameter in all our experiments is the total number of particles N. Like described in 4.4.1, we can determine N from fluorescence measurements. But N can also be determined from absorption images. In the past there has been a large difference of

a factor of $4 - 8$ between the particle numbers calculated by both methods (see [Joc04] and [Bar05a]). With a new and more precise approach we are now able to calculate N from absorption images in agreement with the result from fluorescence measurements. We will present this approach for absorption measurements in the following (see also [Koh07]).

Absorption of light by the cloud leads to a density dependent decrease in intensity $I(x, y, z)$ along the axis z of the imaging beam

$$\frac{dI(x, y, z)}{dz} = -\hbar\omega\Gamma_{light}(x, y)\, n(x, y, z), \tag{4.17}$$

where ω is the imaging laser frequency, $n(x, y, z)$ is the density of the particles and $\Gamma_{light}(x, y)$ is the photon scattering rate of the particles given by

$$\Gamma_{light}(x, y) = \frac{\frac{I(x,y)}{I_S}\frac{\Gamma}{2}}{1 + \frac{I(x,y)}{I_S} + \left(\frac{2\delta}{\Gamma}\right)^2}. \tag{4.18}$$

Here, Γ is the natural linewidth for ^{6}Li, δ is the detuning of the imaging light and I_S the saturation intensity defined by

$$I_S = \frac{\pi h c \Gamma}{3\lambda^3}. \tag{4.19}$$

For ^{6}Li and $\lambda = 671$nm one gets $I_S = 2.56\frac{mW}{cm^2}$. In our experimental setup, we have to include the effective saturation intensity $I_{S,eff} = 2I_S$, as we use only the σ^+-polarized part of our linearly polarized light for absorption.

The saturation parameter I/I_S is a crucial parameter for our approach. In [Joc04] and [Bar05a] we considered I/I_S to be small. We now typically use $I/I_S \approx 4$ in order to suppress noise effects. So we include a not necessarily small I/I_S in the new approach. Our next step in calculating the particle number N is to determine the column density $\tilde{n}(x, y)$, which is defined by

$$\tilde{n}(x, y) = \int dz\, n(x, y, z). \tag{4.20}$$

We introduce the scattering cross section σ as

$$\sigma = \frac{\hbar\omega\Gamma}{2I_S} = \frac{3\lambda^2}{2\pi}, \tag{4.21}$$

and the effective scattering cross section $\sigma_{eff} = \frac{1}{2}\sigma$. Together with the initial intensity $I_0(x, y)$ and an parameter $A = 1 + \left(\frac{2\delta}{\Gamma}\right)^2$ for simplification, we get from equation (4.17)

$$\tilde{n}(x, y) = \frac{1}{\sigma_{eff}}\left(A \ln\frac{I(x, y)}{I_S} - A \ln\frac{I_0(x, y)}{I_S} + \frac{I(x, y)}{I_S} - \frac{I_0(x, y)}{I_S}\right). \tag{4.22}$$

Equation (4.22) includes the detuning δ in the parameter A. For particles at rest, we can provide $\delta \approx 0$ in all our experiments. Photon recoil induces some detuning, but the effects on $\tilde{n}$ can be calculated to be only a few percent [Koh07]. So, we can neglect the detuning and assume $A \approx 1$, which leads to

$$\tilde{n}(x, y) = \frac{4\pi}{3\lambda^2} \left(\ln\left(\frac{I(x, y)}{I_S} \right) + \frac{I_0(x, y)}{I_S} \left(\frac{I(x, y)}{I_S} - 1 \right) \right). \tag{4.23}$$

The terms I/I_S and I_0/I_S in Eq.(4.23) are measured with the calibrated count rate of the CCD chip of our camera. In this way, the column density $\tilde{n}$ and with

$$N = \int \mathrm{d}x\mathrm{d}y \, \tilde{n}(x, y), \tag{4.24}$$

the total number of particles N are determined.

The number of particles which we get from absorption images with this method agrees well with the number we get from fluorescence measurements (see 4.4.1).

Chapter 5

Basic experimental methods

In the previous chapter 4, we presented the details of our experimental apparatus. Before describing the results of our measurements (chapters 6, 7 and 8.1), we introduce some of the basic experimental methods. For all measurements discussed in later chapters, we create a molecular BEC as a starting point. The creation process of a molecular BEC, consisting of the creation of molecules and the evaporation to quantum degeneracy, is described in section 5.1.

After the preparation of a molecular BEC, we characterize our system. To do this, we use standard techniques such as the measurement of the trap frequencies and a controlled change in temperature.

We discuss how the radial trap frequencies are measured in section 5.2. The knowledge of the radial trap frequencies of the optical trapping potential is necessary for the determination of different collective mode frequencies (see 3.2, 3.3 and 3.4). Furthermore, from the trap frequencies in horizontal and vertical direction the ellipticity of the trap can be derived, which enables us to calculate ellipticity corrections for precision measurements of the compression mode frequency (see 3.5.1). Finally, in section 5.3 a description of our scheme for controlled heating is given.

5.1 BEC of molecules

The achievement of the first molecular BEC has been a milestone in the field of ultracold quantum matter [Gre03, Joc03a]. In our experiments, we use the molecular BEC as a starting point for further experiments in the BEC-BCS crossover regime. To create the BEC, we must first create long-living, bosonic molecules. This is described in 5.1.1. The long lifetime of these molecules make them perfectly suited for evaporative cooling. The details of the evaporation process are presented in 5.1.2.

5.1.1 Formation of molecules

We create weakly bound molecules at a magnetic field of 764 G, which is in the vicinity of a magnetic Feshbach resonance of ^{6}Li atoms at 834 G. A description of these molecules, including their binding energy, is given in 2.3.1. These molecules are created by three-body recombination of ^{6}Li atoms [Joc03b] at a fixed magnetic field. We found this to be more efficient than molecule creation schemes that include a sweep across the Feshbach resonance [Cub03]. In the three-body recombination process, a ^{6}Li$_2$ molecule is formed by two atoms. The binding energy of this molecule is released as kinetic energy of the third atom, which can lead to heating. There is an inverse process of dissociation of molecules. This can happen through atom-dimer and dimer-dimer-collisions. This dissociation process is endoergic in contrast to the exoergic three-body-recombination process. At a given temperature a chemical equilibrium of atoms and molecules evolves, where both processes are balanced [Chi04b]. An illustration of this equilibrium is shown in Fig. 5.1.
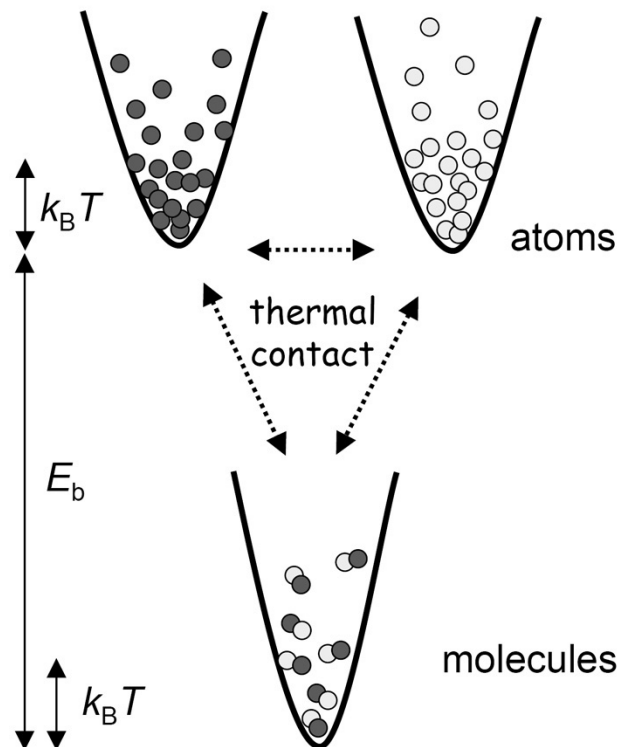
Figure 5.1: Illustration of the thermal equilibrium of atoms and molecules in a trapped gas on the molecular side of the Feshbach resonance. The three sub-systems, atoms in state $|1\rangle$ (compare 2.3.1 for the spin states of ^{6}Li), atoms in state $|2\rangle$ and the molecules are in thermal contact (thermal energy $k_\mathrm{B}T$). Because of their binding energy E_b (see Eq.(2.36)), the molecules are energetically favored. The equilibrium can also be understood in terms of a balance of the chemical processes of exoergic recombination and endoergic dissociation.

5.1.2 Evaporation

The evaporative cooling process in all our experiments takes place at a magnetic field of 764 G, which is also the same field where we create molecules (see 5.1.1 above). At this magnetic field, the scattering length is $a = +4500a_0$, which means strong repulsive interactions between both atoms and molecules (for details of the particle-particle interactions see 2.3.1).

The strong interactions result in high elastic collision rates. Thus thermalization is very efficient. In contrast to this, inelastic collision rates are relatively low, resulting in few losses. Altogether, these conditions are ideal for an evaporative cooling process.
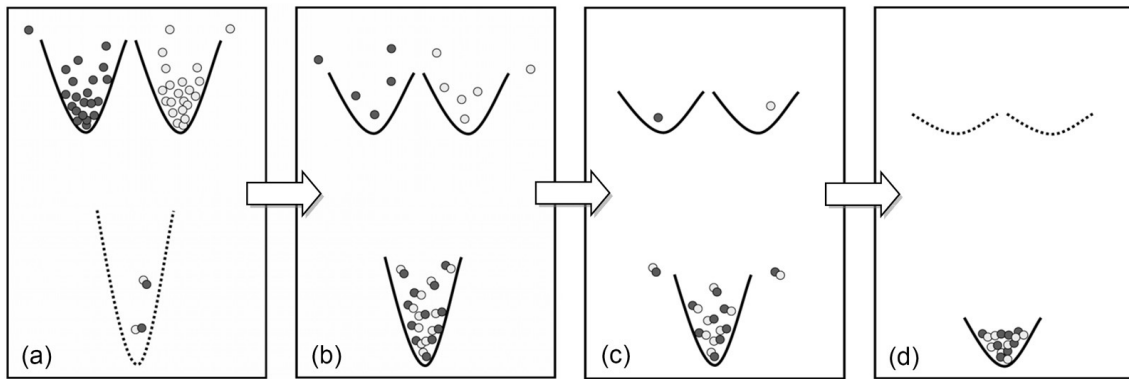
Figure 5.2: Different stages of the evaporative cooling process. (a) At high temperatures, only few molecules are present and the evaporation is mainly driven by elastic collisions in the atomic spin mixture. (b) As the gas gets colder, the chemical atom-molecule equilibrium begins to favor the molecules. (c) By further evaporation all the atoms are removed. This is further enhanced by the fact that the trap depth for the molecules is twice as large as for the atoms. Thus more molecules remain trapped. (d) After all the atoms are removed, the evaporation takes place with a purely molecular gas. Finally the critical temperature T_C is reached and the gas is condensed in a BEC.

An overview of the different stages of the evaporative cooling process of a trapped ensemble of atoms and molecules in thermal equilibrium is given in Fig. 5.2. For decreasing temperatures, the fraction of molecules is increasing. For low trap depths the fermionic atoms lack on trapped states to fill. Furthermore, the trap depth for molecules is twice as large as the one for atoms. This results in an almost pure molecular ensemble that remains in the trap. The bosonic molecules can accumulate in the ground state and in the end condense into a molecular BEC.

The whole evaporation process takes place in a focused-beam optical trap (see 4.2.3). A crucial parameter is the radial beam waist w_0. A larger w_0 results in a larger spatial extension of the dimple trap. This results in a lower trap depth for the molecules at given laser power. A larger waist improves the number of particles loaded into the trap at the beginning of the evaporation process. It also lowers the phase space density and elastic collision rate of the particles in the trap. This makes evaporation

less efficient. For the same reasons, a smaller w_0 results in a more efficient evaporative cooling process that starts with less particles. Therefore we determined the optimal beam waist by optimizing the particle number at the end of the evaporation process. We found it to be $w_0 \approx 54 \, \mu$m.

Using the optimized beam waist, we start the evaporation process with a typical particle number of $N \approx 2 \times 10^6$ atoms. Here the radial trap frequency is $2\pi \times 2.8$ kHz, which corresponds to a trap depth of $160 \, \mu$K. We perform a evaporation ramp of typically 5 s, where we lower the power of the trapping laser exponentially. Finally, we reach an almost pure molecular BEC with a particle number of $N \approx 2 \times 10^5$ molecules. There the radial trap frequency is $2\pi \times 180$ Hz, which corresponds to a trap depth of 680 nK. For our experiment, These are standard conditions for the creation of a molecular BEC. It is possible to reach even colder temperatures and thus create an even purer molecular BEC. However this greatly reduces the particle number. In order to minimize temperature effects (see the precision measurements of the compression mode in chapter 6), we created the coldest possible gas in the manner described above. We achieved an ensemble of about 1×10^5 molecules after lowering the evaporation trap depth to ≈ 500 nK.

5.2 Measurement of trap frequencies

The optical dimple trap (see 4.2.3) is a central part of all our experiments. Therefore, it is important to precisely characterize this trap. this can be done by determining the radial trap frequencies ω_x and ω_y, as they are equal for both trapped atoms and molecules. As all radial oscillation modes depend on the radial trap frequencies, we always normalize the mode frequency on the trap frequency (see chapter 3). Furthermore, ω_x and ω_y are also used to determine the ellipticity of the trap, which results in some corrections on the normalized mode frequencies(see 3.5.1 and 6.4.2).

For a measurement of the radial trap frequencies, we use the radial dipole mode. This mode is also called radial sloshing mode and described in more detail in 5.2.1. An explanation of our fit routine is given in 5.2.2.

5.2.1 Sloshing mode

The radial sloshing mode is a center of mass oscillation of the cloud in the trapping potential. This dipole mode shows no change in volume, surface or rotation angle during oscillation. This contrasts the higher excitation modes presented in chapter 3. Therefore the frequency of this mode is independent of the statistics and two-body interactions within the gas [Dal99a]. In a harmonic potential, the frequency of the sloshing mode in a chosen direction is equal to the trap frequency. For small deviations from the harmonic case, corrections have to be taken into account (see 3.5.2).

In order to excite the sloshing mode, we start with an ultracold cloud (not necessarily a Bose-condensed gas) in the dimple trap. We use our scanning system for an

adiabatic displacement of the trap. This takes about 100 ms. The cloud is displaced and remains in the minimum of the trapping potential. Then the trap is suddenly moved back to its original position. This jump-like motion is too fast for the cloud to follow. So the center of mass of the cloud is displaced from the minimum and the cloud starts oscillating in the initial potential. The amplitude of this displacement is chosen in such a way that the given energy is about 10% of the trap depth. While the cloud is oscillating in the trap, we wait for a time of the order of several tens of ms and then turn off the trap. Next, we image the cloud by time-of-flight imaging. The images are fitted with a two-dimensional fit to a Thomas-Fermi profile. Thus we determine the position of the center of mass of the cloud for different hold times. This yields the frequency of the sloshing mode.
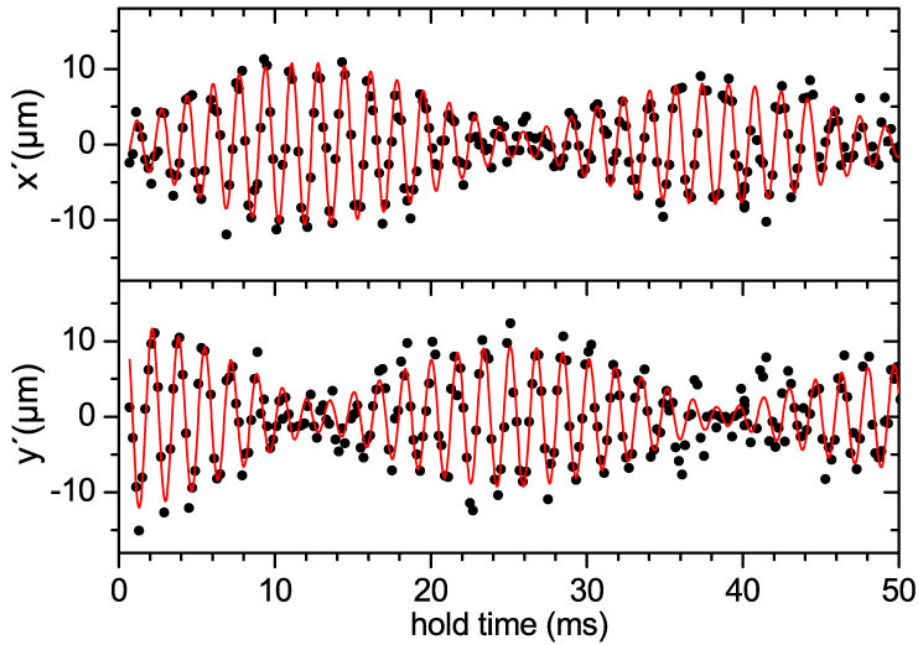
Figure 5.3: Radial sloshing observed at a trap power of 540 mW and $B = 735$ G. The two-dimensional center-of-mass motion is represented in a coordinate system (x', y') rotated by $\sim 45°$ with respect to the principal axes of the trap. The beat signal between the two sloshing eigenmodes demonstrates the ellipticity of the trap. The two eigenfrequencies are determined to be $\omega_x = 2\pi \times 570$Hz and $\omega_y = 2\pi \times 608$Hz by our rotation fit routine(see 5.2.2).

The residual ellipticity of the radial beam profile (see 4.2.3) results in some further complications in determining the trap frequencies. As we want to determine both radial trap frequencies ω_x and ω_y simultaneously in one measurement, we have to excite an oscillation in both x- and y-direction. This is done by displacing the cloud in a direction between the x- and y-direction.This results in a beat between the two eigenmodes of the trap in the new coordinate system x', y' as can be seen in the typical oscillation in Fig. 5.3.

5.2.2 Rotation fit
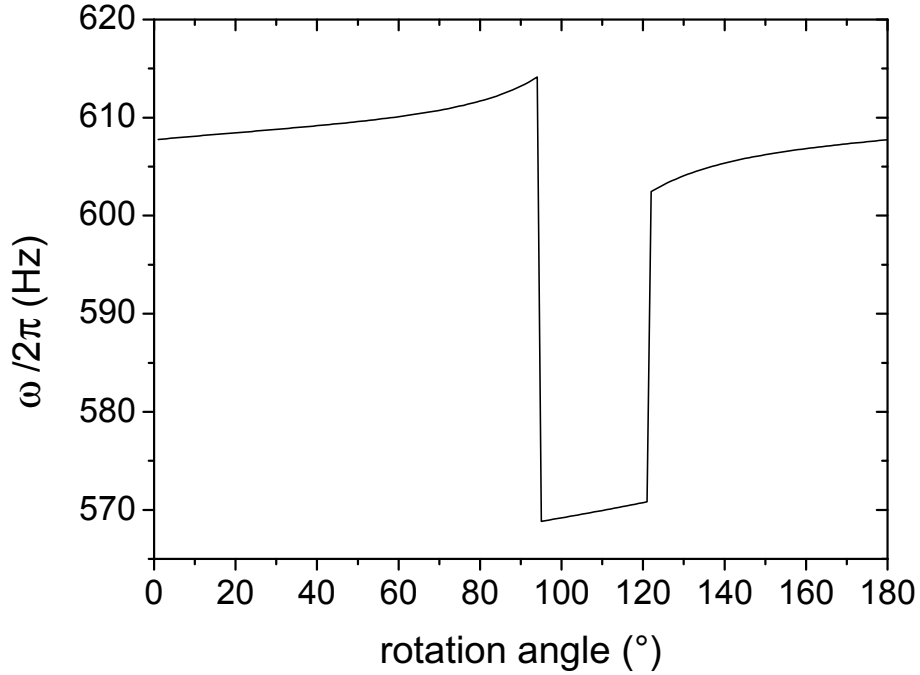
Figure 5.4: Calculated trap frequencies ω for different rotation angles of the fitting routine. The results are based on the raw data shown in Fig. 5.3. Depending on the rotation angle, the fit procedure yields the two different eigenfrequencies of $\omega_x = 2\pi \times 570 \text{Hz}$ and $\omega_y = 2\pi \times 608 \text{Hz}$.

We use a special rotation fit procedure to determine the trap frequencies along the principal axes of an elliptic trapping potential. This procedure yields much better results than a simple two frequency fit of the beat signal. Typical raw data are shown in Fig. 5.3. The coordinate system for our detection, specified by the axes x' and y', is rotated with respect to the coordinate system determined by the principal axes of the elliptic trapping potential x and y. In order to detect the oscillation along the principal axes and the trap frequencies ω_x and ω_y, the coordinate system has to be rotated. This rotation is implemented after evaluation of the center of mass motion. The axes of the rotated coordinate system are called x^* and y^*. We use a fitting routine which stepwise rotates the coordinate system and fits, for each step, a damped oscillation function in x^*- and y^* -direction. The fit function is given by

$$x^*(t) = A \exp(-\kappa t) \cos(\omega_{x^*} t + \phi) + x_0,$$
$$y^*(t) = A \exp(-\kappa t) \cos(\omega_{y^*} t + \phi) + y_0. \tag{5.1}$$

In Eq.(5.1), A is the amplitude of the oscillation, κ is a damping term, ω_{x^*} and ω_{y^*} are the oscillation frequencies, ϕ is a phase and x_0 and y_0 are offsets.

A typical result from this fitting procedure for different rotation angles is given in Fig. 5.4. From all rotation angles, we choose the angle, where the error of the fitting functions along x^* and y^* direction is the smallest. We assume these axes to be the principal axes of the elliptic trapping potential. From the fit function, we find the trap frequencies ω_x and ω_y with typical uncertainties of less than 0.5 %.

5.3 Controlled heating procedure

For some experiments, it is interesting to look at the influence of temperature. Therefore a controlled heating procedure is very useful. In our experiments, we implemented this by first compressing the trap. Then the gas is held in the trap for a variable hold time. During recompression, the trap frequencies are increased up to a value of about $2\pi \times 600$ Hz. This results in a higher density of the trapped cloud, which increases the elastic collision rate. In this way the ensemble is heated up in the recompressed trap without loosing particles for hold times below 2 s. As absolute measurement of the temperature is difficult, we use the normalized damping rate as a sensitive, but uncalibrated thermometer [Kin04a, Kin05a]. The normalized damping rate of an oscillation with the exponential damping constant κ is defined by κ/ω_r. In Fig. 5.5 the dependence of the heating on the hold time in the recompressed trap is displayed.
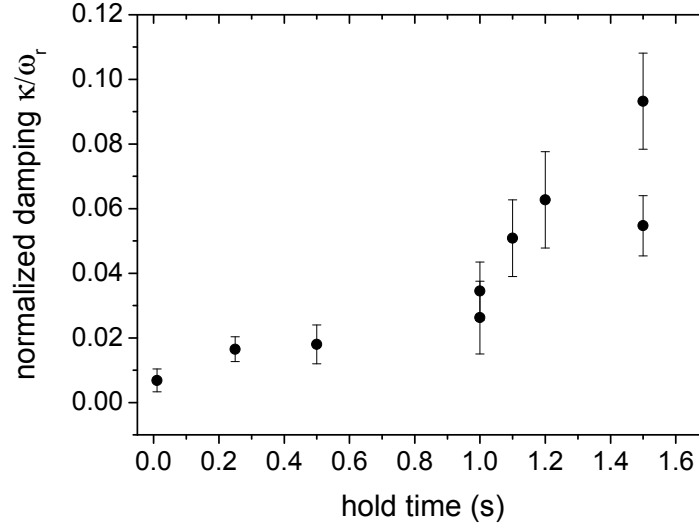
Figure 5.5: Illustration of the effect of the controlled heating procedure. As an uncalibrated thermometer, we show the damping of the compression mode κ normalized to the radial trap frequency ω_r. The longer the hold time in the recompressed trap, the higher the temperature.

Chapter 6

Measurements of the compression mode

In this chapter, we present precision measurements of the radial compression mode, also called radial breathing mode, in an optically trapped, strongly interacting Fermi gas of ^{6}Li atoms. The mode serves as a sensitive probe for the compressibility and thus the equation of state of a superfluid gas in the BEC-BCS crossover [Str04, Hei04, Hu04, Man05, Ast05]. We reach a precision level that allows us to distinguish between the predictions resulting from the equation of state from mean-field BCS theory and QMC calculations. Previous experiments on collective modes, performed at Duke University [Kin04a, Kin04b] and at Innsbruck University [Bar04b], showed frequency changes in the BEC-BCS crossover in both the slow axial mode and the fast radial compression mode of a cigar-shaped sample. The accuracy, however, was insufficient for a conclusive test of the different many-body theories in the strongly interacting regime.

In section 6.1, the theoretical framework of the measurements is given. Section 6.2 describes the experimental setup and methods we used, whereas section 6.3 presents several corrections for experimental imperfections on the data. In section 6.4 the experimental results of precision measurements in the strongly interacting BEC regime (6.4.1) and a reinterpretation of previous results in the whole BEC-BCS crossover (6.4.2) are presented.

6.1   Theoretical predictions

We study a degenerate two-component Fermi gas in the BEC-BCS crossover region [Eag69, Leg80, Noz85, Eng97], where the s-wave scattering length a is comparable with or larger than the interparticle spacing (see also chapter 2). Here, the equation of state is governed by many-body effects. Understanding the equation of state is of fundamental interest and constitutes a difficult task for many-body quantum theories, even in the zero-temperature limit. Therefore a comparison be-

tween precise experimental results and theoretical predictions offers great opportunities for a better understanding of these many-body effects. Mean-field BCS theory [Eag69, Leg80, Noz85, Eng97, Str04, Hei04, Hu04, Man05] provides a reasonable interpolation between the well-understood limits of a weakly interacting BEC and a BCS-type superfluid. More sophisticated crossover approaches using diagrammatic techniques [Pie05] yield quantitatively different results in certain regimes, none of them however providing a complete description of the problem. The most advanced theoretical results were obtained by numerical calculations based on a quantum Monte-Carlo (QMC) approach [Ast04, Ast05].

On the BEC side of the crossover, there are two competing effects in the equation of state. One of these effects is based on the strong interactions in a Bose gas. These cause beyond-mean-field effects associated with quantum depletion, which increase the average energy per particle. To lowest order, this beyond-mean-field effect leads a correction to the equation of state predicted by Lee, Huang, and Yang (LHY) almost 50 years ago [Lee57b, Lee57a]. Beyond mean-field effects are expected to reduce the compressibility of a strongly interacting Bose gas as compared to the weakly interacting case. Contrary to this effect of strong interactions in a Bose gas, the onset of fermionic behavior leads to quite different effects. When approaching the resonance, fermionic behavior emerges and the system loses its purely bosonic character, which increases the compressibility of the strongly interacting gas.

Mean-field BCS theory

Mean-field BCS theory (see also section 3.2) connects the two known limits of a strong-coupling BEC of molecules consisting of two fermionic atoms and a weak-coupling superfluid BCS-state consisting of Cooper-pairs of these fermionic atoms. Starting from usual BCS-theory [Bar57a, Bar57b], the connection to the BCS-limit is done by introducing a mean-field term, which includes pairing interaction in the BEC-BCS crossover region [Eag69, Leg80, Noz85, Eng97]. So, this theory provides relatively simple models for the equation of state in the whole BEC-BCS crossover regime [Str04, Hei04, Hu04, Com04b, Com04a, Kim04b, Kim04a, Pie04, Man05, Bul05, Pie05], which are analytically solvable. A main disadvantage of mean-field BCS theory is the absence of the beyond-mean-field effects mentioned above. Further disadvantages of this theory become obvious as predictions from this model disagree with the values determined by other theoretical and experimental methods.

Quantum Monte Carlo theory

Quantum Monte Carlo theory (see also section 3.2) provides much more advanced models [Car03, Ast04, Ast05]. Based on numerical calculations and some starting conditions, the beyond-mean-field effects as described above are included. This more sophisticated approach does not suffer from disadvantages of the mean-field BCS theory like the disagreement with experimental verified parameters.

One would expect a more precise description from quantum Monte Carlo theory than from mean-field BCS theory. However, the differences in the predicted compression mode frequency ω_c between both models are small. In the strongly interacting BEC regime, the difference between both theories is only of the order of a few percent. Therefore precision measurements are needed to distinguish the theories from each other.

6.2 Experimental realization

A strongly interacting, degenerate gas of ^{6}Li atoms in the lowest two internal states is prepared as described in chapter 5 and our previous publications [Bar04b, Bar04a, Chi04b]. The broad Feshbach resonance centered at a magnetic field of $B = 834\,$G facilitates precise tuning of the *s*-wave scattering length a [Bar05b]. Forced evaporative cooling is performed in a 1030-nm near-infrared laser beam focussed to a waist of $54\,\mu$m at $764\,$G. This waist size is significantly larger than the old value of $24\,\mu$m, which was used in [Bar04a, Bar05b]. So, a deeply degenerate cloud of $N = 2.0(5) \times 10^5$ atoms with even lower temperatures than in the previous experiments is achieved. By adiabatically increasing the trap laser power after cooling, the sample is recompressed to achieve nearly harmonic confinement. In axial direction the gas is magnetically confined in the curvature of the field used for Feshbach tuning with an axial trap frequency of $\omega_z/2\pi = 22.4\,$Hz at $834\,$G. The experiments reported here are performed at two different final values of the laser power of the recompressed trap. At 135 mW (540 mW), the trap is $1.8\,\mu$K ($7.3\,\mu$K) deep and the radial trap frequency is $\omega_r \approx 2\pi \times 290\,$Hz (590 Hz). According to equation (2.26) the Fermi energy of a non-interacting cloud is calculated to $E_F = \hbar^2 k_F^2 / 2m = \hbar(3\omega_r^2 \omega_z N)^{1/3} = k_B \times 500\,$nK (800 nK); here m is the mass of an atom and k_B is Boltzmann's constant.

Compared to our first measurements on collective excitation modes [Bar04b, Bar05a], we have upgraded our apparatus with a two-dimensional acousto-optic deflection system for the trapping beam (see detailed description in 4.2.3) and a new imaging system along the trapping beam axis (see 4.4.2). These two improvements provide us with full access to manipulate and observe the radial motion.

The trap beam profile is somewhat elliptic because of imperfections and aberrations in the optical set up (for the optical set up of the trapping system see section 4.2.3). Already the profile of the laser beam is slightly elliptic. In addition, the optics for the deflection system and the focussing of the beam to the right spot size lead to further imperfections. A main contribution to this imperfections are the aberrations due to the angle of $\sim 45°$ between trapping beam and glass cell. In our previous experiments [Bar04a] the ellipticity was relatively large ($\epsilon \approx 0.2$), of which we were not aware before the apparatus upgrade. This explains the observed quantitative deviations at that time of the compression mode frequencies from the hydrodynamic predictions for a cylindrical trap. To simultaneously excite the two eigenmodes of the radial sloshing motion, we initially displace the trapped sample into a direction between the horizontal

and vertical principal axes of the radial potential. After a variable hold time, during which the cloud oscillates freely, we turn off the optical trap. After typically 4 ms we take an absorption image of the released cloud. The center-of-mass position of the cloud then reflects its momentum at the instant of release. A careful analysis of such data like presented in 5.2.1 allows us to determine the eigenfrequencies ω_x (horizontal sloshing) and ω_y (vertical sloshing) to within a relative uncertainty of typically 2×10^{-3}. We finally derive the mean sloshing frequency $\omega_\perp = \sqrt{\omega_x \omega_y}$ and the ellipticity parameter $\epsilon = (\omega_y - \omega_x)/\omega_\perp$ (see also Eq.(3.49)). For our experimental conditions we find $\epsilon = 0.066$.

To excite the radial compression oscillation we reduce the trap light power for a short time interval of $\sim 100\mu s$, inducing an oscillation with a relative amplitude of typically 10%. After a variable hold time the cloud is released from the trap and an absorption image is taken after typically 4 ms of expansion. From two-dimensional Thomas-Fermi fits to the expanding cloud, we determine the mean cloud radius W_r. From a fit function of a damped harmonic oscillation,

$$W_r(t) = A \, \exp\left(-\kappa t\right) \, \sin\left(2\pi\omega_c t - \phi\right) + y, \tag{6.1}$$

the frequency ω_c and damping rate κ of the radial compression mode can be determined. Note that A is the amplitude, ϕ a phase factor and y a constant offset of this oscillation.
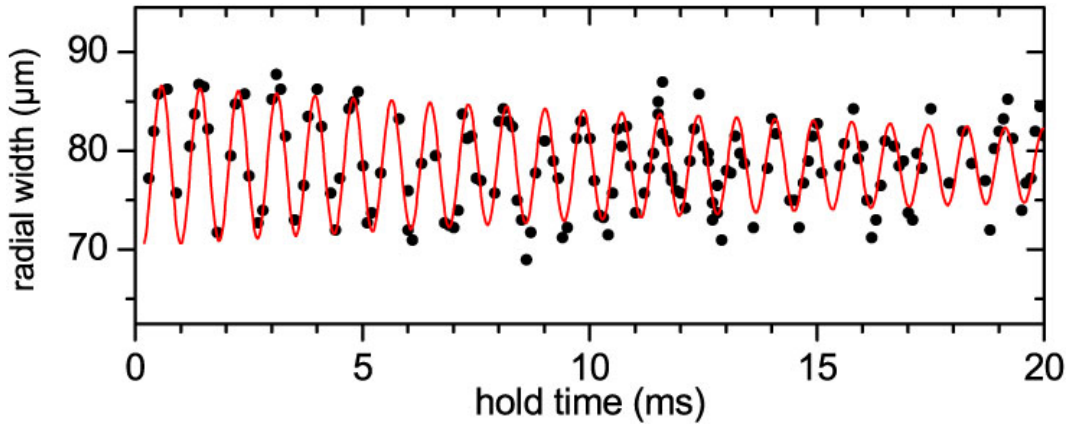
Figure 6.1: Radial compression oscillation observed at a trap power of 540 mW and $B = 735$ G, corresponding to $1/(k_F a) = 1.55$. The radial width is determined by averaging the horizontal and vertical Thomas-Fermi radii after expansion. Here we obtain $\omega_c/2\pi = 1185$Hz.

A typical data set for a measurement of the radial compression mode is shown in Fig. 6.1. The data in Fig. 6.1 has been taken at a magnetic field of 735G and a trap power of 540mW, which corresponds to an interaction parameter $1/(k_F a) = 1.55$. The radial width determined from a Thomas-Fermi fit to the absorption image is plotted versus the hold time in the trap. The oscillation of the width is fitted by the function (6.1), which yields a compression mode frequency of $\omega_c/2\pi = 1185$Hz.

6.3   Corrections of experimental imperfections

Our experiments are performed close to the limit of an elongated harmonic trap potential with cylindrical symmetry. This elementary case is of great general relevance for many quantum gas experiments in optical and magnetic traps (see, e.g. [Che02]). In this idealized case, collective excitations are conveniently normalized to the trap frequency ω_r, which makes the results comparable with theoretical predictions like in section 6.1. The compression mode can then be written as

$$\omega_c = f_c \omega_r, \tag{6.2}$$

where f_c is a dimensionless function of the interaction parameter $1/(k_F a)$ and is related to an effective polytropic index γ of the equation of state (see Eq.(3.7)) by $\omega_c^2 = 2(\gamma + 1)\omega_r^2$ (compare Eq.(3.43)). So, f_c can be written as

$$f_c = \sqrt{2\gamma + 2}\, \omega_c/\omega_r. \tag{6.3}$$

In order to compare our experimental results with theory, we consider the quantity f_c, i.e. the normalized compression mode frequency of the ideal, cylindrically symmetric, elongated trap. We approximate the idealized f_c by the ratio $\omega_c/\omega_\perp$ of the measured compression mode frequency ω_c (from the fit function (6.1)) and the mean sloshing mode frequency $\omega_\perp$. We find, that for our experimental conditions, this approximation is better than one percent. However, an accuracy level of 10^{-3} is desired. To reach this precision level, small effects due to experimental imperfections compared with ideal theoretical conditions have to be taken into account. The most important of these effects stem from the residual trap ellipticity and the anharmonicity of the radial potential in combination with the spatial extension of the trapped sample. We thus introduce two small corresponding corrections, expressing f_c in the form

$$f_c = \left(1 - \sigma\epsilon^2 + b\alpha\right)\omega_c/\omega_\perp. \tag{6.4}$$

6.3.1   Ellipticity corrections

The correction due to an ellipticity of the trapping potential has been calculated in 3.5.1. There, starting from the hydrodynamic eigenfrequency equation (3.52), straightforward calculations and Taylor expansions for small ϵ finally lead to $\omega_c^2 = \omega_\perp^2(2 + 2\gamma)\left(1 + \epsilon^2(\gamma + 2)/4\gamma\right)^2$ (see Eq.(3.55)). By inserting into Eq.(6.4), we get for the ellipticity correction parameter σ

$$\sigma = (\gamma + 2)/4\gamma. \tag{6.5}$$

For all our experiments, the ellipticity correction $\sigma\epsilon^2$ stays well below 6×10^{-3}.

6.3.2 Anharmonicity corrections

The idealized theoretical approach assumes a point-like cloud oscillating in a perfectly harmonic potential. Under real experimental conditions, spatial extension of the cloud and non-harmonic properties of the confining potential have to be taken into account. As described by Eq.(3.62) in 3.5.2, the radial optical potential created by a focused laser beam can be described by $V_{ext}(r) = -V_0 + \frac{1}{2}m\omega_r^2 r^2 - \frac{1}{8V_0}m^2\omega_r^4 r^4$.

Following [Str05, J.K05], we define the anharmonicity parameter α by

$$\alpha = \frac{1}{2}m\omega_r^2 r_{\text{rms}}^2 / V_0. \tag{6.6}$$

We obtain the root-mean-square radius r_{rms} of the trapped cloud from in-situ measurements of axial profiles [Bar04b], using the relation $r_{\text{rms}} = 2\omega_z^2/\omega_r^2 z_{\text{rms}}$. In our experiments α varies between 0.01 and 0.03.

Anharmonicity effects influence the frequency of the radial sloshing $\omega_\perp$ and of the radial compression mode ω_c. As we use the normalized frequency $\omega_c/\omega_\perp$, we have to include corrections on both sloshing and compression mode.

For the sloshing mode in the hydrodynamic regime, one gets according to Eq.(3.64)

$$\omega_\perp = \omega_r\left(1 - \alpha\right). \tag{6.7}$$

The calculation of the anharmonicity correction for the compression mode in the hydrodynamic regime is more complex. Starting from the differential equations for a scaling function (see Eq.(3.65)) one gets after some calculations Eq.(3.70) in 3.5.2. This can be written as

$$\omega_c = \omega_r\sqrt{2\gamma + 2}\left(1 - \alpha\frac{(2 + 5\gamma)(2 + \gamma)}{(2 + 7\gamma)(1 + \gamma)}\right). \tag{6.8}$$

The normalization of the compression to the sloshing mode frequency already removes part of the anharmonicity effects and results in

$$\omega_c/\omega_\perp = \sqrt{2\gamma + 2}\,\frac{\left(1 - \alpha\frac{(2+5\gamma)(2+\gamma)}{(2+7\gamma)(1+\gamma)}\right)}{1 - \alpha}. \tag{6.9}$$

A Taylor expansion with the starting point $\frac{(2+5\gamma)(2+\gamma)}{(2+7\gamma)(1+\gamma)} \approx 1$ simplifies Eq.(6.9) to

$$\omega_c/\omega_\perp = \sqrt{2\gamma + 2}\left/\left(1 + \alpha\left(1 - \frac{(2 + 5\gamma)(2 + \gamma)}{(2 + 7\gamma)(1 + \gamma)}\right)\right)\right. . \tag{6.10}$$

Using Eq.(6.3) and Eq.(6.4) the parameter b can be determined to be

$$b = 1 - \frac{(2 + 5\gamma)(2 + \gamma)}{(2 + 7\gamma)(1 + \gamma)}. \tag{6.11}$$

In the strongly interacting BEC regime, γ lies between $\gamma = 1$ in the weakly interacting BEC limit and $\gamma = 2/3$ in the unitarity limit. Therefore, b lies between $b = 0.167$ and $b = 0.280$ in the limits of weakly interacting BEC and unitarity, respectively. The total anharmonicity correction $b\alpha$ stays below 10^{-2} for all our measurements.

6.3.3   Other types of corrections

We also checked for two other effects. We found that corrections from the finite length of the trapped cloud ($\omega_z \neq 0$) remain well below 10^{-3}. Anharmonicity effects resulting from the non-zero amplitude of the excited oscillations are negligibly small for all our experiments. This was experimentally checked by exciting oscillations with much larger amplitude and measuring the resulting small frequency shifts.

6.4   Results

In this section, we will present the experimental results of measurements of the radial compression mode. According to section 6.2, the cloud is prepared and excited, so that we can determine the frequencies of sloshing and compression mode. The normalized frequency is corrected for experimental imperfections following the approach presented in section 6.3.

In 6.4.1, our latest results on precision measurements in the strongly interacting BEC regime are presented [Alt07]. Some older results [Bar04a] are reinterpreted in 6.4.2 based on improved knowledge of our experimental system [Alt06].

6.4.1   Precision results in the strongly interacting BEC regime

Our measurements on the sloshing and compression modes are summarized in Table 6.1, including the small corrections for ellipticity and anharmonicity. For the data in the strongly interacting BEC regime ($1/k_{\mathrm{F}}a \gtrsim 1$) we used the weaker trap with $\omega_\perp/2\pi \approx 290\,\mathrm{Hz}$ to minimize unwanted heating by inelastic collisions. Closer to resonance ($1/k_{\mathrm{F}}a \lesssim 1$) inelastic processes are strongly suppressed, but the increasing cloud size introduces larger anharmonicity shifts. Here we chose the deeper trap with $\omega_\perp/2\pi \approx 590\,\mathrm{Hz}$. On the BCS side of the resonance we soon observed increased damping as a precursor of the breakdown of hydrodynamics [Bar04a, Kin04b]. We thus restricted our measurements to magnetic fields below $850\,\mathrm{G}$ to ensure low damping rates ($\gamma/\omega_\perp < 0.01$) and superfluid hydrodynamics.

A set of measurements on the sloshing and compression modes (see e.g. Figs. 5.3 and 6.1) at a given magnetic field requires hundreds of experimental cycles and thus takes a few hours under optimum operation conditions. The data summarized in Table 6.1 were taken over about four weeks. Slow drifts and day-to-day variations somewhat influence our experimental parameters. To minimize uncertainties from these effects we always took the sloshing mode reference measurement right before or after the compression mode data. By repeating measurements under identical settings we found a typical remaining relative uncertainty for the normalized compression mode frequencies of 5×10^{-3}, which is about 2-3 times larger than the fit errors of individual measurements.

Table 6.1: Experimental data on radial collective modes in the BEC-BCS crossover. The data in the upper seven (lower eight) rows refer to the sets of measurements taken in the shallower (deeper) trap with $V_0 = 1.8\mu$K and $E_F = 500$ nK ($V_0 = 7.3\mu$K and $E_F = 800$ nK). The values in parentheses indicate 1σ fit uncertainties of individual measurements. Note that a systematic scaling uncertainty of ~4% for $1/k_Fa$ results from the uncertainty in the determination of the atom number $N = 2.0(5) \times 10^5$.

		sloshing		compression		corr.	
B	$1/k_Fa$	$\omega_\perp/2\pi$	ϵ	$\omega_c/2\pi$	$\kappa/\omega_\perp$	$\sigma\epsilon^2$	$b\alpha$
(G)		(Hz)		(Hz)		(10^{-4})	(10^{-4})
727.8	2.21	292.7(5)	0.083(3)	596.3(6)	0.007(2)	48	20
735.1	1.96	298.6(5)	0.091(3)	602.8(8)	0.008(3)	60	26
742.5	1.75	294.5(5)	0.067(3)	593.2(7)	0.005(2)	33	28
749.8	1.55	296.3(4)	0.073(3)	599.0(7)	0.006(2)	38	28
760.9	1.27	296.0(4)	0.088(2)	592.387)	0.009(2)	58	24
771.9	1.03	293.6(7)	0.074(5)	586.2(8)	0.007(3)	41	27
834.1	0	287.5(7)	0.073(5)	519.4(9)	0.014(3)	55	94
752.2	1.07	605.0(9)	0.065(3)	1210.9(12)	0.010(2)	32	13
768.2	0.87	592.5(7)	0.069(2)	1186.6(12)	0.012(2)	36	16
775.6	0.75	590.2(4)	0.060(1)	1170.2(21)	0.007(4)	28	14
782.2	0.64	604.8(9)	0.061(3)	1187.1(16)	0.006(3)	29	16
801.3	0.38	586.8(7)	0.063(2)	1135.2(12)	0.010(2)	33	24
812.3	0.24	586.5(7)	0.058(2)	1106.9(16)	0.014(3)	30	33
834.1	0	596.3(9)	0.070(3)	1089.0(12)	0.010(2)	48	40
849.1	-0.14	583.2(7)	0.052(2)	1046.7(37)	0.007(2)	29	47

In Fig. 6.2 we show our final results on the normalized compression mode frequency in the BEC-BCS crossover. The two theory curves [Ast05] correspond to the equation of state from mean-field BCS theory (lower curve) and the one from quantum Monte-Carlo calculations (upper curve). Our data confirm the quantum Monte-Carlo predictions and rule out the mean-field BCS theory. In the strongly interacting BEC regime ($1/k_Fa \gtrsim 1$) our data are well above the value of 2. This highlights the presence of the long-sought beyond-mean-field effects [Lee57b, Lee57a] in collective modes of a strongly interacting gas [Pit98, Str04].

We also examined the influence of non-zero temperatures onto the compression mode frequency. At unitarity, a recent experiment [Kin05a] has found small frequency upshifts with temperature. For a BEC, however, theory [Gio00] predicts temperature-induced down-shifts, which compete with the up-shifts from beyond-mean-field effects. We have performed a set of measurements on temperature shifts in the strongly interacting BEC regime ($1/k_Fa = 0.94$). Before exciting the collective oscillation, the evaporatively cooled gas was kept in the recompressed trap for a variable hold time of up to 1.5 s. During this time residual heating by inelastic processes slowly increased the temperature, which we observed as a substantial increase of damping with time.
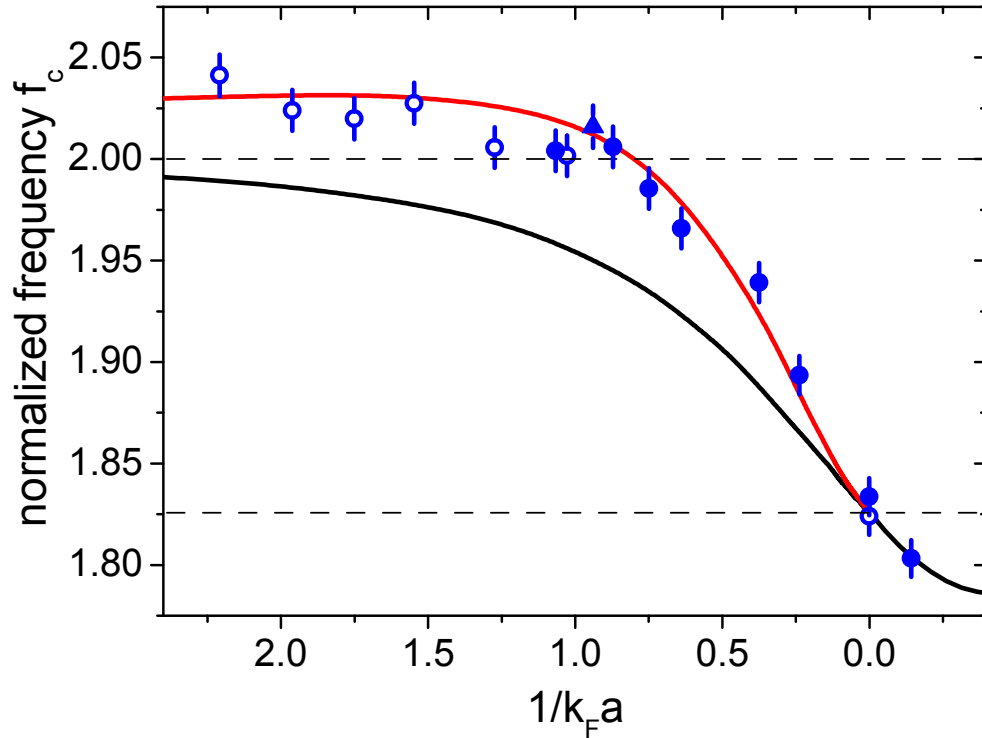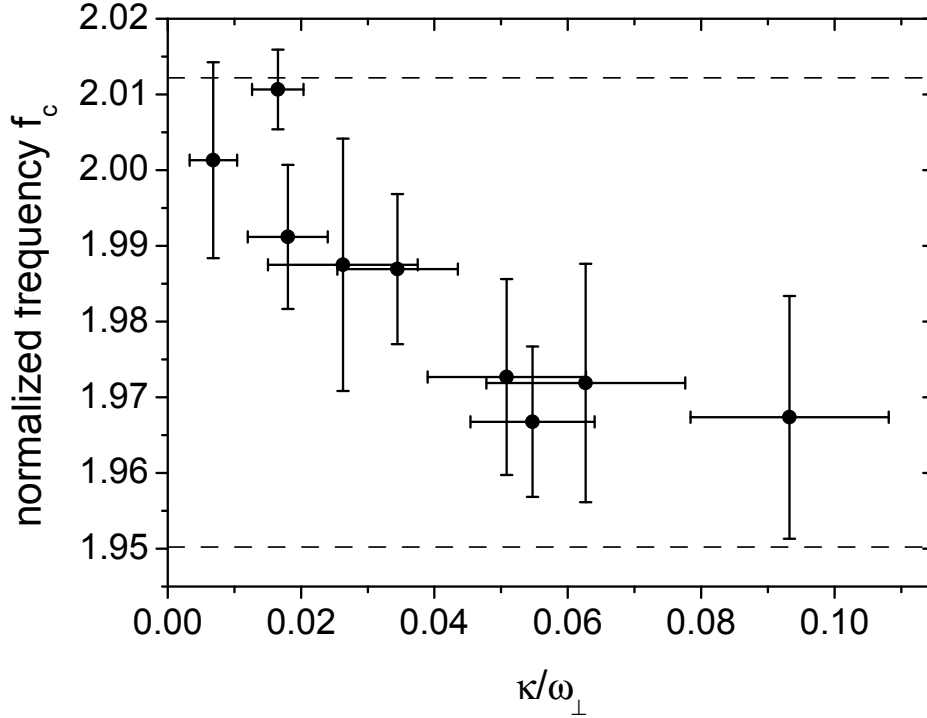
Figure 6.2: Normalized compression mode frequency f_c versus interaction parameter $1/k_F a$. The experimental data include the small corrections for trap ellipticity and anharmonicity and thus can be directly compared to theory in the limit of an elongated harmonic trap with cylindrical symmetry. The open and filled circles refer to the measurements listed in Table 6.1 for $\omega_\perp/2\pi \approx 290\,\mathrm{Hz}$ and $590\,\mathrm{Hz}$, respectively. The error bars indicate the typical scatter of the data points. The triangle shows a zero-temperature extrapolation of the measurements displayed in Fig. 6.3 with the corresponding fit error. The theory curves refer to mean-field BCS theory (lower curve) and quantum Monte Carlo calculations (upper curve) and correspond to the data presented in Ref. [Ast05]. The horizontal dashed lines indicate the values for the BEC limit ($f_c = 2$) and the unitarity limit ($f_c = \sqrt{10/3} = 1.826$).

The damping rate κ thus serves us as a very sensitive, but uncalibrated thermometer [Kin04a, Kin05a]. Fig. 6.3, where we plot the normalized compression mode frequency versus damping rate, clearly shows a temperature-induced down-shift. We note that previous measurements in the strongly interacting BEC regime [Bar04a, Kin04b] were performed at relatively large damping rates in the range between 0.05 and 0.1, where frequency down-shifts are significant. Thus, significant temperature-induced shifts seem to be present in the previous collective mode experiments. In particular

for the strongly interacting BEC regime, temperature shifts in our old data on the axial mode [Bar04a, Bar05a] and data from Duke University on the radial mode [Kin04b] provide a plausible explanation for these measurements being closer to the predictions of mean-field BCS theory than the more advanced quantum Monte Carlo results.

Figure 6.3: Normalized compression mode frequency versus damping rate for $1/k_F a = 0.94$ ($V_0 = 7.3\mu K$). The error bars represent 1σ fit uncertainties. The dashed lines indicate the zero-temperature values predicted by quantum Monte Carlo calculations (upper line) and mean-field BCS theory (lower line).

6.4.2 Reinterpretation of previous results

Besides the precision measurements in the strongly interacting BEC regime presented in 6.4.1, the radial compression mode of an optically trapped, ultracold ^{6}Li Fermi gas in the BEC-BCS crossover regime has already been a focus of study of experimental work performed at Innsbruck University [Bar04a, Bar05a] and at Duke University [Kin04a, Kin04b, Kin05a]. Compared with our old measurements in [Bar04a, Bar05a], the improved experimental setup presented in chapter 4 reaches a level of control which allows us to identify systematic effects in our measurements. With our new knowledge

of the system, we can reinterpret the previous data and resolve the apparent discrepancy between [Bar04a] and the results in [Kin04a, Kin04b] as well as in 6.4.1.

The atoms are trapped by a single focused laser beam resulting in a cigar-shaped trap geometry. In [Bar04a], we assumed cylindrical symmetry along the *z*-axis of the trapping potential, where the trap frequencies ω_x and ω_y in *x*- and *y*-direction are equal. With this assumption we used ω_y as the relevant radial trap frequency ω_r.

The experimental setup of [Bar04a] was only capable to resolve oscillations in *y*- and *z*-direction. With the new imaging system along the *z*-axis (see 4.4.2), we now get full access to the *x*- and *y*-directions and are able to determine the two transverse trapping frequencies individually. In contrast to the assumption of cylindrical symmetry in [Bar04a], we found significant ellipticity of the trap, being characterized by an aspect ratio $\zeta = \omega_x/\omega_y$. For the experimental trap setup of [Bar04a] we found an aspect ratio of $\zeta \approx 0.8$. Note that in the setup in 6.4.1 we use an aspect ratio of $\zeta = 0.94$.

To calculate the frequency ω_c of the compression mode in the elliptic trap, we start from the triaxial eigenfrequency equation (3.21) and neglect the weak confinement in *z*-direction. This gives the collective mode frequencies ω (compression mode and surface mode)

$$\omega^4 - (2 + \gamma)(\omega_x^2 + \omega_y^2)\omega^2 + 4(\gamma + 1)\omega_x^2\omega_y^2 = 0, \qquad (6.12)$$

where γ is the polytropic interaction index (see equation (3.7). From equation (6.12) the frequency of the radial compression mode ω_c can be calculated [Coz03, Pit03]. This results in

$$\left(\frac{\omega_c}{\omega_y}\right)^2 = \frac{1}{2}(2 + \Gamma)\left(1 + \zeta^2\right) + \sqrt{\left(\frac{1}{2}(2 + \Gamma)(1 + \zeta^2)\right)^2 - 4(\Gamma + 1)\zeta^2}, \qquad (6.13)$$

where ω_c is normalized to ω_y, corresponding to the way we presented our data in [Bar04a].

In Fig. 6.4 the experimental data of [Bar04a] and theoretical data [Ast05] corresponding to a mean-field BCS model (lower curve) and a quantum Monte-Carlo model (upper curve), both models assuming $\zeta = 0.8$, are shown. The normalized frequency ω_c/ω_y is plotted versus the magnetic field in exactly the same way like in [Bar04a]. The same data set is plotted versus the interaction parameter $1/k_F a$ in Fig. 6.5, which is comparable to the way the data is presented in [Bar05a].

In the BEC limit ($\gamma = 2$) the data fit well with the theoretically expected value of 1.85. In the unitarity regime at resonance ($\gamma = \frac{2}{3}$), the experimental data also fit well if one includes a small anharmonicity shift, which corrects $\omega_c/\omega_y = 1.62(2)$ to $\omega_c/\omega_y = 1.67(3)$ [Bar04a]. In the strongly interacting BEC regime the data can be compared with the theoretical models using equation (6.13). Above resonance, we see a larger downshift in frequency until a jump to $\omega_c/\omega_y \approx 2$ happens and the frequency remains constant.

In the strongly interacting BEC regime, at magnetic fields just below the Feshbach resonance or $2 > 1/k_F a > 0.5$, the experimental data points lie between both theoretical curves. In our latest precision measurements (see subsection 6.4.1), the data clearly
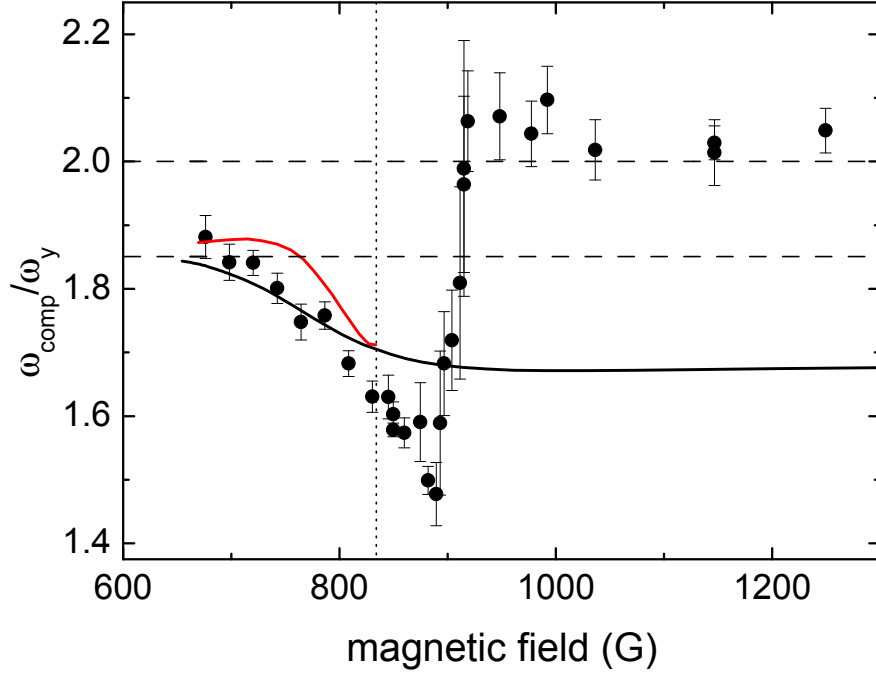
Figure 6.4: Normalized compression mode frequency ω_c/ω_y in the BEC-BCS crossover regime versus magnetic field [Bar04a]. The lower theory curve is based on a mean-field BCS model and the upper curve on a quantum Monte-Carlo model. Both curves correspond to the theoretical data presented in [Ast05]. The horizontal dashed lines indicate the values for the BEC limit ($\omega_c/\omega_y = 1.851$ for $\zeta = 0.8$) and the collisionless limit ($\omega_c/\omega_y = 2$). The vertical dotted line marks the position of the Feshbach resonance at 834.1G [Bar05b].

support the quantum Monte-Carlo model and they also show a downshift in frequency for increased temperatures. This is consistent with the data presented in Fig. 6.5, taking into account the relatively high temperature of the sample. Note that the temperatures in [Bar04a] are higher than in 6.4.1 as the evaporation ramp was not optimized to achieve deepest temperatures and the timing sequence was not optimized to minimize heating.

At magnetic fields above the Feshbach resonance ($1/k_F a \lesssim 0$), the data show a significant downshift compared to the theoretically expected values, which we cannot explain by the elliptical trap. Also other experiments show a similar trend [Kin04b]. The proximity of the energy corresponding to the collective mode frequency to the pairing gap [Com04b] and thermal effects may be possible explanations for this downshift.

At a magnetic field of about 900G ($1/k_F a \approx -0.5$), the normalized frequency shows

a pronounced jump up to the value of approximately 2, which is expected in a collisionless Fermi gas. For the collisionless oscillation along the *y*-axis, the ellipticity of the trap is irrelevant. So the visibility of the jump is clearly enhanced in an elliptic trap, as the lower frequency side of the jump in an elliptic trap is downshifted compared to a cylindrically symmetric trap. This jump marks the transition from hydrodynamic to collisionless behavior. In conclusion, by taking into account the ellipticity of the trap-
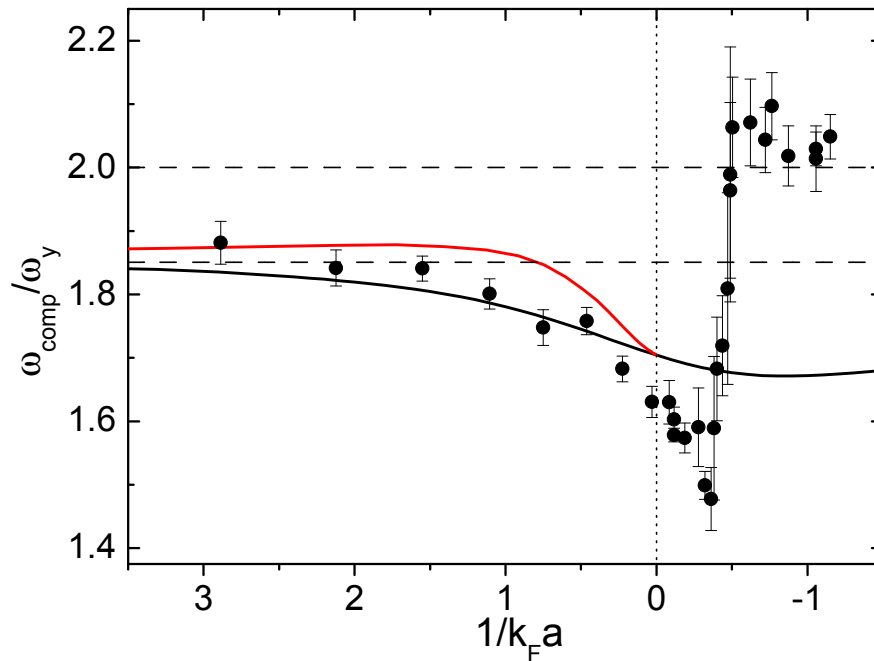
Figure 6.5: Normalized compression mode frequency ω_c/ω_y in the BEC-BCS crossover regime versus interaction parameter $1/k_{\mathrm{F}}a$ (right hand side) [Bar04a]. The lower theory curve is based on a mean-field BCS model and the upper curve on a quantum Monte-Carlo model. Both curves correspond to the theoretical data presented in [Ast05]. The horizontal dashed lines indicate the values for the BEC limit ($\omega_c/\omega_y = 1.851$ for $\zeta = 0.8$) and the collisionless limit ($\omega_c/\omega_y = 2$). The vertical dotted line marks the position of the Feshbach resonance at 834.1G [Bar05b].

ping potential, the results of [Bar04a] now essentially agree with other experimental results [Kin04a, Kin04b, Alt07] and theoretical predictions [Ast05].

Chapter 7

Measurements of the quadrupole surface mode

This chapter describes our experiments with the collective quadrupole surface mode of an ultracold ^{6}Li gas in the BEC-BCS crossover regime. The frequency and damping of the surface mode are examined similar to compression mode experiments. An experimental study of the expansion dynamics also enables us to characterize the oscillation mode in a more detailed way. Our results clearly show a transition from hydrodynamic to collisionless behavior in the ultracold gas. The effects of trap depth and temperature on this transition are discussed.

Interactions play an important role in the field of ultracold fermionic quantum gases [O'H02a, Bou03, Joc03a, Gre03, Zwi03, Bar04b, Reg04, Zwi04, Bou04, Bar04a, Chi04b, Zwi05, Par05]. This is especially true in the BEC-BCS crossover regime where the gas possesses a rich variety of different interaction regimes. There are two important interaction regimes for such gases: The Hydrodynamic and the collisionless regime. In the hydrodynamic regime, long-range interactions between all particles in the gas are present, thus enabling macroscopic gas dynamics. In the collisionless regime, elastic collisions are strongly suppressed due to Pauli blocking.

We can scan through the BEC-BCS crossover by tuning the interactions of fermionic species by using a Feshbach resonance [Bar04b, Reg04, Zwi04, Bou04, Bar04a, Chi04b, Zwi05, Par05]. The broad Feshbach resonance at 834.1G in ^{6}Li [Hou98, Bar05b] is well suited to provide precise control over the interaction properties.

Collective oscillations of an ultracold gas have been shown to be a convenient and powerful tool to probe the interaction regime quite early[Jin96, Mew96, Str96]. In our experiments we realize the limit of an elongated trap with tight confinement along the radial x- and y-directions and weak confinement along the axial z-direction. In this trap geometry a pure collective oscillation can be realized by the radial collective modes.

The radial compression mode of a fermionic ^{6}Li gas in an elongated trap geometry has been subject to experimental research before [Kin04a, Bar04a, Kin04b, Kin05a,

Alt06, Alt07] and is presented in chapter 6 of this thesis. For the compression mode, a transition in frequency between the hydrodynamic and the collisionless regime has been detected.

In this chapter, we show experimental data of the radial quadrupole mode of an ultracold ^{6}Li gas in the crossover regime. Unlike the compression mode, the quadrupole mode is a pure surface mode and independent of the equation of state of the system. Furthermore, expansion effects of the quadrupole mode can also be used as an additional tool to detect the transition from hydrodynamic to collisionless behavior. As the quadrupole mode shows a much larger difference in frequency than the compression mode (see [Str96] and chapter 3), this mode is even better suited to differ between hydrodynamic and collisionless behavior.

For the theoretical background of the quadrupole surface mode see section 3.3. In section 7.1, we will present the experimental setup and procedures we use to excite and explore the collective oscillations. Then section 7.2 will show the effects of expansion dynamics and thermalization of the ultracold gas. Finally, in section 7.3 we will present the results of our measurements.

7.1   Experimental procedure

The apparatus for our experiments is described in chapter 4. As a starting point, we produce a molecular BEC of ^{6}Li$_2$ dimers (see chapter 5 for details). We can control the interactions in the vicinity of a Feshbach resonance, which is centered at 834G [Hou98, Bar05b], by changing an external magnetic bias field. The interactions are characterized by the atomic s-wave scattering length a.

We start our experiments with an ensemble of about $N = 4 \times 10^5$ atoms in an almost pure BEC at a magnetic field of 764 G. In order to vary the properties of the system adiabatically, we linearly ramp to a magnetic field, where the measurements are performed [Bar04b]. The temperature of the gas is typically below 0.1 T_F, unless stated otherwise.

In order to observe the collective oscillations, we take absorption images of the cloud in the x-y-plane after release from the trap. We illuminate the atoms with a probe beam along the z-direction of the cigar-shaped cloud. The probe light causes a resonant excitation of the D2-line, at a wavelength of 671nm. We use dichroic mirrors for combining and separating the probe and the dipole trapping beam. The frequency of the probe beam can be tuned over a range of more than 1GHz, which enables resonant imaging over the whole range of magnetic fields that we create in our experiments.

The gas is confined in a nearly harmonic trapping potential, which shows a axially symmetric, cigar-shaped trap geometry. Optical confinement in radial direction is created by a focused 1030-nm near-infrared laser beam with a waist of $\sim$ 58 μm. The potential in the axial direction consists of a combination of optical and magnetic confinement; the magnetic confinement is dominant under the conditions of the present experiments. We set the laser power to 270 mW, which results in a radial trap frequency

of $\omega_r \approx 2\pi \times 370$ Hz and an axial trap frequency of $\omega_z \approx 2\pi \times 22$ Hz. This corresponds to a Fermi energy of a noninteracting cloud $E_F = \hbar(\omega_r^2 \omega_z 3N)^{1/3} = k_B \times 740$nK.

The position and shape of our trap in the x-y-plane can be manipulated through the
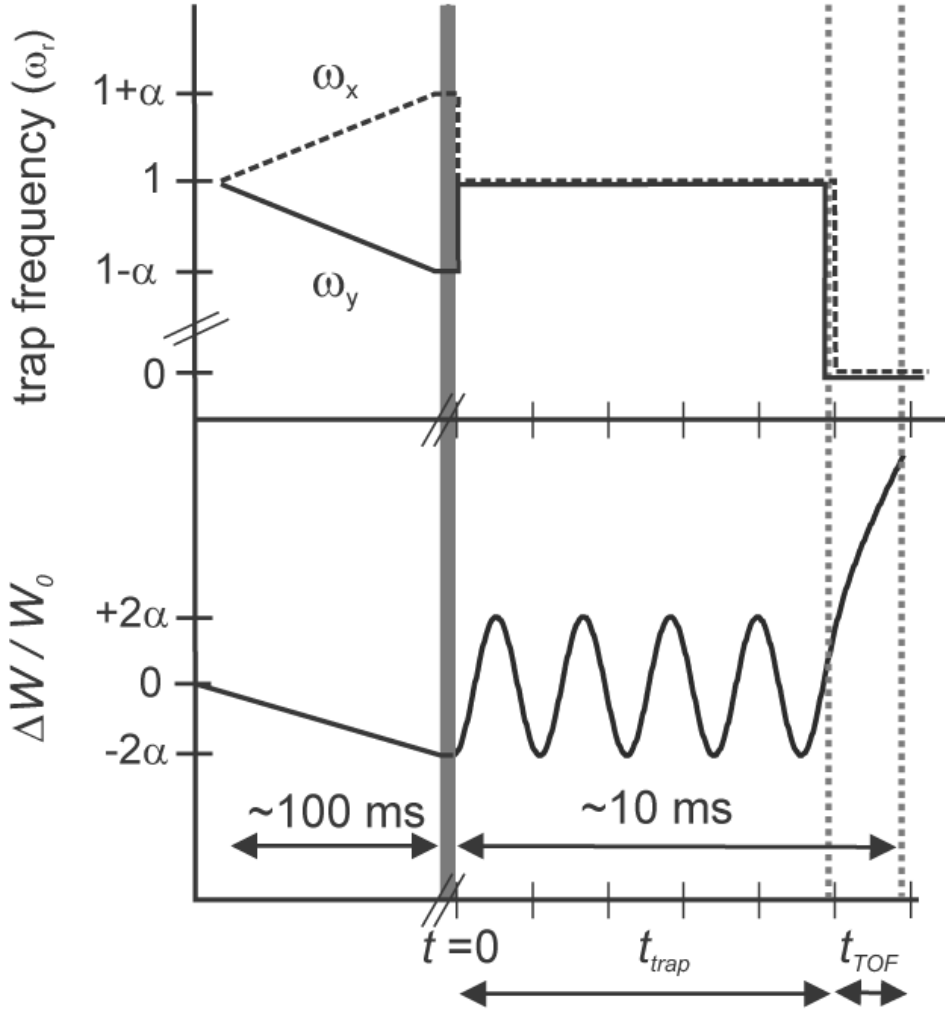
Figure 7.1: Timing scheme for the excitation of the radial quadrupole mode. The ellipticity of the trap is slowly ramped up within 100 ms. This results in a change of α in the trap frequencies, where α characterizes the ellipticity, and sets the initial, normalized deformation $\Delta W/W_0 = -2\alpha$. W_0 is defined as the width of the cloud in the trap without excitation. At $t = 0$, the elliptic deformation is switched off and the oscillation in the trap begins. (Shown here is an oscillation in the hydrodynamic regime.) The oscillation continues until the trap is turned off at $t = t_{trap}$, which is usually between 0 and 10 ms. At $t = t_{trap}$, the cloud is released from the trap and expands for the time t_{TOF}, which is typically 2 ms.

use of a two-dimensional scanning system. This system is a versatile tool that allows to manipulate our optical dipole trap. We can rapidly displace the trap laterally. Fast modulation of the beam position enables us to create time-averaged potentials for the trapped particles [Mil01, Fri01]. The scanning system is constructed by use of two

acousto-optic modulators (AOMs), which are aligned for vertical and horizontal deflection. A more detailed description of this scanning system can be found in 4.2.3 in chapter 4. In our trap configuration, we typically use modulation frequencies of 100kHz. We can create an elliptic potential shape by modulating the trap potential along a specific direction. By choosing a suited modulation function (see 4.2.3), these elliptic potentials are nearly harmonic.

When we excite the quadrupole mode, we first adiabatically deform the trapping potential in $\sim 100\,\mathrm{ms}$ to an elliptic shape. This slow deformation ensures that the cloud stays in thermal equilibrium even in the near-collisionless regime and no excitations occur. We suddenly switch off the deformation leading to an oscillation in the x-y-plane of the elliptic cloud in the originally round trap.

The initial deformation corresponds to different trap frequencies in horizontal and vertical direction where $\omega_{0x} = (1 + \alpha)\omega_r$ and $\omega_{0y} = (1 - \alpha)\omega_r$. The parameter α determines the amplitude of the emerging oscillation; we choose it for most of our measurements (unless stated otherwise) to be $\alpha \approx 0.05$. We increase α by increasing the modulation for the time averaged potential along the y-direction. As the modulation decreases the confinement strength of the dipole trap, we simultaneously ramp up the trap power to ensure that the mean trap frequency $\omega_r = \sqrt{\omega_{0x}\omega_{0y}}$ remains constant. This avoids excitation of the compression mode.

Fig. 7.1 shows the timing scheme for the excitation of the radial quadrupole mode. At $t = 0$, the collective oscillation is excited and the cloud starts oscillating in the trap for a variable time t_{trap}. Horizontal and vertical widths of the cloud, W_x and W_y, oscillate in the trap out of phase with a relative phase shift of π. As an observable, we choose the difference in widths $\Delta W = W_x - W_y$, which cancels out small effects of residual compression oscillations. For normalization, we introduce the width W_0 of the cloud in the trap without excitation.

Experimentally, we determine the collective quadrupole oscillations after suddenly switching off the trap and a subsequent expansion time t_{TOF}. We then take an absorption image of the cloud and determine its horizontal and vertical widths W_x and W_y via a two-dimensional Thomas-Fermi profile fit. From these measurements after expansion, we can determine the in-trap behavior.

Typical data sets of radial quadrupole oscillations are shown in Fig. 7.2. Fig. 7.2(a) shows an oscillation in the hydrodynamic regime; here we observe a weakly damped harmonic oscillation at a small constant offset. In Fig. 7.2(b) shows the observed behavior in the collisionless regime. The frequency of the oscillation is clearly higher than in the hydrodynamic regime. The oscillation shows stronger damping and has an exponentially time-varying offset.

We find that, for both regimes, the dependence of ΔW on t_{trap} can be well described by a fit function

$$
\begin{aligned}
\Delta W = {} & A\, e^{-\kappa t_{\mathrm{trap}}}\, \cos\left(\omega_q t_{\mathrm{trap}} + \phi\right) \\
& + C\, e^{-\xi t_{\mathrm{trap}}} + y_0,
\end{aligned}
\tag{7.1}
$$

which is discussed in more detail in section 7.2.
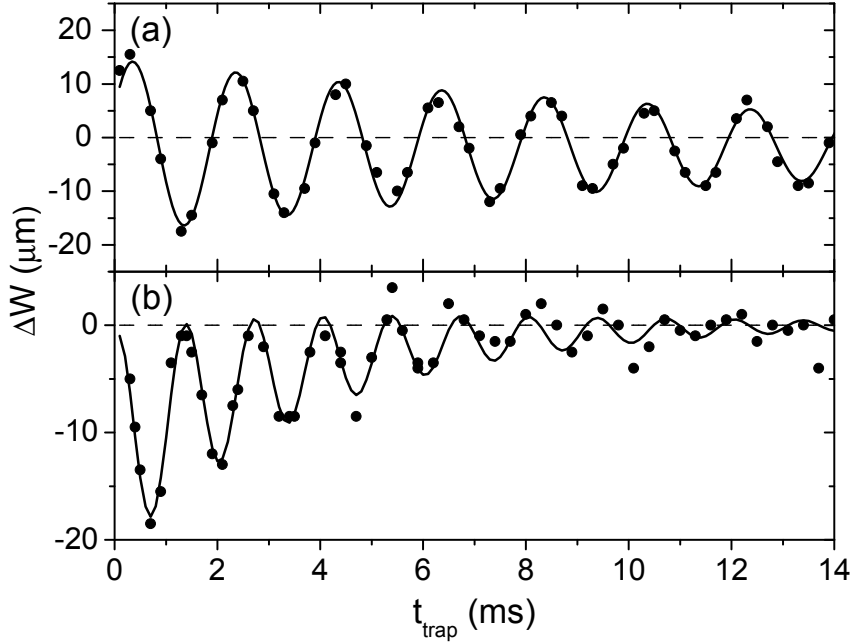
Figure 7.2: Typical radial quadrupole oscillations in the hydrodynamic and collisionless regime. The solid lines show fits to our data according to Eq.(7.1). The dashed lines indicate $\Delta W = 0$. The expansion time t_{TOF} is 2 ms. In (a), the oscillation observed in the hydrodynamic regime in the unitarity limit ($B = 834$G) is shown. In(b), the oscillations observed in the collisionless regime ($B = 1030$G, i.e. $1/k_{\text{F}}a \approx -1.33$) are shown.

Note that the frequency ω_{q} and the damping constant κ are independent of the expansion during t_{TOF} and characterize the behavior of the trapped oscillating atom cloud (see Section 7.3.1). In contrast, the amplitude A and the phase shift ϕ depend on the expansion time and provide further information on the dynamics of the gas. The offset function $C\, e^{-\xi t_{\text{trap}}}$ with amplitude C and damping constant ξ results from thermalization effects and is only relevant in the collisionless regime (see discussion in 7.2.4). The constant offset y_0 results from a slight inhomogeneity of the magnetic field, which gives rise to a weak saddle potential. This increases (decreases) the cloud size in y-direction (x-direction) during expansion.

7.2   Expansion dynamics and thermalization

We introduce a theoretical model to describe the oscillation of the cloud in the trap as well as its expansion after release from the trap. The interplay between the dynamics of the collective mode and the expansion behavior are of particular interest as they

introduce novel methods to determine the collisional regime. This section combines expansion effects and dynamics of the collective mode in a joint description by means of a scaling approach. This scaling approach is used for both the hydrodynamic and the collisionless regime [Bru00, Men02, J.K05]. In 7.2.1 the limit of a hydrodynamic gas is presented, whereas in 7.2.2 the model in the collisionless limit is discussed. Based on these models, we show calculated results for the amplitude and the phase offset after expansion in 7.2.3. A model for the near-collisionless regime, which takes thermalization effects into account and allows us to derive a more sophisticated fit function for our data, is presented in subsection 7.2.4.

We use a scaling approach to describe the cloud at the time t after excitation, like introduced in section 3.1 and [Bru00, Men02, J.K05]. Using the scaling function $b_i(t)$ for $i = x, y$, the width $W_i(t)$ can be written as

$$W_i(t) = b_i(t)W_i(0), \tag{7.2}$$

where $W_x(0) = (1 - \alpha)W_0$ and $W_y(0) = (1 + \alpha)W_0$ are the initial widths at excitation. The initial conditions for the scaling function are $b_i(0) = 1$ and $\dot{b}_i(0) = 0$ (see also [Bru00]).

7.2.1 Dynamic behavior in the hydrodynamic limit

In the hydrodynamic limit, the equations of hydrodynamics lead to Eq.(3.19), which delivers the following differential equations for b_i in an elongated trap geometry

$$\ddot{b}_i = \frac{\omega_{0i}^2}{b_i \left(b_x b_y \right)^\gamma} - b_i \, \omega_i^2, \tag{7.3}$$

where γ is the polytropic index of the equation of state and i stands for x, y. ω_{0x} and ω_{0y} are the trap frequencies of the maximally elliptic trap at the moment of excitation $t = 0$, when the cloud has no further excitation and is in thermal equilibrium. In contrast to this, $\omega_x(t)$ and $\omega_y(t)$ are time dependent. The timing scheme is illustrated in Fig. 7.1. For $0 < t < t_{\text{trap}}$, both trap frequencies are constant at the value of ω_r; for $t > t_{\text{trap}}$, i.e. after release from the trap, $\omega_x(t) = \omega_y(t) = 0$. The following equation summarizes the behavior of the trap frequencies $\omega_i(t)$:

$$\omega_i(t) = \begin{cases} \omega_{0i} & , t = 0 \\ \omega_r & , 0 < t < t_{\text{trap}} \\ 0 & , t > t_{\text{trap}}. \end{cases} \tag{7.4}$$

This enables us to calculate the scaling functions b_x and b_y as solutions of Eq.(7.3) for the in-trap oscillation. In the limit of small amplitudes ($\alpha \ll 1$) solutions are

$$\begin{aligned} b_x &= 1 + \alpha(1 - \cos \omega_q t), \\ b_y &= 1 - \alpha(1 - \cos \omega_q t), \end{aligned} \tag{7.5}$$

where $\omega_q = \sqrt{2}\,\omega_r$ is the radial quadrupole oscillation frequency. Together with Eq.(7.2), we are able to determine the difference in widths of the cloud to be

$$\Delta W = -2\,\alpha W_0 \cos \omega_q t. \tag{7.6}$$

7.2.2 Dynamic behavior in the collisionless limit

Similar to 7.2.1, in the collisionless limit (see also Eq.(3.33)) the following set of equation characterizes b_i, where i stands for x, y,

$$\ddot{b}_i = \frac{\omega_{0i}^2}{b_i^3} - \omega_i^2 b_i. \tag{7.7}$$

In the limit of small amplitudes ($\alpha \ll 1$) solutions of the in-trap oscillation are

$$
\begin{aligned}
b_x &= 1 + \frac{\alpha}{2}(1 - \cos \omega_q t), \\
b_y &= 1 - \frac{\alpha}{2}(1 - \cos \omega_q t),
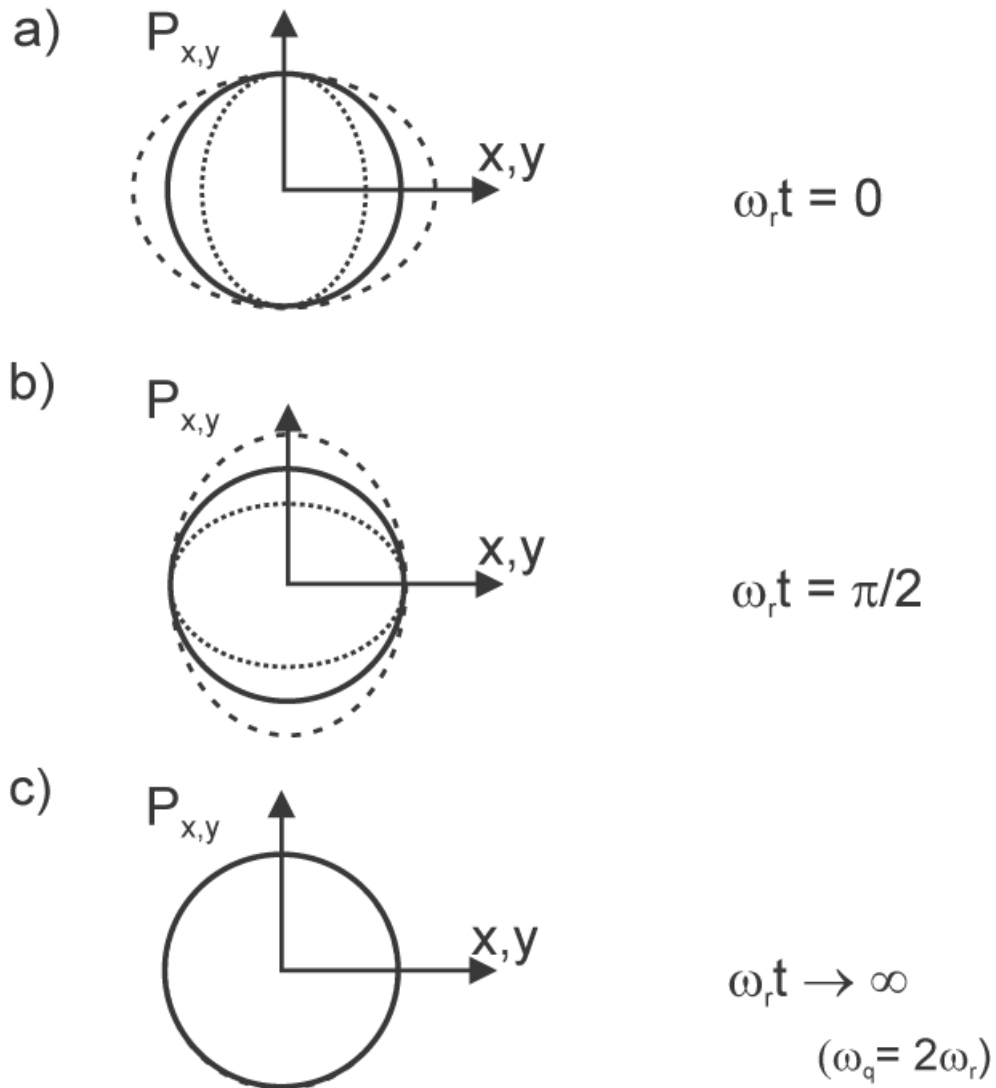\end{aligned}
\tag{7.8}
$$

where $\omega_q = 2\,\omega_r$ is the radial quadrupole oscillation frequency. Together with Eq.(7.2), we are able to determine the difference in widths of the cloud to be

$$\Delta W = -\alpha W_0 \left(1 + \cos \omega_q t\right). \tag{7.9}$$

In contrast to the hydrodynamic limit, the oscillation is initially not centered around $\Delta W = 0$. Furthermore the oscillation has an amplitude $1/2$ of the amplitude in the hydrodynamic gas.

Besides the finding of analytical solutions, it is enlightening to understand the collective oscillations in the collisionless limit by considering the phase space dynamics of the cloud. In Fig. 7.3, we show the contours of phase space distributions in the x- and y- directions. The axes are scaled such that for the round trap, i.e. $\omega_x = \omega_y = \omega_r$, the dynamics of any point in phase space is a simple circular rotation about the origin with frequency ω_r. Thus, the solid circle in Fig. 7.3 (a) indicates an equilibrium phase space contour for the round trap. Right after applying the excitation scheme as described in 7.1, the phase space contours in the x- and y- direction are given by the dashed and dotted ellipses in Fig. 7.3 (a). Since the gas is fully thermalized at the instant of excitation, the initial momentum distribution in x- and y- direction is the same. As time progresses, the elliptic contours will rotate with frequency ω_r (see Fig. 7.3 (b)), which corresponds to oscillations in the trap. We note that both the spatial and the momentum distribution in the x-direction are never larger than the ones in the y-direction. Therefore, ΔW oscillates between $2\alpha W_0$ and zero and the aspect ratio of the cloud never inverts. This is to be compared to the hydrodynamic case where ΔW oscillates between $\pm 2\alpha W_0$.

Residual thermalization effects in a near collisionless gas will damp out the initial oscillation amplitude of αW_0 and one will eventually end up again with a circular phase space contour (see Fig. 7.3 (c)). This is studied in detail in subsection 7.2.4.

a) $P_{x,y}$ ... x,y ... $\omega_r t = 0$

b) $P_{x,y}$ ... x,y ... $\omega_r t = \pi/2$

c) $P_{x,y}$ ... x,y ... $\omega_r t \to \infty$
$(\omega_q = 2\omega_r)$

Figure 7.3: Phase space dynamics for the quadrupole mode in the collisionless regime. Shown are phase space contours of an ensemble of particles which is held in a round trap (i.e. $\omega_x = \omega_y = \omega_r$). In (a) and (b) the situation during the oscillation in the trap is shown for two different times t. The solid line indicates the equilibrium phase space contour (without excitation), whereas the dotted (dashed) line shows the contour in the x (y) direction after excitation of the oscillation mode. (c) After long times, residual thermalization finally damps out the oscillations and leads to a circular phase space contour.

7.2.3 Amplitude and phase on expansion

Here we present our calculated results based on the models in 7.2.1 and 7.2.2 for the hydrodynamic and the collisionless limit, respectively. We show the relative amplitude that is given by the amplitude A (definition see Eq.(7.1)) divided by the average width of the cloud after expansion. Calculations of this relative amplitude are shown in
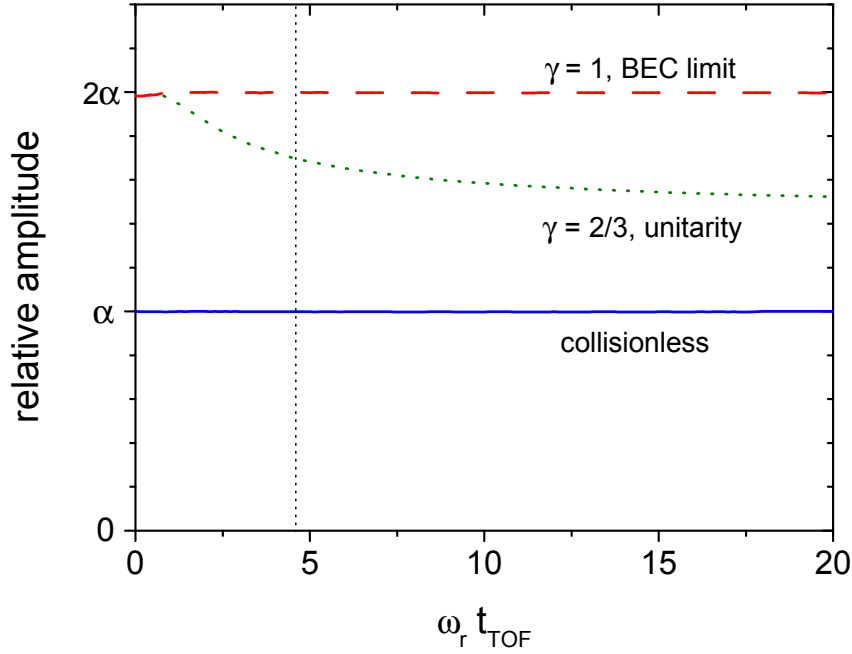
Figure 7.4: Calculated relative amplitude of a surface mode oscillation versus reduced time of flight $\omega_r t_{TOF}$ after release from the trapping potential. The values are calculated for the hydrodynamic (dashed curve: $\gamma = 1$, dotted curve: $\gamma = 2/3$) and collisionless regime (solid curve). The vertical dotted line marks the typical expansion time in our experiments.

Fig. 7.4, whereas calculations and measurements for the phase offset ϕ are shown in Fig. 7.5.

Fig. 7.4 shows the calculated relative amplitude of a surface mode oscillation in the hydrodynamic (dashed and dotted curves) and in the collisionless (solid curve) regime as function of the reduced expansion time $\omega_r t_{TOF}$. The hydrodynamic curves are calculated for the BEC limit of $\gamma = 1$ (upper, dashed curve) and in the unitarity limit of $\gamma = 2/3$ (lower, dotted curve). The amplitude in the collisionless regime is smaller than in the hydrodynamic regime. Initially the amplitude of the excitation is half as large in the collisionless as in the hydrodynamic regime, as already explained in subsection 7.2.2. In expansion the normalized amplitude stays constant in the collisionless regime and in the hydrodynamic regime for $\gamma = 1$. For $\gamma = 2/3$ in the hydrodynamic regime it decreases for longer expansion times.

In Fig. 7.5 we compare experimental data for the phase shift ϕ with numerical simulations. The data have been taken at unitarity where $1/k_F a = 0$ (hydrodynamic, open circles), and on the BCS-side of the resonance at $1/k_F a = -1.34$ (collisionless, closed triangles). The dashed line is based on a model for the hydrodynamic interaction
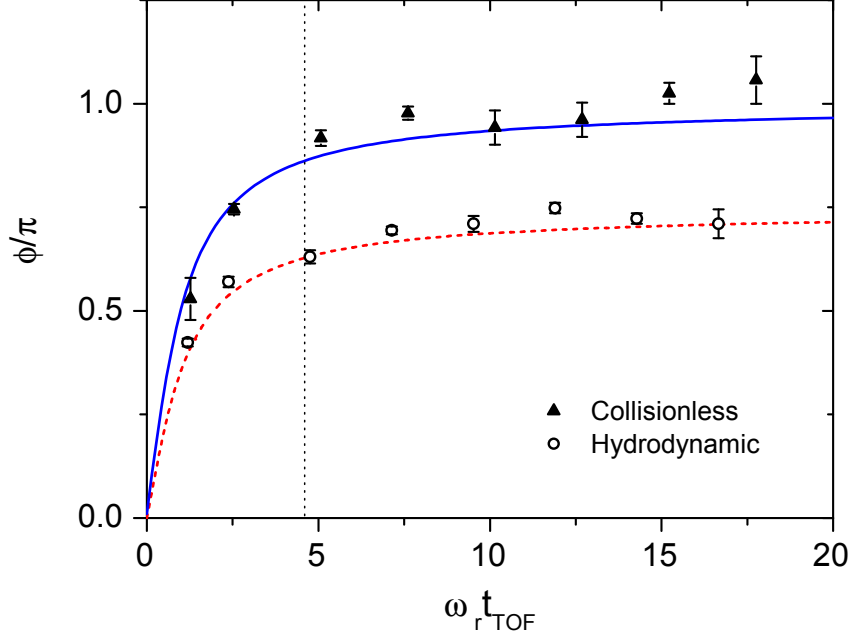
Figure 7.5: Phase ϕ of the collective surface mode as detected by fits according to Eq.(7.1) versus reduced expansion time $\omega_r t_{\text{TOF}}$ at unitarity (open circles) and at $1/k_F a = -1.34$ (filled triangles). The lines are numerical simulations for the hydrodynamic (dashed line) and collisionless regime (solid line). The vertical dotted line marks the typical expansion time in our experiments.

regime and the solid line on a model for the collisionless regime. The data agree with the theoretical model where no free fit parameters are used. This confirms our approach presented above.

7.2.4 Thermalization effects in a near-collisionless gas

Here we describe thermalization effects in a near-collisionless gas that are not included in the model for the collisionless limit in 7.2.2. Despite the word "collisionless" in the name, collisions play a crucial role for thermalization in this case. A typical time scale for thermalization processes is only a few oscillation cycles long. By analyzing the theory, we are able to introduce a universal fit function, as given by Eq.(7.1), which describes the oscillation both in the hydrodynamic and in the near-collisionless regime.

Even though elastic collisions are suppressed in the collisionless regime, the collision rate is still large enough to provide thermalization of the gas. This allows us to prepare the gas in thermal equilibrium at the moment of excitation $t = 0$. During the

oscillation in the trap as well as during expansion thermalization effects can influence the gas.

The measured behavior of the nearly collisionless quadrupole oscillation has two characteristics, see also Fig. 7.2(b): after excitation the oscillation is centered around $\Delta W = (W_x(0) - W_y(0))/2$ whereas after some time it is centered around $\Delta W = 0$. These two limits are consistent with thermalization of the gas on a time scale greater than the period of the oscillation.

In order to model these effects, we follow the theory introduced in 3.1.2 for a near-collisionless gas. We find the differential equations

$$\ddot{b}_i(t) = \omega_{0i}^2 \frac{\vartheta_i}{b_i} - \omega_i^2 b_i(t) \tag{7.10}$$

and

$$\dot{\vartheta}_i(t) = \frac{1}{\tau_R}(\vartheta_i - \bar{\vartheta}) - 2\frac{\dot{b}_i}{b_i}\vartheta_i(t). \tag{7.11}$$

The parameter b_i is the scaling function described earlier in this section; θ_i is a scaling parameter directly related to the temperature and $\bar{\theta} = \frac{1}{3}\Sigma_k\theta_k$. The initial condition for θ_i is $\theta_i(0) = 1$, as long as the gas is in thermal equilibrium at the moment of the excitation. The parameter τ_R is the relaxation time which describes the time scale of collisions. In the collisionless limit, when $\tau_R \to \infty$, the differential equations (7.10) simplify to the simple form in Eq. (7.7). For the hydrodynamic limit ($\tau_R \to 0$), we find Eq. (7.3).

The solutions to these equations depend on the parameter τ_R as can be seen in Fig. 7.6. Our measured data in the collisionless regime are well described by $\omega_r\tau_R \sim$ 2.3 (compare to Fig. 7.2).

We find that the model calculations from (7.10) and (7.11) can be well described with the following fit function

$$\begin{aligned}\Delta W &= A\, e^{-\kappa t_{\mathrm{trap}}}\, \cos\left(\omega_q t_{\mathrm{trap}} + \phi\right) \\ &\quad + C\, e^{-\xi t_{\mathrm{trap}}} + y_0.\end{aligned} \tag{7.12}$$

The first term describes the exponentially damped oscillations. The second term describes the shift of the center of the oscillation in the collisionless regime. The third term y_0 is a constant offset which will be discussed later.

We have used Eq.(7.12) to fit our experimental measurements. We find that the free fit parameters ξ and κ are related through $\xi/\kappa \approx 1.5$ for all our measurements in the near-collisionless regime. In the hydrodynamic regime $C = 0$, and therefore ξ becomes irrelevant.

The constant offset y_0 is due to an experimental artifact that results from a slight inhomogeneity of the magnetic field. At the location of the atoms the inhomogeneous magnetic field leads to a weak saddle potential which causes a slight anisotropic expansion during time of flight. This anisotropy is responsible for a slight offset in ΔW.
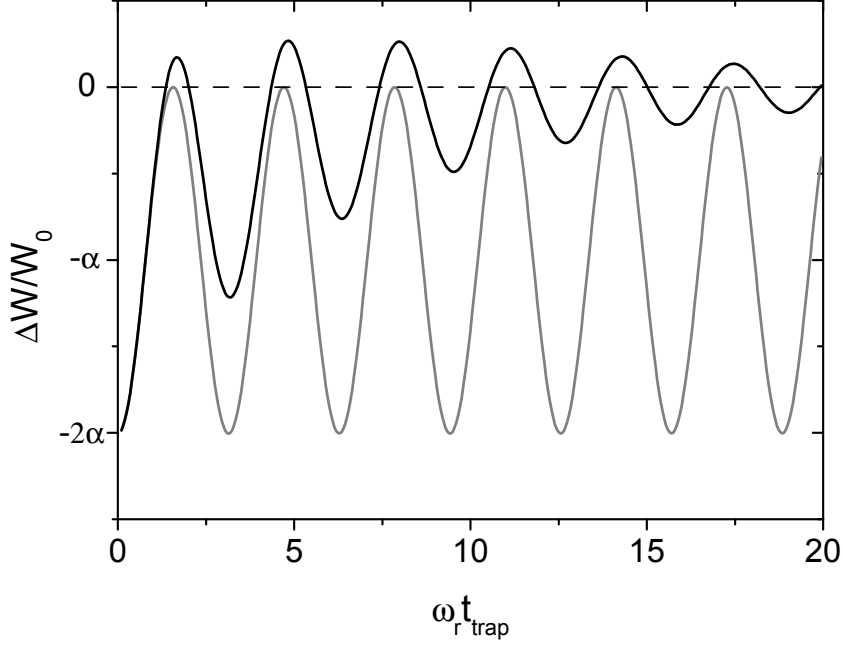
Figure 7.6: Calculated quadrupole oscillations in the near-collisionless regime. The lines show the relative difference in width ΔW as a function of the reduced time $\omega_r t_{trap}$. The oscillation is modeled according to Eq.(7.10) and (7.11). The dark line shows the result of the calculation when $\omega_r \tau_R = 2.3$ and the grey line shows the oscillation in the collisionless limit at $\omega_r \tau_R = 1000$.

7.3   Results

Here we first discuss our measurements of the frequency ω_q and the damping rate κ of the in-trap oscillation (subsection 7.3.1). We then present the data for the phase offset ϕ and the amplitude A (subsection 7.3.2). Finally, we explore the hydrodynamic-to-collisionless transition (subsection 7.3.3). As commonly used in the field of BEC-BCS crossover physics [Var07], the dimensionless parameter $1/k_F a$ is introduced to characterize the interaction regime. The parameter $k_F = \sqrt{2mE_F}/\hbar$ is the Fermi wave number and m is the mass of an atom.

7.3.1   Frequency and damping

In Fig. 7.7, we show the results for the frequency ω_q and the damping rate κ of the radial quadrupole mode throughout the BEC-BCS crossover. Both ω_q and κ are normalized to the trap frequency ω_r, which we determine by a sloshing mode measurement (see
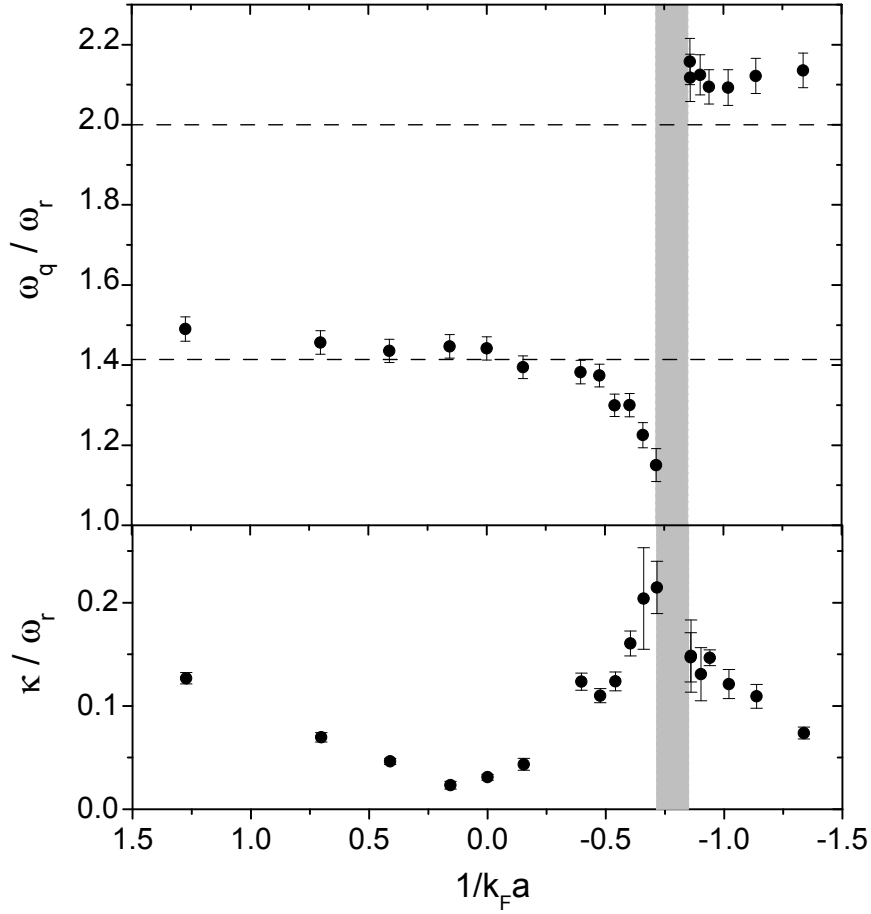
Figure 7.7: Frequency ω_q (upper plot) and damping rate κ (lower plot) of the radial quadrupole mode. Both quantities are normalized to the radial trap frequency ω_r and plotted versus the interaction parameter $1/k_Fa$. The dashed lines indicate the theoretical predictions in the hydrodynamic ($\omega_q/\omega_r = \sqrt{2}$) and in the collisionless limit ($\omega_q/\omega_r = 2$). The shaded area marks the transition from hydrodynamic to collisionless behavior between $1/k_Fa \approx -0.72$ ($B \approx 930\,\text{G}$) and $1/k_Fa \approx -0.85$ ($B \approx 960\,\text{G}$).

section 5.2).

The theoretical normalized frequencies ω_q/ω_r are calculated for perfectly harmonic trapping potentials in an idealized symmetric trap geometry. There are small derivations from this conditions in real experiments. In order to compare the experimental data to the idealized theoretical case, we have to correct our data. The measured normalized frequency ω_q/ω_r of the radial quadrupole mode has to be increased because of two small corrections. The larger correction is based upon a slight anharmonicity

of the trapping potential and the spatial extension of the cloud in the trap. The smaller correction is caused by a small residual ellipticity of the trapping potential.

The potential created by our trapping beam has a Gaussian shape. This results in a nearly harmonic potential in the center of the trap; however, for higher precision one must take into account higher order terms of the potential. Anharmonicity effects influence both our measurements of the sloshing mode frequency, where we determine ω_r, and our measurements of the quadrupole mode frequency ω_q. As we evaluate the normalized frequency ω_q/ω_r, the anharmonicity effects on sloshing and quadrupole mode almost cancel out each other. The small remaining correction to the normalized frequency is included by multiplying with a prefactor $1 + b\sigma$ (see also 3.5.2 and 6.3.2). The anharmonicity parameter σ relates the energy of the oscillation to the total potential depth and is defined by $\sigma = \frac{1}{2}m\omega_r^2 r_{rms}^2/V_0$, where r_{rms} is the root-mean-square radius of the trapped cloud and V_0 is the potential depth. The parameter b depends on the interaction regime. In the hydrodynamic regime, it is given by $(4 + 10\gamma)/(2 + 7\gamma)$, whereas in the collisionless regime b is determined by $6/5$ (see 3.5.2). Here, γ is the polytropic index of the equation of state. In our experiments, typically $b\sigma \approx 0.014$, but $b\sigma$ can rise to an upper limit of $b\sigma < 0.027$.

In the hydrodynamic regime, there is also a correction due to residual ellipticity effects. This correction takes into account that we compare our measurements with a theory for non-elliptic geometries. The ellipticity ϵ of the trap is defined by $\epsilon = (\omega_y - \omega_x)/\omega_r$. In our experiments, the ellipticity is small and given by $\epsilon \approx 0.07$. Therefore, we can apply the ellipticity correction by multiplication of a prefactor $1 + \lambda\epsilon^2$ (see also 3.5.1 and 6.3.1), where the interaction dependent factor λ is given by $(\gamma + 2)/(4\gamma)$. Altogether, $\lambda\epsilon^2$ is smaller than 0.006 for all data points.

The data confirm the expected transition between the hydrodynamic and the collisionless regime on the BCS side of the resonance. The transition is qualitatively different from the hydrodynamic-to-collisionless crossover in a classical gas [Bug05] or in a Fermi gas without superfluidity [Vic00]. Instead of a continuous and monotonous variation of the frequency between the two limits ($\sqrt{2}\,\omega_r$ and $2\,\omega_r$), an abrupt change occurs. When this transition is approached from the hydrodynamic side, a striking frequency downshift shows up as a precursor of the transition to higher frequencies. In the transition region (shaded area in Fig. 7.7), no data points are shown because of the large damping and correspondingly very large uncertainties for the measured frequency.

The damping rate shows similar behavior as in our previous measurements on the radial compression mode (see [Bar04a] and 6.4.2). Maximum damping occurs near the hydrodynamic-to-collisionless transition, whereas minimum damping is observed slightly below the resonance. In general, we find that damping is roughly two times larger for the quadrupole mode than for the compression mode at the same temperature. Note that in the present measurements, the temperatures are somewhat higher than in our compression mode measurements presented in 6.4.1. There are essentially two reasons for the higher temperatures. First, the atoms stay longer in the recompressed trap because of the longer excitation scheme of the quadrupole mode. Second, for

the quadrupole measurements we optimized our evaporative cooling scheme regarding particle number and not temperature. The faster damping of the quadrupole mode is plausible in view of the larger frequency change at the transition.

We now discuss the behavior in different regions in more detail:

$1/k_{\mathrm{F}}a \approx 0$: In the unitarity limit, the normalized frequency agrees well with the theoretically expected value of $\omega_{\mathrm{q}}/\omega_{\mathrm{r}} = \sqrt{2}$ for a hydrodynamic gas, see Eq. (3.44). To check for consistency with previous experiments (see chapter 6), we here also reproduced the frequency $\sqrt{10/3}\,\omega_{\mathrm{r}}$ of the radial compression mode on the 10^{-3} accuracy level. The damping is low for the Fermi gas in the unitarity limit. In contrast to the compression mode, the quadrupole mode frequency stays constant throughout the crossover, indicating that it is independent of the equation of state.

$1/k_{\mathrm{F}}a > 0$: In the strongly interacting BEC regime, there is an increase in the damping and a slight increase in the frequency for increasing $1/k_{\mathrm{F}}a$. As the gas is more susceptible to heating by inelastic processes in the deep molecular regime [Gri07], both effects may be due to a thermal component in this region.

$1/k_{\mathrm{F}}a \approx -0.8$: The frequency exhibits the pronounced "jump" from the hydrodynamic to the collisionless frequency. This transition is accompanied by a pronounced maximum of the damping rate.

$1/k_{\mathrm{F}}a \lesssim -0.8$: The frequency stays almost constant about 5% above the theoretically expected value of $\omega_{\mathrm{q}} = 2\omega_{\mathrm{r}}$. Interaction effects in the attractive Fermi gas may cause this significant upshift, although calculations of mean-field effects [Ped03] predict mean-field shifts below 1%. As we cannot experimentally realize a non-interacting Fermi gas above the resonance, we could not perform further experimental checks. The upshift in this regime thus remains an open question.

$1/k_{\mathrm{F}}a \lesssim 0$ and $1/k_{\mathrm{F}}a \gtrsim -0.8$: In this regime, we detect a substantial down shift in the quadrupole mode frequency. The effect begins to show up already slightly above the resonance ($1/k_{\mathrm{F}}a = 0$) and increases to a magnitude of almost 20% ($\omega_{\mathrm{q}}/\omega_{\mathrm{r}} \approx 1.15$ at $1/k_{\mathrm{F}}a = -0.72$), before the transition to collisionless behavior occurs. Indications of a similar down shift have been observed already in compression mode experiments (compare [Bar04a, Kin04a] and chapter 6), but here the down shift is considerably larger and not blurred by changes in the equation of state.

A plausible explanation for the curious behavior of the collective mode frequency on the BCS side of the resonance is provided by coupling of the oscillation to the pairing gap [Com04b, Chi04b, Gri07]. If we assume that the abrupt transition is caused by pair breaking resulting from resonant coupling of the oscillation to the gap, then the down shift may be interpreted as a coupling effect when the gap is not much larger than the oscillation frequency [Com06, Urb06]. The observed phenomenon still awaits a full theoretical interpretation.

7.3.2 Phase shift and amplitude

Additional information on the interaction regime is provided by the phase shift ϕ and the amplitude A of the observed oscillation (see Eq.(7.1)). This is useful since extremely high damping in the transition region makes a meaningful determination of frequency and damping practically impossible. We find that both amplitude and phase shift, however, can be determined with reasonable uncertainties even in the transition regime.
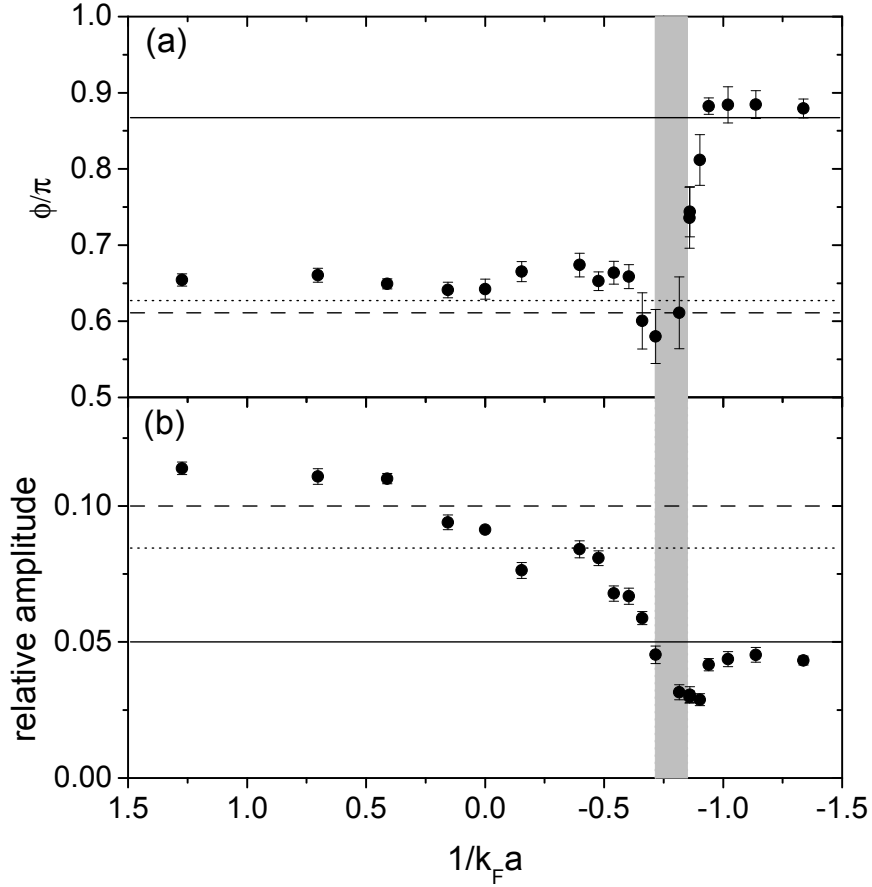
Figure 7.8: (a) Phase shift ϕ and (b) relative amplitude of the quadrupole mode versus interaction parameter $1/k_F a$ after $t_{TOF} = 2$ms expansion. The horizontal lines show calculations from our theoretical model: the solid lines in the collisionless limit, the dotted lines in the hydrodynamic regime at unitarity ($\gamma = 2/3$) and the dashed lines in the hydrodynamic regime in the BEC limit ($\gamma = 1$). These calculated values can be read off from Fig. 7.5 for the phase and Fig. 7.4 for the amplitude. The shaded area marks the transition between hydrodynamic and collisionless behavior between $1/k_F a \approx -0.72$ and $1/k_F a \approx -0.85$ (see also Fig. 7.7).

In the following, we present measurements of phase shift and amplitude. These are

compared to model calculations, which are described in detail earlier in section 7.2.

In Fig. 7.8, the phase ϕ and the relative amplitude are plotted versus the interaction parameter $1/k_\mathrm{F}a$. The relative amplitude is given by the amplitude A (definition see Eq.(7.1)) divided by the average width of the cloud after expansion. The average width is obtained by averaging $(W_\mathrm{x} + W_\mathrm{y})/2$ over one oscillation period using the same data set from which we extract A.

In the transition area around $1/k_\mathrm{F}a = -0.8$, the phase shift ϕ shows the step-like change at the transition from the hydrodynamic to the collisionless regime. This is similar to the jump in frequency in Fig. 7.7. In the collisionless and unitary regimes, the phase agrees with the theoretically expected values (solid line and dotted line, respectively).

As a general trend, the relative amplitude is larger in the hydrodynamic and smaller in the collisionless regime. In the hydrodynamic regime, the relative amplitude decreases for decreasing $1/k_\mathrm{F}a$, which is explained by the change of γ from 1 to 2/3; γ is the polytropic index of the equation of state (see Eq.(3.7)). At unitarity, the relative amplitude agrees well with the numerically calculated value for $\gamma = 2/3$ (dotted line). In the collisionless limit, the relative amplitude is half of the value at unitarity, which is also consistent with our calculations in subsection 7.2.3. We note that at the transition from the hydrodynamic to the collisionless regime, the value of the relative amplitude decreases even below the collisionless value.

In summary, the behavior of the phase shift and the amplitude agrees with our model presented in section 7.2 (see also Fig. 7.4 and Fig. 7.5), in particular the prominent change in the phase offset is confirmed.

7.3.3   Further observations

The measurements presented in the preceding subsections were taken under fixed experimental conditions, where only the scattering length a was varied. In this subsection we investigate how the transition from hydrodynamic to collisionless behavior depends on the experimental parameters excitation amplitude, trap depth and temperature.

In a first set of experiments, we explored whether the position of the transition depends on the excitation amplitude. We increase or decrease the amplitude by a factor of 2. This allows us to compare the oscillations where the amplitude is $\sim 20\,\%$, $\sim 10\,\%$ and $\sim 5\,\%$ of the averaged width. We do not observe any significant change in the position of the transition.

In general, we find that the transition always occurs when the mode frequency is similar to the pairing gap. This is supported by the fact that when we vary the trap depth the transition occurs at a constant scattering length ($a \approx -5000a_0$, B ≈ 960G) and does not depend on $1/k_\mathrm{F}a$. Due to the increased Fermi wave number k_F for the deeper trap configuration, the transition in terms of the interaction parameter shifts from $1/k_\mathrm{F}a \approx -0.8$ to $1/k_\mathrm{F}a \approx -0.5$. A change in laser power of our trapping laser influences both Fermi energy E_F and the frequency ω_q. As we increase the trap power

by a factor of 10, we also increase the radial trap frequencies by a factor of $\sqrt{10} \approx 3.2$. This changes the Fermi energy by a factor of 2.2 and the pairing gap, which scales like the trap frequencies, by roughly a factor of 3 [Chi04b]. These findings suggest that the transition is linked to a coupling of the collective oscillation to the pairing gap. This is also in agreement with earlier results on the radial compression mode [Bar04a, Gri07].
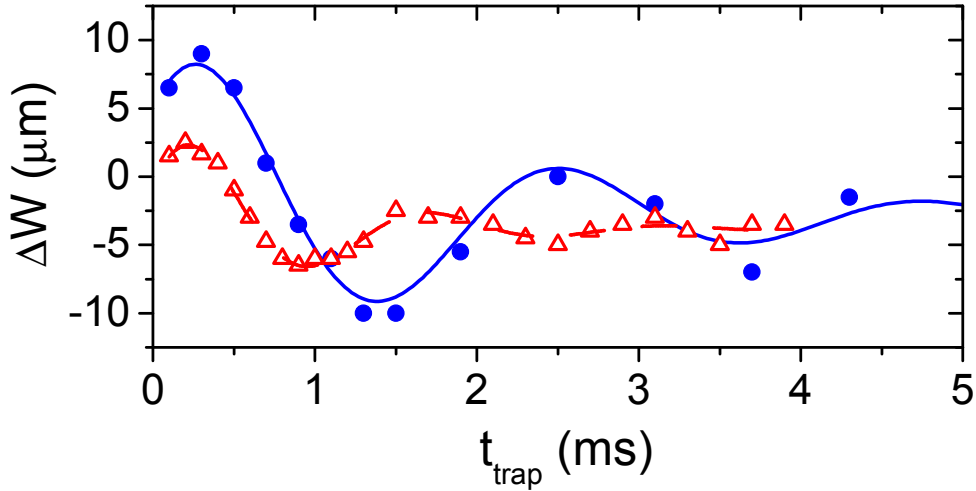
Figure 7.9: Oscillations of the quadrupole surface mode at a magnetic field of 920 G and $1/k_F a = -0.66$. The filled circles correspond to a cold ensemble, whereas the open triangles correspond to a heated ensemble. The solid lines are fits to the data according to Eq.(7.1).

To explore the temperature dependence of the transition between the hydrodynamic and the collisionless phase, we use a controlled heating scheme similar to the one described in section 5.3, where we hold the gas in a recompressed trap and let it heat up. We set the magnetic field to 920G ($1/k_F a = -0.66$), i.e. slightly below the hydrodynamic-to-collisionless transition, where the regime is still clearly hydrodynamic. We observe the oscillations in a gas at the lowest temperature we can achieve in our experiments (filled circles) and in a "hotter" gas (open triangles) in Fig. 7.9. The temperature of the cold gas is $\lesssim 0.1\,T_F$ and we believe the temperature of the heated gas to be $\lesssim 0.2\,T_F$. Figure 7.9 clearly shows that the frequency for the colder ensemble is lower than that of the heated one and the amplitude is lower by roughly a factor of 2. Using our model in section 7.2 this indicates a temperature driven transfer of the ensemble from the hydrodynamic to the collisionless regime.

In this chapter, we have presented measurements on the radial quadrupole mode of an ultracold ^{6}Li Fermi gas in the BEC-BCS crossover. As a pure surface excitation, this elementary mode probes hydrodynamic behavior without being affected by changes in

the equation of state. We have measured the characteristic properties of this collective mode in a wide range of interaction strengths.

Our observations provide new insight into the dynamics of the gas, in particular on the BCS side of the crossover, where the character of the oscillations abruptly changes from hydrodynamic to collisionless behavior. The measurements presented in this chapter show the phenomenon much clearer than in the radial compression mode (see [Bar04a, Kin04a] and 6) and provide quantitative data on the behavior near the transition. In particular, the data show that a substantial down shift of the collective mode frequency occurs in the hydrodynamic regime as a precursor of the transition.

The experimental results support the interpretation that the coupling of oscillation mode and pairing gap [Com04b, Chi04b, Gri07] plays a crucial role for the collective excitation dynamics on the BCS side of the crossover.

Chapter 8

Outlook

In the chapters before, we presented results of experiments with different collective oscillation modes. This chapter gives an outlook on possible future experiments with our experimental apparatus.

The field of collective oscillations in the BEC-BCS crossover still contains many possibilities for future research. We present in section 8.1 first results of experiments with the scissors mode. Further detailed studies of the scissors mode, especially characterizing the temperature dependence of hydrodynamic and collisionless behavior (see 8.2), are pursued at the time this thesis is written. A next step is to examine rotating systems, where the scissors mode again can be a useful tool to distinguish normal and superfluid hydrodynamic behavior (see 8.3).

Furthermore, our apparatus and especially our optical scanning system (see 4.2.3) enable us to create more elaborate optical potentials. So far, we have only used a small fraction of the possibilities this system is providing us. The possibilities that are opened up by the creation of suited optical potentials are described in section 8.4.

8.1   Measurements of the scissors mode

This section describes first results of our measurements of the scissors mode in a non-rotating system. An exploration of the scissors mode in the BEC-BCS crossover offers additional insights to the physics in this regime. This collective mode is independent from the equation of state, unlike the compression mode and similar to the quadrupole surface mode. Compared to the quadrupole surface mode, the scissors mode shows a by a factor of ~ 2 weaker damping. Therefore it is suited to precisely detect the transition between hydrodynamic and collisionless behavior.

The scanning system presented in 4.2.3 enables us to excite a collective oscillation of the scissors mode. The experimental details are presented in the following subsection 8.1.1. First experimental results of the scissors mode in the hydrodynamic and in the collisionless regime are shown in subsection 8.1.2. These results show a transition between both regimes, in agreement with the results for the quadrupole surface mode

(see chapter 7).

8.1.1   Experimental realization

Starting point of our experiments is a molecular BEC (see 5.1). After finishing the evaporation process we adiabatically recompress our all-optical trap. In this way we end up with $N = 4 \times 10^5$ atoms in a cigar-shaped trap with the trap frequencies $\omega_x \approx \omega_y \approx 2\pi \times 365\,\mathrm{Hz}$ and $\omega_z \approx 2\pi \times 22\,\mathrm{Hz}$. During the same time we magnetically tune the atomic s-wave scattering length a via a Feshbach resonance (see [Bar05b] and 2.3.1). So we can reach different interaction strengths in the BEC-BCS crossover.

In order to excite the scissors mode oscillation, we use the possibilities of our scanning system (see 4.2.3) to modulate the trapping potential. We use a fast modulation, i.e. with modulation frequencies of $100\,\mathrm{kHz}$, so that the trapped particles are influenced by the time averaged trapping potential only. We modulate in a way that the extent of the trapped cloud along one direction is twice as large as the extent in the perpendicular direction. The main axis of this elliptic cloud is diagonal to x- and y-direction. This is realized by a modulation with the same amplitude in x- and y-direction that add up to a total modulation amplitude in diagonal direction. By increasing the amplitude of the modulation, we change the shape of the cloud from cylindrically symmetric to elliptic. This increase is done slowly to avoid exciting any other collective modes. A sudden (within $5\mu s$) change in the ratio of the modulation amplitudes in x- and y-direction by a factor of 1.2 results in a sudden change of the angle of the main axis of the ellipse by $\sim 5°$. This sudden change of the angle initiates the oscillation of the cloud.

Absorption imaging is used for detection. We take the image after an expansion time of 0.5 ms after release from the trap. We choose this rather short expansion time to avoid a diminishing of the ellipticity that occurs for longer expansion times. The absorption images are fitted by a two-dimensional fitting routine, which enables a precise determination of the angle α of the main axis. The fitting routine uses a Thomas-Fermi density profile to describe the cloud.

8.1.2   First results

In this section we present our results on the scissors mode in the BEC-BCS crossover for the lowest temperatures that we can reach in our experiments. We mainly focus on measurements of the frequency of the mode. The frequency shows a drastically different behavior in the hydrodynamic than in the collisionless regime. According to the theoretical derivation in 3.4, the scissors mode in the hydrodynamic regime oscillates with the frequency $\omega_s = \sqrt{\omega_x^2 + \omega_y^2}$. In contrast to this, one expects in the collisionless regime a beating of the two oscillation frequencies $\omega_{s+} = |\omega_x + \omega_y|$ and $\omega_{s-} = |\omega_x - \omega_y|$.
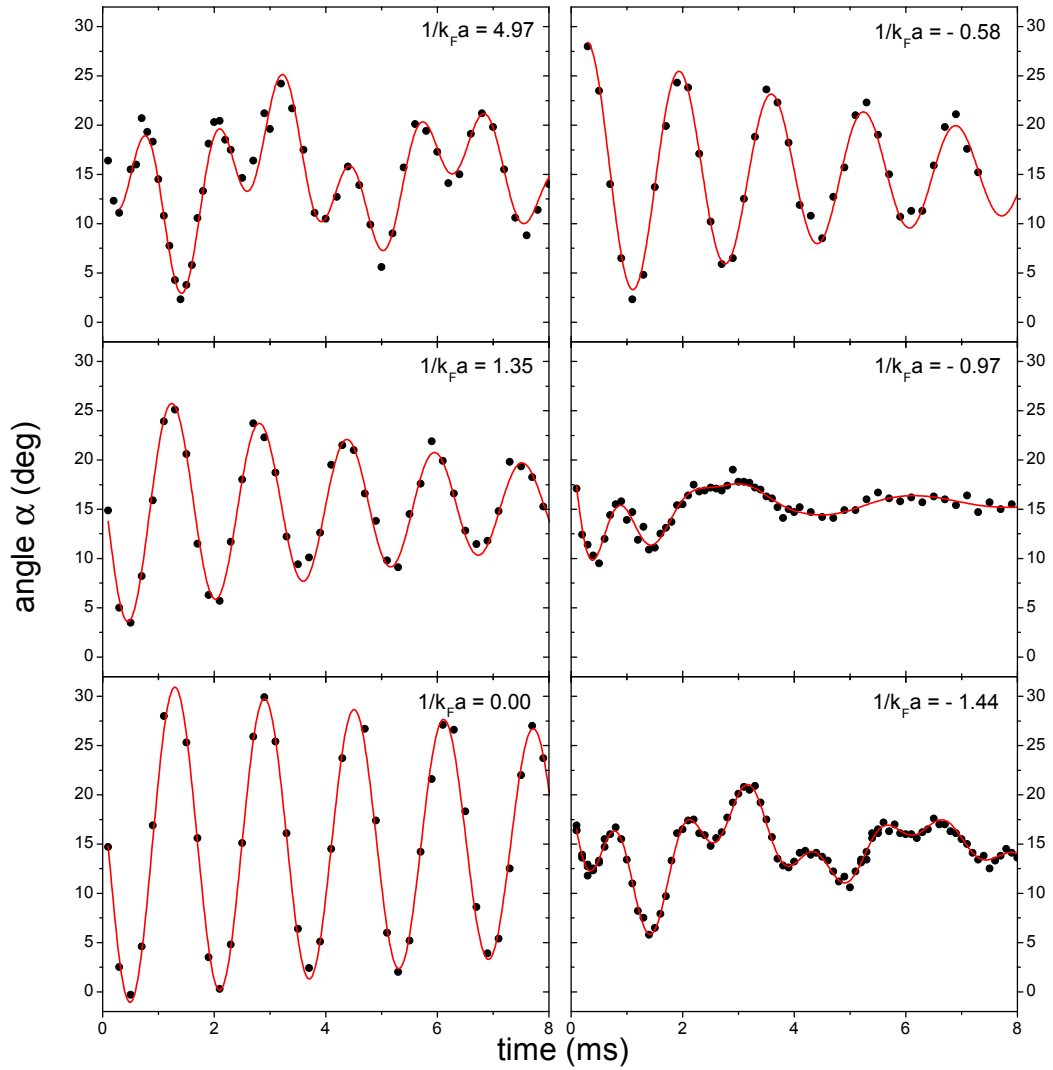
Figure 8.1: Overview of the scissors mode at different positions in the BEC-BCS crossover. Each subfigure shows a raw oscillation of the angle α versus the time in the trap. At $1/k_{\mathrm{F}}a =$ 4.97, the gas is in the collisionless limit and has a characteristic two frequency oscillation. This is due to inelastic processes that heat the system into a thermal molecular gas. For all $1/k_{\mathrm{F}}a$ between 4.97 and 0.58, the gas is hydrodynamic and exhibits a single frequency oscillation with very low damping. At $1/k_{\mathrm{F}}a < -0.58$, the gas shows collisionless behavior again, as the limit of a non-interacting Fermi gas is approached.

Fig. 8.1 shows the oscillation data of the angle α at different positions in the BEC-BCS crossover. We detect three distinct regions. For $1/k_{\mathrm{F}}a < -0.6$, the cloud is a

non-interacting Fermi gas, which results in the expected two frequency collisionless oscillation. For $1/k_Fa > 5$, the gas is heated up due to collisions between atoms and molecules; the resulting gas is much hotter and is also collisionless. For the region in between, where $-0.6 < 1/k_Fa < 5$, the gas is hydrodynamic and exhibits the characteristic single frequency oscillation.

In the hydrodynamic regime, the scissors mode measurements are consistent with our previous study of the radial quadrupole mode (see chapter 7). The distinct transition between hydrodynamic and collisionless behavior occurs at roughly the same magnetic field as with collective mode studies (see [Alt07, Kin04a] and chapters 6 and 7), sound propagation [Jos06], and vortex measurements [Zwi05].

The transition from a hydrodynamic system to a collisionless gas has been described theoretically in [GO99]. Unlike the compression mode experiments, the transition from hydrodynamic to collisionless for the scissors mode is a qualitative one. As shown in Fig. 8.1, the oscillation has single frequency behavior in the hydrodynamic regime and two-frequency character in the collisionless regime. Although the oscillations have additional frequency terms, a single frequency fit function turns out to describe well the measurements in the transition regime.

On resonance, we determine the frequency of the scissors mode to be to be $\omega_{\mathrm{scis}} = \sqrt{\omega_x^2 + \omega_y^2} \times 1.01 \pm 0.01$. This fully agrees with the theoretical expectation of $\sqrt{\omega_x^2 + \omega_y^2}$, as shown in Eq.(3.47).

In the collisionless regime, the beating of the two different frequencies is clearly visible in Fig. 8.1. The frequencies obtained from the data by a two-frequency fit fully agree with the calculated values for $\omega_{\mathrm{s+}}$ and $\omega_{\mathrm{s-}}$.

8.2 Temperature dependence of collective modes

A sensible next step in measurements of collective modes is the exploration of the temperature dependence. A temperature induced transition from the hydrodynamic to the collisionless regime has already been detected with the quadrupole surface mode (see 7.3.3). The transition from hydrodynamic to collisionless behavior of the quadrupole surface mode is accompanied by a peak in damping, as shown in 7.3.1. A similar effect is also expected for the scissors mode. With a controlled heating scheme as described in section 5.3, we are able to deterministically increase the temperature of the system. This enables us to map out the transition between the hydrodynamic and the collisionless regime throughout the BEC-BCS crossover.

The hydrodynamic regime consists of the regime of collisional hydrodynamics and the regime of superfluidity. Therefore a transition within the hydrodynamic regime from the superfluid to the non-superfluid phase is possible. A gas that is superfluid at low temperatures becomes non-superfluid by heating it up above the critical temperature of superfluidity. Similar to the hydrodynamic-to-collisionless transition, a peak in the damping of the scissors mode could also be an indicator of this superfluid-to-

collisional transition in the hydrodynamic regime.

8.3   Rotating systems

It remains a challenge to map out the transition between the normal and the superfluid hydrodynamic phase throughout the whole BEC-BCS crossover. A superfluid gas is an irrotational system, whereas a gas in the non-superfluid hydrodynamic regime can show rotational flow. Therefore rotating systems can provide the possibility to distinguish between both phases. In [Coz03], proposals to distinguish superfluid and collisional hydrodynamics are presented. Starting point for the proposed experiments is a cloud in a slowly rotating, elliptically deformed trapping potential, where Ω is the angular velocity of the slow rotation. Our scanning system enables us to create such a system. Sudden changes of the system result in collective oscillations of the rotating system similar to the scissors mode presented in 3.4 and 8.1.

If the elliptic deformation is suddenly switched off, the gas is in a non-equilibrium state in a axisymmetric trap. This results in an oscillation of the angle α of the principal axis of the gas. In the superfluid regime, α is described by $\tan 2\alpha = 2\Omega/\omega_S \tan \omega_S t$, where the frequency ω_S is defined by $\omega_S = \sqrt{2\omega_r^2 - \Omega^2}$. Here, ω_r is the radial trap frequency. In the collisional hydrodynamic regime, there is an additional slow precession of α, which can be described by $\Omega t/2$.

If the slow rotation is suddenly stopped, the gas first continues rotating, until the restoring force because of the elliptic confining potential results in a collective oscillation. For a superfluid, this collective mode is identical to the scissors mode in a non-rotating hydrodynamic gas (see 3.4). The oscillation is described by a single frequency $\omega_{scis} = \sqrt{\omega_x^2 + \omega_y^2}$, as has been shown in equation (3.47). For a collisional hydrodynamic gas, the oscillation looks qualitatively different, as it consists of a linear combination of two modes with different frequencies. The oscillation is given by $\alpha(t) = \Omega/\omega_S \sin \omega_S t \cos \Omega t$.

8.4   Elaborate optical potentials

The scanning system for our optical trapping potential (see 4.2.3) is capable of creating a variety of different potential geometries (for more details see [Koh07]) . So far, we used the scanning system for the excitation of different collective oscillation modes of the cloud. The creation of more elaborate optical potentials could offer new experimental prospects for the future.

A challenging aim is the creation of a double well potential. Starting with a molecular BEC in a single well optical potential, a smooth transfer into a double well geometry could be possible, where still a BEC is present. This would allow for interference experiments after a release of the BEC from the double well potential. The resulting interference pattern contains valuable information, e.g. about the wavelength of the

matter waves in the BEC. A study of the transformation of the interference pattern in the BEC-BCS crossover could provide interesting new results.

Another interesting opportunity would be the creation of a box-like potential. In a box-like potential, there is a homogeneous density distribution of the trapped particles in contrast to the heterogeneous density distribution in a harmonic trapping potential. This opens up new possibilities for the study of RF-spectra similar to the ones in [Chi04a], as the pairing gap is expected to emerge in a much more pronounced way for a less inhomogeneous Fermi gas. A higher precision in measurements of the pairing gap together with more detailed studies on influences on the pairing gap seem possible.

Appendix A

Publications

Pure gas of optically trapped molecules created from fermionic atoms
S. Jochim, M. Bartenstein, A. Altmeyer, G. Hendl, C. Chin, J. Hecker Denschlag, and R. Grimm
Phys. Rev. Lett. **91**, 240402 (2003). cond-mat/0308095

Bose-Einstein condensation of molecules
S. Jochim, M. Bartenstein, A. Altmeyer, G. Hendl, S. Riedl, C. Chin, J. Hecker Denschlag, and R. Grimm
Science **302**, 2101 (2003); published online 13 Nov 2003 (10.1126/science.1093280)

Crossover from a molecular Bose-Einstein condensate to a degenerate Fermi gas
M. Bartenstein, A. Altmeyer, S. Riedl, S. Jochim, C. Chin, J. Hecker Denschlag, and R. Grimm
Phys. Rev. Lett. **92**, 120401 (2004). cond-mat/0401109

Collective excitations of a degenerate gas at the BEC-BCS crossover
M. Bartenstein, A. Altmeyer, S. Riedl, S. Jochim, C. Chin, J. Hecker Denschlag, and R. Grimm
Phys. Rev. Lett. **92**, 203201 (2004). cond-mat/0403716

Observation of the pairing gap in a strongly interacting Fermi gas
C. Chin, M. Bartenstein, A. Altmeyer, S. Riedl, S. Jochim, J. Hecker Denschlag, and R. Grimm
Science **305**, 1128 (2004); published online 22 July 2004 (10.1126/science.1100818). cond-mat/0405632

Precise determination of 6Li cold collision parameters by radio-frequency spectroscopy on weakly bound molecules
M. Bartenstein, A. Altmeyer, S. Riedl, R. Geursen, S. Jochim, C. Chin, J. Hecker Denschlag, R. Grimm, A. Simoni, E. Tiesinga, C. J. Williams, P. S. Julienne
Phys. Rev. Lett. **94**, 103201 (2005). cond-mat/0408673

Note on "Collective Excitations of a Degenerate gas at the BEC-BCS Crossover", Phys. Rev. Lett. 92, 203201 (2004)
A. Altmeyer, S. Riedl, C. Kohstall, M.J. Wright, J. Hecker Denschlag, R. Grimm
cond-mat/0611285

Precision measurements of collective modes in the BEC-BCS crossover
A. Altmeyer, S. Riedl, C. Kohstall, M. Wright, R. Geursen, M. Bartenstein, C. Chin, J. Hecker Denschlag, R. Grimm
Phys. Rev. Lett. **98**, 040401 (2007), cond-mat/0609390

Dynamics of a strongly interacting Fermi gas: the radial quadrupole mode
A. Altmeyer, S. Riedl, M.J. Wright, C. Kohstall, J. Hecker Denschlag, R. Grimm
submitted for publication, arXiv:0704.3366

Pure Gas of Optically Trapped Molecules Created from Fermionic Atoms

S. Jochim, M. Bartenstein, A. Altmeyer, G. Hendl, C. Chin, J. Hecker Denschlag, and R. Grimm

Institut für Experimentalphysik, Universität Innsbruck, Technikerstraße 25, 6020 Innsbruck, Austria
(Received 5 August 2003; published 8 December 2003)

We report on the production of a pure sample of up to 3×10^5 optically trapped molecules from a Fermi gas of ^{6}Li atoms. The dimers are formed by three-body recombination near a Feshbach resonance. For purification, a Stern-Gerlach selection technique is used that efficiently removes all trapped atoms from the atom-molecule mixture. The behavior of the purified molecular sample shows a striking dependence on the applied magnetic field. For very weakly bound molecules near the Feshbach resonance, the gas exhibits a remarkable stability with respect to collisional decay.

The formation of composite bosons by pairing of fermions is the key to many intriguing phenomena in physics, with superfluidity and superconductivity being prominent examples. In ultracold atomic gases, pairs of fermionic atoms can be combined to form bosonic molecules [1,2] or possibly Cooper pairs [3]. The pairing changes the properties of the gas, highlighted by the prospect of a molecular Bose-Einstein condensate or a Cooper-paired superfluid. The interatomic interactions play a crucial role for the nature of the pairing process. The ability to control the interaction via magnetically tuned Feshbach resonances [4–6] opens up exciting possibilities for experiments on ultracold fermionic gases, e.g., exploring superfluidity in different pairing regimes [7–10].

The formation of molecules near Feshbach resonances in ultracold gases has been reported for bosons [11–14] and fermions [1,2]. In the experiments [1,2,11,12], the molecules coexist with the atoms in a strongly interacting mixture. A generic feature of a Feshbach resonance is the existence of a bound molecular state with a magnetic moment that differs from that of the unbound atom pair. The binding energy thus depends on the magnetic field, and a properly chosen field can resonantly couple colliding atoms into the molecular state. The inherent difference in magnetic moments facilitates a Stern-Gerlach selection of molecules and atoms. Two recent experiments [13,14] demonstrate the separation of the molecular from the atomic cloud in free space.

In this Letter, we report the creation of a pure sample of up to 3×10^5 optically trapped molecules from a fermionic gas of ^{6}Li atoms. After the production of an atom-molecule mixture via three-body collisions, a Stern-Gerlach purification scheme efficiently removes all trapped atoms, while leaving all molecules trapped. This allows us to investigate the intriguing behavior of the pure molecular sample, which strongly depends on the magnetic field.

The lithium isotope ^{6}Li is one of the two prime candidates in current experiments exploring the physics of fermionic quantum gases [15–19], the other one being

^{40}K [1,20]. A spin mixture composed of the lowest two sublevels in the hyperfine manifold of the electronic ground state is stable against two-body decay and exhibits wide magnetic tunability of s-wave interactions via a broad Feshbach resonance at about 850 G [21]. A calculation of the corresponding scattering length a as a function of the magnetic field [22] is shown in Fig. 1(a) [23]. The large cross section for elastic scattering near the resonance can be used for efficient evaporative cooling, in particular, above the resonance at negative scattering length where inelastic loss is negligible [16]. In the region of positive scattering length below the resonance, loss features have been observed [24]. At large positive a, a weakly bound molecular level exists with a binding energy approximately given by $\hbar/(ma^2)$, where $\hbar$ is Planck's constant and m denotes the atomic mass. For the region of interest, Fig. 1(b) shows this binding energy as calculated from the scattering length data [25].

The starting point of our experiments is a sample of 2.5×10^6 ^{6}Li atoms in a standing-wave optical dipole trap realized with a Nd:YAG laser at a wavelength of 1064 nm [19,26]. The 50-50 spin mixture in the lowest two spin states is spread over $\sim$1500 individual lattice sites of the standing-wave trap. In the central region of the trap, a single site contains typically 1800 atoms. The
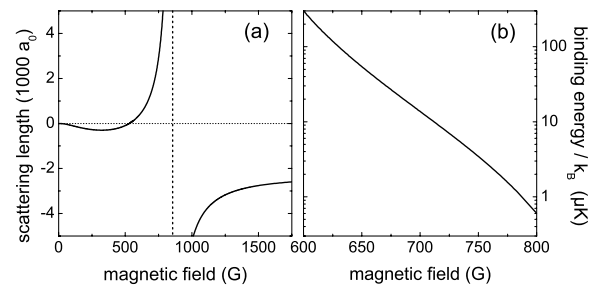

FIG. 1.   (a) Magnetic-field dependence of the s-wave scattering length a in the ^{6}Li spin mixture. An additional, narrow Feshbach resonance near 550 G [22] is omitted in the plot. (b) Binding energy of the weakly bound molecular level in the region of large positive a.

axial and radial trap frequencies are 260 kHz and 390 Hz, respectively. The trap depth is $k_B \times 27 \ \mu$K with k_B denoting Boltzmann's constant. At a temperature of 2.5 μK, peak values for the number density and phase-space density are 3×10^{12} cm^{-3} and 0.04 [27,28], respectively. The ultracold gas is prepared by forced evaporative cooling after loading the optical trap at an initial depth of ~ 1 mK with 8×10^6 atoms from a magneto-optical trap (MOT). The evaporation is performed by ramping down the light intensity in 1 s at a magnetic field of 1200 G. The evaporation initially proceeds with very high efficiency similarly to [16,29], but finally loses its efficiency when the tightly confining lattice potential does not support more than one or two quantum states.

We form molecules in the weakly bound level at a field of 690 G, where we find optimum production rates at a large positive scattering length of $a = +1300a_0$. Here a_0 denotes Bohr's radius. To reach the production field of 690 G, we quickly ramp from the evaporation field of 1200 G down to this value with a speed of -7.5 G/ms. In contrast to other experiments with fermionic atoms [1,2], the molecule formation during this ramp is negligible and the molecules are predominantly formed after the ramp at the fixed production field.

The molecules are detected by dissociating them into atoms [1,2,13,14] and measuring their fluorescence. For this purpose, we apply a ramp across the Feshbach resonance to fields of typically 1200 G (speed $+6$ G/ms). This brings the weakly bound level above the scattering continuum and the molecules quickly dissociate. The dissociation turns out to be insensitive to variations of the ramp speed and the final field. After the dissociation ramp, we immediately ramp down to zero magnetic field. The ramp speed of -12 G/ms is fast enough to avoid molecule formation when crossing the region of positive scattering length. After reaching zero magnetic field, we recapture all atoms into the MOT. Their number is then determined by measuring the emitted fluorescence intensity using a calibrated photodiode [27]. This measurement provides the total atom number $2N_{mol} + N_{at}$, where N_{mol} and N_{at} denote the number of molecules and atoms after the production phase, respectively. To determine N_{at}, we repeat the same measurement without the Feshbach dissociation ramp by immediately ramping down to zero from the production field. The ramp down to zero magnetic field increases the binding energy to a large value of about $k_B \times 80$ mK and the molecules are lost without leading to any fluorescence light in the MOT. The number of molecules N_{mol} is then obtained by taking the difference in atom numbers measured in two subsequent runs with and without the dissociating Feshbach ramp.

The creation of molecules from the atomic gas is demonstrated in Fig. 2 for the optimum production field of 690 G. The time evolution of the measured numbers $2N_{mol} + N_{at}$ and N_{at} is shown together with the corresponding number of molecules $2N_{mol}$. We attribute the molecule formation to three-body recombination into the
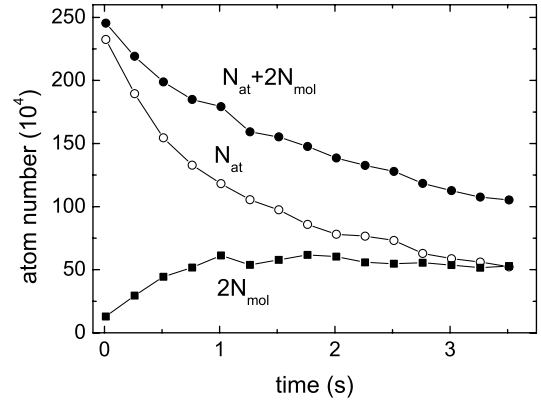

FIG. 2. Formation of molecules at a fixed magnetic field of 690 G. The measured numbers $N_{at} + 2N_{mol}$ and N_{at} are plotted as a function of time together with the resulting number of molecules $2N_{mol}$.

weakly bound state [30,31]. Two-body processes cannot lead to bound dimers as a third particle is required for energy and momentum conservation. The three-body molecule formation process can be modeled with the differential equation $\dot{N}_{mol}/N_{at} = M_3 \langle n_{at}^2 \rangle$, where $\langle n_{at}^2 \rangle$ denotes the mean quadratic density of the atoms. From the initial molecule formation rate of $\dot{N}_{mol} = 3.5 \times 10^5$ s^{-1}, we thus derive a three-body formation coefficient of $M_3 = 1 \times 10^{-25}$ cm^6/s^{-1} [27]. The maximum number of 3×10^5 molecules is reached after about 1 s. For longer times, the fraction of atoms forming molecules approaches a value of $\sim 50\%$.

At the optimum production field of 690 G, the molecular binding energy amounts to $\sim k_B \times 18 \ \mu$K, which is in between the thermal energy of $k_B \times 2.5 \ \mu$K and the trap depth of $k_B \times 27 \ \mu$K for the atoms. For the molecules, the trap depth is a factor of 2 higher because of the 2 times larger polarizability. We have verified this fact by measuring the trap frequencies for atoms and molecules to be equal within the experimental uncertainty of a few percent. After a three-body recombination event both the atom and the molecule remain trapped. We believe that the recombination heat is cooled away by a evaporation of atoms out of the trap. Evaporative loss of molecules is strongly suppressed because of the higher trap depth.

To purify the created molecules we use a Stern-Gerlach selection technique. We apply a magnetic field gradient perpendicular to the standing-wave axis. This pulls particles out of the trap for which the magnetic force is larger than the trapping force. In order to be able to apply large enough field gradients, we lower the trap depth to $k_B \times 19 \ \mu$K while applying the gradient for about 10 ms. Figure 3 demonstrates such a purification at 568 G. While all the atoms are lost above $B'_{at} = 17$ G/cm, the molecules start getting spilled at 20 G/cm, and are lost completely above $B'_{mol} = 32.5$ G/cm. This means that, under suitable conditions, we can remove all the atoms while keeping the molecule number constant.
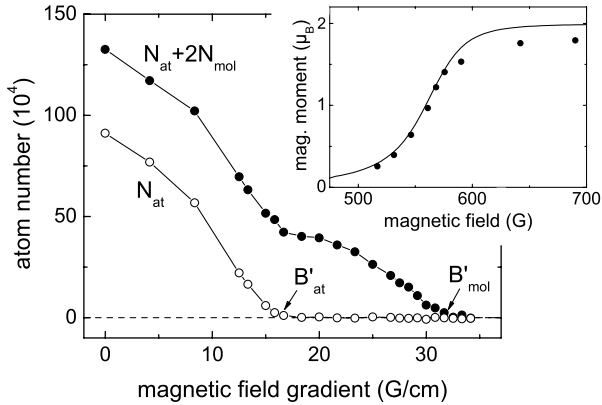

FIG. 3. Stern-Gerlach selection by applying a magnetic field gradient to the trapped atom-molecule mixture at 568 G and a trap depth of $k_B \times 19 \mu K$. Marked are the two gradients where all the atoms and all the molecules are lost. The inset shows the magnetic moment of the molecules estimated from the Stern-Gerlach selection at different magnetic fields together with the theoretical calculation.

The magnetic moment of the molecules μ_{mol} can be estimated to be $\mu_{mol} = 2\mu_{at} B'_{mol}/B'_{at}$, where μ_{at} is the magnetic moment of one free atom. At high magnetic field, μ_{at} equals Bohr's magneton μ_B. The inset of Fig. 3 shows the magnetic moments of the molecules determined at various magnetic fields. The data agree well with the magnetic field dependence calculated from theory (solid curve). We attribute the systematic deviation to slightly different trap parameters for atoms and molecules.

Starting with a pure molecular sample, we study its stability against inelastic molecule-molecule collisions. Corresponding decay curves are displayed in Fig. 4 for two different magnetic fields. At 546 G a rapid nonexponential decay is observed as a clear signature of inelastic molecule-molecule collisions. From the initial decay rate we derive a two-body loss coefficient of 5×10^{-11} cm^3/s [27]. At 690 G, the observed behavior is strikingly different. The molecular sample shows a nearly exponential
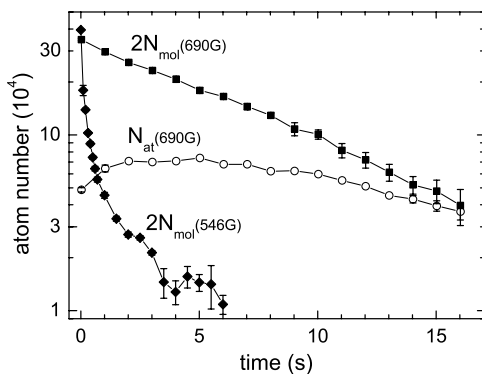
decay with a time constant as long as ~10 s. As similar lifetimes are observed for trapped atom samples under conditions where trapped molecules cannot be created, the observed molecular lifetime can be fully attributed to one-body effects such as heating in the optical trap. For a loss rate coefficient at 690 G our data provide an upper limit of 3×10^{-13} cm^3/s [27], which is surprisingly low for inelastic collisions in a molecular system with many open exit channels.

The data at 690 G show another interesting collisional effect. Atoms reappear after purification of the molecular cloud, see (○) in Fig. 4. For long storage times (~15 s), an atom-molecule mixture is reestablished with a similar fraction of molecules as observed in the initial formation process at the same magnetic field (see Fig. 2). Collisions producing atoms from molecules are endoergic in nature as kinetic energy is required to provide the dissociation energy. The increasing atom fraction does not lead to any increased loss. This shows that the gas is remarkably stable both against molecule-molecule and atom-molecule collisions.

The dependence of the molecular decay on the magnetic field is shown in Fig. 5. Here we store the initially pure gas of 1.8×10^5 molecules at a variable magnetic field for a fixed holding time of 1 s before we measure the number of remaining molecules and atoms. A sharp transition occurs around 650 G. For fields below ~600 G, where the binding energy is relatively large ($> k_B \times 100 \mu K$), the observed decay is very fast and no atoms are found to reappear. Here inelastic collisions apparently lead to a rapid vibrational quenching. Furthermore, the kinetic energy of the molecules cannot provide the necessary energy for collisional dissociation. Consequently, we do not observe any atoms reappearing.

For fields above ~680 G, a completely different behavior is observed. In this regime, no significant loss occurs in the total number $2N_{mol} + N_{at}$. However, an increasing atom fraction is observed as a result of collisional dissociation of the molecules. Here the binding energy

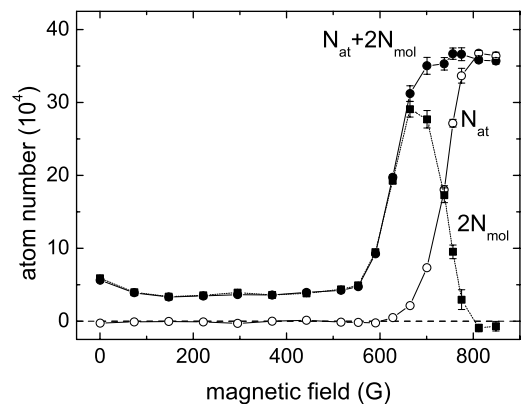FIG. 4. Time evolution of an initially pure sample of molecules at 546 G (◆) and at 690 G (■). At 690 G, atoms are observed to reappear (○).

FIG. 5. Remaining number of atoms N_{at}, $N_{at} + 2N_{mol}$ and $2N_{mol}$ after a 1-s hold time at variable magnetic field starting with a pure molecular sample.

approaches the thermal energy and the sample tends towards a thermal atom-molecule equilibrium. Close to the Feshbach resonance, where the binding energy becomes comparable to thermal energy, the atomic fraction dominates in the atom-molecule mixture.

In conclusion we have produced an ultracold, pure molecular gas of ^{6}Li dimers in an optical dipole trap. Close to the Feshbach resonance, where the molecular binding energy is small, there is a strong coupling of the atomic gas and the molecules. Three-body collisions between atoms form molecules and collisions break up molecules to produce atoms. Our observations show that this exchange between atomic and molecular fraction can be nearly lossless. The long molecular lifetime along with a large elastic collision rate between the particles opens up great perspectives for further evaporative cooling of the molecular gas to Bose-Einstein condensation. Given the maximum molecule number of 3×10^5 and a temperature of about 2.5 μK, we reach a phase-space density of 0.01, only a factor of 4 lower than our initial atomic phase-space density. The molecular sample may be further cooled to condensation by efficient evaporation. Out of a mixture of atoms and molecules, mainly atoms will evaporate because they are more weakly trapped than the molecules. The gas is cooled further when molecules break up into atoms since this is an endoergic process. Once quantum degeneracy is accomplished it will be very interesting to cross the Feshbach resonance in order to observe the transition to a strongly interacting superfluid Fermi gas [7–10].

Note added.—After submission of the present Letter, molecule formation in ^{6}Li using the narrow Feshbach resonance at 543 G was reported by Hulet's group [32].

---

[1] C. A. Regal, C. Ticknor, J. L. Bohn, and D. S. Jin, Nature (London) **424**, 47 (2003).

[2] J. Cubizolles, T. Bourdel, S. J. J. M. F. Kokkelmans, G. V. Shlyapnikov, and C. Salomon, preceding Letter, Phys. Rev. Lett. **91**, 240401 (2003).

[3] H. T. C. Stoof, M. Houbiers, C. Sackett, and R. Hulet, Phys. Rev. Lett. **76**, 10 (1996).

[4] H. Feshbach, Ann. Phys. (Leipzig) **19**, 287 (1962).

[5] S. Inouye, M. Andrews, J. Stenger, H.-J. Miesner, D. Stamper-Kurn, and W. Ketterle, Nature (London) **392**, 151 (1998).

[6] T. Loftus, C. Regal, C. Ticknor, J. Bohn, and D. Jin, Phys. Rev. Lett. **88**, 173201 (2002).

[7] M. Holland, S. J J. M. F. Kokkelmans, M. Chiofalo, and R. Walser, Phys. Rev. Lett. **87**, 120406 (2001).

[8] E. Timmermans, K. Furuya, P. W. Milonni, and A. K. Kerman, Phys. Lett. A **285**, 228 (2001).

[9] M. L. Chiofalo, S. J. J. M. F. Kokkelmans, J. L. Milstein, and M. J. Holland, Phys. Rev. Lett. **88**, 090402 (2002).

[10] Y. Ohashi and A. Griffin, Phys. Rev. Lett. **89**, 130402 (2002).

[11] E. A. Donley, N. R. Claussen, S. T. Thompson, and C. E. Wieman, Nature (London) **417**, 529 (2002).

[12] C. Chin, A. J. Kerman, V. Vuletić, and S. Chu, Phys. Rev. Lett. **90**, 033201 (2003).

[13] J. Herbig, T. Kraemer, M. Mark, T. Weber, C. Chin, H.-C. Nägerl, and R. Grimm, Science **301**, 1510 (2003).

[14] S. Dürr, T. Volz, A. Marte, and G. Rempe, cond-mat/0307440.

[15] A. G. Truscott, K. E. Strecker, W. I. McAlexander, G. B. Partridge, and R. G. Hulet, Science **291**, 2570 (2001).

[16] K. O'Hara, S. Hemmer, M. Gehm, S. Granade, and J. Thomas, Science **298**, 2179 (2002).

[17] T. Bourdel, J. Cubizolles, L. Khaykovich, K. M. F. Magalhães, S. J. J. M. F. Kokkelmans, G. Shlyapnikov, and C. Salomon, Phys. Rev. Lett. **91**, 020402 (2003).

[18] S. Gupta, Z. Hadzibabic, M. Zwierlein, C. Stan, K. Dieckmann, C. H. Schunck, E. G. M. van Kempten, B. J. Verhaar, and W. Ketterle, Science **300**, 1723 (2003).

[19] S. Jochim, M. Bartenstein, G. Hendl, J. Hecker Denschlag, R. Grimm, A. Mosk, and M. Weidemüller, Phys. Rev. Lett. **89**, 273202 (2002).

[20] G. Modugno, G. Roati, F. Riboli, F. Ferlaino, R. J. Brecha, and M. Inguscio, Science **297**, 2240 (2002).

[21] M. Houbiers, H. T. C. Stoof, W. McAlexander, and R. Hulet, Phys. Rev. A **57**, R1497 (1998).

[22] K. O'Hara, S. Hemmer, S. Granade, M. Gehm, J. Thomas, V. Venturi, E. Tiesinga, and C. Williams, Phys. Rev. A **66**, 041401(R) (2002).

[23] The exact resonance position is uncertain within a few 10 G [17], whereas the location of the zero-crossing has been determined to 529 G within 3 G [19,22].

[24] K. Dieckmann, C. Stan, S. Gupta, Z. Hadzibabic, C. Schunck, and W. Ketterle, Phys. Rev. Lett. **89**, 203201 (2002).

[25] From the scattering length data [22], we calculate the binding energy $\hbar^2/[m(a - \bar{a})^2]$ including a correction with $\bar{a} = 29.8 a_0$ for lithium. See G. Gribakin and V. Flambaum, Phys. Rev. A **48**, 546 (1993).

[26] A. Mosk, S. Jochim, H. Moritz, T. Elsässer, M. Weidemüller, and R. Grimm, Opt. Lett. **26**, 1837 (2001).

[27] With fluorescence detection, we can determine the absolute atom number only within a factor of 2. All the derived quantities are subject to this systematic error.

[28] With a ground-state population of 99% in the tightly confined direction, each lattice site contains a quasi-2D gas. This fact is taken into account in our calculations of number and phase-space densities.

[29] S. R. Granade, M. E. Gehm, K. M. O'Hara, and J. E. Thomas, Phys. Rev. Lett. **88**, 120405 (2002).

[30] H. Suno, B. D. Esry, and C. H. Greene, Phys. Rev. Lett. **90**, 053202 (2003).

[31] D. Petrov, Phys. Rev. A **67**, 010703(R) (2003).

[32] K. E. Strecker, G. B. Partridge, and R. G. Hulet, Phys. Rev. Lett. **91**, 080406 (2003).

Bose-Einstein Condensation of Molecules

S. Jochim,[1] M. Bartenstein,[1] A. Altmeyer,[1] G. Hendl,[1] S. Riedl,[1] C. Chin,[1] J. Hecker Denschlag,[1] R. Grimm[1,2]*

We report on the Bose-Einstein condensation of more than 10^5 Li$_2$ molecules in an optical trap starting from a spin mixture of fermionic lithium atoms. During forced evaporative cooling, the molecules are formed by three-body recombination near a Feshbach resonance and finally condense in a long-lived thermal equilibrium state. We measured the characteristic frequency of a collective excitation mode and demonstrated the magnetic field–dependent mean field by controlled condensate spilling.

Since the first experiments on Bose-Einstein condensation (BEC) in ultracold atomic gases in 1995 (*1–3*), atoms of eight chemical elements have been condensed. BEC of more complex objects such as molecules or Cooper-paired atoms will open up many new avenues of research because they offer new degrees of freedom. An intriguing example is the fundamental change in quantum statistics when paired fermions form composite bosons. Recent experiments have demonstrated the formation of molecules in ultracold atomic gases of bosons (*4–9*) and fermions (*10–13*). Experiments starting with atomic BEC show the creation of molecular clouds at the threshold to quantum degeneracy (*7*) or clearly in that regime (*9*), but not in a thermal equilibrium state. In most of these experiments, weakly bound dimers are produced via magnetically tuned Feshbach resonances (*14*). Such a scattering resonance occurs when a free colliding atom pair energetically coincides with a bound molecular state. On the side of the resonance where the energy of the molecular level is below the dissociation limit, a weakly bound dimer state exists. The experiments indicate an important difference between weakly bound dimers composed of bosonic and of fermionic atoms. Dimers of bosons show a quick decay via inelastic atom-molecule or molecule-molecule collisions (*9*), so that quantum-degenerate molecular clouds can only be created in a transient regime. In contrast, the dimers of fermions exhibit a remarkable stability (*11–13, 15*). Such molecular gases have been observed with lifetimes far longer than the time scales for elastic collisions and thermalization. This fact has been explained by a fermionic suppression of vibrational quenching in molecule collisions (*16*). Their stability allows us to use bosonic mole-

cules composed of fermionic atoms to achieve molecular BEC in thermal equilibrium.

Our experiment is based on evaporative cooling of an optically trapped mixture of fermionic ^{6}Li atoms in the two lowest spin states (*11–13, 17–21*). During the cooling process, a large number of bosonic dimers are formed by three-body recombination and finally condense into a molecular BEC. The spin mixture exhibits a broad Feshbach resonance at a magnetic field of about 850 G (*18, 19, 22, 23*), which leads to a pronounced magnetic field dependence of the scattering length a (Fig. 1) that characterizes the s-wave interactions. Dimers in a single weakly bound state can be formed in the range of large positive a with a binding energy of $\hbar^2/(ma^2)$, where $\hbar$ is Planck's constant h divided by 2π and m is the mass of a ^{6}Li atom. This has been observed in magnetic field–dependent loss features (*24*) and changes in the interaction energy of the gas (*21*). Two recent experiments have directly demonstrated the presence of these molecules and investigated some of their properties (*12, 13*). For negative scattering length, no weakly bound dimer state exists. For negative scattering length, where a weakly bound dimer state does not exist, the ^{6}Li gas exhibits a remarkable stability against collisional decay, and deeply degenerate Fermi gases have been created (*20*).

Our optical dipole trap is realized with a single Gaussian laser beam at a wavelength of 1030 nm, which is focused to a waist of 23 μm. At the full power of $P_0 = 10.5$ W, the radial and axial oscillation frequencies are $\Omega_r/2\pi = 14.5$ kHz and $\Omega_z/2\pi = 140$ Hz, respectively, and the atom trap is $U_0 \approx k_B \times 800$ μK deep (k_B denotes Boltzmann's constant). When the power P is reduced to a relative value $p = P/P_0$, the optical trap frequencies follow $p^{1/2}\Omega_i (i = r, z)$ and the trap depth for the atoms is $U_{at} = pU_0$. Our magnetic field B used for Feshbach tuning exhibits a curvature that gives rise to an additional contribution to the trapping potential. For the tight radial confinement of the optical trap, this effect is negligibly small. For the weak axis, however, a magnetic trap-

ping effect becomes important with decreasing p. Taking this into account, the axial trap frequency is given by $\omega_z = \sqrt{p\Omega_z^2 + \omega_m^2}$. Here $\omega_m/2\pi = 24.5$ Hz $\times \sqrt{B/\text{kG}}$ is the magnetic contribution, which is precisely known for our coils. For weak traps with $p \ll 0.03$ ($U_{at}/k_B \ll 25$ μK), the magnetic contribution dominates, and the axial confinement is harmonic with a corresponding frequency known on the percent level. In this regime, the mean trap frequency is given by $\overline{\omega} = (p\Omega_r^2\omega_m)^{1/3}$. For the weakly bound ^{6}Li dimers, all external forces are twice the ones on the individual atoms. Thus, the molecular trap is two times deeper than the atom trap ($U_{mol} = 2U_{at}$), and the trap frequencies are identical. Gravity is compensated for by a magnetic field gradient of 1.1 G/cm.

We start the evaporation process with ~1.5×10^6 atoms at a temperature of ~80 μK, a peak number density of ~10^{14} cm^{-3}, and a peak phase-space density of ~5×10^{-3}. The mean elastic collision rate is as high as ~5×10^4 s^{-1}. These excellent starting conditions are obtained by a two-stage loading process. The atoms are loaded into the dipole trap from another deep, large-volume standing wave trap (*25*), which itself is loaded from a magneto-optical trap. Forced evaporative cooling is then performed by reducing the trap power (*17, 20*). We use a simple exponential ramp with a relative power $p(t) = \exp(-t/\tau)$, where the time constant $\tau = 0.23$ s is experimentally optimized. A feedback system allows us to precisely control the laser power to levels well below $p = 10^{-4}$.

BEC of weakly bound molecules occurs when we perform evaporative cooling at a large positive scattering length of $a \approx +3500a_0$, where a_0 is Bohr's radius. In this case, the evaporation process shows a strikingly different behavior in comparison with the corresponding situation at large negative scattering length, where no dimers can be produced.

First we discuss the creation of a degenerate Fermi gas without the possibility of molecule formation at a magnetic field of 1176 G, where $a \approx -3500a_0$ (*23*). Here the evaporation pro-
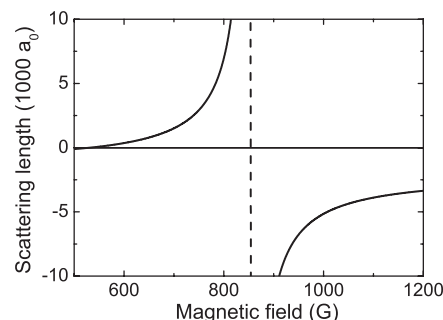

Fig. 1. Feshbach resonance at ~850 G in a mixture of the two lowest spin states of ^{6}Li (*18*). The s-wave scattering length a is plotted as a function of the magnetic field B.

[1]Institut für Experimentalphysik, Universität Innsbruck, Technikerstraβe 25, 6020 Innsbruck, Austria. [2]Institut für Quantenoptik und Quanteninformation, Österreichische Akademie der Wissenschaften, 6020 Innsbruck, Austria.

*To whom correspondence should be addressed. E-mail: rudolf.grimm@uibk.ac.at

ceeds in a very similar way as that described in (17, 20). The measured atom number N (26) first follows a scaling law $N/N_0 = p^\alpha$ (27), with $\alpha \approx 0.25$. In this regime, the temperature of the gas is typically a factor of 10 below the trap depth (27), and the elastic collision rate stays well above 10^4 s^{-1}. The crossover to Fermi degeneracy, where the thermal energy $k_B T$ reaches the Fermi energy $E_F = \hbar \overline{\omega} (3N)^{1/3}$, takes place at $p \approx 0.05$ ($U_{at}/k_B \approx 40$ μK). By further decreasing p, the trap depth $U_{at} \propto p$ decreases faster than the Fermi energy $E_F \propto p^{1/3}$. A threshold occurs when E_F reaches U_{at} and the trap is filled up to the "rim." Further decrease of p then leads to a spilling of atoms out of the trap and thus to a rapid decrease of N with p. Our data (Fig. 2) clearly show this spilling effect for $p < 1 \times 10^{-3}$ ($U_{at}/k_B < 800$ nK). Modeling the spilling curves provides us with an upper bound of $k_B T < 0.2 E_F$ for the temperature in terms of the Fermi energy. In the regime of a completely filled shallow trap, the number of atoms in the two-component spin mixture is given by two times the number of quantum states in the trap. A numerical calculation, shown in Fig. 2, confirms this interpretation of our data.

The same evaporation procedure is performed at a magnetic field of 764 G, where the scattering length $a \approx +3500 a_0$ (23) has essentially the same magnitude but opposite sign. Here the weakly bound dimers have a binding energy of ~2 μK, and their formation has been observed in several experiments (12, 13, 21). In order to detect the molecules, we dissociate them and measure the number of resulting atoms (26). For this purpose, we abruptly turn on the full trap power, which strongly heats the sample and leads to collisional dissociation. In order to ensure that we dissociate all molecules, we also apply a magnetic field ramp across the Feshbach resonance (13). The number of atoms measured after the dissociation process thus yields the number of free atoms together with atoms having formed molecules.

Below $p = 1 \times 10^{-3}$ the measured atom numbers (solid circles in Fig. 2) show a striking difference in comparison with the case of the degenerate Fermi gas. Down to a power level of $p = 3 \times 10^{-4}$ ($U_{mol}/k_B \approx 480$ nK), the trap holds almost all particles and contains up to 20 times more atoms than would be possible for fermions. Hence, the trapped sample can no longer be an atomic Fermi gas. The trap is filled with bosonic molecules in the weakly bound state (28). The lifetime of the molecular ensemble, for which we measure about 20 s at a fixed trap depth of $U_{mol}/k_B \approx 560$ nK, exceeds the time scale of elastic collisions (~100 μs) by several orders of magnitude. This highlights the fact that the molecular cloud exists in a thermal equilibrium state.

The formation of molecules during the evaporative cooling process can be understood

Fig. 2. Evaporative cooling results obtained on both sides of the Feshbach resonance. We measure the number of trapped particles (the number of all atoms that are free or bound in long-range dimers) as a function of the relative laser power p at the end of an exponential evaporation ramp $p(t) = \exp(-t/230 \text{ ms})$. The trap depth for atoms is $U_{at}/k_B = p \times 800$ μK, whereas for molecules it is two times larger ($U_{mol} = 2U_{at}$). The

measurements taken at 1176 G with negative scattering length $a \approx -3500 a_0$ (open circles) show the spilling of a degenerate Fermi gas when the trap depth reaches the Fermi energy. The solid line shows the maximum number of trapped atoms in a two-component Fermi gas according to a numerical calculation of the number of quantum states in our trap. The dashed lines indicate the corresponding uncertainty range due to the limited knowledge of the experimental parameters. The measurements at 764 G with positive scattering length $a \approx +3500 a_0$ (solid circles) exhibit a striking increase of the trapped particle number at low values of p, which is due to the formation of molecules. The inset shows the optimum production of molecules in the magnetic field range where a weakly bound level exists. Here the total number of particles is measured for various magnetic fields at a fixed final ramp power $p = 2.8 \times 10^{-4}$ ($U_{mol}/k_B \approx 440$ nK).

in terms of a chemical atom-molecule equilibrium (29, 30). Exothermal three-body recombination processes compete with dissociation by endothermal two-body processes. When the gas is cooled down, the equilibrium shifts to an increasing fraction of molecules. Because atom-atom, atom-molecule, and molecule-molecule collisions have comparable cross sections near the resonance (16), evaporation continues at about the same speed. In the final stage of cooling, all relevant energies, such as the thermal energy $k_B T$ and the trap depths U_{at} and U_{mol}, are far below the binding energy $\hbar^2/(ma^2)$, so that in chemical equilibrium one is left with an essentially pure sample of molecules. The fact that the binding energy of ~2 μK at our optimized magnetic field of 764 G is a few times larger than the final trap depth (inset, Fig. 1) fits well into this picture.

The observation that a large number of $N_{mol} \approx 1.5 \times 10^5$ molecules is confined in our very shallow, only 480 nK deep trap under thermal equilibrium conditions already shows that a molecular BEC is formed. The trap offers about 10 times more quantum states for dimers as compared to the case of atoms discussed before (31). Because we observe a factor of ~20 more particles than for the degenerate atomic Fermi gas, the molecular gas is necessarily quantum degenerate. Because of the high elastic collision rates, which stay well above 10^3 s^{-1} even for very shallow traps, the sample is also thermalized. The temperature then is a small fraction of the trap depth. According to standard evaporation theory (27), we can typically assume $T \approx 0.1 U_{mol}/k_B \approx 50$ nK. This is well below the critical temperature for BEC, for

which we calculate $T_C = \hbar \overline{\omega} k_B^{-1} (N_{mol}/1.202)^{1/3} = 280$ nK. Because the condensate fraction is given by $1 - (T/T_C)^3$, these arguments show that the molecular BEC must be almost pure.

To investigate the molecular condensate, we have studied a characteristic collective excitation mode (32, 33). For a cigar-shaped sample in the Thomas-Fermi limit, well fulfilled in our experiment, such a quadrupolar mode is expected at a frequency of $\sqrt{5/2}\,\omega_z = 2\pi \times 33.8$ Hz. We perform our measurement at $p = 3.5 \times 10^{-4}$ ($U_{mol}/k_B \approx 560$ nK) with a trapped sample of ~10^5 molecules. We apply a sinusoidal modulation to the magnetic field with an amplitude of 3.5 G to modulate the molecular scattering length $a_m \propto a$ (16) with a relative amplitude of about 5%. After 2 s of continuous excitation, we measure the remaining number of particles in the trap. The resonance manifests itself in a sharp dip in the number of particles (Fig. 3). The observed resonance frequency of 33.6 Hz is in remarkable agreement with the expectation. We point out that a noncondensed gas deep in the hydrodynamic regime would show a similar frequency of 33.2 Hz (34), but thermalization in our shallow trap excludes this scenario (35). The measured collective excitation frequency rules out a gas in the collisionless regime, which would show its resonant loss at $2\omega_z = 2\pi \times 42.8$ Hz, and thus again confirms the thermalization of the sample. The observed narrow resonance width of ~1 Hz shows a very low damping rate and is consistent with an almost pure BEC (33, 36).

An essential property of a BEC is its mean field potential $U_{MF} = 4\pi n a_m \hbar^2/(2m)$ resulting
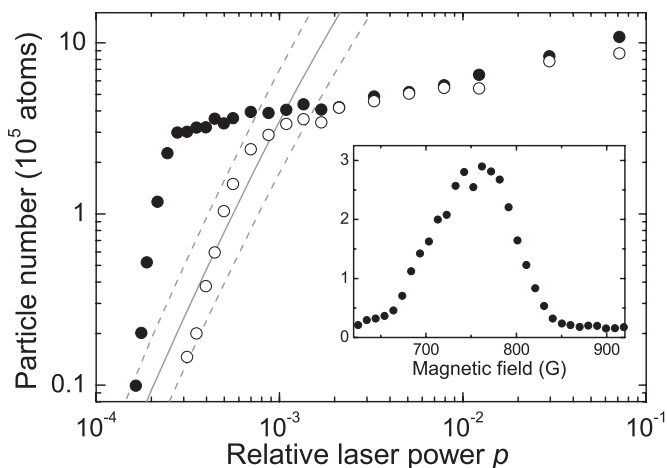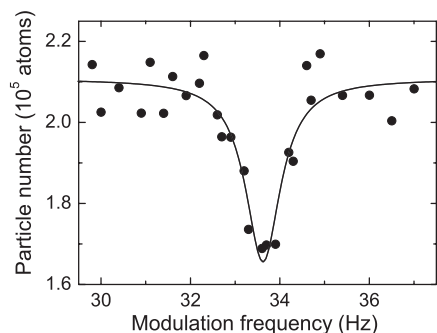
Fig. 3. Resonance of a collective excitation mode at $\sqrt{5/2}\,\omega_z$. The oscillation is excited by magnetic modulation of the molecular BEC mean field. The solid curve shows a Lorentzian fit to the data.

from s-wave interactions; here n denotes the molecular density. For our molecular BEC with large positive a_m, the mean field is repulsive and thus stabilizes the BEC against collapse and decay. In a trap of finite depth, however, the mean field repulsion limits the maximum number of trappable molecules. When the chemical potential μ reaches the trap depth, a similar spilling effect is expected as we see for the Fermi gas, but for weaker traps. The decrease of our molecular signal (Fig. 2) below $p = 3 \times 10^{-4}$ ($U_{mol}/k_B \approx 480$ nK) may be explained by such a spilling effect.

We used spilling in a controlled way to demonstrate the mean field of the molecular BEC and to investigate its dependence on the magnetic field. After producing the BEC at a magnetic field of $B_1 = 772$ G and $p = 3.5 \times 10^{-4}$ ($U_{mol}/k_B \approx 560$ nK), we adiabatically tilt the vertical trapping potential by application of a magnetic field gradient B' that is smoothly ramped up within 50 ms. The number of remaining particles as a function of the applied field gradient (Fig. 4) shows the loss of molecules resulting from the reduced trap depth. When the magnetic field is kept at the evaporation field of $B_1 = 772$ G, where $a = 4100 a_0$ (23), even very weak gradients lead to loss (open circles in Fig. 4). This indicates that the chemical potential is close to the potential depth, so that the trap is full. The chemical potential can be lowered by reducing the scattering length. For this purpose, we ramp the magnetic field to a smaller value. A spilling curve taken at $B_2 = 731$ G, where $a = 2200 a_0$ (23), indeed shows a markedly different behavior (solid circles in Fig. 4). Here small gradients do not lead to any loss and the curve thus shows a flat top. For gradients $|B'|$ exceeding 0.65 G/cm, molecules get spilled until everything is lost at $|B'| = 1.3$ G/cm. The sharp onset of the spilling confirms the essentially pure nature of the BEC.

A comparison of the two spilling curves in Fig. 4 provides us with information on the ratio of the scattering lengths a_m at the two magnetic fields B_1 and B_2. In the spilling region above $|B'| = 0.65$ G/cm, the trap is full in both cases,
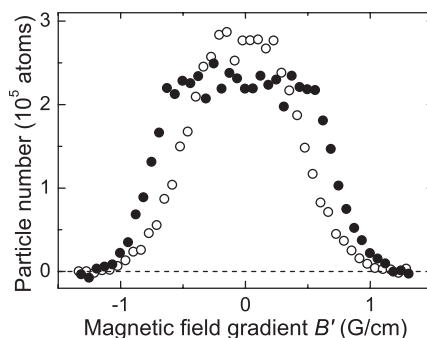
Fig. 4. Controlled spilling of the BEC by application of a magnetic field gradient B'. This variable gradient is applied in addition to the constant gradient of 1.1 G/cm that we use for gravity compensation. The data are taken at the two different magnetic fields $B_1 = 772$ G (open circles) and $B_2 = 731$ G (solid circles), where the mean field of the BEC is different by a factor of ~ 2.

and the trapped particle number is inversely proportional to a_m. Comparing the two spilling curves in that region, we obtain a scattering length ratio of $a_m(B_1)/a_m(B_2) = 2.4(2)$. This factor is indeed close to the factor of 1.9 (23) expected from the proportionality of atomic and molecular scattering lengths $a_m \propto a$ (16) and the dependence of a shown in Fig. 1. This observation demonstrates the mean field of the molecular BEC together with its magnetic tunability.

The ability to control interactions in a Bose condensed ensemble of paired fermionic atoms has many exciting prospects (37, 38). It opens up unique ways to cool a fermionic gas far below the Fermi temperature (39) and to study different regimes of superfluidity (40–43). The experimental exploration of the strongly interacting crossover regime between a BEC-like and a Cooper-paired phase is a particular challenge and promises more insight into the physical mechanisms underlying superconductivity.

References and Notes
1. M. Anderson, J. Ensher, M. Matthews, C. Wieman, E. Cornell, *Science* **269**, 198 (1995).
2. K. Davis *et al.*, *Phys. Rev. Lett.* **75**, 3969 (1995).
3. C. Bradley, C. Sackett, J. Tollett, R. Hulet, *Phys. Rev. Lett.* **75**, 1687 (1995).
4. R. Wynar, R. S. Freeland, D. J. Han, C. Ryu, D. J. Heinzen, *Science* **287**, 1016 (2000).
5. E. A. Donley, N. R. Claussen, S. T. Thompson, C. E. Wieman, *Nature* **417**, 529 (2002).
6. C. Chin, A. J. Kerman, V. Vuletić, S. Chu, *Phys. Rev. Lett.* **90**, 033201 (2003).
7. J. Herbig *et al.*, *Science* **301**, 1510 (2003); published online 21 August 2003 (10.1126/science.1088876).
8. S. Dürr, T. Volz, A. Marte, G. Rempe, preprint available at http://arxiv.org/abs/cond-mat/0307440.
9. K. Xu, *et al.* preprint available at http://arxiv.org/abs/cond-mat/0310027.
10. C. A. Regal, C. Ticknor, J. L. Bohn, D. S. Jin, *Nature* **424**, 47 (2003).
11. K. E. Strecker, G. B. Partridge, R. G. Hulet, *Phys. Rev. Lett.* **91**, 080406 (2003).
12. J. Cubizolles, T. Bourdel, S. J. J. M. F. Kokkelmans, G. V. Shlyapnikov, C. Salomon, preprint available at http://arxiv.org/abs/cond-mat/0308018.
13. S. Jochim *et al.*, *Phys. Rev. Lett.*, in press (preprint available at http://arxiv.org/abs/cond-mat/0308095).
14. S. Inouye *et al.*, *Nature* **392**, 151 (1998).
15. C. A. Regal, M. Greiner, D. S. Jin, preprint available at http://arxiv.org/abs/cond-mat/0308606.
16. D. S. Petrov, C. Salomon, G. V. Shlyapnikov, preprint available at http://arxiv.org/abs/cond-mat/0309010.
17. S. Granade, M. E. Gehm, K. M. O'Hara, J. E. Thomas, *Phys. Rev. Lett.* **88**, 120405 (2002).
18. K. M. O'Hara *et al.*, *Phys. Rev. A* **66**, 041401 (2002).
19. S. Jochim *et al.*, *Phys. Rev. Lett.* **89**, 273202 (2002).
20. K. M. O'Hara, S. L. Hemmer, M. E. Gehm, S. R. Granade, J. E. Thomas, *Science* **298**, 2179 (2002); published online 7 November 2002 (10.1126/science.1079107).
21. T. Bourdel *et al.*, *Phys. Rev. Lett.* **91**, 020402 (2003).
22. M. Houbiers, H. T. C. Stoof, W. McAlexander, R. Hulet, *Phys. Rev. A* **57**, R1497 (1998).
23. The position of the Feshbach resonance is known to within a few tens of Gauss. All numbers given for the scattering lengths and binding energies are subject to a corresponding systematic error.
24. K. Dieckmann *et al.*, *Phys. Rev. Lett.* **89**, 203201 (2002).
25. A. Mosk *et al.*, *Opt. Lett.* **26**, 1837 (2001).
26. We measure the atom number via fluorescence detection after recapture into a magneto-optical trap. In order to avoid molecule formation and loss when the Feshbach tuning field is ramped down before detection, we heat the sample by abruptly turning on the full laser power of the optical dipole trap. At low phase-space densities, the thermal gas is not affected by the downward Feshbach ramp (13).
27. K. M. O'Hara, M. E. Gehm, S. R. Granade, J. E. Thomas, *Phys. Rev. A* **64**, 051403 (2001).
28. We know that only the weakly bound state is populated, because the release of binding energy in a three-body process would otherwise lead to immediate trap loss. Moreover, our dissociation-based detection is sensitive only to molecules in this state.
29. C. Chin, R. Grimm, preprint available at http://arxiv.org/abs/cond-mat/0309078.
30. S. J. J. M. F. Kokkelmans, G. V. Shlyapnikov, C. Salomon, preprint available at http://arxiv.org/abs/cond-mat/0308384.
31. For the harmonically approximated trap with same frequencies and twice the depth, the molecules have eight times more quantum states than the atoms. The lower ω_z at 764 G as compared to 1176 G gives another factor of 1.24.
32. S. Stringari, *Phys. Rev. Lett.* **77**, 2360 (1996).
33. D. M. Stamper-Kurn, H.-J. Miesner, S. Inouye, M. R. Andrews, W. Ketterle, *Phys. Rev. Lett.* **81**, 500 (1998).
34. D. Guéry-Odelin, F. Zambelli, J. Dalibard, S. Stringari, *Phys. Rev. A* **60**, 4851 (1999).
35. A noncondensed ensemble in the hydrodynamic regime, where the elastic collision rate exceeds all other time scales, would rapidly cool down by evaporation to temperatures far below the trap depth and thus form a BEC.
36. D. S. Jin, M. R. Matthews, J. R. Ensher, C. E. Wieman, E. A. Cornell, *Phys. Rev. Lett.* **78**, 764 (1997).
37. L. Pitaevskii, S. Stringari, *Science* **298**, 2144 (2002).
38. A. Cho, *Science* **301**, 750 (2003).
39. L. D. Carr, G. V. Shlyapnikov, Y. Castin, preprint available at http://arxiv.org/abs/cond-mat/0308306.
40. H. T .C. Stoof, M. Houbiers, C. Sackett, R. Hulet, *Phys. Rev. Lett.* **76**, 10 (1996).
41. M. Holland, S. J. J. M. F. Kokkelmans, M. L. Chiofalo, R. Walser, *Phys. Rev. Lett.* **87**, 120406 (2001).
42. E. Timmermans, K. Furuya, P. W. Milonni, A. K. Kerman, *Phys. Lett. A* **285**, 228 (2001).
43. Y. Ohashi, A. Griffin, *Phys. Rev. Lett.* **89**, 130402 (2002).
44. We thank P. Zoller for very useful discussions and for stimulating the measurement of the collective excitation frequency. We acknowledge support by the Austrian Science Fund (FWF) within Spezialforschungsbereich 15 (project part 15) and by the European Union through the Cold Molecules Training and Mobility of Researchers Network under contract no. HPRN-CT-2002-00290. C.C. is a Lise-Meitner fellow of the FWF.

Crossover from a Molecular Bose-Einstein Condensate to a Degenerate Fermi Gas

M. Bartenstein,[1] A. Altmeyer,[1] S. Riedl,[1] S. Jochim,[1] C. Chin,[1] J. Hecker Denschlag,[1] and R. Grimm[1,2]

[1]*Institut für Experimentalphysik, Universität Innsbruck, Technikerstraße 25, 6020 Innsbruck, Austria*
[2]*Institut für Quantenoptik und Quanteninformation, Österreichische Akademie der Wissenschaften, 6020 Innsbruck, Austria*

We demonstrate a reversible conversion of a $^6Li_2$ molecular Bose-Einstein condensate to a degenerate Fermi gas of atoms by adiabatically crossing a Feshbach resonance. By optical *in situ* imaging, we observe a smooth change of the cloud size in the crossover regime. On the Feshbach resonance, the ensemble is strongly interacting and the measured cloud size is 75(7)% of the one of a noninteracting zero-temperature Fermi gas. The high condensate fraction of more than 90% and the adiabatic crossover suggest our Fermi gas to be cold enough to form a superfluid.

Bose-Einstein condensation (BEC) of molecules formed by fermionic atoms was recently demonstrated [1–4]. The tunability of interactions in such systems provides a unique possibility to explore the Bose-Einstein condensate to Bardeen-Cooper-Schrieffer (BEC-BCS) crossover [5], an intriguing interplay between the superfluidity of bosons and Cooper pairing of fermions. While the BEC and BCS limits are both well understood, the crossover takes place in a strongly interacting regime, which represents a challenge for many-body theory.

Feshbach resonances [6] play a central role to control two-body interaction and have been used for conversion between fermionic atoms and bosonic molecules [7–10]. They are also the experimental key to investigate phenomena related to the BEC-BCS crossover. For example, it has been predicted in Ref. [11] that a pure molecular BEC can be converted into a superfluid Fermi gas by an adiabatic passage over the Feshbach resonance. Moreover, in the crossover regime where the interactions are unitarity limited, a universal behavior is expected [12,13]. Ultracold gases in that regime may provide new insights into other strongly interacting systems such as high-T_c superconductors, ^3He superfluids, and neutron stars.

A spin mixture of ^6Li atoms in the lowest two hyperfine sublevels is an excellent system to investigate the crossover [14,15] based on a broad Feshbach resonance at a magnetic field of $B = 850$ G [16–18]. An efficient formation of ultracold molecules has been realized by three-body recombination [10,19], or by sweeping the magnetic field across the resonance [8]. The long lifetime of the molecules permits efficient evaporation [1,8,10] and facilitates slow, adiabatic changes of the system.

In this work, we explore the regime where the BEC-BCS crossover is expected by analyzing the density profiles of the trapped cloud at different magnetic fields. Our experimental setup is described in Ref. [1]. We load 2×10^6 precooled ^6Li atoms into a single focused-beam dipole trap, which is generated by a 10 W Yb:YAG laser operating at a wavelength of 1030 nm. We evaporatively cool the cloud by exponentially lowering the trap depth with a time constant of 460 ms. The radial and axial trap frequencies are $\omega_r/2\pi = 110$ Hz$(P/\text{mW})^{1/2}$ and $\omega_z/2\pi = (600B/\text{kG} + 0.94P/\text{mW})^{1/2}$ Hz, respectively, where P is the laser power. The curvature of the magnetic field that we use for Feshbach tuning results in a magnetic contribution to the axial trapping. In the low power range where the molecular BEC is formed ($P < 50$ mW), the axial confinement is predominantly magnetic. During the whole evaporation process, the magnetic field is kept at $B = 764$ G. At this field the molecular binding energy is $\sim k_B \times 2\ \mu$K, where k_B is Boltzmann's constant. For the scattering length of elastic molecule-molecule collisions, we expect $a_{mol} = 2200a_0$, based on the predicted relation of $a_{mol} = 0.6a$ [20] and an atomic scattering length of $a = 3500a_0$ [17]. Here a_0 is Bohr's radius. Using radio-frequency spectroscopy which allows us to distinguish signals from atoms and molecules [7], we observe a complete atom to molecule conversion when the thermal energy of the particles is reduced to values well below the molecular binding energy.

For detection we apply *in situ* absorption imaging to record spatial density profiles of the trapped ensemble. To image at high magnetic fields, we illuminate the cloud for 20 μs with a probe beam (intensity 0.5 mW/cm^2) tuned to the atomic $|2S_{1/2}, m_J = -1/2, m_I = 0\rangle \rightarrow |2P_{3/2}, m_J' = -3/2, m_I' = 0\rangle$ transition. The probe beam dissociates the molecules and is used to image the resulting atom cloud [3]. Compared to the absorption imaging of unbound atoms, we found that the detection efficiency of the molecules approaches 100% at fields higher than 750 G and $\sim$50% at 650 G. The difference is due to the Franck-Condon wave function overlap, which favors fields closer to the resonance where the interatomic separation in the molecular state is larger. In our cigar-shaped trap, the radial cloud size is on the order of our imaging resolution of 10 μm, while the axial cloud size of typically $\sim$100 μm can be accurately measured. We therefore obtain axial density distributions from images integrated radially.

To measure the condensate fraction, we adiabatically reduce the magnetic field from 764 to 676 G in a 200-ms linear ramp after completion of the evaporation ramp. This reduces the scattering length a_{mol} and thus increases the visibility of the characteristic bimodal distribution. Figure 1(a) shows a bimodal profile observed in this way with $N_{mol} = N/2 = 4 \times 10^5$ molecules remaining at a final evaporation ramp power of 28 mW. A Gaussian fit to the thermal wings (dashed line) yields a temperature of $T = 430$ nK, which is a factor of 7.5 below the calculated trap depth of 3.2 μK. The observed condensate fraction of $\sim 20\%$ is consistent with $1 - (T/T_c)^3$, where $T_c = 0.8 k_B^{-1} \hbar \bar{\omega} (N_{mol}/1.202)^{1/3} = 500$ nK is the critical temperature, $\bar{\omega} = (\omega_r^2 \omega_z)^{1/3}$ is the mean vibration frequency, and the factor of 0.8 takes into account the $\sim 20\%$ downshift in T_c due to interactions [21].

We obtain pure molecular condensates when we continue the evaporation process down to final power levels of a few mW. Figure 1(b) shows an essentially pure condensate of $N_{mol} = 2.0 \times 10^5$ molecules obtained at a final power of 3.8 mW, where the trap depth is 450 nK. The density profile is well fit by a Thomas-Fermi density distribution $\propto (1 - z^2/z_{TF}^2)^2$ with a radius $z_{TF} = 105$ μm. The corresponding peak molecular density is 1.2×10^{13} cm^{-3}. In the image a thermal component is not discernable. A careful analysis of the profile provides us with a lower bound of 90% for the condensate fraction. For the chemical potential of the BEC, we obtain $\mu = \frac{1}{2} m_{mol} \omega_z^2 z_{TF}^2 = k_B \times 130$ nK. Here $m_{mol} = 2m$ is the mass of the ^{6}Li dimer. Based on the prediction $a_{mol} = 0.6a = 650a_0$, the calculated chemical potential of $\frac{1}{2}(15 \hbar^2 N_{mol} \bar{\omega}^3 a_{mol} \sqrt{m_{mol}})^{2/5} = k_B \times 155$ nK is consistent

with the observed value of $k_B \times 130$ nK considering the experimental uncertainty. In particular, the particle number is calibrated to within a factor of 1.5 through fluorescence imaging [10].

The pure molecular BEC at 764 G serves as our starting point for exploring the crossover to the degenerate Fermi gas. Before we change the magnetic field, we first adiabatically increase the trap power from 3.8 to 35 mW in a 200-ms exponential ramp. The higher power provides a trap depth of $\sim k_B \times 2$ μK for the atoms, which is roughly a factor of 2 above the Fermi energy, and avoids spilling of the Fermi gas produced at magnetic fields above the resonance [1]. The compression increases the peak density of the condensate by a factor of 2.5. All further experiments reported here are performed in the recompressed trap with $\omega_r/2\pi = 640$ Hz and $\omega_z/2\pi = (600B/\text{kG} + 32)^{1/2}$ Hz.

We measure the lifetime of the BEC in the compressed trap at 764 G to be 40 s. The peak molecular density is estimated to be $n_{mol} = (15/8\pi)(\omega_r/\omega_z)^2 N_{mol}/z_{TF}^3 = 1.0(5) \times 10^{13}$ cm^{-3}. This provides an upper bound for the binary loss coefficient of 1×10^{-14} cm^3/s, and is consistent with previous measurements in thermal molecular gases [8,10] together with the predicted scattering length scaling [20] and the factor-of-2 suppression of binary collision loss in a condensate.

For exploring the crossover to a Fermi gas we apply slow magnetic-field ramps. To ensure their adiabaticity, we performed several test experiments. In one series of measurements we ramped up the field from 764 to 882 G and back to 764 G with variable ramp speed. This converts the molecular BEC into a strongly interacting Fermi gas and vice versa. Therefore substantial changes are expected in the cloud size. After the up-and-down ramp, we observe an axial oscillation of the ensemble at the quadrupolar excitation frequency [1,22]. This collective oscillation is the lowest excitation mode of the system and is thus sensitive to nonadiabaticity effects. We observe axial oscillations with relative amplitudes of $>$ 5% for ramp speeds above 1.2 G/ms. For ramp speeds of 0.6 G/ms and lower, the axial oscillation was no longer visible.

We also checked the reversibility of the crossover process by linearly ramping up the magnetic field from 764 to 1176 G and down again to 764 G within 2 s (ramp speed of ± 0.41 G/ms). In Fig. 2, we compare the axial profile taken after this ramp ($\bullet$) with the corresponding profile obtained after 2 s at fixed magnetic field ($\circ$). The comparison does not show any significant deviation. This highlights that the conversion into a Fermi gas and its back-conversion into a molecular BEC are lossless and proceed without noticeable increase of the entropy.

To investigate the spatial profile of the trapped gas in different regimes, we start with the molecular BEC at 764 G and change the magnetic field in 1-s linear ramps to final values between 740 and 1440 G. Images are then taken at the final ramp field. To characterize the size of
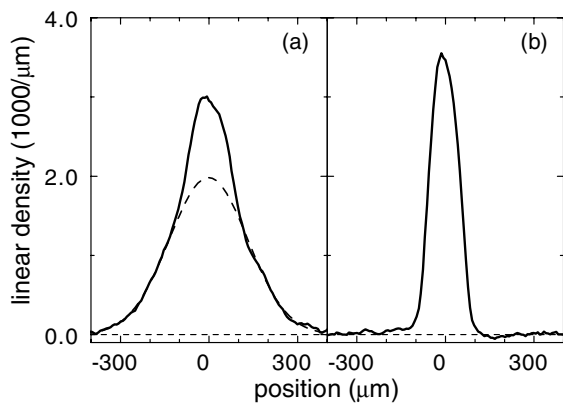

FIG. 1. Axial density profiles of a partially condensed (a) and fully condensed (b) molecular cloud. The profiles are derived from averaging seven *in situ* images taken at a magnetic field of $B = 676$ G after evaporation at the production field of 764 G. (a) When the evaporation ramp is stopped with 4×10^5 molecules at a final laser power of 28 mW, a characteristic bimodal distribution is observed with a condensate fraction of $\sim 20\%$. The dashed curve shows Gaussian fit to the thermal fraction. (b) At a final laser power of 3.8 mW, an essentially pure condensate of 2×10^5 molecules is obtained.
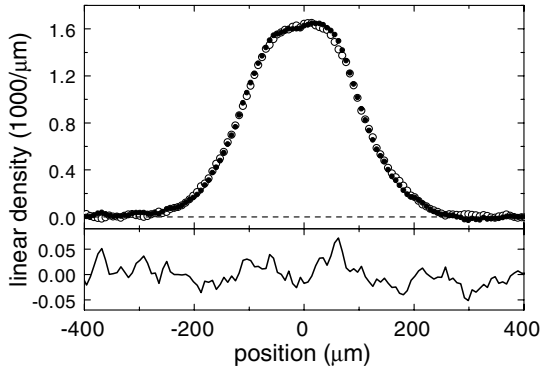
FIG. 2. Axial profile of a molecular BEC at 764 G (●) after its conversion into a Fermi gas at 1176 G and subsequent back conversion. Two 1-s magnetic field ramps are applied in this reversible process. For reference we show the corresponding profile observed without the magnetic field ramp (○). The density profiles are obtained by averaging over 50 images. The difference shown in the lower graph is consistent with the drifts of a residual interference pattern in the images.

the trapped gas, we determine the root-mean-squared axial size z_{rms}. This rms size is related to the axial radius z_{TF} by $z_{rms} = z_{TF}/\sqrt{7}$ in the case of a pure BEC in the Thomas-Fermi limit and by $z_{rms} = z_{TF}/\sqrt{8}$ in the cases of zero-temperature noninteracting or strongly interacting Fermi gases [23].

Figure 3(b) shows how the measured axial size z_{rms} changes with the magnetic field. For comparison, Fig. 3(a) displays the magnetic-field dependence of the atomic scattering length a. Up to 950 G, an increase in z_{rms} is due to the crossover from the molecular BEC to the degenerate Fermi gas. For higher magnetic fields, the axial cloud size of the Fermi gas shrinks with B as the axial magnetic confinement increases ($\omega_z \propto \sqrt{B}$).

For the following discussions, we normalize the observed size to the one expected for a noninteracting Fermi gas. In particular, this removes the explicit trap dependence. In Fig. 3(c), we show the normalized axial size $\zeta = z_{rms}/z_0$, where $z_0 = (E_F/4m\omega_z^2)^{1/2}$ is the rms axial size of a noninteracting zero-temperature Fermi gas with $N = 4 \times 10^5$ atoms. The Fermi energy $E_F = \hbar^2 k_F^2/2m = \hbar\bar{\omega}(3N)^{1/3}$ amounts to $k_B \times 1.1\ \mu K$ at 850 G, and the Fermi wave number k_F corresponds to a length scale of $k_F^{-1} = 3600 a_0$.

Below the Feshbach resonance, the observed dependence of the cloud size agrees well with the mean-field behavior of a BEC in the Thomas-Fermi limit. In this regime, the normalized size is given by $\zeta = 0.688(a_{mol}/a)^{1/5}(E_F/E_b)^{1/10}$, where $E_b = \hbar^2/ma^2$ is the molecular binding energy. Figure 3(c) shows the corresponding curve (solid line) calculated with $a_{mol}/a = 0.6$ [20]. This BEC limit provides a reasonable approximation up to ~800 G; here the molecular gas interaction parameter is $n_{mol}a_{mol}^3 \approx 0.08$. Alternatively, the interaction strength can be expressed as $k_F a \approx 1.9$.
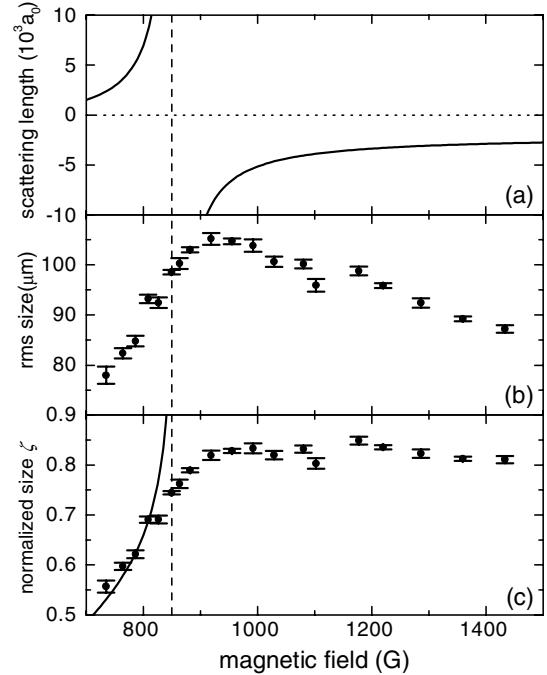

FIG. 3. Axial cloud size measurements across the Feshbach resonance. In (a) the atomic scattering length a is shown according to [17]; the resonance at 850 G is marked by the vertical dashed line. The data in (b) display the measured rms cloud sizes. In (c), the same data are plotted after normalization to a noninteracting Fermi gas. The solid line shows the expectation from BEC mean-field theory with $a_{mol} = 0.6a$. In (b) and (c), the error bars show the statistical error of the size measurements from typically five individual images.

The crossover to the Fermi gas is observed in the vicinity of the Feshbach resonance between 800 and 950 G; here ζ smoothly increases with the magnetic field until it levels off at 950 G, where the interaction strength is characterized by $k_F a \approx -1.9$. Our results suggest that the crossover occurs within the range of $-0.5 \lesssim (k_F a)^{-1} \lesssim 0.5$, which corresponds to the strongly interacting regime. The smoothness of the crossover is further illustrated in Fig. 4. Here the spatial profiles near the resonance show the gradually increasing cloud size without any noticeable new features.

On resonance a universal regime is realized [12–14], where scattering is fully governed by unitarity and the scattering length drops out of the description. Here the normalized cloud size can be written as $\zeta = (1 + \beta)^{1/4}$, where β parametrizes the mean-field contribution to the chemical potential in terms of the local Fermi energy [14]. At 850 G our measured value of $\zeta = 0.75 \pm 0.07$ provides $\beta = -0.68^{+0.13}_{-0.10}$. Here the total error range includes all statistic and systematic uncertainties with the particle number giving the dominant contribution. Note that the uncertainty in the Feshbach resonance position is not included in the errors [18]. Our experimental results reveal a stronger interaction effect than previous measurements that yielded $\beta = -0.26(7)$ at $T = 0.15 T_F$ [14]
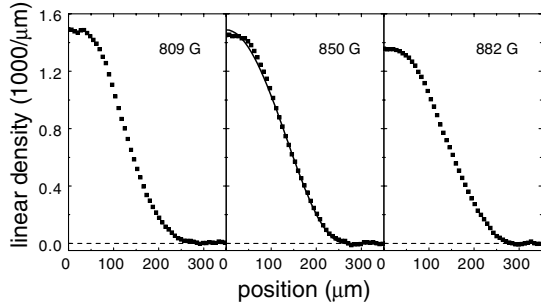
FIG. 4. Observed axial density profiles near the Feshbach resonance, averaged over 50 images and symmetrized to reduce imaging imperfections. The rms cloud sizes are 93, 99, and 103 μm at $B = 809$, 850, and 882 G, respectively. For comparison, the on-resonance data at 850 G are shown together with a fit by the expected profile $\propto (1 - z^2/z_{TF}^2)^{5/2}$. The small deviation near the top is due to a residual interference pattern in the images.

and $\beta \approx -0.3$ at $T = 0.6T_F$ [15]. Our value of β lies within the range of the theoretical predictions for a zero-temperature Fermi gas: -0.67 [12,24], -0.43 [24], and, in particular, $-0.56(1)$ from a recent quantum Monte Carlo calculation [25].

Beyond the Feshbach resonance, in the Fermi gas regime above 950 G, we observe an essentially constant normalized cloud size of $\zeta = 0.83 \pm 0.07$. In this regime, the interaction parameter $k_F a$ is calculated to vary between -2 (at 950 G) and -0.8 (at 1440 G), which allows us to estimate ζ to vary between 0.90 and 0.95 based on the interaction energy calculations in Ref. [12]. Our observed values are somewhat below this expectation, which requires further investigation.

In summary, we have demonstrated the smooth crossover from a molecular condensate of ^{6}Li dimers to an atomic Fermi gas. Since the conversion is adiabatic and reversible, the temperature of the Fermi gas can be estimated from the conservation of entropy [11]. Our high condensate fraction of $> 90\%$ suggests a very small entropy which in the Fermi gas limit corresponds to an extremely low temperature of $k_B T < 0.04 E_F$. In this scenario, superfluidity can be expected to extend from the molecular BEC regime into the strongly interacting Fermi gas regime above the Feshbach resonance where $k_F a \lesssim -0.8$. Our experiment thus opens up intriguing possibilities to study atomic Cooper pairing and superfluidity in resonant quantum gases.

[1] S. Jochim *et al.*, Science **302**, 2101 (2003); published online 13 November 2003 (www.sciencemag.org/cgi/content/abstract/1093280v1).

[2] M. Greiner, C. A. Regal, and D. S. Jin, Nature (London) **426**, 537 (2003).

[3] M. Zwierlein *et al.*, Phys. Rev. Lett. **91**, 250401 (2003).

[4] T. Bourdel *et al.*, cond-mat/0403091.

[5] A. J. Leggett, in *Modern Trends in the Theory of Condensed Matter*, edited by A. Pekalski and R. Przystawa (Springer-Verlag, Berlin, 1980); P. Nozières and S. Schmitt-Rink, J. Low Temp. Phys. **59**, 195 (1985); M. Drechsler and W. Zwerger, Ann. Phys. (Leipzig) **1**, 15 (1992); E. Timmermans, K. Furuya, P. W. Milonni, and A. K. Kerman, Phys. Lett. A **285**, 228 (2001); M. Holland, S.. J. M. F. Kokkelmans, M. L. Chiofalo, and R. Walser, Phys. Rev. Lett. **87**, 120406 (2001); Y. Ohashi and A. Griffin, Phys. Rev. Lett. **89**, 130402 (2002); R. Combescot, Phys. Rev. Lett. **91**, 120401 (2003); A. Perali, P. Pieri, and G. C. Strinati, Phys. Rev. A **68**, 031601(R) (2003); J. Stajic *et al.*, cond-mat/0309329.

[6] E. Tiesinga, B. J. Verhaar, and H. T. C. Stoof, Phys. Rev. A **47**, 4114 (1993); S. Inouye *et al.*, Nature (London) **392**, 151 (1998).

[7] C. A. Regal, C. Ticknor, J. L. Bohn, and D. S. Jin, Nature (London) **424**, 47 (2003).

[8] J. Cubizolles *et al.*, Phys. Rev. Lett. **91**, 240401 (2003).

[9] K. E. Strecker, G. B. Partridge, and R. G. Hulet, Phys. Rev. Lett. **91**, 080406 (2003).

[10] S. Jochim *et al.*, Phys. Rev. Lett. **91**, 240402 (2003).

[11] L. D. Carr, G. V. Shlyapnikov, and Y. Castin, cond-mat/0308306.

[12] H. Heiselberg, Phys. Rev. A **63**, 043606 (2001).

[13] T.-L. Ho, Phys. Rev. Lett. **92**, 090402 (2004).

[14] K. M. O'Hara *et al.*, Science **298**, 2179 (2002); M. E. Gehm *et al.*, Phys. Rev. A **68**, 011401 (2003).

[15] T. Bourdel *et al.*, Phys. Rev. Lett. **91**, 020402 (2003).

[16] M. Houbiers, H. T. C. Stoof, W. McAlexander, and R. Hulet, Phys. Rev. A **57**, R1497 (1998).

[17] K. M. O'Hara *et al.*, Phys. Rev. A **66**, 041401(R) (2002).

[18] The resonance position is uncertain within a few 10 G.

[19] C. Chin and R. Grimm, cond-mat/0309078.

[20] D. S. Petrov, C. Salomon, and G. V. Shlyapnikov, cond-mat/0309010.

[21] S. Giorgini, L. P. Pitaevskii, and S. Stringari, Phys. Rev. A **54**, R4633 (1996).

[22] S. Stringari, Phys. Rev. Lett. **77**, 2360 (1996).

[23] We fit the density profiles with the function $\rho(z) = \rho_0 (1 - z^2/z_r^2)^\alpha$, where ρ_0, z_r, and $2 \le \alpha \le 2.5$ are free parameters. This function interpolates between the density profile of a pure BEC in the Thomas-Fermi limit with $\alpha = 2$ and a zero-temperature noninteracting or strongly interacting Fermi gas with $\alpha = 2.5$. The rms cloud size z_{rms} is obtained from z_r and α by $z_{rms} = z_r/\sqrt{3 + 2\alpha}$.

[24] G. A. Baker, Phys. Rev. C **60**, 054311 (1999).

[25] J. Carlson, S.-Y. Chang, V. R. Pandharipande, and K. E. Schmidt, Phys. Rev. Lett. **91**, 050401 (2003).

Collective Excitations of a Degenerate Gas at the BEC-BCS Crossover

M. Bartenstein,[1] A. Altmeyer,[1] S. Riedl,[1] S. Jochim,[1] C. Chin,[1] J. Hecker Denschlag,[1] and R. Grimm[1,2]

[1]*Institut für Experimentalphysik, Universität Innsbruck, Technikerstraße 25, 6020 Innsbruck, Austria*
[2]*Institut für Quantenoptik und Quanteninformation, Österreichische Akademie der Wissenschaften, 6020 Innsbruck, Austria*
(Received 29 March 2004; published 19 May 2004)

We study collective excitation modes of a fermionic gas of ^{6}Li atoms in the BEC-BCS crossover regime. While measurements of the axial compression mode in the cigar-shaped trap close to a Feshbach resonance confirm theoretical expectations, the radial compression mode shows surprising features. In the strongly interacting molecular BEC regime, we observe a negative frequency shift with increasing coupling strength. In the regime of a strongly interacting Fermi gas, an abrupt change in the collective excitation frequency occurs, which may be a signature for a transition from a superfluid to a collisionless phase.

The crossover from a Bose-Einstein condensate (BEC) to a Bardeen-Cooper-Schrieffer (BCS) superfluid has for decades attracted considerable attention in many-body theory [1]. Bose-Einstein condensates of molecules formed by fermionic atoms of ^{6}Li and ^{40}K [2–5] provide a unique system to experimentally explore this BEC-BCS crossover. In such ultracold gases magnetically tuned scattering resonances, known as Feshbach resonances, allow one to control and vary the interaction strength over a very broad range. Recent experiments have entered the crossover regime and yield results on the interaction strength by measuring the cloud size [6] and expansion energy [5]. Moreover, two experiments [7,8] have demonstrated the condensed nature of fermionic atom pairs in the crossover regime.

Important questions are related to superfluidity in the crossover regime [9]. When a molecular BEC is converted into an ultracold Fermi gas [6], one can expect ultralow temperatures and superfluidity to extend far into the Fermi gas regime [10]. Detection tools to probe superfluidity in this regime are therefore requested. The investigation of collective excitation modes [11] is well established as a powerful method to gain insight into the physical behavior of ultracold quantum gases in different regimes of Bose [12] and Fermi gases [13]. A recent paper [14] points out an interesting dependence of the collective frequencies in the BEC-BCS crossover of a superfluid Fermi gas. Superfluidity implies a hydrodynamic behavior which can cause substantial changes in the excitation spectrum and in general very low damping rates. However, in the crossover regime the strong interaction between the particles also results in hydrodynamic behavior in the normal, nonsuperfluid phase. Therefore the interpretation of collective modes in the BEC-BCS crossover in terms of superfluidity is not straightforward and needs careful investigation to identify the different regimes.

In this Letter, we report on measurements of fundamental collective excitation modes in the BEC-BCS crossover for various coupling strengths in the low-temperature limit. In Ref. [2], we have already presented a first measurement of the collective excitation of a molecular BEC in the limit of strong coupling. As described previously [2,6], we work with a spin mixture of ^{6}Li atoms in the two lowest internal states. For exploring different interaction regimes, we use a broad Feshbach resonance, the position of which we determined to 837(5) G [15]. The different interaction regimes can be characterized by the coupling parameter $1/(k_F a)$, where a represents the atom-atom scattering length and k_F is the Fermi wave number. Well below the Feshbach resonance ($B < 700$ G), we can realize the molecular BEC regime with $1/(k_F a) \gg 1$. On resonance, we obtain the unitarity-limited regime of a universal fermionic quantum gas with $1/(k_F a) = 0$ [16]. An interacting Fermi gas of atoms is realized beyond the resonance where $1/(k_F a) < 0$.

The starting point of our experiments is a cigar-shaped molecular BEC produced by evaporative cooling in an optical dipole trap in the same way as described in Ref. [6]. Radially the sample is confined by a 35-mW laser beam (wavelength 1030 nm) focused to a waist of 25 μm. The radial vibration frequency is $\omega_r \approx 2\pi \times 750$ Hz. The axial vibration frequency is $\omega_z = 2\pi \times (601B/\text{kG} + 11)^{1/2}$ Hz, where the predominant contribution stems from magnetic confinement caused by the curvature of the Feshbach tuning field B, and a very small additional contribution arises from the weak axial optical trapping force.

For exploring collective excitations in the BEC-BCS crossover regime, we ramp the magnetic field from the evaporation field of 764 G, where the molecular BEC is formed, to fields between 676 and 1250 G within 1 s. In previous work [6], we have shown that the conversion to an atomic Fermi gas proceeds in an adiabatic and reversible way, i.e., without increase of entropy. From the condensate fraction in the BEC limit, for which we measure more than 90% [6], we can give upper bounds for the temperature in both the BEC limit and the noninteracting Fermi gas limit of $T < 0.46T_{\text{BEC}}$ and $T < 0.03T_F$ [10], respectively. Here T_{BEC} (T_F) denotes the

critical temperature (Fermi temperature). With a total number of atoms $N \approx 4 \times 10^5$ (free atoms and atoms bound to molecules) and a geometrically averaged trap frequency at 837 G of $\bar{\omega} = (\omega_r^2 \omega_z)^{1/3} \approx 2\pi \times 230 \, \text{Hz}$, we calculate a Fermi energy $E_F = \hbar^2 k_F^2/2m = \hbar\bar{\omega}(3N)^{1/3} = k_B \times 1.2 \, \mu\text{K}$ for a noninteracting cloud, where m is the mass of an atom and k_B is Boltzmann's constant.

To excite the *axial* compression mode at a given magnetic field, we increase the optical confinement in a 10-ms time interval by a factor of 1.5. The laser power is varied slow enough for the radial motion to follow adiabatically, but fast enough to induce axial oscillations. The relative amplitude of the resulting axial oscillation is kept small, typically $\sim 10\%$. We observe the oscillation by *in situ* imaging of the cloud [6] after a variable hold time t at constant trap parameters. To determine the collective oscillation frequency Ω_z and the damping rate Γ_z, we fit a damped harmonic oscillation $z(t) = z_0 + A_z \exp(-\Gamma_z t) \times \sin(\Omega_z t + \phi_z)$ to the observed time evolution of the cloud size, where z_0, A_z, and ϕ_z are additional fit parameters.

The measured oscillation frequencies and damping rates are shown in Fig. 1. The data are normalized to the axial trap frequency ω_z, as determined by excitation of the axial sloshing mode. We point out that the axial confinement is harmonic because of the dominant magnetic trapping, and we can measure ω_z with a 10^{-3} precision. In the BEC limit, the measured collective fre-

FIG. 1 (color online).   Measured frequency Ω_z and damping rate Γ_z of the axial compression mode, normalized to the trap frequency ω_z. In the upper graph, the dashed lines indicate the BEC limit of $\Omega_z/\omega_z = \sqrt{5/2}$ and the collisionless Fermi gas limit with $\Omega_z/\omega_z = 2$. The insets show the data in the resonance region. Here the vertical dotted line indicates the resonance position at 837(5) G. The star marks the theoretical prediction of $\Omega_z/\omega_z = \sqrt{12/5}$ in the unitarity limit. In the lower inset, the dotted line is a third-order polynomial fit to the data.

quencies are in agreement with the expected $\Omega_z/\omega_z = \sqrt{5/2} = 1.581$ [11,17]. With increasing magnetic field, we observe a decrease in the collective excitation frequency until a minimum is reached at about 900 G, i.e., in the regime of a strongly interacting Fermi gas where $1/(k_F a) \approx -0.5$. With further increasing magnetic field and decreasing interaction strength, we then observe a gradual increase of the collective frequency toward $\Omega_z/\omega_z = 2$. The latter value is expected for a collisionless degenerate Fermi gas, where the elastic collision rate is strongly reduced by Pauli blocking. Because of the large damping rates in the transition regime between hydrodynamic and collisionless behavior, the excitation frequencies cannot be determined with high accuracy. The observed axial damping is consistent with a gradual transition between these two regimes [18].

The insets of Fig. 1 show a zoom-in of the data for the resonance region between 750 and 900 G. The collective frequency that we measure on resonance exhibits the small 2% down-shift expected for the unitarity limit ($\Omega_z/\omega_z = \sqrt{12/5} = 1.549$) [14]. For the damping rate, we observe a clear minimum at a magnetic field of 815(10) G, which is close to the resonance position. It is interesting to note that this damping minimum coincides with the recent observation of a maximum fraction of condensed fermionic atom pairs in Ref. [18]. For the minimum damping rate, we obtain the very low value of $\Gamma_z/\omega_z \approx 0.0015$, which corresponds to a $1/e$ damping time of ~ 5 s.

To excite the *radial* compression mode, we reduce the optical confinement for 50 μs, which is short compared with the radial oscillation period of 1.3 ms. In this short interval the cloud slightly expands radially, and then begins to oscillate when the trap is switched back to the initial laser power. The relative oscillation amplitude is $\sim 10\%$. To detect the radial oscillation, we turn off the trapping laser after various delay times t and measure the radial size $r(t)$ after 1.5 ms of expansion. The measured radial size $r(t)$ reflects the oscillating release energy. From the corresponding experimental data, we extract the excitation frequency Ω_r and damping Γ_r by fitting the radial cloud size to $r(t) = r_0 + A_r \exp(-\Gamma_r t)\sin(\Omega_r t + \phi_r)$, where r_0, A_r, and ϕ_r are additional fit parameters. Typical radial oscillation curves are shown in Fig. 2.

The magnetic-field dependence of the radial excitation frequency Ω_r and the damping rate Γ_r is shown in Fig. 3. Here we normalize the data to the trap frequency ω_r, which we obtain by measuring the radial sloshing mode at the given magnetic field [19]. This normalization suppresses anharmonicity effects in the measured compression mode frequency to below 3% [21]. For low magnetic fields, the measured frequency ratio approaches the BEC limit [11,22] ($\Omega_r/\omega_r = 2$). With increasing magnetic field, i.e., increasing interaction strength, we observe a large down-shift of the frequency. On resonance ($B = 837$ G), we observe $\Omega_r/\omega_r = 1.62(2)$. Above resonance, i.e., with the gas entering the strongly interacting Fermi
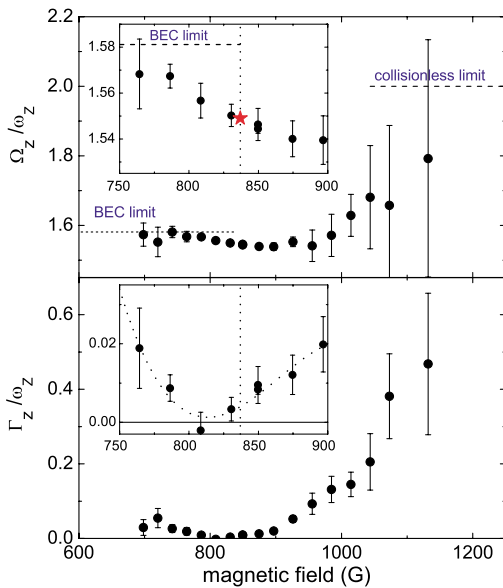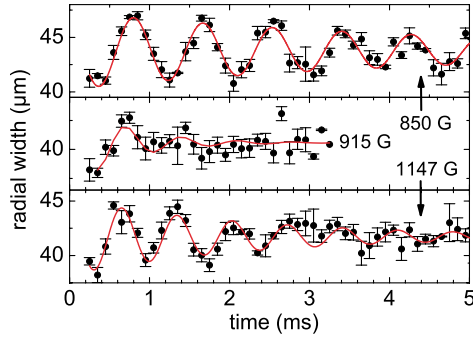
FIG. 2 (color online). Oscillations of the radial compression mode at different magnetic fields in the strongly interacting Fermi gas regime. The solid lines show fits by damped harmonic oscillations.

gas regime, the oscillation frequency further decreases until a maximum shift of almost 30% $[\Omega_r/\omega_r = 1.42(5)]$ is reached at $B = 890$ G. With further increasing magnetic field, i.e., decreasing interaction strength, an abrupt change to $\Omega_r/\omega_r \approx 2$ is observed. For $B > 920$ G our data are consistent with a Fermi gas in the collisionless regime. The damping of the radial compression mode is small in the BEC limit and reaches a minimum close to the unitarity regime. At $B = 910$ G, where the abrupt change occurs, we observe very strong damping (see also middle trace in Fig. 2).

We have performed further experiments to check our data on the radial compression mode for systematic effects. We have repeated the measurements after recompressing the trap to 9 times higher trap laser power
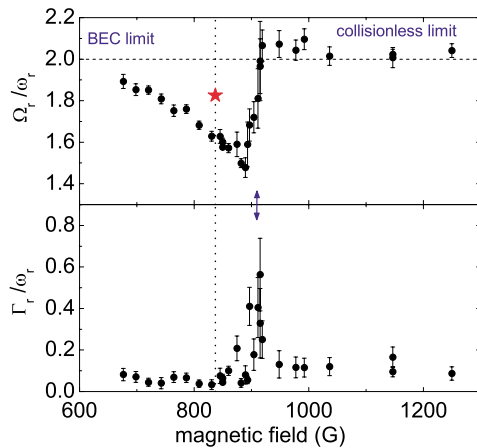

FIG. 3 (color online). Measured frequency Ω_r and damping rate Γ_r of the radial compression mode, normalized to the trap frequency (sloshing mode frequency) ω_r. In the upper graph, the dashed line indicates $\Omega_r/\omega_r = 2$, which corresponds to both the BEC limit and the collisionless Fermi gas limit. The vertical dotted line marks the resonance position at 837(5) G. The star indicates the theoretical expectation of $\Omega_r/\omega_r = \sqrt{10/3}$ in the unitarity limit. A striking change in the excitation frequency occurs at ~910 G (arrow) and is accompanied by anomalously strong damping.

($\omega_r \approx 2.4$ kHz). The corresponding data confirm all our observations in the shallower trap. In particular, the negative frequency shift and the sudden change in the collective frequency show up in essentially the same way. The recompressed trap also allows us to eliminate a small residual anharmonicity shift from our measurement of the collective frequency at 837 G, and we obtain $\Omega_r/\omega_r = 1.67(3)$ for the harmonic trap limit. We have also checked that the frequency of the compression mode in the resonance region does not depend on the way we prepare the ultracold gas. Direct evaporation at a fixed magnetic field, without starting from a molecular BEC, leads to the same collective frequency. Preliminary measurements at higher temperatures, however, show a trend towards smaller frequency shifts in the radial compression mode and to smoother changes of the collective frequency.

Our measurements on the radial compression mode show *three surprises*. The corresponding features, which we discuss in the following, cannot be explained on the basis of available theoretical models and suggest new physics in the BEC-BCS crossover regime.

Surprise one.—For a strongly interacting BEC, Ref. [23] has predicted up-shifts of the collective frequencies with increasing coupling strength based on beyond mean-field theory corrections [24]. Applying these predictions to a molecular BEC in the crossover regime, the collective excitation frequencies should follow $\delta\Omega_i/\Omega_i = c_i\sqrt{n_m a_m^3}$ ($i = z, r$), where n_m is the peak molecular number density and $a_m = 0.6a$ [25] is the molecule-molecule scattering length. For our highly elongated trap geometry, the numerical factors are $c_r = 5c_z = 0.727$. In contrast to these expectations, we observe a strong frequency down-shift in the radial direction. Using the above formula to fit the first four data points, we obtain a negative coefficient of $c_r = -1.2(3)$. For the axial oscillation we obtain $c_z = -0.04(5)$. Note that a substantial down-shift in radial direction is observed even at the low magnetic field of 676 G where the molecular gas parameter is relatively small ($n_m a_m^3 = 0.001$). Apparently, the beyond mean-field theory of a BEC is not adequate to describe the transition from a molecular BEC to a strongly interacting gas in the BEC-BCS crossover.

Surprise two.—The universal character of the strongly interacting quantum gas on resonance suggests a simple equation of state for which one expects $\Omega_z/\omega_z = \sqrt{12/5} = 1.549$ and $\Omega_r/\omega_r = \sqrt{10/3} = 1.826$ for the collective excitation frequencies [14]. While our measurements confirm the predicted axial frequency, we obtain a different frequency in the radial direction of $\Omega_r/\omega_r = 1.67(3)$.

Surprise three.—The abrupt change of the excitation frequency and the large damping rate are not expected in a normal degenerate Fermi gas, where the collective excitation frequency is expected to vary smoothly from the hydrodynamic regime to the collisionless one. Furthermore, for the damping rate of the radial mode in the

transition regime, a maximum value of $\Gamma_r/\omega_r = 0.09$ is calculated in Ref. [18]. Our measured damping rate of $\Gamma_r/\omega_r \approx 0.5$ is clearly inconsistent with this prediction for the normal (nonsuperfluid) hydrodynamic regime. However, both the sudden change of the collective frequency and a strong damping are expected for a transition from the superfluid to the normal phase [26].

In conclusion, our experiments demonstrate that the collective modes of a degenerate gas in the BEC-BCS crossover region show a pronounced dependence on the coupling strength and thus provide valuable information on the physical behavior of the system. For the axial compression mode, the frequency shift observed in the unitarity limit confirms theoretical expectations. However, the radial compression mode reveals a surprising behavior. In the strongly interacting BEC regime, the observed frequency shifts have an opposite sign as compared to expectations from beyond mean-field theory and the frequency shift on resonance is even larger than expected. The most striking feature is an abrupt change of the radial collective frequency in the regime of a strongly attractive Fermi gas where $1/(k_F a) \approx -0.5$. The transition is accompanied by very strong damping. The observation supports an interpretation in terms of a transition from a hydrodynamic to a collisionless phase. A superfluid scenario for the hydrodynamic case seems plausible in view of current theories on resonance superfluidity [9] and the very low temperatures provided by the molecular BEC [10]. A definite answer, however, to the sensitive question of superfluidity requires further careful investigations, e.g., on the temperature dependence of the phase transition.

Note added.—A recent paper by John Thomas' group [27] reports on measurements of the radial compression mode in the resonance region, which show much weaker frequency shifts than we observe. This apparent discrepancy needs further investigation.

[1] A. J. Leggett, in *Modern Trends in the Theory of Condensed Matter*, edited by A. Pekalski and R. Przystawa (Springer-Verlag, Berlin, 1980); P. Nozières and S. Schmitt-Rink, J. Low Temp. Phys. **59**, 195 (1985); E. Timmermans, K. Furuya, P. W. Milonni, and A. K. Kerman, Phys. Lett. A **285**, 228 (2001); J. N. Milstein, S. J. J. M. F. Kokkelmans, and M. J. Holland, Phys. Rev. A **66**, 043604 (2002); Y. Ohashi and A. Griffin, Phys. Rev. Lett. **89**, 130402 (2002); R. Combescot, Phys. Rev. Lett. **91**, 120401 (2003); A. Perali, P. Pieri, and G. C. Strinati, Phys. Rev. A **68**, 031601(R) (2003); J. Stajic *et al.*, cond-mat/0309329.

[2] S. Jochim *et al.*, Science **302**, 2101 (2003).

[3] M. Greiner, C. A. Regal, and D. S. Jin, Nature (London) **426**, 537 (2003).

[4] M. W. Zwierlein *et al.*, Phys. Rev. Lett. **91**, 250401 (2003).

[5] T. Bourdel *et al.*, cond-mat/0403091.

[6] M. Bartenstein *et al.*, Phys. Rev. Lett. **92**, 120401 (2004).

[7] C. A. Regal, M. Greiner, and D. S. Jin, Phys. Rev. Lett. **92**, 040403 (2004).

[8] M. W. Zwierlein *et al.*, Phys. Rev. Lett. **92**, 120403 (2004).

[9] M. Holland *et al.*, Phys. Rev. Lett. **87**, 120406 (2001).

[10] L. D. Carr, G. V. Shlyapnikov, and Y. Castin, Phys. Rev. Lett. **92**, 150404 (2004).

[11] S. Stringari, Phys. Rev. Lett. **77**, 2360 (1996).

[12] L. Pitaevski and S. Stringari, *Bose-Einstein Condensation* (Clarendon, Oxford, 2003), and references therein.

[13] G. M. Bruun and C. W. Clark, Phys. Rev. Lett. **83**, 5415 (1999); G. M. Bruun and B. R. Mottelson, Phys. Rev. Lett. **87**, 270403 (2001); A. Minguzzi and M. P. Tosi, Phys. Rev. A **63**, 023609 (2001).

[14] S. Stringari, Europhys. Lett. **65**, 749 (2004).

[15] We determined the resonance position by measuring the molecular binding energy using radio-frequency spectroscopy as introduced in C. A. Regal, C. Ticknor, J. L. Bohn, and D. S. Jin, Nature (London) **424**, 47 (2003).

[16] H. Heiselberg, Phys. Rev. A **63**, 043606 (2001).

[17] M.-O. Mewes *et al.*, Phys. Rev. Lett. **77**, 988 (1996).

[18] L. Vichi, J. Low Temp. Phys. **121**, 177 (2000).

[19] We excite the radial sloshing mode by pulsed application of a vertical magnetic gradient. With increasing magnetic field and, thus, increasing radial cloud size, the anharmonicity of the Gaussian-shaped radial potential leads to a decrease of the sloshing mode frequency. For $\omega_r/2\pi$, we observe a corresponding decrease from 765 Hz at 676 G to 710 Hz at magnetic fields above 1.2 kG; at 837 G we obtain 740 Hz. Our measurements of the sloshing mode frequency agree well with an expected scaling of the lowest-order anharmonicity correction with the squared cloud size [20].

[20] S. Stringari (private communication).

[21] The anharmonicity corrections to frequencies of both the compression mode (Ω_r) and the sloshing mode (ω_r) scale in the same way with the increasing cloud size with a slightly larger prefactor for the compression mode [20]. Our normalization Ω_r/ω_r reduces the anharmonicity effect by typically a factor of 5.

[22] F. Chevy *et al.*, Phys. Rev. Lett. **88**, 250402 (2002).

[23] L. Pitaevski and S. Stringari, Phys. Rev. Lett. **81**, 4541 (1998).

[24] T. D. Lee, K. W. Huang, and C. N. Yang, Phys. Rev. **106**, 1135 (1957).

[25] D. S. Petrov, C. Salomon, and G. V. Shlyapnikov, cond-mat/0309010.

[26] M. A. Baranov and D. S. Petrov, Phys. Rev. A **62**, 041601 (2000).

[27] J. Kinast *et al.*, Phys. Rev. Lett. **92**, 150402 (2004).

16. A. vanOtterlo et al., Phys. Rev. B **52**, 16176 (1995).
17. G. Schmid, S. Todo, M. Troyer, A. Dorneich, Phys. Rev. Lett. **88**, 167208 (2002).
18. A. Görlitz, Phys. Rev. Lett. **87**, 130402 (2001).
19. M. Greiner, I. Bloch, O. Mandel, T. W. Hänsch, T. Esslinger, Appl. Phys. B **73**, 769 (2001).
20. M. T. DePue, C. McCormick, S. L. Winoto, S. Oliver, D. S. Weiss, Phys. Rev. Lett. **82**, 2262 (1999).
21. B. L. Tolra et al., Phys. Rev. Lett. **92**, 190401 (2004).
22. H. Moritz, T. Söferle, M. Köhl, T. Esslinger, Phys. Rev. Lett. **91**, 250402 (2003).
23. T. Söferle, H. Moritz, C. Schori, M. Köhl, T. Esslinger, Phys. Rev. Lett. **92**, 130403 (2004).
24. B. Paredes et al., Nature **429**, 277 (2004).
25. V. Dunjko, V. Lorent, M. Olshanii, Phys. Rev. Lett. **86**, 5413 (2001).
26. M. Greiner, O. Mandel, T. Esslinger, T. W. Hänsch, I. Bloch, Nature **415**, 39 (2002).
27. T. Kinoshita, T. Wenger, D. S. Weiss, in preparation.
28. D. J. Han, M. T. DePue, D. S. Weiss, Phys. Rev. A **63**, 023405 (2001).
29. M. T. DePue, S. L. Winoto, D. J. Han, D. S. Weiss, Opt. Commun. **180**, 73 (2000).
30. S. L. Winoto, M. T. DePue, N. E. Bramall, D. S. Weiss, Phys. Rev A, **59**, R19 (1999).
31. We thank M. Olshanii, K. Gibble, and J. Banavar for useful discussions and V. Dunjko for providing us with the exact 1D Bose gas theory curves. This work was supported by the NSF grant no. PHY-0137477.

Observation of the Pairing Gap in a Strongly Interacting Fermi Gas

C. Chin,[1] M. Bartenstein,[1] A. Altmeyer,[1] S. Riedl,[1] S. Jochim,[1] J. Hecker Denschlag,[1] R. Grimm[1,2]*

We studied fermionic pairing in an ultracold two-component gas of ^{6}Li atoms by observing an energy gap in the radio-frequency excitation spectra. With control of the two-body interactions through a Feshbach resonance, we demonstrated the dependence of the pairing gap on coupling strength, temperature, and Fermi energy. The appearance of an energy gap with moderate evaporative cooling suggests that our full evaporation brought the strongly interacting system deep into a superfluid state.

The spectroscopic observation of a pairing gap in the 1950s marked an important experimental breakthrough in research on superconductivity (*1*). The gap measurements provided a key to investigating the paired nature of the particles responsible for the frictionless current in metals at very low temperatures. The ground-breaking Bardeen-Cooper-Schrieffer (BCS) theory, developed at about the same time, showed that two electrons in the degenerate Fermi sea can be coupled by an effectively attractive interaction and will form a delocalized, composite particle with bosonic character. BCS theory predicted that the gap in the low-temperature limit is proportional to the critical temperature T_c for the phase transition, in agreement with the experimental measurements. In general, the physics of superconductivity and superfluidity go far beyond the weak-coupling limit of BCS theory. In the limit of strong coupling, paired fermions form localized bosons, and the system can undergo Bose-Einstein condensation (BEC). The BCS limit and the BEC limit are connected by a smooth BCS-BEC crossover, which has been a subject of great theoretical interest for more than three decades (*2–5*). The formation of pairs generally represents a key ingredient of superfluidity in fermionic sys-tems, and the gap energy is a central quantity to characterize the pairing regime.

The rapid progress in experiments with ultracold degenerate Fermi gases (*6*) has opened up a unique testing ground to study phenomena related to pairing and superfluidity at densities typically a billion times below the ones in usual condensed-matter systems. In cold-atom experiments, magnetically tuned scattering resonances (Feshbach resonances) serve as a powerful tool to control the two-body coupling strength in the gas (*7*). On the basis of such a resonance, a strongly interacting degenerate Fermi gas was recently realized (*8*). A major breakthrough then followed, with the creation of Bose-Einstein condensates of molecular dimers composed of fermionic atoms (*9–13*), which corresponds to the realization of a BEC-type superfluid in the strong coupling limit. By variation of the coupling strength, subsequent experiments (*12, 14–18*) began to explore the crossover to a BCS-type system. This BEC-BCS crossover is closely linked to the predicted "resonance superfluidity" (*19–22*) and a "universal" behavior of a Fermi gas with resonant interactions (*23, 24*). The observation of the condensation of atom pairs (*15, 16*) and measurements of collective oscillations (*17, 18*) support the expected superfluidity at presently attainable temperatures in Fermi gases with resonant interactions.

We prepared our ultracold gas of fermionic ^{6}Li atoms in a balanced spin-mixture of the two lowest sub-states $|1\rangle$ and $|2\rangle$ of the electronic $1s^2 2s$ ground state, employing methods of laser cooling and trapping and subsequent evaporative cooling (*9*). A magnetic field B in the range between 650 to 950 G was applied for Feshbach tuning through a broad resonance centered at the field $B_0 \approx 830$ G. In this high-field range, the three lowest atomic levels form a triplet of states $|1\rangle$, $|2\rangle$, and $|3\rangle$, essentially differing by the orientation of the nuclear spin ($m_I = 1, 0, -1$, where m_I is the nuclear magnetic quantum number). In the resonance region with $B < B_0$, the s-wave scattering length a for collisions between atoms in states $|1\rangle$ and $|2\rangle$ is positive. Here, two-body physics supports a weakly bound molecular state with a binding energy $E_b = \hbar^2/(ma^2)$, where $\hbar$ is Planck's constant h divided by 2π and m is the atomic mass. Molecules formed in this state can undergo BEC (*9–13*). At $B = B_0$, the two-body interaction is resonant ($a \to \pm\infty$), corresponding to a vanishing binding energy of the molecular state. Beyond the resonance ($B > B_0$), the scattering length is negative ($a < 0$), which leads to an effective attraction. Here, two-body physics does not support a weakly bound molecular level, and pairing can only occur because of many-body effects.

Our experimental approach (*9, 14*) facilitated preparation of the quantum gas in various regimes with controlled temperature, Fermi energy, and interaction strength. We performed evaporative cooling under conditions (*25*) in which an essentially pure molecular Bose-Einstein condensate containing $N = 4 \times 10^5$ paired atoms could be created as a starting point for the experiments. The final laser power of the evaporation ramp allowed us to vary the temperature T. The Fermi energy E_F (Fermi temperature $T_F = E_F/k_B$, with Boltzmann's constant k_B) was controlled by a recompression of the gas, which we performed by increasing the trap laser power after the cooling process (*25*). We then varied the interaction strength by slowly changing the magnetic field to the desired final value. The adiabatic changes applied to the gas after evaporative cooling proceeded with conserved entropy (*14*). Lacking a reliable method to determine the temperature T of a deeply degenerate, strongly interacting Fermi gas in a direct way, we characterized the system by the temperature T' measured after an isentropic conversion into the BEC limit (*25*). For

[1]Institut für Experimentalphysik, Universität Innsbruck, Technikerstraße 25, 6020 Innsbruck, Austria. [2]Institut für Quantenoptik und Quanteninformation, Österreichische Akademie der Wissenschaften, 6020 Innsbruck, Austria.

*To whom correspondence should be addressed. E-mail: rudolf.grimm@uibk.ac.at

a deeply degenerate Fermi gas, the true temperature T is substantially below our observable T' (*25, 26*), but a general theory for this relation is not yet available.

Radio-frequency (RF) spectroscopy has been introduced as a powerful tool to study interaction effects in ultracold Fermi gases (*27–29*). Molecular binding energies have been measured for ^{40}K atoms (*29*), for which the potential of the method to observe fermionic pairing gap energies has also been pointed out. RF spectroscopy has been applied to ^{6}Li atoms to study interaction effects up to magnetic fields of 750 G (*28*). One important observation was the absence of mean-field shifts in the strongly interacting regime. This effect can be attributed to the fact that, in the relevant magnetic-field range, all s-wave scattering processes between ^{6}Li atoms in the states $|1\rangle$, $|2\rangle$, and $|3\rangle$ are simultaneously unitarity-limited. This property of ^{6}Li is very favorable for RF spectroscopy because it suppresses shifts and broadening by mean-field effects.

We drove RF transitions from state $|2\rangle$ to the empty state $|3\rangle$ at ~80 MHz and monitored the loss of atoms in state $|2\rangle$ after weak excitation by a 1-s RF pulse, using state-selective absorption imaging (*14*). Our experiment was optimized to obtain a resolution of ~100 Hz, corresponding to an intrinsic sensitivity to interaction effects on the scale of ~5 nK, which is more than two orders of magnitude below the typical Fermi temperatures.

We recorded RF spectra for different degrees of cooling and in various coupling regimes (Fig. 1). We realized the molecular regime at $B = 720$ G ($a = +120$ nm). For the resonance region, we examined two different magnetic fields, because the precise resonance location B_0 is not exactly known. Our two values $B = 822$ G (*16*) and 837 G (*13, 18*) may be considered as lower and upper bounds for B_0. We also studied the regime beyond the resonance with a large negative scattering length at $B = 875$ G ($a \approx -600$ nm). Spectra taken in a "hot" thermal sample at $T \approx 6T_F$ (where $T_F = 15$ μK) show the narrow atomic $|2\rangle \rightarrow |3\rangle$ transition line (Fig. 1, top) and serve as a frequency reference. We present our spectra as a function of the RF offset with respect to the bare atomic transition frequency.

Spectral signatures of pairing have been theoretically considered (*30–34*). A clear signature of the pairing process is the emergence of a double-peak structure in the spectral response as a result of the coexistence of unpaired and paired atoms. The pair-related peak is located at a higher frequency than the unpaired-atoms signal, because energy is required for pair breaking. For understanding of the spectra, both the homogeneous line shape of the pair signal (*31, 33*) and the inhomogeneous line broadening due to the density distribution in the harmonic trap need to be taken into account

(*34*). As an effect of inhomogeneity, fermionic pairing due to many-body effects takes place predominantly in the central high-density region of the trap, and unpaired atoms mostly populate the outer region of the trap where the density is low (*34–36*). The spectral component corresponding to the pairs thus shows a large inhomogeneous broadening in addition to the homogeneous width of the pair-breaking signal. For the unpaired atoms, the homogeneous line is narrow and the effects of inhomogeneity and mean-field shifts are negligible. These arguments explain why the RF spectra in general show a relatively sharp peak for the unpaired atoms together with a broader peak attributed to the pairs.

We observed clear double-peak structures already at $T'/T_F = 0.5$, which we obtained with moderate evaporative cooling down to a laser power of $P = 200$ mW (Fig. 1, middle, $T_F = 3.4$ μK). In the molecular regime $B = 720$ G, the sharp atomic peak was well separated from the broad dissociation signal (*29*), which showed a molecular binding energy of $E_b = h \times 130$ kHz $= k_B \times 6.2$ μK. For $B \rightarrow B_0$, the peaks began to overlap. In the resonance region [822 G and 837 G (Fig. 1)], we still observed a relatively narrow atomic peak at the original position together with a pair signal. For magnetic fields beyond the resonance, we could resolve the double-peak structure for fields up to ~900 G.

For $T'/T_F < 0.2$, realized with a deep evaporative cooling ramp down to an optical

trap power of $P = 3.8$ mW, we observed the disappearance of the narrow atomic peak in the RF spectra (Fig. 1, bottom, $T_F = 1.2$ μK). This shows that essentially all atoms were paired. In the BEC limit (720 G), the dissociation line shape is identical to the one observed in the trap at higher temperature and Fermi energy. Here the localized pairs are molecules with a size much smaller than the mean interparticle spacing, and the dissociation signal is independent of the density. In the resonance region [822 G and 837 G (Fig. 1)], the pairing signal shows a clear dependence on density (Fermi energy), which becomes even more pronounced beyond the resonance (875 G). We attribute this to the fact that the size of the pairs becomes comparable to or larger than the interparticle spacing. In addition, the narrow width of the pair signal in this regime (Fig. 1, bottom, $B = 875$ G) indicates a pair localization in momentum space to well below the Fermi momentum $\hbar k_F = \sqrt{2mE_F}$ and thus a pair size exceeding the interparticle spacing.

To quantitatively investigate the crossover from the two-body molecular regime to the fermionic many-body regime, we measured the pairing energy in a range between 720 and 905 G. The measurements were performed after deep evaporative cooling ($T'/T_F < 0.2$) for two different Fermi temperatures, $T_F = 1.2$ μK and $T_F = 3.6$ μK (Fig. 2). As an effective pairing gap, we defined $\Delta\nu$ as the frequency difference between the pair-signal maximum and the bare atomic resonance. In the BEC limit, the effec-
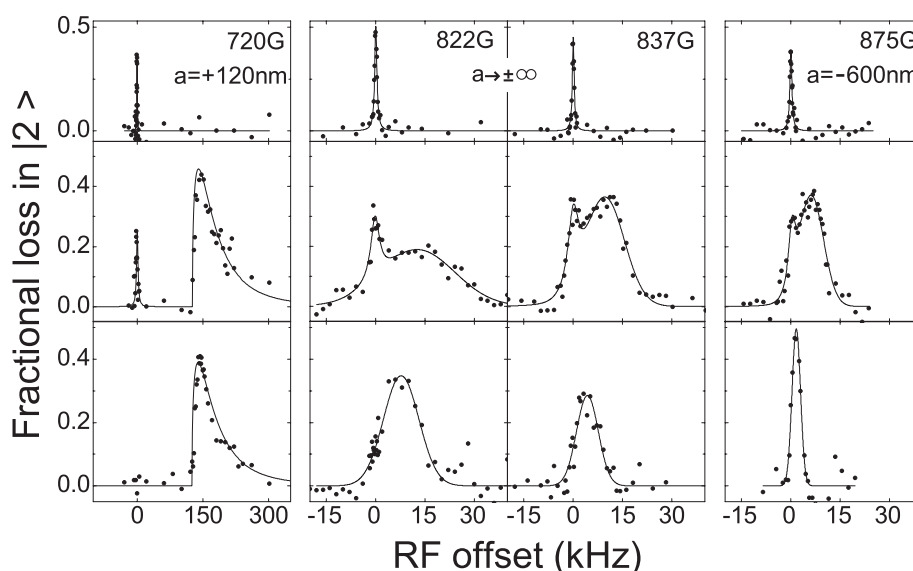
Fig. 1. RF spectra for various magnetic fields and different degrees of evaporative cooling. The RF offset ($k_B \times 1$ μK $\cong h \times 20.8$ kHz) is given relative to the atomic transition $|2\rangle \rightarrow |3\rangle$. The molecular limit is realized for $B = 720$ G (first column). The resonance regime is studied for $B = 822$ G and $B = 837$ G (second and third columns). The data at 875 G (fourth column) explore the crossover on the BCS side. Top row, signals of unpaired atoms at $T' \approx 6T_F$ ($T_F = 15$ μK); middle row, signals for a mixture of unpaired and paired atoms at $T' = 0.5T_F$ ($T_F = 3.4$ μK); bottom row, signals for paired atoms at $T' < 0.2T_F$ ($T_F = 1.2$ μK). The true temperature T of the atomic Fermi gas is below the temperature T', which we measured in the BEC limit. The solid lines are introduced to guide the eye.

1129
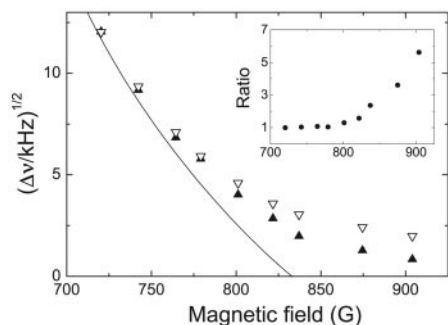
Fig. 2. Measurements of the effective pairing gap $\Delta\nu$ as a function of the magnetic field B for deep evaporative cooling and two different Fermi temperatures, $T_F = 1.2$ μK (solid symbols) and 3.6 μK (open symbols). The solid line shows $\Delta\nu$ for the low-density limit, where it is essentially given by the molecular binding energy (25). Inset: The ratio of the effective pairing gaps measured at the two different Fermi energies.

tive pairing gap $\Delta\nu$ simply reflects the molecular binding energy E_b (Fig. 2, solid line) (25). With an increasing magnetic field, in the BEC-BCS crossover, $\Delta\nu$ shows an increasing deviation from this low-density molecular limit and smoothly evolves into a density-dependent many-body regime where $h\Delta\nu < E_F$.

A comparison of the pairing energies at the two different Fermi energies (Fig. 2, inset) provides further insight into the nature of the pairs. In the BEC limit, $\Delta\nu$ is solely determined by E_b and thus does not depend on E_F. In the universal regime on resonance, E_F is the only energy scale, and we indeed observed the effective pairing gap $\Delta\nu$ to increase linearly with the Fermi energy. We found a corresponding relation $h\Delta\nu \approx 0.2$ E_F. Beyond the resonance, where the system is expected to change from a resonant to a BCS-type behavior, $\Delta\nu$ was found to depend more strongly on the Fermi energy and the observed gap ratio further increased. We interpret this in terms of the increasing BCS character of pairing, for which an exponential dependence $h\Delta\nu/E_F \propto \exp(-\pi/2k_F|a|)$ is expected.

In a further series of measurements (Fig. 3), we applied a controlled heating method to study the temperature dependence of the gap in a way that allowed us to keep all other parameters constant. After production of a pure molecular Bose-Einstein condensate ($T' < 0.2T_F$) in the usual way, we adiabatically changed the conditions to $B = 837$ G and $T_F = 1.2$ μK. We then increased the trap laser power by a factor of nine (T_F increased to 2.5 μK), using exponential ramps of different durations. For fast ramps, this recompression was nonadiabatic and increased the entropy. By variation of the ramp time, we explored a range from our lowest temperatures up to $T'/T_F = 0.8$. The emergence of the gap with decreasing temperature is clearly visible in the RF spectra (Fig. 3). The marked increase of $\Delta\nu$ for decreasing temperature is
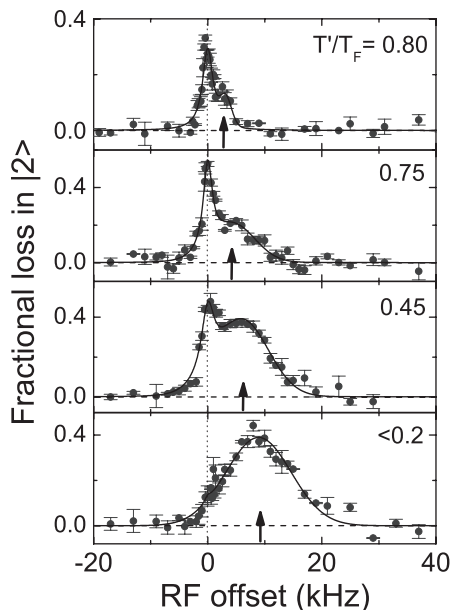
Fig. 3. RF spectra measured at $B = 837$ G and $T_F = 2.5$ μK for different temperatures T' adjusted by controlled heating. The solid lines are fits to guide the eye, using a Lorentzian curve for the atom peak and a Gaussian curve for the pair signal. The vertical dotted line marks the atomic transition, and the arrows indicate the effective pairing gap $\Delta\nu$.

in good agreement with theoretical expectations for the pairing gap energy (5).

The conditions of our experiment were theoretically analyzed for the case of resonant two-body interaction (34). The calculated RF spectra are in agreement with our experimental results and demonstrate how a double-peak structure emerges as the gas is cooled below $T/T_F \approx 0.5$ and how the atomic peak disappears with further decreasing temperature. In particular, the work clarifies the role of the "pseudo-gap" regime (5, 22), in which pairs are formed before superfluidity is reached. According to the calculated spectra, the atomic peak disappears at temperatures well below the critical temperature for the phase-transition to a superfluid. A recent theoretical study of the BCS-BEC crossover at finite temperature (36) predicted the phase-transition to a superfluid to occur at a temperature that on resonance is only ~30% below the point where pair formation sets in.

We have observed fermionic pairing already after moderate evaporative cooling. With much deeper cooling applied, the unpaired atom signal disappeared from our spectra. This observation shows that pairing takes place even in the outer region of the trapped gas where the density and the local Fermi energy are low. Our results thus strongly suggest that a resonance superfluid is formed in the central region of the trap (34). Together with the observations of resonance condensation of fermionic pairs (15, 16) and weak damping of collective excitations (17,

18), our observation of the pairing gap provides a strong case for superfluidity in experiments on resonantly interacting Fermi gases.

References and Notes

1. M. Tinkham, *Introduction to Superconductivity* (McGraw-Hill, New York, ed. 2, 1996).
2. D. M. Eagles, *Phys. Rev.* **186**, 456 (1969).
3. A. J. Leggett, in *Modern Trends in the Theory of Condensed Matter*, A. Pekalski, R. Przystawa, Eds. (Springer-Verlag, Berlin, 1980), pp. 13–27.
4. P. Nozières, S. Schmitt-Rink, *J. Low Temp. Phys.* **59**, 195 (1985).
5. Q. Chen, J. Stajic, S. Tan, K. Levin, in preparation (available at http://arxiv.org/abs/cond-mat/0404274).
6. A. Cho, *Science* **301**, 750 (2003).
7. S. Inouye *et al.*, *Nature* **392**, 151 (1998).
8. K. M. O'Hara, S. L. Hemmer, M. E. Gehm, S. R. Granade, J. E. Thomas, *Science* **298**, 2179 (2002); published online 7 Nov 2002 (10.1126/science.1079107).
9. S. Jochim *et al.*, *Science* **302**, 2101 (2003); published online 13 November 2003 (10.1126/science.1093280).
10. M. Greiner, C. A. Regal, D. S. Jin, *Nature* **426**, 537 (2003).
11. M. W. Zwierlein *et al.*, *Phys. Rev. Lett.* **91**, 250401 (2003).
12. T. Bourdel *et al.*, *Phys. Rev. Lett.* **93**, 050401 (2004).
13. R. Hulet, paper presented at the Kauli Institute for Theoretical Physics Conference on Quantum Gases, Santa Barbara, CA, 10 to 14 May 2004.
14. M. Bartenstein *et al.*, *Phys. Rev. Lett.* **92**, 120401 (2004).
15. C. A. Regal, M. Greiner, D. S. Jin, *Phys. Rev. Lett.* **92**, 040403 (2004).
16. M. W. Zwierlein *et al.*, *Phys. Rev. Lett.* **92**, 120403 (2004).
17. J. Kinast, S. L. Hemmer, M. E. Gehm, A. Turlapov, J. E. Thomas, *Phys. Rev. Lett.* **92**, 150402 (2004).
18. M. Bartenstein *et al.*, *Phys. Rev. Lett.* **92**, 203201 (2004).
19. M. Holland, S. J. J. M. F. Kokkelmans, M. L. Chiofalo, R. Walser, *Phys. Rev. Lett.* **87**, 120406 (2001).
20. E. Timmermans, K. Furuya, P. W. Milonni, A. K. Kerman, *Phys. Lett. A* **285**, 228 (2001).
21. Y. Ohashi, A. Griffin, *Phys. Rev. Lett.* **89**, 130402 (2002).
22. J. Stajic *et al.*, *Phys. Rev. A.* **69**, 063610 (2004).
23. H. Heiselberg, *Phys. Rev. A.* **63**, 043606 (2001).
24. T.-L. Ho, *Phys. Rev. Lett.* **92**, 090402 (2004).
25. Materials and methods are available as supporting material on *Science* Online.
26. L. D. Carr, G. V. Shlyapnikov, Y. Castin, *Phys. Rev. Lett.* **92**, 150404 (2004).
27. C. Regal, D. Jin, *Phys. Rev. Lett.* **90**, 230404 (2003).
28. S. Gupta *et al.*, *Science* **300**, 1723 (2003); published online 8 May 2003 (10.1126/science.1085335).
29. C. A. Regal, C. Ticknor, J. L. Bohn, D. S. Jin, *Nature* **424**, 47 (2003).
30. P. Törmä, P. Zoller, *Phys. Rev. Lett.* **85**, 487 (2000).
31. J. Kinnunen, M. Rodriguez, P. Törmä, *Phys. Rev. Lett.* **92**, 230403 (2004).
32. H. P. Büchler, P. Zoller, W. Zwerger, in preparation (available at http://arxiv.org/abs/cond-mat/0404116).
33. R. B. Diener, T.-L. Ho, in preparation (available at http://arxiv.org/abs/cond-mat/0405174).
34. J. Kinnunen, M. Rodriguez, P. Törmä, *Science* **305**, 1131; published online 22 July 2004 (10.1126/science.1100782).
35. A. Bulgac, in preparation (available at http://arxiv.org/abs/cond-mat/0309358).
36. A. Perali, P. Pieri, L. Pisani, G. C. Strinati, *Phys. Rev. Lett.* **92**, 220404 (2004).
37. We thank P. Törmä for a stimulating exchange of results and very useful discussions and W. Zwerger and H. P. Büchler for many stimulating discussions. Supported by the Austrian Science Fund (FWF) within spezial forschungsbereich 15 (project part 15) and by the European Union in the frame of the Cold Molecules Training and Mobility of Researchers Network under contract no. HPRN-CT-2002-00290. C.C. is a Lise-Meitner research fellow of the FWF.

P H Y S I C A L R E V I E W L E T T E R S

Precise Determination of ^{6}Li Cold Collision Parameters by Radio-Frequency Spectroscopy on Weakly Bound Molecules

M. Bartenstein,[1] A. Altmeyer,[1] S. Riedl,[1] R. Geursen,[1] S. Jochim,[1] C. Chin,[1,*] J. Hecker Denschlag,[1] and R. Grimm[1,2]

[1]*Institut für Experimentalphysik, Universität Innsbruck, Technikerstraße 25, 6020 Innsbruck, Austria*
[2]*Institut für Quantenoptik und Quanteninformation, Österreichische Akademie der Wissenschaften, 6020 Innsbruck, Austria*

A. Simoni,[†] E. Tiesinga, C. J. Williams, and P. S. Julienne

*Atomic Physics Division, National Institute of Standards and Technology,
100 Bureau Drive Stop 8423, Gaithersburg, Maryland 20899, USA*
(Received 28 August 2004; published 18 March 2005)

We employ radio-frequency spectroscopy on weakly bound ^{6}Li$_2$ molecules to precisely determine the molecular binding energies and the energy splittings between molecular states for different magnetic fields. These measurements allow us to extract the interaction parameters of ultracold ^{6}Li atoms based on a multichannel quantum scattering model. We determine the singlet and triplet scattering lengths to be $a_s = 45.167(8)a_0$ and $a_t = -2140(18)a_0$ $(1a_0 = 0.052\,917\,7$ nm), and the positions of the broad Feshbach resonances in the energetically lowest three s-wave scattering channels to be 83.41(15), 69.04(5), and 81.12(10) mT.

Molecular level structure near a collision threshold uniquely determines the scattering properties of ultracold atoms. When a molecular state is tuned near the scattering threshold, the atomic scattering amplitude can be resonantly altered. Magnetically tuned Feshbach resonances [1] in ultracold fermionic gases have recently led to ground-breaking observations, including the condensation of molecules [2−6] and the studies of the crossover physics from a molecular Bose-Einstein condensate (BEC) to atomic Cooper pairs in the Bardeen-Cooper-Schrieffer state (BEC-BCS crossover) [5,7,8]. These studies are of general importance in physics as the ultracold Fermi gas provides a unique model system for other strongly interacting fermionic systems [9].

In spin mixtures of ^{6}Li atoms, a broad Feshbach resonance in the energetically lowest s-wave channel [10] allows for precise interaction tuning. This, together with the extraordinary stability of the system against inelastic decay [2,11], makes ^{6}Li the prime candidate for BEC-BCS crossover studies. A precise knowledge of the magnetic-field dependent scattering properties is crucial for a quantitative comparison of the experimental results with crossover theories. Of particular importance is the precise value of the magnetic field where the s-wave scattering diverges. At this unique point, the strongly interacting fermionic quantum gas is expected to exhibit universal properties [12]. Previous experiments explored the ^{6}Li resonance by measuring inelastic decay [13], elastic collisions [14,15], and the interaction energy [16], but could locate the exact resonance point only to within a range between 80 and 85 mT.

An ultracold gas of weakly bound molecules is an excellent starting point to explore the molecular energy structure near threshold [17]. An improved knowledge on the exact ^{6}Li resonance position was recently obtained in an experiment that observed the controlled dissociation of weakly bound ^{6}Li$_2$ molecules induced by magnetic-field ramps [18]. These measurements provided a lower bound of 82.2 mT for the resonance position. Studies of systematic effects suggested an upper bound of 83.4 mT. Within this uncertainty range, however, we observe the physical behavior of the ultracold gas to exhibit a substantial dependence on the magnetic field [8]. In this Letter, we apply radio-frequency (rf) spectroscopy [17,19] on weakly bound molecules to precisely determine the interaction parameters of cold ^{6}Li atoms. Together with a multichannel quantum scattering model, we obtain a full characterization of the two-body scattering properties, essential for BEC-BCS crossover physics.

The relevant atomic states are the lowest three sublevels in the ^{6}Li ground state manifold, denoted by $|1\rangle$, $|2\rangle$, and $|3\rangle$. Within the magnetic-field range investigated in this experiment, these levels form a triplet of states, essentially differing by the orientation of the nuclear spin ($m_I = 1, 0, -1$). Figure 1 shows the energy level structure of the two scattering channels $|1\rangle + |2\rangle$ and $|1\rangle + |3\rangle$, denoted by $(1, 2)$ and $(1, 3)$, respectively. The broad Feshbach resonance occurs in the $(1, 2)$ channel near 83 mT. When the magnetic field is tuned below the resonance, atoms in the $(1, 2)$ channel can form weakly bound molecules [20]. For the $(1, 3)$ channel, a similar Feshbach resonance [19] occurs near 69 mT.

Starting with molecules formed in the $(1, 2)$ channel, we drive the rf transition to the $(1, 3)$ channel at various magnetic-field values B. The rf excitation can dissociate a molecule into two free atoms (bound-free transition; see Fig. 1) [17] or, for $B < 69$ mT, it can also drive the transition between the molecular states in the $(1, 2)$ and $(1, 3)$ channels (bound-bound transition). In both processes, the rf excitation results in loss of molecules in the
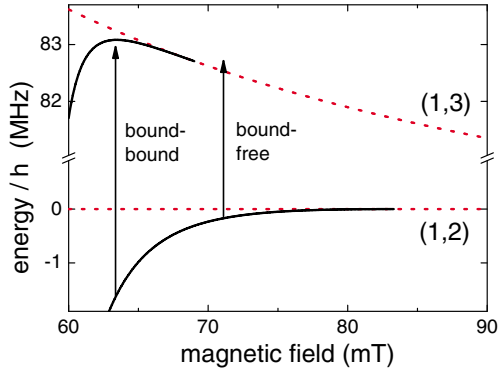
FIG. 1 (color online). Energy level structure near the Li$_2$ dissociation threshold as a function of magnetic field B. The threshold energy of the $(1, 3)$ scattering channel (upper dotted line) is plotted relative to the $(1, 2)$ threshold (lower dotted line). In the $(1, 2)$ channel, a molecular state (lower solid line) exists below the Feshbach resonance at ~ 83 mT. In the $(1, 3)$ channel, another molecular state (upper solid line) exists below the resonance at ~ 69 mT. The bound-free and bound-bound transitions of molecules in the $(1, 2)$ channel are illustrated by the arrows.

$(1, 2)$ channel. This loss constitutes our experimental signal. We perform measurements at different magnetic fields for both the bound-free and the bound-bound transitions.

Our experimental procedure is similar to Ref. [8]. The optically trapped sample is cooled by forced evaporation at a magnetic field of 76.4 mT. With deep cooling we routinely produce a BEC of 2×10^5 molecules [2], which at the lowest trap laser power of 3.8 mW has a peak density of 4×10^{12} cm^{-3}. After evaporation we linearly ramp the field to a specific value between 66 and 72 mT in typically 200 ms. We then apply a single rf pulse for 200 ms with its frequency tuned close to the atomic transition $|2\rangle$ to $|3\rangle$. Following the rf pulse, we apply state-selective absorption imaging, which is sensitive to free atoms in state $|2\rangle$ and molecules in the $(1, 2)$ channel.

To precisely determine the magnetic field, we employ rf spectroscopy on a "hot" thermal sample of 2×10^6 atoms at a temperature $T \approx 90 \ \mu$K (about 6 times the Fermi temperature T_F) with the highest trap laser power of 10.5 W. Under these conditions we do not observe any density-dependent frequency shifts, in agreement with [19]. The rf transition energy then corresponds to the internal energy difference hf_0 between the states $|2\rangle$ and $|3\rangle$, where h is Planck's constant. This energy is magnetic-field dependent and the transition frequency is about 83 MHz in the magnetic-field range we study. The measured transition has a narrow linewidth of less than 1 kHz, and the center position can be determined to within a few hundred Hz. This high resolution allows us to calibrate our magnetic field to an accuracy of a few μT based on the Breit-Rabi formula and the ^{6}Li parameters given in [21].

For bound-free transitions, the molecules in the $(1, 2)$ channel make a transition to the $(1, 3)$ scattering continuum. The excitation rate from a stationary molecule to an atomic scattering state with kinetic energy $2E_k$ is deter-

mined by the Franck-Condon factor between the bound and free wave functions [22]. From energy conservation, $2E_k$ is related to the rf transition energy hf by $hf = hf_0 + E_b + 2E_k$, where E_b is the binding energy of the molecules in the $(1, 2)$ channel. The variation of the Franck-Condon factor with atomic kinetic energy leads to a broad and asymmetric dissociation line shape [22].

Rf dissociation spectra taken at 72.0 and 69.5 mT for a molecular BEC in a weak optical trap are shown in Fig. 2. An important feature of the spectra is the sharp rising edge on the low frequency side. This threshold corresponds to the dissociation of a molecule into two atoms with zero relative momentum. Therefore, the position of the edge relative to the atomic transition directly indicates the molecular binding energy.

We determine the dissociation threshold and thus the molecular binding energy by fitting the full line shape. The line shape function [22] depends on both the $(1, 2)$ molecular binding energy E_b and the scattering length a_{13} in the $(1, 3)$ channel. In the range of magnetic fields we investigate, a_{13} is much larger than the interaction range of the van der Waals potential of $\sim 30 a_0$. The line shape function $P(E)$ is then well approximated by [22]

$$P(E) \propto E^{-2}(E - E_b)^{1/2}(E - E_b + E')^{-1}, \qquad (1)$$

where $E = hf - hf_0$ and $E' = \hbar^2/ma_{13}^2$. From the fits to the experimental data [23], we determine the threshold positions, given in Table I. Together with the atomic transition frequencies, we conclude that the molecular binding energies are $E_b = h \times 134(2)$ kHz at 72.013(4) mT and $E_b = h \times 277(2)$ kHz at 69.483(4) mT.
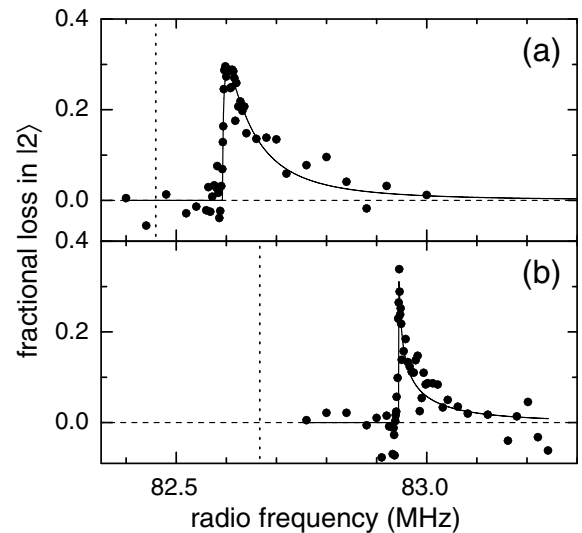

FIG. 2. Bound-free rf spectra at 72.013(4) mT (a) and 69.483(4) mT (b). Fractional loss in state $|2\rangle$ is measured as a function of the radio frequency. The solid lines represent a fit based on Eq. (1). The atomic transition frequencies, which are measured independently, are indicated by the vertical dashed lines.

TABLE I. Comparison between our experimental and theoretical results. The magnetic field B is determined from the measured atomic transition frequency f_0. The molecular transition frequency f_{mol} refers to the resonance peak for bound-bound transitions (upper two rows) or the dissociation threshold (lower two rows). The values in parentheses indicate 1σ uncertainties.

		f_{mol} (MHz)	
B (mT)	f_0 (MHz)	Experimental	Theory
66.1436(20)	82.968 08(20)	83.6645(3)	83.6640(10)
67.6090(30)	82.831 84(30)	83.2966(5)	83.2973(10)
69.4826(40)	82.666 86(30)	82.9438(20)	82.9419(13)
72.0131(40)	82.459 06(30)	82.5928(20)	82.5910(13)

For magnetic field $B < 69$ mT, we can drive the rf transition between the $(1, 2)$ and $(1, 3)$ molecular states. Here, the resonance frequency is given by the energy difference of the two molecular states. To avoid possible systematic mean-field shifts at these lower magnetic fields [19], we prepare a thermal mixture of atoms and molecules with temperature $T \approx T_F$ by a controlled heating method [8]. Rf spectroscopy is performed at 67.6 and 66.1 mT. The bound-bound transition signal at 66.1 mT is shown in Fig. 3. By fitting the narrow transition line with a Lorentzian profile, we determine the resonance frequency; see Table I. Notably, below the resonance in the $(1, 3)$ channel at ~69 mT, the bound-free transition is much weaker due to a Fano-type interference effect [22].

Because of the high precision of the measured transition frequencies, a careful analysis of systematic effects is necessary. Possible systematic shifts include differential light shifts of the two molecular states and density-dependent many-body shifts. In order to characterize these possible systematic errors, we experimentally investigate these shifts by varying the trap depth of the optical potential. In a deeper trap, both the differential light shifts and mean-field shifts are expected to increase. We repeat the
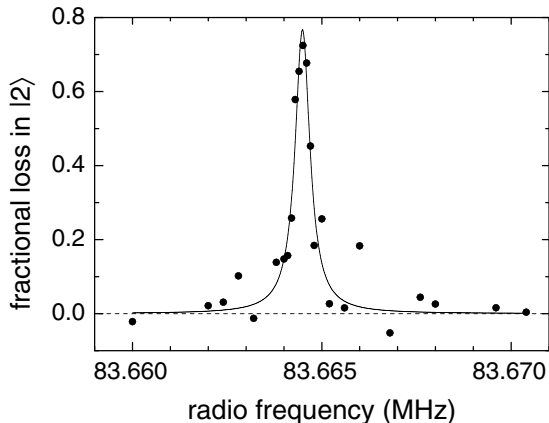

FIG. 3. Bound-bound rf spectrum at 66.144(2) mT. The fractional population loss in state $|2\rangle$ shows a narrow resonance. We determine the center position to be 83.6645(3) MHz from a Lorentzian fit (solid line).

bound-free and bound-bound rf spectroscopy for different trap laser powers in a range between 3.8 and 310 mW. At a typical magnetic field of $B = 69$ mT the peak number density of a molecular BEC is thereby varied between 8×10^{12} cm^{-3} and 5×10^{13} cm^{-3}. Within our statistical uncertainties we do not see any systematic density-dependent shifts.

Given the measured data summarized in Table I, it is possible to predict the location of the scattering resonances in the $(1, 2)$, $(1, 3)$, and $(2, 3)$ channels if we have an accurate theoretical model of the collision. We use a standard multichannel model for the interaction of two ^{2}S atoms with nuclear spin [24] to calculate the scattering lengths and bound state energies for these channels. It is necessary to include s waves only in the basis set, since we find that there is a negligible change within the experimental uncertainties if we also include higher partial waves in the basis set. The interaction potential model is the same as described in Ref. [14]. It uses a combination of Rydberg-Klein-Rees and *ab initio* potentials for the singlet ($^1\Sigma_g^+$) and triplet ($^3\Sigma_u^+$) states at short range and joins them smoothly onto long range potentials based on the exchange [25] and van der Waals dispersion energy [26], the lead term of which is $C_6 = 1393.39(16)$ au (1 au $= 9.573\,44 \times 10^{-26}$ J nm^6). As in Ref. [14], the singlet $^1\Sigma_g^+$ and triplet $^3\Sigma_u^+$ scattering lengths, a_s and a_t, respectively, are varied by making small variations to the inner wall of the potential. Once a_s and a_t are specified, all other scattering and bound state properties for all channels of two ^{6}Li atoms are uniquely determined, including the positions of the resonances. Consequently, varying a_s and a_t to fit the binding energies and energy differences from rf spectroscopy determines the values of these two free parameters.

Fitting the data of the present experiment determines $a_s = 45.167(8)a_0$ and $a_t = -2140(18)a_0$. The uncertainty includes both the uncertainty in the measured value of the magnetic field and the uncertainty in the rf measurements. Our scattering lengths agree within the uncertainties with previous determinations: $a_s = 45.1591(16)a_0$ [18] and $a_t = -2160(250)a_0$ [27]. Table I shows a comparison of the measured and best fit calculated energies. The calculated positions of the broad s-wave resonances for the $(1, 2)$, $(1, 3)$, and $(2, 3)$ channels are 83.41(15), 69.04(5), and 81.12(10) mT, respectively.

Figure 4 shows the scattering lengths calculated for several different channels in the magnetic-field range of interest to BEC-BCS crossover experiments. We find that the formula $a = a_b[1 + \Delta(B - B_0)^{-1}][1 + \alpha(B - B_0)]$ fits the calculated scattering lengths to better than 99% over the range of 60 to 120 mT. This expression includes the standard Feshbach resonance term [28] with the background scattering length a_b, resonance position B_0, and resonance width Δ, and a leading-order correction parametrized by α. The respective values for a_b, B_0, Δ, and α are $-1405a_0$, 83.4149 mT, 30.0 mT, and 0.0040 mT^{-1} for channel $(1, 2)$, $-1727a_0$, 69.043 mT, 12.23 mT, and
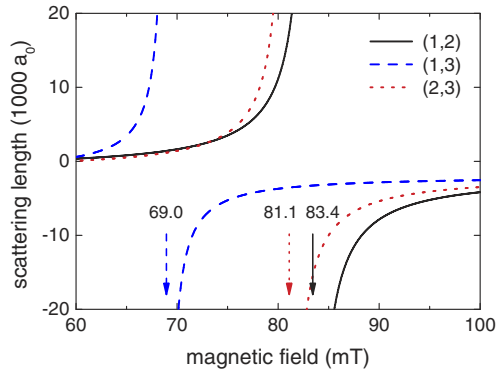
FIG. 4 (color online). Scattering lengths versus magnetic field from multichannel quantum scattering calculations for the (1, 2), (1, 3), and (2, 3) scattering channels. The arrows indicate the resonance positions.

0.0020 mT^{-1} for channel (1, 3), and $-1490a_0$, 81.122 mT, 22.23 mT, and $0.003\,95$ mT^{-1} for channel (2, 3).

The (1, 3) channel molecular bound state can decay to the (1, 2) channel by a very weak spin-dipolar coupling. We have used the methods of Ref. [29] to calculate the two-body lifetime of the (1, 3) bound state due to predissociation to the (1, 2) channel and find that it is very long, greater than 10 s at 60.0 mT, increasing to 1000 s at 68.5 mT very close to resonance. However, (1, 3) molecules might be quenched by collisions with $|2\rangle$ atoms or (1, 2) channel molecules, since with three different spin states involved in the collision, there would be no fermionic suppression of collision rates according to the mechanism of Ref. [11].

In conclusion, radio-frequency spectroscopy on ultra-cold, weakly bound molecules allowed us to precisely determine the molecular binding energies and the energy splittings between two molecular states for different magnetic fields. Based on the measured data and a multichannel quantum scattering model, we determine the scattering lengths as a function of magnetic field and the Feshbach resonance positions in the lowest three channels with unprecedented precision. With these data, we can fully characterize the interaction strength between particles in the BEC-BCS crossover regime for future experiments based on ^{6}Li atoms.

---

*Present address: Department of Physics and the James Franck Institute, University of Chicago, Chicago, IL 60637, USA.

†Present address: UMR 6627 du CNRS, Lab. de Physique des Atomes, Lasers, Molécules et Surfaces, Université de Rennes, France.

[1] E. Tiesinga, B. J. Verhaar, and H. T. C. Stoof, Phys. Rev. A **47**, 4114 (1993); S. Inouye *et al.*, Nature (London) **392**, 151 (1998).

[2] S. Jochim *et al.*, Science **302**, 2101 (2003).

[3] M. Greiner, C. A. Regal, and D. S. Jin, Nature (London) **426**, 537 (2003).

[4] M. Zwierlein *et al.*, Phys. Rev. Lett. **91**, 250401 (2003).

[5] T. Bourdel *et al.*, Phys. Rev. Lett. **93**, 050401 (2004).

[6] R. G. Hulet, in Proceedings of the KITP Conference on Quantum Gases, Santa Barbara, CA, 2004 (unpublished).

[7] M. Bartenstein *et al.*, Phys. Rev. Lett. **92**, 120401 (2004); C. A. Regal, M. Greiner, and D. S. Jin, Phys. Rev. Lett. **92**, 040403 (2004); M. W. Zwierlein *et al.*, Phys. Rev. Lett. **92**, 120403 (2004); J. Kinast *et al.*, Phys. Rev. Lett. **92**, 150402 (2004); M. Bartenstein *et al.*, Phys. Rev. Lett. **92**, 203201 (2004).

[8] C. Chin *et al.*, Science **305**, 1128 (2004).

[9] D. M. Eagles, Phys. Rev. **186**, 456 (1969); A. J. Leggett, in *Modern Trends in the Theory of Condensed Matter*, edited by A. Pekalski and R. Przystawa (Springer-Verlag, Berlin, 1980); P. Nozières and S. Schmitt-Rink, J. Low Temp. Phys. **59**, 195 (1985); Q. Chen, J. Stajic, S. Tan, and K. Levin, cond-mat/0404274.

[10] M. Houbiers, H. T. C. Stoof, W. I. McAlexander, and R. G. Hulet, Phys. Rev. A **57**, R1497 (1998).

[11] D. S. Petrov, C. Salomon, and G. V. Shlyapnikov, Phys. Rev. Lett. **93**, 090404 (2004).

[12] H. Heiselberg, Phys. Rev. A **63**, 043606 (2001); T.-L. Ho, Phys. Rev. Lett. **92**, 090402 (2004).

[13] K. Dieckmann *et al.*, Phys. Rev. Lett. **89**, 203201 (2002).

[14] K. M. O'Hara *et al.*, Phys. Rev. A **66**, 041401(R) (2002).

[15] S. Jochim *et al.*, Phys. Rev. Lett. **89**, 273202 (2002).

[16] T. Bourdel *et al.*, Phys. Rev. Lett. **91**, 020402 (2003).

[17] C. A. Regal, C. Ticknor, J. L. Bohn, and D. S. Jin, Nature (London) **424**, 47 (2003).

[18] C. H. Schunck *et al.*, cond-mat/0407373 [Phys. Rev. A (to be published)].

[19] S. Gupta *et al.*, Science **300**, 1723 (2003).

[20] J. Cubizolles *et al.* Phys. Rev. Lett. **91**, 240401 (2003); S. Jochim *et al.*, Phys. Rev. Lett. **91**, 240402 (2003).

[21] J. Vanier and C. Audoin, *The Quantum Physics of Atomic Frequency Standards* (Adam Hilger Ltd., Bristol, 1989).

[22] C. Chin and P. Julienne, Phys. Rev. A **71**, 012713 (2005).

[23] We assume an exponential decay of the particle number and fit $1 - e^{-\iota P(E)}$ to the loss signal, where ι depends on the rf power. In principle, we can also determine interaction parameters from E'. However, our fits yield large uncertainties for E'.

[24] H. T. C. Stoof, J. M. V. A. Koelman, and B. J. Verhaar, Phys. Rev. B **38**, 4688 (1988).

[25] R. Côté, A. Dalgarno, and M. J. Jamieson, Phys. Rev. A **50**, 399 (1994).

[26] Z.-C. Yan, J. F. Babb, A. Dalgarno, and G. W. F. Drake, Phys. Rev. A **54**, 2824 (1996).

[27] E. R. I. Abraham, W. I. McAlexander, J. M. Gerton, R. G. Hulet, R. Côté, and A. Dalgarno, Phys. Rev. A **55**, R3299 (1997).

[28] A. J. Moerdijk, B. J. Verhaar, and A. Axelsson, Phys. Rev. A **51**, 4852 (1995).

[29] T. Köhler, E. Tiesinga, and P. S. Julienne, Phys. Rev. Lett. **94**, 020402 (2005).

Note on "Collective Excitations of a Degenerate Gas at the BEC-BCS Crossover", Phys. Rev. Lett. 92, 203201 (2004)

A. Altmeyer,[1] S. Riedl,[1,2] C. Kohstall,[1] M.J. Wright,[1] J. Hecker Denschlag,[1] and R. Grimm[1,2]

[1]*Inst. of Experimental Physics and Center for Quantum Physics, Univ. Innsbruck, 6020 Innsbruck, Austria*
[2]*Inst. for Quantum Optics and Quantum Information, Acad. of Sciences, 6020 Innsbruck, Austria*
(Dated: November 16, 2006)

We present a reinterpretation of our previous results on the radial compression mode of a degenerate quantum gas in the BEC-BCS crossover in [1]. We show that our former data are consistent with other experimental and theoretical work, when the ellipticity of the optical trapping potential in [1] is properly taken into account .

The radial compression mode of an optically trapped, ultracold ^{6}Li Fermi gas in the BEC-BCS crossover regime has been a focus of study of experimental work performed at Innsbruck University [1, 2] and at Duke University [3, 4, 5]. In our most recent work [2], we reached a level of control which allows us to identify systematic effects in our measurements. With our new knowledge of the system, we can reinterpret the previous data and resolve the apparent discrepancy between [1] and [2, 3, 4].

The atoms are trapped by a single focused laser beam resulting in a cigar-shaped trap geometry. In [1], we assumed cylindrical symmetry along the z-axis of the trapping potential, where the trap frequencies ω_x and ω_y in x- and y-direction are equal. With this assumption we used ω_y as the relevant radial trap frequency ω_r.

The experimental setup of [1] was only capable to resolve oscillations in y- and z-direction. With a new imaging system along the z-axis we now get full access to the x- and y-directions and are able to determine the two transverse trapping frequencies individually. In contrast to the assumption of cylindrical symmetry in [1], we found significant ellipticity of the trap, being characterized by an aspect ratio $\zeta = \omega_x/\omega_y$. For the experimental trap setup of [1] we found an aspect ratio of $\zeta \approx 0.8$ [7].

To calculate the frequency ω_c of the compression mode in the elliptic trap, we start from the triaxial eigenfrequency equation (e.g. [6]) and neglect the weak confinement in z-direction. This gives the collective mode frequencies ω (compression mode and surface mode)

$$\omega^4 - (2 + \Gamma)(\omega_x^2 + \omega_y^2)\omega^2 + 4(\Gamma + 1)\omega_x^2\omega_y^2 = 0, \tag{1}$$

where Γ is the polytropic interaction index. From equation (1) the frequency of the radial compression mode ω_c can be calculated [6]. This results in

$$\left(\frac{\omega_c}{\omega_y}\right)^2 = \frac{1}{2}\left(2 + \Gamma\right)\left(1 + \zeta^2\right) + \sqrt{\left(\frac{1}{2}\left(2 + \Gamma\right)\left(1 + \zeta^2\right)\right)^2 - 4\left(\Gamma + 1\right)\zeta^2}, \tag{2}$$

where ω_c is normalized to ω_y, corresponding to the way we presented our data in [1].

In Fig. 1 the experimental data of [1] and theoretical data [8] corresponding to a mean-field BCS model (lower curve) and a quantum Monte-Carlo model (upper curve), both models assuming $\zeta = 0.8$, are shown. The same data set is plotted versus the magnetic field (left-hand side) and the interaction parameter $1/k_F a$ (right-hand side), where a represents the atom-atom scattering length and k_F is the Fermi wave number.

In the BEC limit ($\Gamma = 2$) the data fit well with the theoretically expected value of 1.85. In the unitarity regime at resonance ($\Gamma = \frac{2}{3}$), the experimental data also fit well if one includes a small anharmonicity shift, which corrects $\omega_c/\omega_y = 1.62(2)$ to $\omega_c/\omega_y = 1.67(3)$ [1]. In the strongly interacting BEC regime the data can be compared with the theoretical models using equation (2). Above resonance, we see a larger downshift in frequency until a jump to $\omega_c/\omega_y \approx 2$ happens and the frequency remains constant.

In the strongly interacting BEC regime, at magnetic fields just below the Feshbach resonance or $2 > 1/k_F a > 0.5$, the experimental data points lie between both theoretical curves. In our latest precision measurements [2], the data clearly support the quantum Monte-Carlo model and they also show a downshift in frequency for increased temperatures. This is consistent with the data presented in Fig. 1, taking into account the relatively high temperature of the sample. Note that the temperatures in [1] are higher than in [2] as the evaporation ramp was not optimized to achieve deepest temperatures and the timing sequence was not optimized to minimize heating.

At magnetic fields above the Feshbach resonance ($1/k_F a \lesssim 0$), the data show a significant downshift compared to the theoretically expected values, which we cannot explain by the elliptical trap. Also other experiments show a similar trend [4, 10]. The proximity of the energy corresponding to the collective mode frequency to the pairing gap [11] and

thermal effects may be possible explanations for this downshift.

At a magnetic field of about 900G ($1/k_F a \approx -0.5$), the normalized frequency shows a pronounced jump up to the value of approximately 2, which is expected in a collisionless Fermi gas. For the collisionless oscillation along the y-axis, the ellipticity of the trap is irrelevant. So the visibility of the jump is clearly enhanced in an elliptic trap, as the lower frequency side of the jump in an elliptic trap is downshifted compared to a cylindrically symmetric trap. This jump marks the transition from hydrodynamic to collisionless behavior.
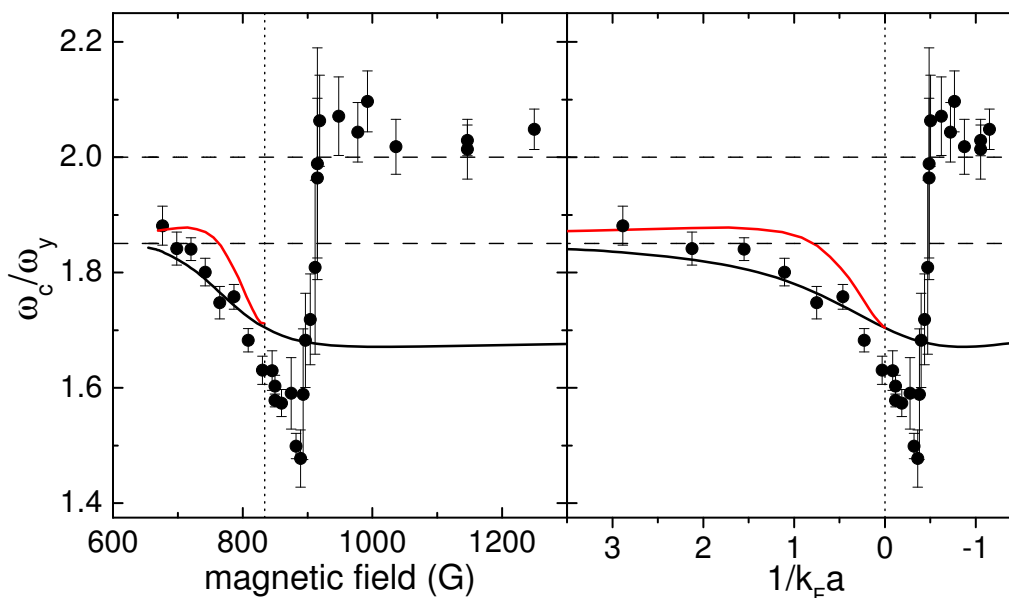

FIG. 1: Normalized compression mode frequency ω_c/ω_y in the BEC-BCS crossover regime versus magnetic field (left hand side) and interaction parameter $1/k_F a$ (right hand side) [1]. The lower theory curve is based on a mean-field BCS model and the upper curve on a quantum Monte-Carlo model. Both curves correspond to the theoretical data presented in [8]. The horizontal dashed lines indicate the values for the BEC limit ($\omega_c/\omega_y = 1.851$ for $\zeta = 0.8$) and the collisionless limit ($\omega_c/\omega_y = 2$). The vertical dotted line marks the position of the Feshbach resonance at 834.1G [9].

In conclusion, by taking into account the ellipticity of the trapping potential, the results of [1] now essentially agree with other experimental results [2, 3, 4] and theoretical predictions [8].

[1] M. Bartenstein *et al.*, Phys. Rev. Lett. **92**, 203201 (2004).
[2] A. Altmeyer *et al.*, cond-mat/0609390.
[3] J. Kinast *et al.*, Phys. Rev. Lett. **92**, 150402 (2004).
[4] J. Kinast, A. Turlapov, and J. E. Thomas, Phys. Rev. A **70**, 051401(R) (2004).
[5] J. Kinast, A. Turlapov, and J. E. Thomas, Phys. Rev. Lett. **94**, 170404 (2005).
[6] M. Cozzini, and S. Stringari, Phys. Rev. Lett. **91**, 070401 (2003).
[7] In the new setup we use an aspect ratio of $\zeta = 0.94$.
[8] G. E. Astrakharchik, R. Combescot, X. Leyronas, and S. Stringari, Phys. Rev. Lett. **95**, 030404 (2005).
[9] M. Bartenstein *et al.*, Phys. Rev. Lett. **94**, 103201 (2005).
[10] A. Altmeyer, PhD thesis, Univ. Innsbruck, in preparation.
[11] R. Combescot, and X. Leyronas, Phys. Rev. Lett. **93**, 138901 (2004).

PHYSICAL REVIEW LETTERS

Precision Measurements of Collective Oscillations in the BEC-BCS Crossover

A. Altmeyer,[1] S. Riedl,[1,2] C. Kohstall,[1] M. J. Wright,[1] R. Geursen,[1] M. Bartenstein,[1] C. Chin,[3]
J. Hecker Denschlag,[1] and R. Grimm[1,2]

[1]*Institute of Experimental Physics and Center for Quantum Physics, University of Innsbruck, 6020 Innsbruck, Austria*
[2]*Institute for Quantum Optics and Quantum Information, Academy of Sciences, 6020 Innsbruck, Austria*
[3]*James Franck Institute, Physics Department of the University of Chicago, Chicago, Illinois 60637, USA*

We report on precision measurements of the frequency of the radial compression mode in a strongly interacting, optically trapped Fermi gas of ^{6}Li atoms. Our results allow for a test of theoretical predictions for the equation of state in the BEC-BCS crossover. We confirm recent quantum Monte Carlo results and rule out simple mean-field BCS theory. Our results show the long-sought beyond-mean-field effects in the strongly interacting Bose-Einstein condensation (BEC) regime.

PACS numbers: 03.75.Ss, 05.30.Fk, 32.80.Pj, 34.50.−s

Ultracold, strongly interacting Fermi gases [1–13] have attracted considerable attention over the past few years, serving as unique model systems to create, control, and investigate novel states of quantum matter. Experimentally, the availability of such systems has opened up exciting possibilities to study many-body quantum phenomena like molecular Bose-Einstein condensation (BEC) [3] and the crossover from BEC to a Bardeen-Cooper-Schrieffer (BCS) type superfluid [4–13]. These experiments may also lead to a better understanding of strongly interacting quantum systems in different areas of physics, ranging from high-T_c superconductors to neutron stars and the quark-gluon plasma.

A degenerate two-component Fermi gas undergoes the BEC-BCS crossover [14] when the s-wave scattering length a is varied from positive to negative values across a scattering resonance. In the crossover region, where a is comparable with or larger than the interparticle spacing, the equation of state is governed by many-body effects. Understanding the equation of state is a fundamentally important challenge and constitutes a difficult task for many-body quantum theories, even in the zero-temperature limit. Mean-field BCS theory [14] provides a reasonable interpolation between the well-understood limits. More sophisticated crossover approaches [15] yield quantitatively different results in certain regimes, none of them, however, providing a complete description of the problem. The most advanced theoretical results were obtained by numerical calculations based on a quantum Monte Carlo (QMC) approach [16].

On the BEC side of the crossover, there is an interesting competition in the equation of state between the strong interactions in a Bose gas and the onset of fermionic behavior. For a strongly interacting Bose gas, one can expect quantum depletion to increase the average energy per particle. To lowest order, this beyond-mean-field effect leads a correction to the equation of state predicted by Lee, Huang, and Yang (LHY) almost 50 years ago [17]. Beyond mean field effects are expected to reduce the compressi-

bility of a strongly interacting Bose gas as compared to the weakly interacting case. However, when approaching the resonance, fermionic behavior emerges and the system loses its purely bosonic character, which increases the compressibility of the strongly interacting gas. Mean-field BCS theory does not contain beyond-mean-field effects and the LHY correction is absent there. However, the QMC results predict beyond-mean-field effects to be visible on the BEC side of the crossover [16].

In this Letter, we report on precision measurements of the radial compression mode in an optically trapped, strongly interacting Fermi gas of ^{6}Li atoms. The mode serves as a sensitive probe for the compressibility and thus the equation of state of a superfluid gas in the BEC-BCS crossover [18,19]. We reach a precision level that allows us to distinguish between the predictions resulting from mean-field BCS theory and QMC calculations. Previous experiments on collective modes, performed at Duke University [8,11] and at Innsbruck University [9], showed frequency changes in the BEC-BCS crossover in both the slow axial mode and the fast radial compression mode of a cigar-shaped sample. The accuracy, however, was insufficient for a conclusive test of the different many-body theories in the strongly interacting regime.

We prepare a strongly interacting, degenerate gas of ^{6}Li atoms in the lowest two internal states as described in our previous publications [4,9,10]. The broad Feshbach resonance centered at a magnetic field of $B = 834$ G facilitates precise tuning of the scattering length a [20]. Forced evaporative cooling is performed in a 1030-nm near-infrared laser beam focussed to a waist of 54 μm at 764 G. This results in a deeply degenerate cloud of $N = 2.0(5) \times 10^5$ atoms. By adiabatically increasing the trap laser power after cooling, the sample is recompressed to achieve nearly harmonic confinement. In the axial direction the gas is magnetically confined in the curvature of the field used for Feshbach tuning with an axial trap frequency of $\omega_z/2\pi = 22.4$ Hz at 834 G. The experiments reported here are performed at two different final values of the laser

power of the recompressed trap. At 135 mW (540 mW), the trap is 1.8 μK (7.3 μK) deep and the radial trap frequency is $\omega_r \approx 2\pi \times 290$ Hz (590 Hz). The Fermi energy of a noninteracting cloud is calculated to $E_F = \hbar^2 k_F^2/2m = \hbar(3\omega_r^2\omega_z N)^{1/3} = k_B \times 500$ nK (800 nK); here m is the mass of an atom and k_B is Boltzmann's constant.

Since our first measurements on collective excitation modes [9], we have upgraded our apparatus with a two-dimensional acousto-optical deflection system for the trapping beam and a new imaging system along the trapping beam axis. These two improvements provide us with full access to manipulate and observe the radial motion.

The trap beam profile is somewhat elliptic because of imperfections and aberrations in the optical set up. To simultaneously excite the two eigenmodes of the radial sloshing motion, we initially displace the trapped sample into a direction between the horizontal and vertical principal axes of the radial potential. After a variable hold time, during which the cloud oscillates freely, we turn off the optical trap. After a time of flight of typically 4 ms we take an absorption image of the released cloud. The center-of-mass position of the cloud then reflects its momentum at the instant of release. The experimental results in Fig. 1 demonstrate the sloshing with a beat between the two eigenmodes. A careful analysis of such data [21] allows us to determine the eigenfrequencies ω_x (horizontal sloshing) and ω_y (vertical sloshing) to within a relative uncertainty of typically 2×10^{-3}. We finally derive the mean sloshing frequency $\omega_\perp = \sqrt{\omega_x \omega_y}$ and the ellipticity parameter $\epsilon = (\omega_y - \omega_x)/\omega_\perp$.

To excite the radial compression oscillation we reduce the trap light power for a short time interval of $\sim 100 \mu$s, inducing an oscillation with a relative amplitude of typi-

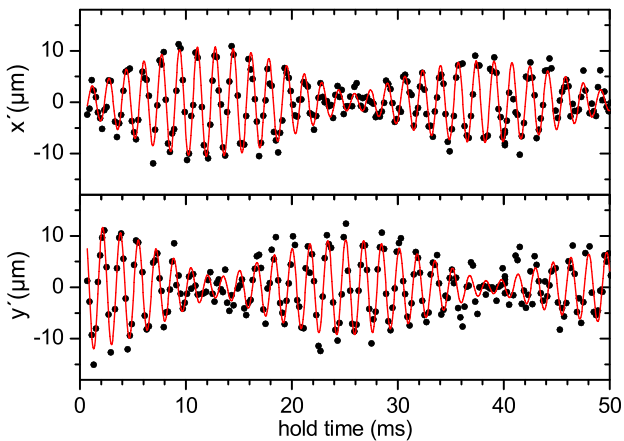cally 10%. After a variable hold time the cloud is released from the trap. From fits of two-dimensional Thomas-Fermi profiles to images of the expanding cloud taken 4 ms after release, we determine the mean cloud radius. A typical set of measurements is shown in Fig. 2. A fit of a damped harmonic oscillation to such data yields the frequency ω_c and damping rate γ of the radial compression mode.

Our experiments are performed close to the limit of an elongated harmonic trap potential with cylindrical symmetry. This elementary case is of great general relevance for many quantum gas experiments in optical and magnetic traps (see, e.g., [22]), and collective excitations are conveniently normalized to the radial trap frequency ω_r [18,19]. The compression mode frequency can then be written as $\omega_c = f_c \omega_r$, where f_c is a dimensionless function of the interaction parameter $1/k_F a$ and is related to an effective polytropic index Γ [18,19] of the equation of state by $\omega_c^2 = 2(\Gamma + 1)\omega_r^2$.

In order to compare our experimental results with theory, we consider the quantity f_c, i.e., the normalized compression mode frequency of the ideal, cylindrically symmetric, elongated trap. We find, that for our experimental conditions, f_c is approximated by the ratio $\omega_c/\omega_\perp$ of the measured compression mode (ω_c) and mean sloshing mode ($\omega_\perp$) frequencies to better than 1%. On the desired accuracy level of 10^{-3}, however, two small effects have to be taken into account: the residual trap ellipticity and the anharmonicity of the radial potential in combination with the spatial extension of the trapped sample. We thus introduce two small corresponding corrections, expressing f_c in the form $f_c = (1 - \kappa \epsilon^2 + b\alpha)\omega_c/\omega_\perp$.

For the ellipticity correction $\kappa \epsilon^2$, a straightforward solution of the hydrodynamic eigenfrequency equation [21] yields $\kappa = (2 + \Gamma)/4\Gamma$, where Γ can be approximated by $\Gamma = (\omega_c/\omega_\perp)^2/2 - 1$. For the anharmonicity correction, the parameter $\alpha = \frac{1}{2} m\omega_\perp^2 r_{rms}^2/U_0$ relates the potential energy associated with the root-mean-square radius r_{rms} [23] of the trapped cloud to the trap depth. The coefficient b results from the differential anharmonicity shifts in the compression and sloshing modes and can be calculated according to [21,24,25]. We obtain [21] $b = 0.167$ and 0.280 in the limits of BEC and unitarity, respectively.

FIG. 1 (color online). Radial sloshing observed at a trap power of 540 mW and $B = 735$ G ($1/k_F a = 1.55$). The two-dimensional center-of-mass motion is represented in a coordinate system (x', y') rotated by 45° with respect to the principal axes of the trap. The beat signal between the two sloshing eigenmodes demonstrates the ellipticity of the trap with the two eigenfrequencies $\omega_x/2\pi = 570$ Hz and $\omega_y/2\pi = 608$ Hz (ellipticity $\epsilon = 0.066$).
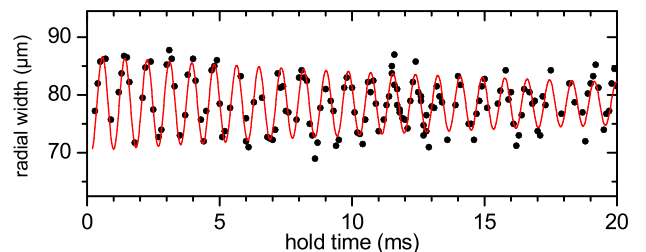

FIG. 2 (color online). Radial compression oscillation observed for the same conditions as the sloshing mode data in Fig. 1. The radial width is determined by averaging the horizontal and vertical Thomas-Fermi radii after expansion. Here we obtain $\omega_c/2\pi = 1185$ Hz.

Our measurements on the sloshing and compression modes are summarized in Table I, including the two small corrections. For the data in the strongly interacting BEC regime $(1/k_F a \gtrsim 1)$ we used the weaker trap with $\omega_\perp/2\pi \approx 290$ Hz to minimize unwanted heating by inelastic collisions. Closer to resonance $(1/k_F a \lesssim 1)$ inelastic processes are strongly suppressed, but the increasing cloud size introduces larger anharmonicity shifts. Here we chose the deeper trap with $\omega_\perp/2\pi \approx 590$ Hz. On the BCS side of the resonance we observed increased damping as a precursor of the breakdown of hydrodynamics [9,11]. We thus restricted our measurements to magnetic fields below 850 G to ensure low damping rates $(\gamma/\omega_\perp < 0.01)$ and superfluid hydrodynamics.

At a given magnetic field, a set of measurements on the sloshing and compression modes typically takes a few hours. To minimize uncertainties from slow drifts and day-to-day variations we always took the sloshing mode reference measurement right before or after the compression mode data. By repeating measurements under identical settings we found a typical remaining fractional uncertainty for the normalized compression mode frequencies of 5×10^{-3}, which is about $2-3$ times larger than the fit errors of individual measurements.

In Fig. 3 we show our final results on the normalized compression mode frequency in the BEC-BCS crossover. The two theory curves [19] correspond to the equation of state from mean-field BCS theory (lower curve) and the one from quantum Monte Carlo calculations (upper curve). Our data confirm the quantum Monte Carlo predictions and

rule out the mean-field BCS theory. In the strongly interacting BEC regime $(1/k_F a \gtrsim 1)$ our data are well above the value of 2. This highlights the presence of the long-sought beyond-mean-field effects [17] in collective modes of a strongly interacting gas [18,26].

We finally address the question of how nonzero temperatures influence the compression mode frequency. At unitarity, a recent experiment [27] has found small frequency upshifts with temperature. For a BEC, however, theory [28] predicts temperature-induced down-shifts, which compete with the up-shifts from beyond-mean-field effects. We have performed a set of measurements on temperature shifts in the strongly interacting BEC regime $(1/k_F a = 0.94)$. Before exciting the collective oscillation, the evaporatively cooled gas was kept in the recompressed trap for a variable hold time of up to 1.5 s. During this time residual heating by inelastic processes slowly increased the temperature, which we observed as a substantial increase of damping with time. The damping rate γ thus serves us as a very sensitive, but uncalibrated thermometer [8,27]. Figure 4, where we plot the normalized compression mode frequency versus damping rate, clearly shows a temperature-induced down-shift. We note that previous measurements in the strongly interacting BEC regime [9,11] were performed at relatively large damping rates

TABLE I. Experimental data on radial collective modes in the BEC-BCS crossover. The data in the upper seven (lower eight) rows refer to the sets of measurements taken in the shallower (deeper) trap with $U_0 = 1.8$ μK and $E_F = 500$ nK ($U_0 = 7.3$ μK and $E_F = 800$ nK). The values in parentheses indicate 1σ fit uncertainties of individual measurements. Note that a systematic scaling uncertainty of $\sim 4\%$ for $1/k_F a$ results from the uncertainty in the atom number $N = 2.0(5) \times 10^5$.

		Sloshing		Compression		Correction	
B	$1/k_F a$	$\omega_\perp/2\pi$	ϵ	$\omega_c/2\pi$	$\gamma/\omega_\perp$	$\kappa\epsilon^2$	$b\alpha$
(G)		(Hz)		(Hz)		(10^{-4})	
727.8	2.21	292.7(5)	0.083(3)	596.3(6)	0.007(2)	48	20
735.1	1.96	298.6(5)	0.091(3)	602.8(8)	0.008(3)	60	26
742.5	1.75	294.5(5)	0.067(3)	593.2(7)	0.005(2)	33	28
749.8	1.55	296.3(4)	0.073(3)	599.0(7)	0.006(2)	38	28
760.9	1.27	296.0(4)	0.088(2)	592.3(7)	0.009(2)	58	24
771.9	1.03	293.6(7)	0.074(5)	586.2(8)	0.007(3)	41	27
834.1	0	287.5(7)	0.073(5)	519.4(9)	0.014(3)	55	94
757.2	1.07	605.0(9)	0.065(3)	1210.9(12)	0.010(2)	32	13
768.2	0.87	592.5(7)	0.069(2)	1186.6(12)	0.012(2)	36	16
775.6	0.75	590.2(4)	0.060(1)	1170.2(21)	0.007(4)	28	14
782.2	0.64	604.8(9)	0.061(3)	1187.1(16)	0.006(3)	29	16
801.3	0.38	586.8(7)	0.063(2)	1135.2(12)	0.010(2)	33	24
812.3	0.24	586.5(7)	0.058(2)	1106.9(16)	0.014(3)	30	33
834.1	0	596.3(9)	0.070(3)	1089.0(12)	0.010(2)	48	40
849.1	-0.14	583.2(7)	0.052(2)	1046.7(37)	0.007(2)	29	47

FIG. 3 (color online). Normalized compression mode frequency f_c versus interaction parameter $1/k_F a$. The experimental data include the small corrections for trap ellipticity and anharmonicity and can thus be directly compared to theory in the limit of an elongated harmonic trap with cylindrical symmetry. The open and closed circles refer to the measurements listed in Table I for $\omega_\perp/2\pi \approx 290$ Hz and 590 Hz, respectively. The error bars indicate the typical scatter of the data points. The filled triangle shows a zero-temperature extrapolation of the measurements displayed in Fig. 4. The theory curves refer to mean-field BCS theory (lower curve) and QMC calculations (upper curve) and correspond to the data presented in Ref. [19]. The horizontal dashed lines indicate the values for the BEC limit ($f_c = 2$) and the unitarity limit ($f_c = \sqrt{10/3} = 1.826$).

FIG. 4. Normalized compression mode frequency f_c versus damping rate for $1/k_F a = 0.94$ ($U_0 = 7.3\ \mu$K). The error bars represent 1σ fit uncertainties. The dashed lines indicate the zero-temperature values predicted by QMC calculations (upper line) and mean-field BCS theory (lower line).

in the range between 0.05 and 0.1, where frequency downshifts are significant.

With our new knowledge on systematic frequency shifts in collective mode measurements, let us comment on the previous experiments performed in Innsbruck [9] and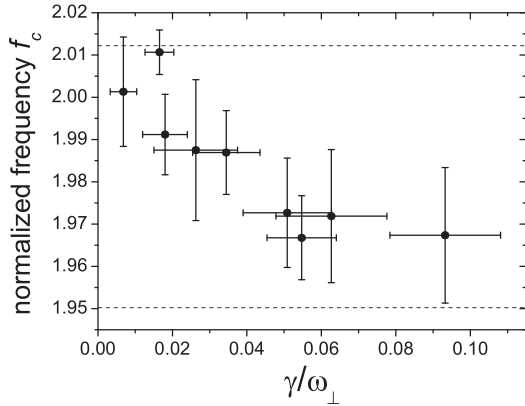 at Duke University [8,11]. We have reanalyzed our old data on the radial compression mode and identified a previously undetermined ellipticity of $\epsilon \approx 0.2$ as the main problem in our data interpretation [29]. The fact that we had normalized the compression mode frequency to the vertical trap frequency (ω_c/ω_y) led to a substantial down-shift in the hydrodynamic regime, but not in the collisionless regime. We furthermore believe that significant temperature shifts were present in the previous collective mode experiments. In particular for the strongly interacting BEC regime temperature shifts in our old data on the axial mode [9] and the Duke data on the radial mode [11] provide a plausible explanation for these measurements being closer to the predictions of mean-field BCS theory than to the more advanced QMC results.

In conclusion, our work shows that collective modes allow for precision tests of many-body theories in strongly interacting quantum gases. In future experiments, the observation of collective oscillation modes will serve as a powerful tool to investigate strongly interacting superfluids in a more general context, e.g., in mixtures of fermionic quantum gases.

[1] K. M. O'Hara *et al.*, Science **298**, 2179 (2002).
[2] T. Bourdel *et al.*, Phys. Rev. Lett. **91**, 020402 (2003).
[3] S. Jochim *et al.*, Science **302**, 2101 (2003); M. Greiner, C. A. Regal, and D. S. Jin, Nature (London) **426**, 537 (2003); M. W. Zwierlein *et al.*, Phys. Rev. Lett. **91**, 250401 (2003).
[4] M. Bartenstein *et al.*, Phys. Rev. Lett. **92**, 120401 (2004).
[5] C. A. Regal, M. Greiner, and D. S. Jin, Phys. Rev. Lett. **92**, 040403 (2004).
[6] M. W. Zwierlein *et al.*, Phys. Rev. Lett. **92**, 120403 (2004).
[7] T. Bourdel *et al.*, Phys. Rev. Lett. **93**, 050401 (2004).
[8] J. Kinast *et al.*, Phys. Rev. Lett. **92**, 150402 (2004).
[9] M. Bartenstein *et al.*, Phys. Rev. Lett. **92**, 203201 (2004).
[10] C. Chin *et al.*, Science **305**, 1128 (2004).
[11] J. Kinast, A. Turlapov, and J. E. Thomas, Phys. Rev. A **70**, 051401(R) (2004).
[12] M. W. Zwierlein *et al.*, Nature (London) **435**, 1047 (2005).
[13] G. B. Partridge *et al.*, Phys. Rev. Lett. **95**, 020404 (2005).
[14] D. M. Eagles, Phys. Rev. **186**, 456 (1969); A. J. Leggett, in *Modern Trends in the Theory of Condensed Matter*, edited by A. Pekalski and R. Przystawa (Springer-Verlag, Berlin, 1980); P. Nozières and S. Schmitt-Rink, J. Low Temp. Phys. **59**, 195 (1985); J. R. Engelbrecht, M. Randeria, and C. Sá de Melo, Phys. Rev. B **55**, 15 153 (1997).
[15] P. Pieri, L. Pisani, and G. C. Strinati, Phys. Rev. B **72**, 012506 (2005).
[16] G. E. Astrakharchik, J. Boronat, J. Casulleras, and S. Giorgini, Phys. Rev. Lett. **93**, 200404 (2004).
[17] T. D. Lee and C. N. Yang, Phys. Rev. **105**, 1119 (1957); T. D. Lee, K. Huang, and C. N. Yang, Phys. Rev. **106**, 1135 (1957).
[18] S. Stringari, Europhys. Lett. **65**, 749 (2004); H. Heiselberg, Phys. Rev. Lett. **93**, 040402 (2004); H. Hu, A. Minguzzi, X.-J. Liu, and M. P. Tosi, Phys. Rev. Lett. **93**, 190403 (2004); A. Bulgac and G. F. Bertsch, Phys. Rev. Lett. **94**, 070401 (2005); Y. E. Kim and A. L. Zubarev, Phys. Rev. A **70**, 033612 (2004); N. Manini and L. Salasnich, Phys. Rev. A **71**, 033625 (2005).
[19] G. E. Astrakharchik, R. Combescot, X. Leyronas, and S. Stringari, Phys. Rev. Lett. **95**, 030404 (2005).
[20] M. Bartenstein *et al.*, Phys. Rev. Lett. **94**, 103201 (2005).
[21] A. Altmeyer, Ph.D. thesis, University Innsbruck (to be published).
[22] F. Chevy *et al.*, Phys. Rev. Lett. **88**, 250402 (2002).
[23] We obtain r_{rms} from *in situ* measurements of axial profiles [4], using the relation $r_{\mathrm{rms}} = 2\omega_z^2/\omega_r^2 z_{\mathrm{rms}}$.
[24] S. Stringari (private communication).
[25] J. Kinast, Ph.D. thesis, Duke University, 2006.
[26] L. Pitaevskii and S. Stringari, Phys. Rev. Lett. **81**, 4541 (1998).
[27] J. Kinast, A. Turlapov, and J. E. Thomas, Phys. Rev. Lett. **94**, 170404 (2005).
[28] S. Giorgini, Phys. Rev. A **61**, 063615 (2000).
[29] A. Altmeyer *et al.*, cond-mat/0611285.

Dynamics of a strongly interacting Fermi gas: the radial quadrupole mode

A. Altmeyer,[1] S. Riedl,[1,2] M. J. Wright,[1] C. Kohstall,[1] J. Hecker Denschlag,[1] and R. Grimm[1,2]

[1]*Inst. of Experimental Physics and Center for Quantum Physics, Univ. Innsbruck, 6020 Innsbruck, Austria*
[2]*Inst. for Quantum Optics and Quantum Information, Acad. of Sciences, 6020 Innsbruck, Austria*
(Dated: April 25, 2007)

We report on measurements of an elementary surface mode in an ultracold, strongly interacting Fermi gas of ^{6}Li atoms. The radial quadrupole mode allows us to probe hydrodynamic behavior in the BEC-BCS crossover without being influenced by changes in the equation of state. We examine frequency and damping of this mode, along with its expansion dynamics. In the unitarity limit and on the BEC side of the resonance, the observed frequencies agree with standard hydrodynamic theory. However, on the BCS side of the crossover, a striking down shift of the oscillation frequency is observed in the hydrodynamic regime as a precursor to an abrupt transition to collisionless behavior; this indicates coupling of the oscillation to fermionic pairs.

PACS numbers: 34.50.-s, 05.30.Fk, 39.25.+k, 32.80.Pj

I. INTRODUCTION

The advent of ultracold, strongly interacting Fermi gases [1, 2], molecular Bose-Einstein condensates [3, 4, 5], and fermionic condensates [6, 7] has opened up unique possibilities to study the fundamental physics of interacting fermions. The availability of controllable model systems with tunable interactions provides unprecedented experimental access to the many-body physics of fermionic quantum systems, which is of great fundamental importance for various branches of physics [8].

A fundamental problem, which has been discussed in the theoretical literature for decades [9, 10, 11, 12], is the crossover from Bose-Einstein condensation (BEC) to a macroscopic quantum state in the Bardeen-Cooper-Schrieffer (BCS) regime. In this crossover, the nature of pairing changes from the formation of bosonic molecules by fermionic atoms to pairing supported by many-body effects. With novel model systems now available in ultracold Fermi gases, the BEC-BCS crossover has recently stimulated a great deal of interest in both theory and experiment [8].

Collective excitation modes in trapped ultracold Fermi gases provide powerful tools to investigate the macroscopic properties of a system in the BEC-BCS crossover [13]. For experiments of this class, ultracold ^{6}Li gases have excellent properties. This is because of their stability in the molecular regime [3, 14, 15] and precise magnetic tunability of interactions based on a broad Feshbach resonance [16, 17]. Early experiments on collective modes in the BEC-BCS crossover provided evidence for superfluidity [18] and showed a striking transition from hydrodynamic to collisionless behavior [19]. More recent experiments yielded a precision test of the equation of state [20]. The previous experiments have focussed on collective modes with compression character, where both the hydrodynamic properties and the equation of state determine the mode frequency [18, 19, 20, 21, 22, 23].
In this Article, we report on measurements of a *pure surface mode* in the BEC-BCS crossover, which provides new insight into the dynamics of the system. The "radial quadrupole mode" in an elongated trap, the fundamentals of which are discussed in Sec. II, allows for a test of hydrodynamic behavior without being influenced by changes in the equation of state. In Sec. III, we present our experimental setup and the main procedures. We introduce a tool to excite collective oscillations with an acousto-optic scanning system. The results of our measurements, presented in Sec. IV, provide us with new insight on the abrupt transition from hydrodynamic to collisionless behavior, first observed in [19]. The present work provides strong evidence that quasi-static hydrodynamic theory [24] does not apply to collective modes of a strongly interacting fermionic superfluid, when the oscillation frequencies approach the pairing gap [25].

II. RADIAL QUADRUPOLE MODE

The confining potential in our experiments is close to the limit of an elongated harmonic trap with cylindrical symmetry. In this case, we can consider purely radial collective oscillations, neglecting the axial motion. The frequencies of the radial modes can be expressed in units of the radial trap frequency ω_r. We note that our experiments are performed in a three-dimensional regime, where the energy $\hbar\omega_r$ is typically a factor of 30 below the chemical potential and finite-size effects can be neglected.

In this situation, there are two elementary collective modes of the system, the radial compression mode and the radial quadrupole mode [13, 26]. We focus on the quadrupole mode, which is illustrated in Fig. 1. This mode corresponds to an oscillating radial deformation, which can be interpreted as a standing surface wave. The mode was first demonstrated in atomic BEC experiments [27] and applied to investigate rotating systems [28], but so far it has not been studied in strongly interacting Fermi gases.

Being a pure surface mode, the frequency ω_q of the radial quadrupole mode does not depend on the compressibility of the system. The frequency ω_q does not depend on the

radial quadrupole mode
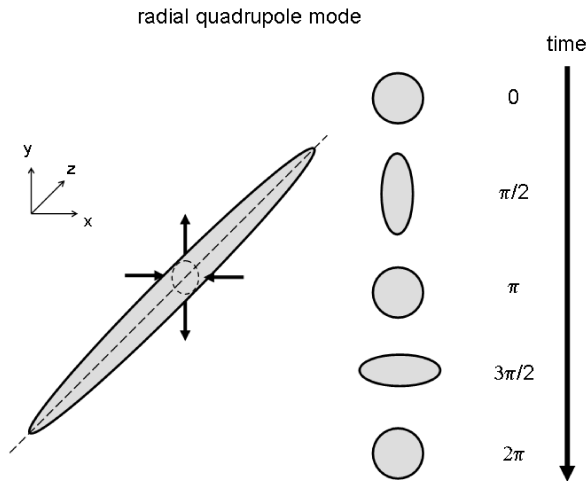
time

0

$\pi/2$

π

$3\pi/2$

2π

FIG. 1: Illustration of the radial quadrupole mode as an elementary collective excitation of an elongated, trapped atom cloud.

equation of state but on the collisional properties. In the hydrodynamic regime, whether the gas is a superfluid or a classical gas with a collision rate strongly exceeding the radial trap frequency, the frequency of this mode is given by [26]

$$\omega_q = \sqrt{2}\,\omega_r. \tag{1}$$

In contrast, for a collisionless gas, where the atoms freely oscillate in the trap, the frequency is

$$\omega_q = 2\,\omega_r. \tag{2}$$

Because ω_q is insensitive to the compressibility of the gas and the difference between the collisonless and the hydrodynamic frequencies is large, the radial quadrupole mode can serve as an excellent tool to probe pure hydrodynamics. Particularly interesting is the transition from hydrodynamic to collisionless behavior at lowest temperatures. Such a change occurs in a strongly interacting Fermi gas on the BCS side of the resonance [19, 21, 23]. Near this transition, measurements on the compression mode indicated frequency down shifts, which raised questions concerning the validity of standard hydrodynamic theory in this interaction regime [29, 30]. Previous experiments could not unambiguously identify the origin of frequency shifts near the hydrodynamic-to-collisionless transition, which is a particular motivation for probing the crossover gas with the radial quadrupole mode.

III. EXPERIMENTAL PROCEDURE

The apparatus and the basic preparation methods for experiments with a strongly interacting Fermi gas of ^{6}Li atoms have been described in our previous work

[3, 19, 25, 31]. As a starting point, we produce a molecular BEC of ^{6}Li$_2$ [3, 31]. By changing an external magnetic field, we can control the inter-particle interactions in the vicinity of a Feshbach resonance, which is centered at 834G [16, 17]. The interactions are characterized by the atomic s-wave scattering length a.

We start our experiments with an ensemble of about $N = 4 \times 10^5$ atoms in an almost pure BEC at a magnetic field of 764 G. In order to change the properties of the system adiabatically, we slowly ramp to the final magnetic field, where the measurements are performed [31]. The temperature of the gas is typically below 0.1 T_F, unless stated otherwise.

In order to observe the collective oscillations, we take absorption images of the cloud in the x-y-plane after release from the trap. We illuminate the atoms with a probe beam along the z-direction of the cigar-shaped cloud. The probe light causes a resonant excitation of the D2-line, at a wavelength of 671nm. We use dichroic mirrors for combining and separating the probe and the dipole trapping beam. The frequency of the probe beam can be tuned over a range of more than 1GHz, which enables resonant imaging over the whole range of magnetic fields that we create in our experiments.

The gas is confined in a nearly harmonic trapping potential, which has an axially symmetric, cigar-shaped trap geometry. Optical confinement in the radial direction is created by a focused 1030-nm near-infrared laser beam with a waist of ~ 58 μm. The potential in the axial direction consists of a combination of optical and magnetic confinement [3]; the magnetic confinement is dominant under the conditions of the present experiments. We set the laser power to 270 mW, which results in a radial trap frequency of $\omega_r \approx 2\pi \times 370$ Hz and an axial trap frequency of $\omega_z \approx 2\pi \times 22$ Hz at a magnetic field of 764 G. The trap frequencies correspond to a Fermi energy of a noninteracting cloud $E_F = \hbar(\omega_r^2 \omega_z 3N)^{1/3} = k_B \times 740$nK.

In order to excite collective oscillations, we suddenly change the optical trapping potential. The position and shape of our trapping potential in the x-y-plane can be manipulated through the use of a two-dimensional scanning system. One feature of the system is that we can rapidly displace the trap laterally. Fast modulation of the beam position enables us to create time-averaged potentials [32, 33].

The scanning system is constructed by use of two acousto-optic modulators (AOMs), which are aligned for vertical and horizontal deflections. Fig. 2 illustrates the principle of our scanning system for one direction. A collimated beam passes through an AOM and is deflected depending on the driving frequency. A lens is placed at a distance of one focal length behind the AOM, so that the deflection results in a parallel displacement of the beam. By changing the driving frequency of the AOM, the lateral position of the focus is shifted. This system enables us to displace the focus of the trapping beam in the horizontal and the vertical direction by up to four times the beam waist in all directions. Furthermore, the deflec-
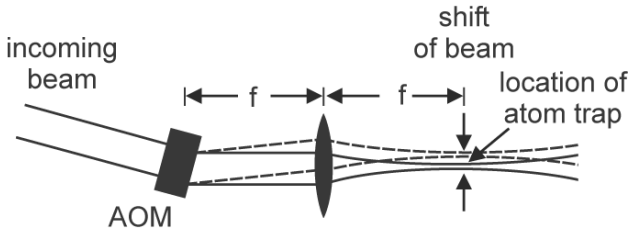
FIG. 2: Schematic illustration of the scanning system. A wide collimated beam passes through an AOM. The resulting deflection angle depends on the driving frequency of the AOM. The beam passes through a lens at the distance of one focal length behind the AOM. The lens focuses the beam for atom trapping. A change in deflection angle results in a parallel shift of the beam position in the focal plane. The solid and dashed lines show the beam path for different deflection angles. The zeroth order beam is not shown.
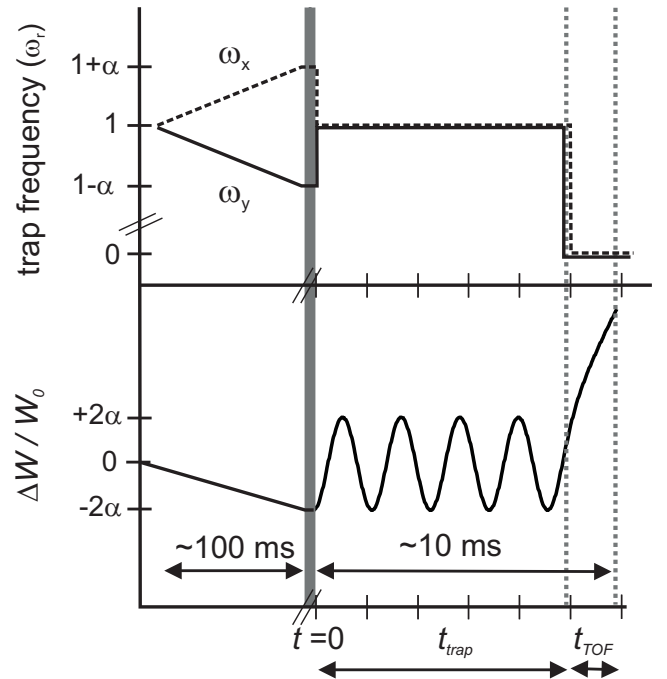

FIG. 3: Timing scheme for the excitation of the radial quadrupole mode. The ellipticity of the trap is slowly ramped up within 100 ms. This results in a change of α in the trap frequencies, where α characterizes the ellipticity, and sets the initial, normalized deformation $\Delta W/W_0 = -2\alpha$. W_0 is defined as the width of the cloud in the trap without excitation. At $t = 0$, the elliptic deformation is switched off and the oscillation in the trap begins. (Shown here is an oscillation in the hydrodynamic regime.) The oscillation continues until the trap is turned off at $t = t_{\mathrm{trap}}$, which is usually between 0 and 10 ms. At $t = t_{\mathrm{trap}}$, the cloud is released from the trap and expands for the time t_{TOF}, which is typically 2 ms.

tion can be modulated by frequencies of up to $\sim 1\mathrm{MHz}$ within 3dB bandwidth. In our trap configuration, we use modulation frequencies of 100kHz, which greatly exceeds the trap frequency. We create elliptic potentials, i.e. potentials with $\omega_{\mathrm{x}} \neq \omega_{\mathrm{y}}$, by modulating the trap position along a specific direction. We use this for the excitation of the quadrupole mode. By choosing a suited modulation function [34], these elliptic potentials are nearly harmonic.

When we excite the quadrupole mode, we first adiabatically deform the trapping potential in $\sim 100\,\mathrm{ms}$ to an elliptic shape. This slow deformation ensures that the cloud stays in thermal equilibrium even in the near-collisionless regime and no excitations occur. We suddenly switch off the deformation leading to an oscillation in the x-y-plane of the elliptic cloud in the originally round trap.

The initial deformation corresponds to different trap frequencies in horizontal and vertical direction where $\omega_{0\mathrm{x}} = (1 + \alpha)\omega_{\mathrm{r}}$ and $\omega_{0\mathrm{y}} = (1 - \alpha)\omega_{\mathrm{r}}$. The parameter α determines the amplitude of the emerging oscillation; we choose it for most of our measurements (unless stated otherwise) to be $\alpha \approx 0.05$. We increase α by increasing the modulation for the time averaged potential along the y-direction. As the modulation decreases the confinement strength of the dipole trap, we simultaneously ramp up the trap power to ensure that the mean trap frequency $\omega_{\mathrm{r}} = \sqrt{\omega_{0\mathrm{x}}\omega_{0\mathrm{y}}}$ remains constant. This avoids excitation of the compression mode.

Fig. 3 shows the timing scheme for the excitation of the radial quadrupole mode. At $t = 0$, the collective oscillation is excited and the cloud starts oscillating in the trap for a variable time t_{trap}. Horizontal and vertical widths of the cloud, W_{x} and W_{y}, oscillate in the trap out of phase with a relative phase shift of π. As an observable, we choose the difference in widths $\Delta W = W_{\mathrm{x}} - W_{\mathrm{y}}$, which cancels out small effects of residual compression oscillations. For normalization, we introduce the width W_0 of the cloud in the trap without excitation.

Experimentally, we determine the collective quadrupole oscillations after suddenly switching off the trap and a subsequent expansion time t_{TOF}. We then take an absorption image of the cloud and determine its horizontal and vertical widths W_{x} and W_{y} via a two-dimensional Thomas-Fermi profile fit. From these measurements after expansion, we can determine the in-trap behavior.

Typical data sets of radial quadrupole oscillations are shown in Fig. 4. Fig. 4(a) shows an oscillation in the hydrodynamic regime; here we observe a weakly damped harmonic oscillation centered about a small constant offset. Fig. 4(b) shows the typical behavior in the collisionless regime. The frequency of the oscillation is clearly higher than in the hydrodynamic regime. The oscillation shows stronger damping and has an exponentially time-varying offset.

We find that, for both regimes, the dependence of ΔW on t_{trap} can be well described by the fit function

$$\begin{aligned}
\Delta W = {} & A\, e^{-\kappa t_{\mathrm{trap}}}\, \cos\left(\omega_{\mathrm{q}} t_{\mathrm{trap}} + \phi\right) \\
& + C\, e^{-\xi t_{\mathrm{trap}}} + y_0,
\end{aligned} \tag{3}$$
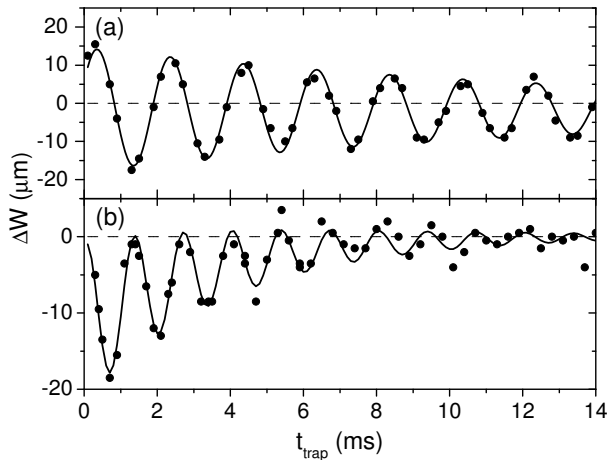
A. Frequency and damping

FIG. 4: Typical radial quadrupole oscillations in the hydrodynamic (a) and collisionless (b) regimes. The solid lines show fits to our data according to Eq.(3). The dashed lines indicate $\Delta W = 0$. The expansion time t_{TOF} is 2 ms. In (a), the oscillation in the unitarity limit ($B = 834\,\text{G}$) is shown, whereas (b) shows the oscillations for $B = 1132\,\text{G}$ ($1/k_{\text{F}}a \approx -1.34$).
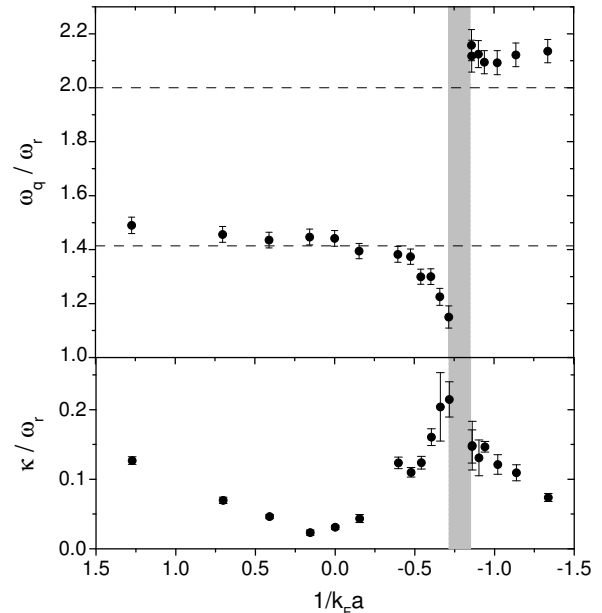

FIG. 5: Frequency ω_q (upper plot) and damping rate κ (lower plot) of the radial quadrupole mode. Both quantities are normalized to the radial trap frequency ω_r and plotted versus the interaction parameter $1/k_{\text{F}}a$. The dashed lines indicate the theoretical predictions in the hydrodynamic ($\omega_q/\omega_r = \sqrt{2}$) and in the collisionless limit ($\omega_q/\omega_r = 2$). The shaded area marks the transition from hydrodynamic to collisionless behavior between $1/k_{\text{F}}a \approx -0.72$ ($B \approx 930\,\text{G}$) and $1/k_{\text{F}}a \approx -0.85$ ($B \approx 960\,\text{G}$).

which is explained in detail in Appendix B.

Note that the frequency ω_q and the damping constant κ are independent of the expansion during t_{TOF} and characterize the behavior of the trapped oscillating atom cloud. In contrast, the amplitude A and the phase shift ϕ depend on the expansion time and provide further information on the dynamics of the gas. The offset function $C\,e^{-\xi t_{\text{trap}}}$ with amplitude C and damping constant ξ results from thermalization effects and is only relevant in the collisionless regime (see discussion in Appendix B). The constant offset y_0 results from a slight inhomogeneity of the magnetic field, which gives rise to a weak saddle potential. This increases (decreases) the cloud size in y-direction (x-direction) during expansion.

IV. EXPERIMENTAL RESULTS

Here we first discuss our measurements of the frequency ω_q and the damping rate κ of the in-trap oscillation (Sec. IV A). We then present the data for the phase offset ϕ and the amplitude A (Sec. IV B). Finally, we explore the hydrodynamic-to-collisionless transition (Sec. IV C). As commonly used in the field of BEC-BCS crossover physics [8], the dimensionless parameter $1/k_{\text{F}}a$ is introduced to characterize the interaction regime. The parameter $k_{\text{F}} = \sqrt{2mE_{\text{F}}}/\hbar$ is the Fermi wave number and m is the mass of an atom.

In Fig. 5, we show the results for the frequency ω_q and the damping rate κ of the radial quadrupole mode throughout the BEC-BCS crossover. Both ω_q and κ are normalized to the trap frequency ω_r, which we determine by a sloshing mode measurement [20]. We include small corrections resulting from anharmonicity of the trapping potential and the residual ellipticity of the trap (see appendix C).

The data confirm the expected transition between the hydrodynamic and the collisionless regime on the BCS side of the resonance (see Sec. II). The transition is qualitatively different from the hydrodynamic-to-collisionless crossover in a classical gas [35] or in a Fermi gas without superfluidity [36]. Instead of a continuous and monotonous variation of the frequency between the two limits ($\sqrt{2}\,\omega_r$ and $2\,\omega_r$), an abrupt change occurs. When this transition is approached from the hydrodynamic side, a striking frequency downshift shows up as a precursor of the transition to higher frequencies. In the transition region (shaded area in Fig. 5), no data points are shown because of the large damping and correspondingly

very large uncertainties for the measured frequency.

The damping rate shows similar behavior as in our previous measurements on the radial compression mode [19, 23]. Maximum damping occurs near the hydrodynamic-to-collisionless transition, whereas minimum damping is observed slightly below the resonance. In general, we find that damping is roughly two times larger for the quadrupole mode than for the compression mode at the same temperature [37]. The faster damping of the quadrupole mode is plausible in view of the larger frequency change at the transition.

We now discuss the behavior in different regions in more detail:

$1/k_{\mathrm{F}}a \approx 0$: In the unitarity limit, the normalized frequency agrees well with the theoretically expected value of $\omega_{\mathrm{q}}/\omega_{\mathrm{r}} = \sqrt{2}$ for a hydrodynamic gas, see Eq. (1). To check for consistency with previous experiments [20], we here also reproduced the frequency $\sqrt{10/3}\,\omega_{\mathrm{r}}$ of the radial compression mode on the 10^{-3} accuracy level. The damping is low for the Fermi gas in the unitarity limit. In contrast to the compression mode, the quadrupole mode frequency stays constant throughout the crossover, indicating that it is independent of the equation of state.

$1/k_{\mathrm{F}}a > 0$: In the strongly interacting BEC regime, there is an increase in the damping and a slight increase in the frequency for increasing $1/k_{\mathrm{F}}a$. As the gas is more susceptible to heating by inelastic processes in the deep molecular regime [13], both effects may be due to a thermal component in this region.

$1/k_{\mathrm{F}}a \approx -0.8$: The frequency exhibits the pronounced "jump" from the hydrodynamic to the collisionless frequency. This transition is accompanied by a pronounced maximum of the damping rate.

$1/k_{\mathrm{F}}a \lesssim -0.8$: The frequency stays almost constant about 5% above the theoretically expected value of $\omega_{\mathrm{q}} = 2\omega_{\mathrm{r}}$. Interaction effects in the attractive Fermi gas may cause this significant upshift, although calculations of mean-field effects [38] predict mean-field shifts below 1%. As we cannot experimentally realize a non-interacting Fermi gas above the resonance, we could not perform further experimental checks. The upshift in this regime thus remains an open question.

$1/k_{\mathrm{F}}a \lesssim 0$ and $1/k_{\mathrm{F}}a \gtrsim -0.8$: In this regime, we detect a substantial down shift in the quadrupole mode frequency. The effect begins to show up already slightly above the resonance ($1/k_{\mathrm{F}}a = 0$) and increases to a magnitude of almost 20% ($\omega_{\mathrm{q}}/\omega_{\mathrm{r}} \approx 1.15$ at $1/k_{\mathrm{F}}a = -0.72$), before the transition to collisionless behavior occurs. Indications of a similar down shift have been observed already in compression mode experiments [19, 21, 23], but here the down shift is considerably larger and not blurred by changes in the equation of state.

A plausible explanation for the curious behavior of the collective mode frequency on the BCS side of the resonance is provided by coupling of the oscillation to the pairing gap [13, 25, 29]. If we assume that the abrupt transition is caused by pair breaking resulting from resonant coupling of the oscillation to the gap, then the down shift may be interpreted as a coupling effect when the gap is not much larger than the oscillation frequency [30, 39]. The observed phenomenon still awaits a full theoretical interpretation.

B. Phase shift and amplitude

Additional information on the interaction regime is provided by the phase shift ϕ and the amplitude A of the observed oscillation (see Eq.(3)). This is useful since extremely high damping in the transition region makes a meaningful determination of frequency and damping practically impossible. We find that both amplitude and phase shift, however, can be determined with reasonable uncertainties even in the transition regime.

In the following, we present measurements of phase shift and amplitude. These are compared to model calculations, which are described in detail in appendix A.

In Fig. 6, the phase ϕ and the relative amplitude are plotted versus the interaction parameter $1/k_{\mathrm{F}}a$. The relative amplitude is given by the amplitude A (definition see Eq.(3)) divided by the average width of the cloud after expansion. The average width is obtained by averaging $(W_{\mathrm{x}} + W_{\mathrm{y}})/2$ over one oscillation period using the same data set from which we extract A.

In the transition area around $1/k_{\mathrm{F}}a = -0.8$, the phase shift ϕ shows the step-like change at the transition from the hydrodynamic to the collisionless regime. This is similar to the jump in frequency in Fig. 5. In the collisionless and unitary regimes, the phase agrees with the theoretically expected values (solid line and dotted line, respectively).

As a general trend, the relative amplitude is larger in the hydrodynamic and smaller in the collisionless regime. In the hydrodynamic regime, the relative amplitude decreases for decreasing $1/k_{\mathrm{F}}a$, which is explained by the change of γ from 1 to 2/3; γ is the polytropic index of the equation of state (see Appendix A). At unitarity, the relative amplitude agrees well with the numerically calculated value for $\gamma = 2/3$ (dotted line). In the collisionless limit, the relative amplitude is half of the value at unitarity, which is also consistent with our calculations in App. A 3. We note that at the transition from the hydrodynamic to the collisionless regime, the value of the relative amplitude decreases even below the collisionless value.

In summary, the behavior of the phase shift and the amplitude agrees with our model presented in Appendix A
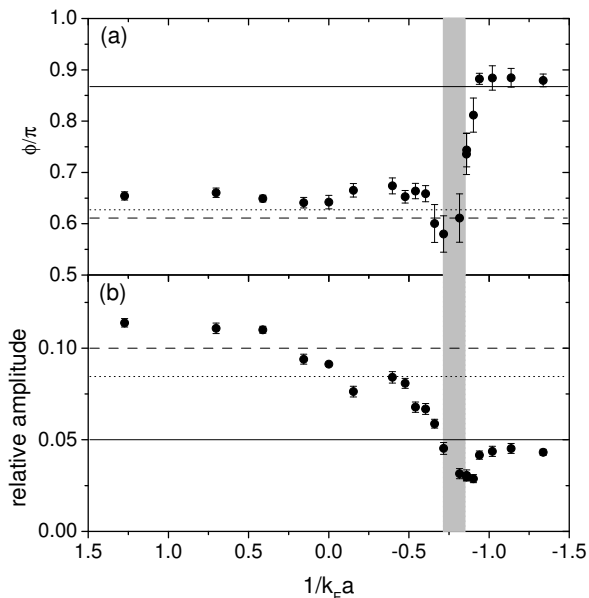
FIG. 6: (a) Phase shift ϕ and (b) relative amplitude of the quadrupole mode versus interaction parameter $1/k_F a$ after $t_{\rm TOF} = 2$ms expansion. The horizontal lines show calculations from our theoretical model: the solid lines in the collisionless limit, the dotted lines in the hydrodynamic regime at unitarity ($\gamma = 2/3$) and the dashed lines in the hydrodynamic regime in the BEC limit ($\gamma = 1$). These calculated values can be read off from Fig. 10 for the phase and Fig. 9 for the amplitude. The shaded area marks the transition between hydrodynamic and collisionless behavior between $1/k_F a \approx -0.72$ and $1/k_F a \approx -0.85$ (see also Fig. 5).

(see also Fig. 9 and Fig. 10), in particular the prominent change in the phase offset is confirmed.

C.   Further observations

The measurements presented in the preceding subsections were taken under fixed experimental conditions, where only the scattering length a was varied. In this subsection we investigate how the transition from hydrodynamic to collisionless behavior depends on the experimental parameters excitation amplitude, trap depth and temperature.

In a first set of experiments, we explored whether the position of the transition depends on the excitation amplitude. We increase or decrease the amplitude by a factor of 2. This allows us to compare the oscillations where the amplitude is ~ 20 %, ~ 10 % and ~ 5 % of the averaged width. We do not observe any significant change in the position of the transition.

In general, we find that the transition always occurs when the mode frequency is similar to the pairing gap.

This is supported by the fact that when we vary the trap depth the transition occurs at a constant scattering length ($a \approx -5000 a_0$, B ≈ 960G) and does not depend on $1/k_F a$ [40]. A change in laser power of our trapping laser influences both Fermi energy E_F and the frequency $\omega_{\rm q}$. As we increase the trap power by a factor of 10, we also increase the radial trap frequencies by a factor of $\sqrt{10} \approx 3.2$. This changes the Fermi energy by a factor of 2.2 and the pairing gap, which scales like the trap frequencies, by roughly a factor of 3 [25]. These findings suggest that the transition is linked to a coupling of the collective oscillation to the pairing gap. This is also in agreement with earlier results on the radial compression mode [13, 19].
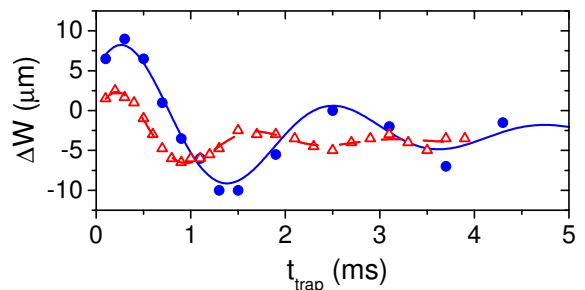
FIG. 7: (color online) Oscillations of the quadrupole surface mode at a magnetic field of 920 G and $1/k_F a = -0.66$. The filled circles correspond to a cold ensemble, whereas the open triangles correspond to a heated ensemble. The solid lines are fits to the data according to Eq.(3).

To explore the temperature dependence of the transition between the hydrodynamic and the collisionless phase, we use a controlled heating scheme similar to the one described in [20], where we hold the gas in a recompressed trap and let it heat up. We set the magnetic field to 920G ($1/k_F a = -0.66$), i.e. slightly below the hydrodynamic-to-collisionless transition, where the regime is still clearly hydrodynamic. We observe the oscillations in a gas at the lowest temperature we can achieve in our experiments (filled circles) and in a "hotter" gas (open triangles) in Fig. 7. The temperature of the cold gas is $\lesssim 0.1\,T_{\rm F}$ and we believe the temperature of the heated gas to be $\lesssim 0.2\,T_{\rm F}$. Figure 7 clearly shows that the frequency for the colder ensemble is lower than that of the heated one and the amplitude is lower by roughly a factor of 2. Using our model in Appendix A this indicates a temperature driven transfer of the ensemble from the hydrodynamic to the collisionless regime.

Thus we find that the radial quadrupole mode is suited to detect temperature induced changes of the collisional regime of the gas. An exploration of the phase diagram of our system depending on temperature is possible, but

beyond the scope of this article. In our lab, work is currently in progress on the radial scissors mode, which turns out to be an even better tool for the exploration of temperature effects.

V. CONCLUSIONS

We have presented measurements on the radial quadrupole mode of an ultracold ^{6}Li Fermi gas in the BEC-BCS crossover. As a pure surface excitation, this elementary mode probes hydrodynamic behavior without being affected by changes in the equation of state. We have measured the characteristic properties of this collective mode in a wide range of interaction strengths.

Our observations provide new insight into the dynamics of the gas, in particular on the BCS side of the crossover, where the character of the oscillations abruptly changes from hydrodynamic to collisionless behavior. Our measurements presented in this paper show the phenomenon much clearer than in the radial compression mode [19, 21, 23] and provide quantitative data on the behavior near the transition. In particular, the data show that a substantial down shift of the collective mode frequency occurs in the hydrodynamic regime as a precursor of the transition.

The experimental results support the interpretation that the coupling of oscillation mode and pairing gap [13, 25, 29] plays a crucial role for the collective excitation dynamics on the BCS side of the crossover. We anticipate that our new quantitative data on the hydrodynamic-to-collisionless transition will stimulate further theoretical investigations on this intriguing phenomenon.

APPENDIX A: SCALING APPROACH AND EXPANSION EFFECTS

Here we present a theoretical model to describe the oscillation of the cloud in the trap as well as its expansion after release; the model adopts the scaling approach applied in [41, 42, 43]. The interplay between the dynamics of the collective mode and the expansion behavior is of particular interest as it introduces novel methods to investigate the collisional regime. We use a scaling approach for both the hydrodynamic and the collisionless regime [41, 42, 43]. In App. A 1, the limit of a hydrodynamic gas is presented, whereas in App. A 2, the model in the collisionless regime is discussed. Based on these models, we show calculated results for the amplitude and the phase after expansion in App. A 3.

The scaling approach describes the cloud at the time t after excitation [41, 42, 43]. Using the scaling function $b_i(t)$ for $i = x, y$, the width $W_i(t)$ for all times $t > 0$ can be written as

$$W_i(t) = b_i(t)W_i(0), \tag{A1}$$

where $W_x(0) = (1 - \alpha)W_0$ and $W_y(0) = (1 + \alpha)W_0$ are the initial widths at excitation and W_0 is the width of the cloud without excitation. The initial conditions for the scaling function are $b_i(0) = 1$ and $\dot{b}_i(0) = 0$.

1. Dynamic behavior in the hydrodynamic limit

In the hydrodynamic limit, the equations of hydrodynamics lead to the following differential equations for b_x and b_y [42]

$$
\begin{aligned}
\ddot{b}_x &= \frac{\omega_{0x}^2}{b_x \left(b_x b_y\right)^{\gamma}} - b_x \, \omega_x^2, \\
\ddot{b}_y &= \frac{\omega_{0y}^2}{b_y \left(b_x b_y\right)^{\gamma}} - b_y \, \omega_y^2,
\end{aligned}
\tag{A2}
$$

where γ is the polytropic index of the equation of state and $b_z(t) = 1$ for our elongated trap geometry. The parameters ω_{0x} and ω_{0y} are the trap frequencies at the moment of excitation ($t = 0$), when the cloud has no further excitation and is in thermal equilibrium. In contrast to this, $\omega_x(t)$ and $\omega_y(t)$ are the time dependent trap frequencies. The timing scheme is illustrated in Fig. 3. The following equation summarizes the behavior of the trap frequencies $\omega_i(t)$:

$$
\omega_i(t) = \begin{cases} \omega_{0i} & , \, t = 0 \\ \omega_{\mathrm{r}} & , \, 0 < t < t_{\mathrm{trap}} \\ 0 & , \, t > t_{\mathrm{trap}}. \end{cases}
\tag{A3}
$$

This enables us to calculate the scaling functions b_x and b_y as solutions of Eq.(A2) for the in-trap oscillation. In the limit of small amplitudes ($\alpha \ll 1$) solutions are

$$
\begin{aligned}
b_x &= 1 + \alpha(1 - \cos \omega_{\mathrm{q}} t), \\
b_y &= 1 - \alpha(1 - \cos \omega_{\mathrm{q}} t),
\end{aligned}
\tag{A4}
$$

where $\omega_{\mathrm{q}} = \sqrt{2}\,\omega_{\mathrm{r}}$ is the radial quadrupole oscillation frequency. Together with Eq.(A1), we are able to determine the difference in widths of the cloud to be

$$\Delta W = -2\,\alpha W_0 \cos \omega_{\mathrm{q}} t. \tag{A5}$$

2. Dynamic behavior in the collisionless limit

In the collisionless limit, the following set of two uncoupled equations characterizes b_i, where i stands for x, y, [43]

$$\ddot{b}_i = \frac{\omega_{0i}^2}{b_i^3} - b_i \omega_i^2. \tag{A6}$$

In the limit of small amplitudes ($\alpha \ll 1$) solutions of the in-trap oscillation are

$$
\begin{aligned}
b_x &= 1 + \frac{\alpha}{2}(1 - \cos \omega_q t), \\
b_y &= 1 - \frac{\alpha}{2}(1 - \cos \omega_q t),
\end{aligned} \tag{A7}
$$

where $\omega_q = 2\omega_r$ is the radial quadrupole oscillation frequency. Together with Eq.(A1), we are able to determine the difference in widths of the cloud to be

$$\Delta W = -\alpha W_0 \left(1 + \cos \omega_q t\right). \tag{A8}$$

In contrast to the hydrodynamic limit, the oscillation is initially not centered around $\Delta W = 0$. Furthermore the oscillation has an amplitude $1/2$ of the amplitude in the hydrodynamic gas.

Besides the finding of analytical solutions, it is enlightning to understand the collective oscillations in the collisionless limit by considering the phase space dynamics of the cloud. In Fig. 8, we show the contours of phase space distributions in the x- and y- directions. The axes are scaled such that for the round trap, i.e. $\omega_x = \omega_y = \omega_r$, the dynamics of any point in phase space is a simple circular rotation about the origin with frequency ω_r. Thus, the solid circle in Fig. 8 (a) indicates an equilibrium phase space contour for the round trap. Right after applying the excitation scheme as described in Sec. III the phase space contours in the x- and y- direction are given by the dashed and dotted ellipses in Fig. 8 (a). Since the gas is fully thermalized at the instant of excitation, the initial momentum distribution in x- and y- direction is the same. As time progresses, the elliptic contours will rotate with frequency ω_r (see Fig. 8 (b)), which corresponds to oscillations in the trap. We note that both the spatial and the momentum distribution in the x-direction are never larger than the ones in the y-direction. Therefore, ΔW oscillates between $2\alpha W_0$ and zero and the aspect ratio of the cloud never inverts. This is to be compared to the hydrodynamic case where ΔW oscillates between $\pm 2\alpha W_0$.

Residual thermalization effects in a near collisionless gas will damp out the initial oscillation amplitude of αW_0 and one will eventually end up again with a circular phase space contour (see Fig. 8 (c)). This is studied in detail in Appendix B.

3. Amplitude and phase on expansion

Here we present our calculated results based on the models in App. A 1 and App. A 2 for the hydrodynamic
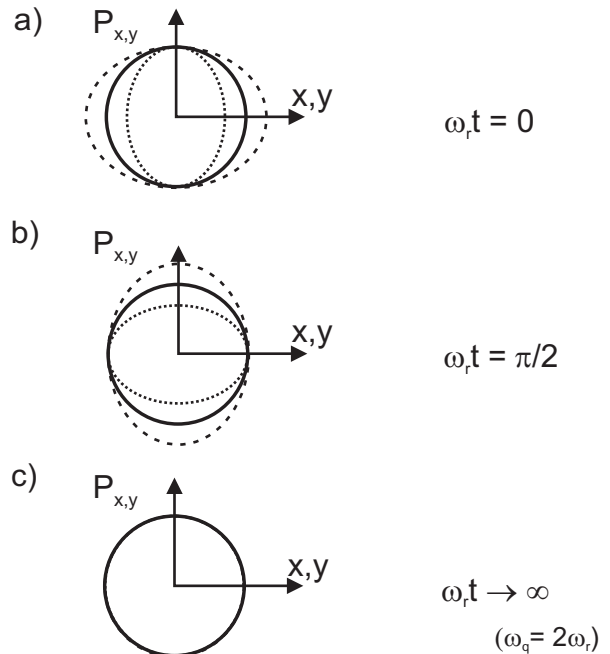

FIG. 8: Phase space dynamics for the quadrupole mode in the collisionless regime. Shown are phase space contours of an ensemble of particles which is held in a round trap (i.e. $\omega_x = \omega_y = \omega_r$). In (a) and (b) the situation during the oscillation in the trap is shown for two different times t. The solid line indicates the equilibrium phase space contour (without excitation), whereas the dotted (dashed) line shows the contour in the x (y) direction after excitation of the oscillation mode. (c) After long times, residual thermalization finally damps out the oscillations and leads to a circular phase space contour.

and the collisionless limit, respectively. We show the relative amplitude that is given by the amplitude A (definition see Eq.(3)) divided by the average width of the cloud after expansion (for definition details see Sec. IV B). Calculations of this relative amplitude are shown in Fig. 9, whereas calculations and measurements for the phase offset ϕ are shown in Fig. 10.

Fig. 9 shows the calculated relative amplitude of a surface mode oscillation in the hydrodynamic (dashed and dotted curves) and in the collisionless (solid curve) regime as function of the reduced expansion time $\omega_r t_{\mathrm{TOF}}$. The hydrodynamic curves are calculated for the BEC limit of $\gamma = 1$ (upper, dashed curve) and in the unitarity limit of $\gamma = 2/3$ (lower, dotted curve). The amplitude in the collisionless regime is smaller than in the hydrodynamic regime. Initially the amplitude of the excitation is half as large in the collisionless as in the hydrodynamic regime, as already explained in App. A 2. In expansion the normalized amplitude stays constant in the collisionless regime and in the hydrodynamic regime for $\gamma = 1$. For $\gamma = 2/3$ in the hydrodynamic regime it decreases for longer expansion times.
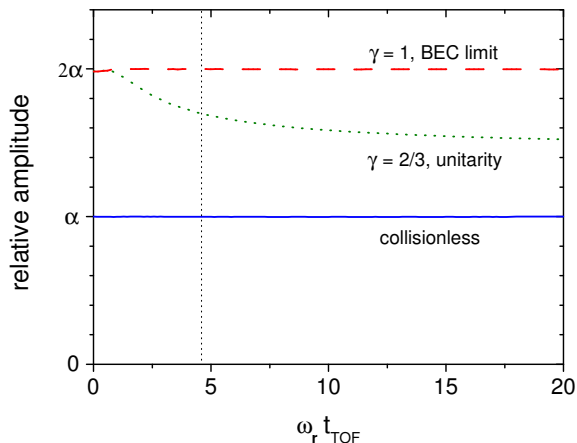
FIG. 9: (color online). Calculated relative amplitude of a surface mode oscillation versus reduced time of flight $\omega_r t_{\text{TOF}}$ after release from the trapping potential. The values are calculated for the hydrodynamic (dashed curve: $\gamma = 1$, dotted curve: $\gamma = 2/3$) and collisionless regime (solid curve). The vertical dotted line marks the typical expansion time in our experiments.

FIG. 10: (color online) Phase ϕ of the collective surface mode as detected by fits according to Eq.(3) versus reduced expansion time $\omega_r t_{\text{TOF}}$ at unitarity (open circles) and at $1/k_F a = -1.34$ (filled triangles). The lines are numerical simulations for the hydrodynamic (dashed line) and collisionless regime (solid line). The vertical dotted line marks the typical expansion time in our experiments.

In Fig. 10 we compare experimental data for the phase shift ϕ with numerical simulations. The data have been taken at unitarity where $1/k_F a = 0$ (hydrodynamic, open circles), and on the BCS-side of the resonance at $1/k_F a = -1.34$ (collisionless, closed triangles). The dashed line is based on a model for the hydrodynamic interaction regime and the solid line on a model for the collisionless regime. The data agree with the theoretical model where no free fit parameters are used. This confirms our approach presented above.

APPENDIX B: THERMALIZATION EFFECTS IN A NEAR-COLLISIONLESS GAS

Here we describe thermalization effects in a near-collisionless gas that are not included in the model for the collisionless limit in App. A 2. Despite the word "collisionless", collisions play a crucial role for thermalization for our experimental parameters. A typical time scale for thermalization processes is only a few oscillation cycles long. By analyzing the theory, we are able to introduce a universal fit function, as given by Eq.(3), which describes the oscillation both in the hydrodynamic and in the near-collisionless regime.

The measured behavior of the nearly collisionless quadrupole oscillation (see Fig. 4) has two characteristics: after excitation the oscillation is centered around $\Delta W = (W_x(0) - W_y(0))/2$, then after some time it is centered around $\Delta W = 0$. These two limits are consis-

tent with thermalization of the gas on a relevant time scale greater than the period of the oscillation.

In order to model these effects, we follow a theory based on a classical gas in the transition between the hydrodynamic and the collisionless behavior described in [38]. An application of this theory for the compression mode in the hydrodynamic regime has been used in [41]. Here we will handle thermalization effects of the quadrupole mode in the near-collisionless regime.

Using the classical Boltzmann-Vlasov kinetic equation in the relaxation-time approximation and ignoring mean field effects one can derive the following coupled differential equations [38]

$$\ddot{b}_i = \omega_{0i}^2 \frac{\theta_i}{b_i} - \omega_i^2 b_i \qquad (B1)$$

and

$$\dot{\theta}_i = \frac{1}{\tau_R}(\theta_i - \bar{\theta}) - 2\frac{\dot{b}_i}{b_i}\theta_i. \qquad (B2)$$

The parameter b_i is the scaling function described earlier in Appendix A; θ_i is a scaling parameter directly related to the temperature and $\bar{\theta} = \frac{1}{3}\Sigma_k \theta_k$. The initial condition for θ_i is $\theta_i(0) = 1$, as long as the gas is in thermal equilibrium at the moment of the excitation. The parameter τ_R is the relaxation time which describes the time scale of collisions. In the collisionless limit, when $\tau_R \to \infty$, the differential equations (B1) simplify to the simple form in Eq. (A6). For the hydrodynamic limit ($\tau_R \to 0$), we find Eq. (A2).

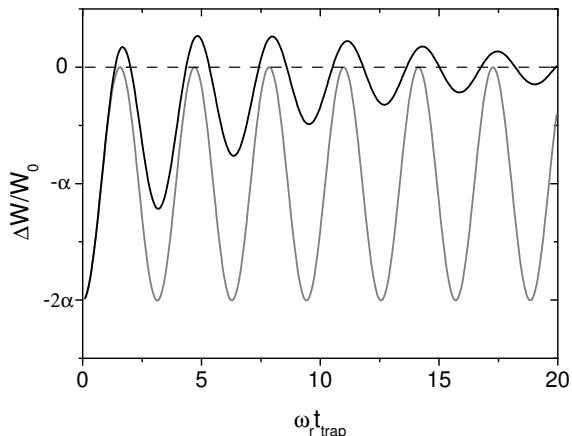FIG. 11: Calculated quadrupole oscillations in the near-collisionless regime. The lines show the relative difference in width ΔW as a function of the reduced time $\omega_r t_{\text{trap}}$. The oscillation is modeled according to Eq.(B1) and (B2). The dark line shows the result of the calculation when $\omega_r \tau_R = 2.3$ and the grey line shows the coscillation in the collisionless limit at $\omega_r \tau_R = 1000$.

The solutions to these equations depend on the parameter τ_R as can be seen in Fig. 11. Our measured data in the collisionless regime are well described by $\omega_r \tau_R \sim 2.3$ (compare to Fig. 4).

The universal fit function

We find that the model calculations from (B1) and (B2) can be well described with the following fit function

$$
\begin{aligned}
\Delta W = \ & A\ e^{-\kappa t_{\text{trap}}}\ \cos\left(\omega_q t_{\text{trap}} + \phi\right) \\
& + C\ e^{-\xi t_{\text{trap}}} + y_0.
\end{aligned} \tag{B3}
$$

The first term describes the exponentially damped oscillations. The second term describes the shift of the center of the oscillation in the collisionless regime. The third term y_0 is a constant offset which will be discussed later.

We have used Eq.(B3) to fit our experimental measurements. We find that the free fit parameters ξ and κ are related through $\xi/\kappa \approx 1.5$ for all our measurements in the near-collisionless regime. In the hydrodynamic regime $C = 0$, and therefore ξ becomes irrelevant.

The constant offset y_0 is due to an experimental artifact that results from a slight inhomogeneity of the magnetic field. At the location of the atoms the inhomogeneous magnetic field leads to a weak saddle potential which causes a slight anisotropic expansion during time of flight. This anisotropy is responsible for a slight offset in ΔW.

APPENDIX C: CORRECTIONS TO THE NORMALIZED FREQUENCY

The theoretical normalized frequencies ω_q/ω_r are calculated for perfectly harmonic trapping potentials in an idealized symmetric trap geometry. There are small derivations from this conditions in real experiments. In order to compare the experimental data to the idealized theoretical case, we have to correct our data. The measured normalized frequency ω_q/ω_r of the radial quadrupole mode has to be increased because of two small corrections. The larger correction is based upon a slight anharmonicity of the trapping potential and the spatial extension of the cloud in the trap. The smaller correction is caused by a small residual ellipticity of the trapping potential.

The potential created by our trapping beam has a Gaussian shape. This results in a nearly harmonic potential in the center of the trap; however, for higher precision one must take into account higher order terms of the potential. Anharmonicity effects influence both our measurements of the sloshing mode frequency, where we determine ω_r, and our measurements of the quadrupole mode frequency ω_q. As we evaluate the normalized frequency ω_q/ω_r, the anharmonicity effects on sloshing and quadrupole mode almost cancel out each other. The small remaining correction to the normalized frequency is included by multiplying with a prefactor $1 + b\sigma$ [20, 44]. The anharmonicity parameter σ relates the energy of the oscillation to the total potential depth and is defined by $\sigma = \frac{1}{2} m \omega_r^2 r_{\text{rms}}^2 / V_0$, where r_{rms} is the root-mean-square radius of the trapped cloud and V_0 is the potential depth. The parameter b depends on the interaction regime. In the hydrodynamic regime, it is given by $(4+10\gamma)/(2+7\gamma)$, whereas in the collisionless regime b is determined by $6/5$ [44]. Here, γ is the polytropic index of the equation of state. In our experiments, typically $b\sigma \approx 0.014$, but $b\sigma$ can rise to an upper limit of $b\sigma < 0.027$.

In the hydrodynamic regime, there is also a correction due to residual ellipticity effects. This correction takes into account that we compare our measurements with a theory for non-elliptic geometries. The ellipticity ϵ of the trap is defined by $\epsilon = (\omega_y - \omega_x)/\omega_r$. In our experiments, the ellipticity is small and given by $\epsilon \approx 0.07$. Therefore, we can apply the ellipticity correction by multiplication of a prefactor $1 + \lambda\epsilon^2$ [20, 44], where the interaction dependent factor λ is given by $(\gamma + 2)/(4\gamma)$. Altogether, $\lambda\epsilon^2$ is smaller than 0.006 for all data points.

[1] K. M. O'Hara, S. L. Hemmer, M. E. Gehm, S. R. Granade, and J. E. Thomas, Science **298**, 2179 (2002).

[2] T. Bourdel, J. Cubizolles, L. Khaykovich, K. M. F. Ma-

galhães, S. J. J. M. F. Kokkelmans, G. V. Shlyapnikov, and C. Salomon, Phys. Rev. Lett. **91**, 020402 (2003).

[3] S. Jochim, M. Bartenstein, A. Altmeyer, G. Hendl, S. Riedl, C. Chin, J. Hecker Denschlag, and R. Grimm, Science **302**, 2101 (2003).

[4] M. Greiner, C. A. Regal, and D. S. Jin, Nature **426**, 537 (2003).

[5] M. W. Zwierlein, C. A. Stan, C. H. Schunck, S. M. F. Raupach, S. Gupta, Z. Hadzibabic, and W. Ketterle, Phys. Rev. Lett. **91**, 250401 (2003).

[6] C. A. Regal, M. Greiner, and D. S. Jin, Phys. Rev. Lett. **92**, 040403 (2004).

[7] M. W. Zwierlein, C. A. Stan, C. H. Schunck, S. M. F. Raupach, A. J. Kerman, and W. Ketterle, Phys. Rev. Lett. **92**, 120403 (2004).

[8] *Ultracold Fermi Gases*, Proceedings of the International School of Physics "Enrico Fermi", Course CLXIV, Varenna, 20 - 30 June 2006, edited by M. Inguscio, W. Ketterle, and C. Salomon.

[9] D. M. Eagles, Phys. Rev. **186**, 456 (1969).

[10] A. J. Leggett, in *Modern Trends in the Theory of Condensed Matter*, edited by A. Pekalski and R. Przystawa (Springer Verlag, Berlin, 1980), vol. 115 of *Lecture Notes in Physics*, p. 13.

[11] P. Nozières and S. Schmitt-Rink, J. Low Temp. Phys. **59**, 195 (1985).

[12] J. R. Engelbrecht, M. Randeria, and C. A. R. Sá de Melo, Phys. Rev. B **55**, 15153 (1997).

[13] R. Grimm, in [8]; cond-mat/0703091.

[14] J. Cubizolles, T. Bourdel, S. J. J. M. F. Kokkelmans, G. V. Shlyapnikov, and C. Salomon, Phys. Rev. Lett. **91**, 240401 (2003).

[15] S. Jochim, M. Bartenstein, A. Altmeyer, G. Hendl, C. Chin, J. Hecker Denschlag, and R. Grimm, Phys. Rev. Lett. **91**, 240402 (2003).

[16] M. Houbiers, H. T. C. Stoof, W. I. McAlexander, and R. G. Hulet, Phys. Rev. A **57**, R1497 (1998).

[17] M. Bartenstein, A. Altmeyer, S. Riedl, R. Geursen, S. Jochim, C. Chin, J. Hecker Denschlag, R. Grimm, A. Simoni, E. Tiesinga, C. J. Williams, and P. S. Julienne, Phys. Rev. Lett. **94**, 103201 (2005).

[18] J. Kinast, S. L. Hemmer, M. E. Gehm, A. Turlapov, and J. E. Thomas, Phys. Rev. Lett. **92**, 150402 (2004).

[19] M. Bartenstein, A. Altmeyer, S. Riedl, S. Jochim, C. Chin, J. Hecker Denschlag, and R. Grimm, Phys. Rev. Lett. **92**, 203201 (2004).

[20] A. Altmeyer, S. Riedl, C. Kohstall, M. Wright, R. Geursen, M. Bartenstein, C. Chin, J. Hecker Denschlag, and R. Grimm, Phys. Rev. Lett. **98**, 040401 (2007).

[21] J. Kinast, A. Turlapov, and J. E. Thomas, Phys. Rev. A **70**, 051401(R) (2004).

[22] J. Kinast, A. Turlapov, and J. E. Thomas, Phys. Rev. Lett. **94**, 170404 (2005).

[23] A. Altmeyer, S. Riedl, C. Kohstall, M. Wright, J. Hecker Denschlag, and R. Grimm, cond-mat/0611285.

[24] S. Stringari, in [8]; cond-mat/0702526.

[25] C. Chin, M. Bartenstein, A. Altmeyer, S. Riedl, S. Jochim, J. Hecker Denschlag, and R. Grimm, Science **305**, 1128 (2004).

[26] S. Stringari, Phys. Rev. Lett. **77**, 2360 (1996).

[27] R. Onofrio, D.S. Durfee, C. Raman, M. Köhl, C.E. Kuklewicz, and W. Ketterle, Phys. Rev. Lett. **84**, 810 (2000).

[28] V. Bretin, P. Rosenbusch, F. Chevy, G.V. Shlyapnikov, and J. Dalibard, Phys. Rev. Lett. **90**, 100404 (2003).

[29] R. Combescot, and X. Leyronas, Phys. Rev. Lett. **93**, 138901 (2004).

[30] R. Combescot, M. Yu. Kagan, and S. Stringari, cond-mat/0607493.

[31] M. Bartenstein, A. Altmeyer, S. Riedl, S. Jochim, C. Chin, J. Hecker Denschlag, and R. Grimm, Phys. Rev. Lett. **92**, 120401 (2004).

[32] V. Milner, J. L. Hanssen, W. C. Campbell, and M. G. Raizen, Phys. Rev. Lett. **86**, 1514 (2001).

[33] N. Friedman, A. Kaplan, D. Carasso, and N. Davidson, Phys. Rev. Lett. **86**, 1518 (2001).

[34] We use a periodic modulation with an arc sine-like function. This results in much better harmonic potentials than a simple sawtooth modulation ramp [45].

[35] Ch. Buggle, P. Pedri, W. von Klitzing, and J. T. M. Walraven, Phys. Rev. A **72**, 043610 (2005).

[36] L. Vichi, J. Low. Temp. Phys. **121**, 177 (2000).

[37] Note that in the present measurements, the temperatures are somewhat higher than in our recent compression mode measurements [20]. There are esentially two reasons for the higher temperatures. First, the atoms stay longer in the recompressed trap because of the longer excitation scheme of the quadrupole mode. Second, for the quadrupole measurements we optimized our evaporative cooling scheme regarding particle number and not temperature.

[38] P. Pedri, D. Guéry-Odelin, and S. Stringari, Phys. Rev. A. **68**, 043608 (2003).

[39] Michael Urban, cond-mat/0612361.

[40] Due to the increased Fermi wave number k_F for the deeper trap configuration, the transition in terms of the interaction parameter shifts from $1/k_F a \approx -0.8$ to $1/k_F a \approx -0.5$.

[41] J. Kinast, PhD thesis, Duke University (2006).

[42] C. Menotti, P. Pedri,and S. Stringari, Phys. Rev. Lett. **89**, 250402 (2002).

[43] G. M. Bruun, and C. W. Clark, Phys. Rev. A **61**, 061601(R) (2000).

[44] A. Altmeyer, PhD thesis, Univ. Innsbruck, in preparation.

[45] C. Kohstall, diploma thesis, Univ. Innsbruck (2007).

156

References

[Alt06]   A. Altmeyer, S. Riedl, C. Kohstall, M. Wright, J. H. Denschlag, and R. Grimm, *Note on "Collective Excitations of a Degenerate Gas at the BEC-BCS Crossover", Phys. Rev. Lett. 92, 203201 (2004)* (2006), http://xxx.lanl.gov/abs/cond-mat/0611285.

[Alt07]   A. Altmeyer, S. Riedl, C. Kohstall, M. Wright, R. Geursen, M. Bartenstein, C. Chin, J. H. Denschlag, and R. Grimm, *Precision Measurements of Collective Oscillations in the BEC-BCS Crossover*, Phys. Rev. Lett. **98**, 040401 (2007).

[And95]   M. H. Anderson, J. R. Ensher, M. R. Matthews, C. E. Wieman, and E. A. Cornell, *Observation of Bose-Einstein Condensation in a Dilute Atomic Vapor*, Science **269**, 198 (1995).

[Ari77]   E. Arimondo, M. Inguscio, and P. Violino, *Experimental determination of the hyperfine structure in the alkali atoms*, Rev. Mod. Phys. **49**, 31 (1977).

[Ast04]   G. E. Astrakharchik, J. Boronat, J. Casulleras, and S. Giorgini, *Equation of State of a Fermi Gas in the BEC-BCS Crossover: A Quantum Monte Carlo Study*, Phys. Rev. Lett. **93**, 200404 (2004).

[Ast05]   G. E. Astrakharchik, R. Combescot, X. Leyronas, and S. Stringari, *Equation of State and Collective Frequencies of a Trapped Fermi Gas along the BEC-Unitarity Crossover*, Phys. Rev. Lett. **95**, 030404 (2005).

[Aub06]   S. Aubin, S. Myrskog, M. H. T. Extavour, L. J. Leblanc, D. Mckay, A. Stummer, and J. H. Thywissen, *Rapid sympathetic cooling to Fermi degeneracy on a chip*, Nature Phys. **2**, 384 (2006).

[Bar57a]   J. Bardeen, L. N. Cooper, and J. R. Schrieffer, *Microscopic Theory of Superconductivity*, Phys. Rev. **106**, 162 (1957).

[Bar57b]   J. Bardeen, L. N. Cooper, and J. R. Schrieffer, *Theory of Superconductivity*, Phys. Rev. **108**, 1175 (1957).

References

[Bar04a]   M. Bartenstein, A. Altmeyer, S. Riedl, S. Jochim, C. Chin, J. Hecker Den-schlag, and R. Grimm, *Collective excitations of a degenerate gas at the BEC-BCS crossover*, Phys. Rev. Lett. **92**, 203201 (2004).

[Bar04b]   M. Bartenstein, A. Altmeyer, S. Riedl, S. Jochim, C. Chin, J. Hecker Den-schlag, and R. Grimm, *Crossover from a Molecular Bose-Einstein Con-densate to a Degenerate Fermi Gas*, Phys. Rev. Lett. **92**, 120401 (2004).

[Bar05a]   M. Bartenstein, *From Molecules to Cooper Pairs: Experiments in the BEC-BCS Crossover*, Ph.D. thesis, Universität Innsbruck (2005).

[Bar05b]   M. Bartenstein, A. Altmeyer, S. Riedl, R. Geursen, S. Jochim, C. Chin, J. Hecker Denschlag, R. Grimm, A. Simoni, E. Tiesinga, C. J. Williams, and P. S. Julienne, *Precise determination of ^6Li cold collision parameters by radio-frequency spectroscopy on weakly bound molecules*, Phys. Rev. Lett. **94**, 103201 (2005).

[Bay96]   G. Baym and C. J. Pethick, *Ground-State Properties of Magnetically Trapped Bose-Condensed Rubidium Gas*, Phys. Rev. Lett. **76**, 6 (1996).

[Bog47]   N. Bogolubov, *On the theory of superfluidity*, J. Phys. **11**, 23 (1947).

[Bou03]   T. Bourdel, J. Cubizolles, L. Khaykovich, K. M. F. Magalhães, S. J. J. M. F. Kokkelmans, G. V. Shlyapnikov, and C. Salomon, *Measurement of the In-teraction Energy near a Feshbach Resonance in a ^6Li Fermi Gas*, Phys. Rev. Lett. **91**, 020402 (2003).

[Bou04]   T. Bourdel, L. Khaykovich, J. Cubizolles, J. Zhang, F. Chevy, M. Teich-mann, L. Tarruell, S. J. J. M. F. Kokkelmans, and C. Salomon, *Experimen-tal Study of the BEC-BCS Crossover Region in Lithium 6*, Phys. Rev. Lett. **93**, 050401 (2004).

[Bra95]   C. C. Bradley, C. A. Sackett, J. J. Tollett, and R. G. Hulet, *Evidence of Bose-Einstein Condensation in an Atomic Gas with Attractive Interactions*, Phys. Rev. Lett. **75**, 1687 (1995), *ibid.* **79**, 1170 (1997).

[Bra06]   E. Braaten and H.-W. Hammer, *Universality in few-body systems with large scattering length*, Phys. Rep. **428**, 259 (2006).

[Bru00]   G. M. Bruun and C. W. Clark, *Ideal gases in time-dependent traps*, Phys. Rev. A **61**, 061601(R) (2000).

[Bug05]   C. Buggle, P.Pedri, W. von Klitzing, and J. Walraven, *Shape oscillations in nondegenerate Bose gases: Transition from the collisionless to the hydro-dynamic regime*, Phys. Rev. A **72**, 043610 (2005).

[Bul05]   A. Bulgac and G. F. Bertsch, *Collective oscillations of a trapped Fermi gas near the unitary limit*, Phys. Rev. Lett. **94**, 070401 (2005).

[Car03]   J. Carlson, S.-Y. Chang, V. Pandharipande, and K. Schmidt, *Superfluid Fermi Gases with Large Scattering Length*, Phys. Rev. Lett. **91**, 050401 (2003).

[Cas96]   Y. Castin and R. Dum, *Bose-Einstein Condensates in Time-Dependent Traps*, Phys. Rev. Lett. **77**, 5315 (1996).

[Che02]   F. Chevy, V. Bretin, P. Rosenbusch, K. W. Madison, and J. Dalibard, *Transverse Breathing Mode of an Elongated Bose-Einstein Condensate*, Phys. Rev. Lett. **88**, 250402 (2002).

[Che04]   Q. Chen, J. Stajic, S. Tan, and K. Levin, *BCS-BEC Crossover: From High Temperature Superconductors to Ultracold Superfluids*, Physics Reports **412**, 1 (2004).

[Chi02]   M. L. Chiofalo, S. J. J. M. F. Kokkelmans, J. N. Milstein, and M. J. Holland, *Signatures of Resonance Superfluidity in a Quantum Fermi Gas*, Phys. Rev. Lett. **88**, 090402 (2002).

[Chi04a]   C. Chin, M. Bartenstein, A. Altmeyer, S. Riedl, S. Jochim, J. Hecker Denschlag, and R. Grimm, *Observation of the pairing gap in a strongly interacting Fermi gas*, Science **305**, 1128 (2004), published online 22 July 2004; 10.1126/science.1100818.

[Chi04b]   C. Chin and R. Grimm, *Thermal equilibrium and efficient evaporation of an ultracold atom-molecule mixture*, Phys. Rev. A **69**, 033612 (2004).

[Com04a]   R. Combescot and X. Leyronas, *Axial collective excitations of a degenerate Fermi gas in the BEC to unitarity crossover*, Europhys. Lett. **68**, 762 (2004).

[Com04b]   R. Combescot and X. Leyronas, *Comment on "Collective excitations of a degenerate gas in the BEC-BCS crossover"*, Phys. Rev. Lett. **93**, 138901 (2004).

[Com06]   R. Combescot, M. Kagan, and S.Stringari, *Collective mode of homogeneous superfluid Fermi gases in the BEC-BCS crossover* (2006), http://arxiv.org/abs/cond-mat/0607493.

[Coo56]   L. N. Cooper, *Bound Electron Pairs in a Degenerate Fermi Gas*, Phys. Rev. **104**, 1189 (1956).

References

[Coz03]   M. Cozzini and S. Stringari, *Fermi Gases in Slowly Rotating Traps: Superfluid versus Collisional Hydrodynamics*, Phys. Rev. Lett. **91**, 070401 (2003).

[Cub03]   J. Cubizolles, T. Bourdel, S. Kokkelmans, G. Shlyapnikov, and C. Salomon, *Production of Long-Lived Ultracold Li_2 Molecules from a Fermi Gas*, Phys. Rev. Lett. **91**, 240401 (2003).

[Dal97a]   F. Dalfovo, S. Giorgini, M. Guilleumas, L. Pitaevskii, and S. Stringari, *Collective and single-particle excitations of a trapped Bose gas*, Phys. Rev. A **56**, 3840 (1997).

[Dal97b]   F. Dalfovo, C. Minniti, and L. P. Pitaevskii, *Frequency shift and mode coupling in the nonlinear dynamics of a Bose-condensed gas*, Phys. Rev. A **56**, 4855 (1997).

[Dal99a]   F. Dalfovo, S. Giorgini, L. P. Pitaevskii, and S. Stringari, *Theory of Bose-Einstein condensation in trapped gases*, Rev. Mod. Phys. **71**, 463 (1999).

[Dal99b]   J. Dalibard, *Collisional dynamics of ultra-cold atomic gases*, in: M. Inguscio, S. Stringari, and C. E. Wieman (Eds.), *Proceedings of the International School of Physics - Enrico Fermi*, 321, IOS Press, 1999.

[Dav95]   K. B. Davis, M.-O. Mewes, M. R. Andrews, N. J. van Druten, D. S. Durfee, D. M. Kurn, and W. Ketterle, *Bose-Einstein Condensation in a Gas of Sodium Atoms*, Phys. Rev. Lett. **75**, 3969 (1995).

[DeM99]   B. DeMarco and D. S. Jin, *Onset of Fermi Degeneracy in a Trapped Atomic Gas*, Science **285**, 1703 (1999).

[DeM01]   B. DeMarco, S. B. Papp, and D. S. Jin, *Pauli Blocking of Collisions in a Quantum Degenerate Atomic Fermi Gas*, Phys. Rev. Lett. **86**, 5409 (2001).

[Die02]   K. Dieckmann, C. A. Stan, S. Gupta, Z. Hadzibabic, C. H. Schunck, and W. Ketterle, *Decay of an Ultracold Fermionic Lithium Gas near a Feshbach Resonance*, Phys. Rev. Lett. **89**, 203201 (2002).

[Die04]   R. B. Diener and T.-L. Ho, *The Condition for Universality at Resonance and Direct Measurement of Pair Wavefunctions Using rf Spectroscopy* (2004), http://arxiv.org/abs/cond-mat/0405174.

[Eag69]   D. M. Eagles, *Possible Pairing without Superconductivity at Low Carrier Concentrations in Bulk and Thin-Film Superconducting Semiconductors*, Phys. Rev. **186**, 456 (1969).

[Edw96]   M. Edwards, P. A. Ruprecht, K. Burnett, R. J. Dodd, and C. W. Clark, *Collective Excitations of Atomic Bose-Einstein Condensates*, Phys. Rev. Lett. **77**, 1671 (1996).

[Els00]   T. Elsässer, *Stehwellenfalle in einem Resonator*, diploma thesis, Max-Planck-Institut für Kernphysik, Heidelberg (2000).

[Eng97]   J. R. Engelbrecht, M. Randeria, and C. A. R. Sá de Melo, *BCS to Bose crossover: Broken-symmetry state*, Phys. Rev. B **55**, 15153 (1997).

[Fer99]   G. Ferrari, *Collisional relaxation in a fermionic gas*, Phys. Rev. A **59**, R4125 (1999).

[Fes58]   H. Feshbach, *A Unified Theory of Nuclear Reactions*, Ann. Phys. **5**, 337 (1958).

[Fet96]   A. L. Fetter, *Ground state and excited states of a trapped dilute condensed Bose gas*, Czech. J. Phys. **46**, 3063 (1996).

[Fri01]   N. Friedman, A. Kaplan, D. Carasso, and N. Davidson, *Observation of Chaotic and Regular Dynamics in Atom-Optics Billiards*, Phys. Rev. Lett. **86**, 1518 (2001).

[Geh03]   M. E. Gehm, S. L. Hemmer, S. R. Granade, K. M. O'Hara, and J. E. Thomas, *Mechanical stability of a strongly interacting Fermi gas of atoms*, Phys. Rev. A **68**, 011401(R) (2003).

[Gio00]   S. Giorgini, *Collisionless dynamics of dilute Bose gases: Role of quantum and thermal fluctuations*, Phys. Rev. A **61**, 063615 (2000).

[GO99]   D. Guéry-Odelin and S. Stringari, *Scissors Mode and Superfluidity of a Trapped Bose-Einstein Condensed Gas*, Phys. Rev. Lett. **83**, 4452 (1999).

[Gor61]   L. P. Gorkov and T. K. Melik-Barkhudarov, *Contribution to the theory of superfluidity in an imperfect Fermi gas*, Sov. Phys. JETP **13**, 1018 (1961).

[Gra02]   S. R. Granade, M. E. Gehm, K. M. O'Hara, and J. E. Thomas, *All-Optical Production of a Degenerate Fermi Gas*, Phys. Rev. Lett. **88**, 120405 (2002).

[Gre03]   M. Greiner, C. A. Regal, and D. S. Jin, *Emergence of a molecular Bose-Einstein condensate from a Fermi gas*, Nature **426**, 540 (2003), doi:10.1038/nature02199; Published online 26 November 2003.

[Gre05]   M. Greiner, C. C. A. Regal, and D. S. Jin, *Probing the excitation spectrum of a Fermi gas in the BCS-BEC crossover regime*, Phys. Rev. Lett. **94**, 070403 (2005).

References

[Gri93] G. F. Gribakin and V. V. Flambaum, *Calculation of the scattering length in atomic collisions using the semiclassical approximation*, Phys. Rev. A **48**, 546 (1993).

[Gri00] R. Grimm, M. Weidemüller, and Y. Ovchinnikov, *Optical dipole traps for neutral atoms*, Adv. At. Mol. Opt. Phys. **42** (2000).

[Gri07] R. Grimm, *Ultracold Fermi gases in the BEC-BCS crossover: a review from the Innsbruck perspective*, in: M. Inguscio, W. Ketterle, and C. Salomon (Eds.), *Ultracold Fermi Gases, Proceedings of the International School of Physics "Enrico Fermi", Course CLXIV, Varenna, 20 - 30 June 2006*, ?, ?, 2007.

[Gro61] E. P. Gross, *Structure in Quantized Vortex in Boson Systems*, Il Nuovo Cimento **20**, 454 (1961).

[Gup04] S. Gupta, Z. Hadzibabic, J. Anglin, and W. Ketterle, *Collisions in Zero Temperature Fermi Gases*, Phys. Rev. Lett. **92**, 100401 (2004).

[Had02] Z. Hadzibabic, C. A. Stan, K. Dieckmann, S. Gupta, M. W. Zwierlein, A. Görlitz, and W. Ketterle, *Two-Species Mixture of Quantum Degenerate Bose and Fermi Gases*, Phys. Rev. Lett. **88**, 160401 (2002).

[Hän80] T. W. Hänsch and B. Couillaud, *Laser frequency stabilization by polarization spectroscopy of a reflecting reference cavity*, Opt. Commun. **35**, 441 (1980).

[Hei01] H. Heiselberg, *Fermi systems with long scattering lengths*, Phys. Rev. A **63**, 043606 (2001).

[Hei04] H. Heiselberg, *Collective Modes of Trapped Gases at the BEC-BCS Crossover*, Phys. Rev. Lett. **93**, 040402 (2004).

[Hen03] G. Hendl, *Atom - Atom Wechselwirkung in einem ultrakalten, fermionischen Gas*, diploma thesis, Universität Innsbruck (2003).

[Ho04a] T.-L. Ho, *Universal Thermodynamics of Degenerate Quantum Gases in the Unitarity Limit*, Phys. Rev. Lett. **92**, 090402 (2004).

[Ho04b] T.-L. Ho and E. J. Mueller, *High Temperature Expansion Applied to Fermions near Feshbach Resonance*, Phys. Rev. Lett. **92**, 160404 (2004).

[Hol01] M. Holland, S. J. J. M. F. Kokkelmans, M. L. Chiofalo, and R. Walser, *Resonance Superfluidity in a Quantum Degenerate Fermi Gas*, Phys. Rev. Lett. **87**, 120406 (2001).

[Hou98] M. Houbiers, H. T. C. Stoof, W. I. McAlexander, and R. G. Hulet, *Elastic and inelastic collisions of Li-6 atoms in magnetic and optical traps*, Phys. Rev. A **57**, R1497 (1998).

[Hu04] H. Hu, A. Minguzzi, X.-J. Liu, and M. P. Tosi, *Collective modes and ballistic expansion of a Fermi gas in the BCS-BEC crossover*, Phys. Rev. Lett. **93**, 190403 (2004).

[Hua57] K. Huang and C. N. Yang, *Quantum-Mechanical Many-Body Problem with Hard-Sphere Interaction*, Phys. Rev. **105**, 767 (1957).

[Hua87] K. Huang, *Statistical Mechanics*, John Wiley & Sons, 1987, 2nd ed.

[Ino98] S. Inouye, M. R. Andrews, J. Stenger, H.-J. Miesner, D. M. Stamper-Kurn, and W. Ketterle, *Observation of Feshbach resonances in a Bose-Einstein condensate*, Nature **392**, 151 (1998).

[Iud78] N. L. Iudice and F. Palumbo, *New Isovector Collective Modes in Deformed Nuclei*, Phys. Rev. Lett. **41**, 1532 (1978).

[Jen04] A. S. Jensen, K. Riisager, D. V. Fedorov, and E. Garrido, *Structure and reactions of quantum halos*, Rev. Mod. Phys. **76**, 215 (2004).

[Jin96] D. S. Jin, J. R. Ensher, M. R. Matthews, C. E. Wieman, and E. A. Cornell, *Collective Excitations of a Bose-Einstein Condensate in a Dilute Gas*, Phys. Rev. Lett. **77**, 420 (1996).

[Jin97] D. S. Jin, M. R. Matthews, J. R. Ensher, C. E. Wieman, and E. A. Cornell, *Temperature-Dependent Damping and Frequency Shifts in Collective Excitations of a Dilute Bose-Einstein Condensate*, Phys. Rev. Lett. **78**, 764 (1997).

[J.K05] J.Kinast, *Thermodynamics And Superfluidity Of A Strongly Interacting Fermi Gas*, Ph.D. thesis, Duke University (2005).

[Joc00] S. Jochim, *Aufbau einer Apparatur zum magnetooptischen Einfang von fermionischen Lithiumatomen*, diploma thesis, Max-Planck-Institut für Kernphysik, Heidelberg (2000).

[Joc02] S. Jochim, M. Bartenstein, G. Hendl, J. Hecker Denschlag, R. Grimm, A. Mosk, and M. Weidemüller, *Magnetic Field Control of Elastic Scattering in a Cold Gas of Fermionic Lithium Atoms*, Phys. Rev. Lett. **89**, 273202 (2002).

[Joc03a] S. Jochim, M. Bartenstein, A. Altmeyer, G. Hendl, S. Riedl, C. Chin, J. Hecker Denschlag, and R. Grimm, *Bose-Einstein Condensation of Molecules*, Science **301**, 2101 (2003), published online 13 November 2003; 10.1126/science.1093280.

References

[Joc03b] S. Jochim, M. Bartenstein, A. Altmeyer, G. Hendl, C. Chin, J. Hecker Denschlag, and R. Grimm, *Pure Gas of Optically Trapped Molecules Created from Fermionic Atoms*, Phys. Rev. Lett. **91**, 240402 (2003).

[Joc04] S. Jochim, *Bose-Einstein Condensation of Molecules*, Ph.D. thesis, Universität Innsbruck (2004).

[Jos06] J. Joseph, B. Clancy, L. Luo, J. Kinast, A. Turlapov, and J. Thomas, *Sound propagation in a Fermi gas near a Feshbach resonance* (2006), http://xxx.lanl.gov/abs/cond-mat/0612567v1.

[Kag96] Y. Kagan, E. L. Surkov, and G. V. Shlyapnikov, *Evolution of a Bose-condensed gas under variations of the confining potential*, Phys. Rev. A **54**, R1753 (1996).

[Ket99] W. Ketterle, D. S. Durfee, and D. M. Stamper-Kurn, *Making, probing and understanding Bose-Einstein condensates*, in: M. Inguscio, S. Stringari, and C. E. Wieman (Eds.), *Proceedings of the International School of Physics - Enrico Fermi*, 67, IOS Press, 1999.

[Kim04a] Y. E. Kim and A. L. Zubarev, *Dynamics of Strongly Interacting Fermi Gases of Atoms in a Harmonic Trap*, Phys. Lett. A **327**, 397 (2004).

[Kim04b] Y. E. Kim and A. L. Zubarev, *Time-dependent density-functional theory for trapped strongly interacting fermionic atoms*, Phys. Rev. A **70**, 033612 (2004).

[Kin04a] J. Kinast, S. L. Hemmer, M. E. Gehm, A. Turlapov, and J. E. Thomas, *Evidence for Superfluidity in a Resonantly Interacting Fermi Gas*, Phys. Rev. Lett. **92**, 150402 (2004).

[Kin04b] J. Kinast, A. Turlapov, and J. E. Thomas, *Breakdown of hydrodynamics in the radial breathing mode of a strongly interacting Fermi gas*, Phys. Rev. A **70**, 051401(R) (2004).

[Kin05a] J. Kinast, A. Turlapov, and J. E. Thomas, *Damping of a Unitary Fermi Gas*, Phys. Rev. Lett. **94**, 170404 (2005).

[Kin05b] J. Kinast, A. Turlapov, and J. E. Thomas., *Heat Capacity of a Strongly Interacting Fermi Gas*, Science Express (2005), published online 27 January 2005; 10.1126/science.1109220.

[Köh05] M. Köhl, H. Moritz, T. Stöferle, K. Günter, and T. Esslinger, *Fermionic Atoms in a Three Dimensional Optical Lattice: Observing Fermi Surfaces, Dynamics, and Interactions*, Phys. Rev. Lett. **94** (2005).

[Koh07]   C. Kohstall, *A New Toolbox for Experiments with Ultracold ^6Li*, diploma thesis, Universität Innsbruck (2007).

[Kok02]   S. J. J. M. F. Kokkelmans, J. N. Milstein, M. L. Chiofalo, R. Walser, and M. J. Holland1, *Resonance superfluidity: Renormalization of resonance scattering theory*, Phys. Rev. A **65**, 053617 (2002).

[Lan77]   L. D. Landau and E. M. Lifshitz, *Quantum Mechanics: Non-Relativistic Theory*, Pergamon Press, Oxford, 1977, 3rd ed.

[Lee57a]   T. D. Lee, K. Huang, and C. N. Yang, *Eigenvalues and Eigenfunctions of a Bose System of Hard Spheres and Its Low-Temperature Properties*, Phys. Rev. **106**, 1135 (1957).

[Lee57b]   T. D. Lee and C. N. Yang, *Many-Body Problem in Quantum Mechanics and Quantum Statistical Mechanics*, Phys. Rev. **105**, 1119 (1957).

[Leg80]   A. J. Leggett, *Diatomic Molecules and Cooper Pairs*, in: A. Pekalski and R. Przystawa (Eds.), *Modern Trends in the Theory of Condensed Matter*, 13–27, Springer-Verlag, Berlin, 1980.

[Lip83]   E. Lipparini and S. Stringari, *Isovector M1 rotational states in deformed nuclei*, Phys. Lett. B **130**, 139 (1983).

[Man05]   N. Manini, L. Salasnicheras, and S. Giorgini, *Bulk and Collective Properties of a Dilute Fermi Gas in the BCS-BEC Crossover*, Phys. Rev. A **71**, 033625 (2005).

[Mar00]   O. M. Maragó, S. A. Hopkins, J. Arlt, E. Hodby, G. Heckenblaikner, and C. J. Foot, *Observation of the Scissors Mode and Evidence for Superfluidity of a Trapped Bose-Einstein Condensed Gas*, Phys. Rev. Lett. **84**, 2056 (2000).

[Men02]   C. Menotti, P. Pedri, and S. Stringari, *Expansion of an Interacting Fermi Gas*, Phys. Rev. Lett. **89**, 250402 (2002).

[Mew96]   M.-O. Mewes, M. R. Andrews, N. J. van Druten, D. M. Kurn, D. S. Durfee, C. G. Townsend, and W. Ketterle, *Collective Excitations of a Bose-Einstein Condensate in a Magnetic Trap*, Phys. Rev. Lett. **77**, 988 (1996).

[Mil01]   V. Milner, J. L. Hanssen, W. C. Campbell, and M. G. Raizen, *Optical Billiards for Atoms*, Phys. Rev. Lett. **86**, 1514 (2001).

[Mil02]   J. N. Milstein, S. J. J. M. F. Kokkelmans, and M. J. Holland, *Resonance theory of the crossover from Bardeen-Cooper-Schrieffer superfluidity to Bose-Einstein condensation in a dilute Fermi gas*, Phys. Rev. A **66**, 043604 (2002).

References

[Mor01]   H. Moritz, *Fermionisches Lithium in einer Resonatordipolfalle*, diploma thesis, Max-Planck-Institut für Kernphysik, Heidelberg (2001).

[Noz85]   P. Nozières and S. Schmitt-Rink, *Bose Condensation in an Attractive Fermion Gas: From Weak to Strong Coupling Superconductivity*, J. Low Temp. Phys. **59**, 195 (1985).

[O'H02a] K. M. O'Hara, S. L. Hemmer, M. E. Gehm, S. R. Granade, and J. E. Thomas, *Observation of a Strongly Interacting Degenerate Fermi Gas of Atoms*, Science **298**, 2179 (2002).

[O'H02b] K. M. O'Hara, S. L. Hemmer, S. R. Granade, M. E. Gehm, J. E. Thomas, V. Venturi, E. Tiesinga, and C. J. Williams, *Measurement of the zero crossing in a Feshbach resonance of fermionic ^{6}Li*, Phys. Rev. A **66**, 041401(R) (2002).

[Oha02]   Y. Ohashi and A. Griffin, *BCS-BEC Crossover in a Gas of Fermi Atoms with a Feshbach Resonance*, Phys. Rev. Lett. **89**, 130402 (2002).

[Ono00]   R. Onofrio, D. S. Durfee, C. Raman, M. Köhl, C. E. Kuklewicz, and W. Ketterle, *Surface Excitations of a Bose-Einstein Condensate*, Phys. Rev. Lett. **84**, 810 (2000).

[Osp06]   C. Ospelkaus, S. Ospelkaus, K. Sengstock, and K. Bongs, *Interaction-Driven Dynamics of [sup 40]K-[sup 87]Rb Fermion-Boson Gas Mixtures in the Large-Particle-Number Limit*, Phys. Rev. Lett. **96** (2006).

[Par05]   G. B. Partridge, K. E. Strecker, R. I. Kamar, M. W. Jack, and R. G. Hulet, *Molecular Probe of Pairing in the BEC-BCS Crossover*, Phys. Rev. Lett. **95**, 020404 (2005).

[Ped03]   P. Pedri, D. Guéry-Odelin, and S. Stringari, *Dynamics of a classical gas including dissipative and mean-field effects*, Phys. Rev. A **68**, 043608 (2003).

[Per04]   A. Perali, P. Pieri, L. Pisani, and G. C. Strinati, *BCS-BEC Crossover at Finite Temperature for Superfluid Trapped Fermi Atoms*, Phys. Rev. Lett. **92**, 220404 (2004).

[Pet02]   C. J. Pethick and H. Smith, *Bose-Einstein Condensation in Dilute Gases*, Cambridge University Press, 2002.

[Pet04]   D. Petrov, C. Salomon, and G. Shlyapnikov, *Weakly bound dimers of fermionic atoms*, Phys. Rev. Lett. **93**, 090404 (2004).

[Pet05]   D. S. Petrov, C. Salomon, and G. V. Shlyapnikov, *Scattering properties of weakly bound dimers of fermionic atoms*, Phys. Rev. A **71**, 012708 (2005).

[Phi98]   W. D. Phillips, *Laser cooling and trapping of neutral atoms*, Rev. Mod. Phys. **70**, 721 (1998).

[Pie04]   P. Pieri, L. Pisani, and G. C. Strinati, *BCS-BEC crossover at finite temperature in the broken-symmetry phase*, Phys. Rev. B **70**, 094508 (2004).

[Pie05]   P. Pieri, L. Pisani, and G. C. Strinati, *Comparison between a diagrammatic theory for the BCS-BEC crossover and quantum Monte Carlo results*, Phys. Rev. B **72**, 012506 (2005).

[Pin97]   P. W. H. Pinkse, A. Mosk, M. Weidemüller, M. W. Reynolds, T. W. Hijmans, and J. T. M. Walraven, *Adiabatically Changing the Phase-Space Density of a Trapped Bose Gas*, Phys. Rev. Lett. **78**, 990 (1997).

[Pit61]   L. P. Pitaevskii, *Vortex lines in an imperfect Bose gas*, Sov. Phys. JETP **13**, 451 (1961).

[Pit98]   L. Pitaevskii and S. Stringari, *Elementary Excitations in Trapped Bose-Einstein Condensed Gases Beyond the Mean-Field Approximation*, Phys. Rev. Lett. **81**, 4541 (1998).

[Pit03]   L. Pitaevskii and S. Stringari, *Bose-Einstein Condensation*, Oxford University Press, 2003.

[Raa87]   E. L. Raab, M. Prentiss, A. Cable, S. Chu, and D. E. Pritchard, *Trapping of Neutral Sodium Atoms with Radiation Pressure*, Phys. Rev. Lett. **59**, 2631 (1987).

[Ran95]   M. Randeria, *Crossover from BCS Theory to Bose-Einstein Condensation*, in: A. Griffin, D. Snoke, and S. Stringari (Eds.), *Bose-Einstein Condensation*, 355–392, Cambridge Univ. Press, Cambridge, 1995.

[Reg03]   C. A. Regal, C. Ticknor, J. L. Bohn, and D. S. Jin, *Creation of ultracold molecules from a Fermi gas of atoms*, Nature **424**, 47 (2003).

[Reg04]   C. A. Regal, M. Greiner, and D. S. Jin, *Observation of Resonance Condensation of Fermionic Atom Pairs*, Phys. Rev. Lett. **92**, 040403 (2004).

[Rie04]   S. Riedl, *Untersuchung stark wechselwirkender fermionischer Quantengase mittels Absorptionsabbildung*, diploma thesis, Universität Innsbruck (2004).

[Roa02]   G. Roati, F. Riboli, G. Modugno, and M. Inguscio, *Fermi-Bose Quantum Degenerate ^{40}K-^{87} Rb Mixture with Attractive Interaction*, Phys. Rev. Lett. **89**, 150403 (2002).

References

[Ryc04]   D. Rychtarik, B. Engeser, H.-C. Ngerl, and R. Grimm, *Two-Dimensional Bose-Einstein Condensate in an Optical Surface Trap*, Phys. Rev. Lett. **92**, 173003 (2004).

[Sch99]   U. Schünemann, H. Engler, R. Grimm, M. Weidemüller, and M. Zielonkowski, *Simple scheme for tunable frequency offset locking of two lasers*, Rev. Sci. Instr. **70**, 242 (1999).

[Sch01]   F. Schreck, L. Khaykovich, K. L. Corwin, G. Ferrari, T. Bourdel, J. Cubizolles, and C. Salomon, *Quasipure Bose-Einstein Condensate Immersed in a Fermi Sea*, Phys. Rev. Lett. **87**, 080403 (2001).

[Sch05]   C. H. Schunck, M. W. Zwierlein, C. A. Stan, S. M. F. Raupach, W. Ketterle, A. Simoni, E. Tiesinga, C. J. Williams, and P. S. Julienne, *Feshbach resonances in fermionic 6Li*, Phys. Rev. A **71**, 045601 (2005).

[Sil05]   C. Silber, S. Gunther, C. Marzok, B. Deh, P. W. Courteille, and C. Zimmermann, *Quantum-Degenerate Mixture of Fermionic Lithium and Bosonic Rubidium Gases*, Phys. Rev. Lett. **95** (2005).

[Sin96]   K. G. Singh and D. S. Rokhsar, *Collective Excitations of a Confined Bose Condensate*, Phys. Rev. Lett. **77**, 1667 (1996).

[SK98a]   D. M. Stamper-Kurn, H.-J. Miesner, A. P. Chikkatur, S. Inouye, J. Stenger, and W. Ketterle, *Reversible Formation of a Bose-Einstein Condensate*, Phys. Rev. Lett. **81**, 2194 (1998).

[SK98b]   D. M. Stamper-Kurn, H.-J. Miesner, S. Inouye, M. R. Andrews, and W. Ketterle, *Collisionless and Hydrodynamic Excitations of a Bose-Einstein Condensate*, Phys. Rev. Lett. **81**, 500 (1998).

[Str96]   S. Stringari, *Collective Excitations of a Trapped Bose-Condensed Gas*, Phys. Rev. Lett. **77**, 2360 (1996).

[Str03]   K. E. Strecker, G. B. Partridge, and R. G. Hulet, *Conversion of an Atomic Fermi Gas to a Long-Lived Molecular Bose Gas*, Phys. Rev. Lett. **91**, 080406 (2003).

[Str04]   S. Stringari, *Collective oscillations of a trapped Fermi gas near a Feshbach resonance*, Europhys. Lett. **65**, 749 (2004).

[Str05]   S. Stringari (2005), private communication.

[Tie93]   E. Tiesinga, B. J. Verhaar, and H. T. C. Stoof, *Threshold and resonance phenomena in ultracold ground-state collisions*, Phys. Rev. A **47**, 4114 (1993).

[Tim01]   E. Timmermans, K. Furuya, P. W. Milonni, and A. K. Kerman, *Prospect of creating a composite Fermi-Bose superfluid*, Phys. Lett. A **285**, 228 (2001).

[Tin66]   M. Tinkham, *Introduction to Superconductivity*, McGraw-Hill, New York, 1966.

[Tru01]   A. G. Truscott, K. E. Strecker, W. I. McAlexander, G. B. Partridge, and R. G. Hulet, *Observation of Fermi Pressure in a Gas of Trapped Atoms*, Science **291**, 2570 (2001).

[Urb06]   M. Urban, *Coupling of hydrodynamics and quasiparticle motion in collective modes of superfluid trapped Fermi gases* (2006), http://arxiv.org/cond-mat/0612361.

[Var07]   in: M. Inguscio, W. Ketterle, and C. Salomon (Eds.), *Ultracold Fermi Gases, Proceedings of the International School of Physics "Enrico Fermi", Course CLXIV, Varenna, 20 - 30 June 2006*, ?, ?, 2007.

[Vic00]   L. Vichi, *Collisional Damping of the Collective Oscillations of a Trapped Fermi Gas*, J. Low. Temp. Phys. **121**, 177 (2000).

[Web03]   T. Weber, J. Herbig, M. Mark, H.-C. Nägerl, and R. Grimm, *Bose-Einstein Condensation of Cesium*, Science **299**, 232 (2003).

[Wya92]   J. C. Wyant and K. Creath, *Basic Wavefront Aberration Theory for Optical Metrology*, Applied optics and optical engineering **9** (1992).

[Zha04]   J. Zhang, E. G. M. van Kempen, T. Bourdel, L. Khaykovich, J. Cubizolles, F. Chevy, M. Teichmann, L. Tarruell, S. J. J. M. F. Kokkelmans, and C. Salomon, *P-wave Feshbach resonances of ultra-cold ^6Li*, Phys. Rev. A **70**, 030702(R) (2004).

[Zwi03]   M. W. Zwierlein, C. A. Stan, C. H. Schunck, S. M. F. Raupach, S. Gupta, Z. Hadzibabic, and W. Ketterle, *Observation of Bose-Einstein Condensation of Molecules*, Phys. Rev. Lett. **91**, 250401 (2003).

[Zwi04]   M. Zwierlein, C. A. Stan, C. H. Schunck, S. M. F. Raupach, A. J. Kerman, and W. Ketterle, *Condensation of Pairs of Fermionic Atoms near a Feshbach Resonance*, Phys. Rev. Lett. **92**, 120403 (2004).

[Zwi05]   M. Zwierlein, J. Abo-Shaeer, A. Schirotzek, C. Schunck, and W. Ketterle, *Vortices and Superfluidity in a Strongly Interacting Fermi Gas*, Nature **435**, 1047 (2005).

Acknowledgement

It's time to thank all the people for the help during my time as a PhD-student here in Innsbruck. Experimental physics is teamwork and only together with a good team you will have any success.

I would like to thank my advisor Rudi Grimm for his support and advice. He is an enthusiastic physicist 24 hours a day and knows how to transfer this enthusiasm and fascination for physics to the members of his group.

Without the Li-team, this thesis would not have been possible. Stefan went together with me through ups and downs of the experiment. If you need someone to fix things, he's the man. Matt joined us as a postdoc and was my personal advisor for the English language. In this way the language level of this thesis is not as bad as it would have been. Christoph did a fantastic job during his diploma work. He will hopefully soon rejoin the team and keep on questioning things, which is very helpful in improving the experiment. Edmundo is the most recent member of the Li-team. His background in theory is a valuable contribution to our discussions, but I'm sure he will also become a proper experimentalist. Johannes was a help in the organization of the experiment and a critical proof-reader of papers. Once something written gets his O.K., you needn't worry about any referee's comment. I would also like to thank a lot the former team members Selim and Markus. They introduced me to this startling experiment and taught me a lot of things. Cheng was a unique motivator and excellent physicist at his fruitful stays in Innsbruck. Also Gerhard and Reece as former Li-team members contributed a lot to the success of the experiment. Furthermore, I would like to thank Hélène and Regis for their help during their internships.

I benefited a lot from the know-how, but also from the good working atmosphere in our group. Therefore thank you to Hanns-Christoph, Florian, Francesca, Gabriel, Steven, Devang, Martin, Mattias, Elmar, Sascha, Flo, Almar, Michael, Charly, Stefan, Frederik, Gregor, Eric, Klaus, Birgit, Clarice, Hans, Toni, Manfred, Christian, Andrea, Gabriel, Harald, Andreas, Marie and the former group members Tobias, Bastian, Jens, Matthias, Ina, Antti, Phillipp, Peter, Michael, David and Tino.

Furthermore I thank our secretary Christine for all her help, Manuel and Artur at the electronics workshop, the people at the mechanical workshop and the secretaries.

Thanks to you all!

Schließlich ein großes Danke an meine Familie für die Unterstützung während dieses Kapitels meines Lebens.